Unsteady Evaporation of Water from Wire Mesh Structures at Sub-Atmospheric Pressures

Dissertation

Rahel Volmer

TECHNISCHE
UNIVERSITÄT
DARMSTADT

Fraunhofer
ISE

Unsteady Evaporation of Water from Wire Mesh Structures at Sub-Atmospheric Pressures

DISSERTATION

by

Rahel Volmer

submitted in fulfillment of the requirements for the degree of

Doktor-Ingenieur (Dr.-Ing.)

at the Department of Mechanical Engineering

of the Technische Universität Darmstadt

First Examiner:	Prof. Dr.-Ing. Peter Stephan
Second Examiner:	Prof. Dr.-Ing. habil. Andrea Luke

Date of submission:	August 11, 2020
Date of oral examination:	December 16, 2020

Darmstadt 2020

Rahel Volmer:
Unsteady Evaporation of Water from Wire Mesh Structures at Sub-Atmospheric Pressures
Darmstadt (Germany), Technische Universität Darmstadt

Thesis published online on TUprints in 2021
Date of oral examination: December 16, 2020

URN: urn:nbn:de:tuda-tuprints-185748
URL: https://tuprints.ulb.tu-darmstadt.de/id/eprint/18574

VORWORT

Diese Arbeit entstand im Rahmen meiner Beschäftigung und Forschungsaktivitäten am Fraunhofer-Institut für Solare Energiesysteme (ISE) in Freiburg in der Abteilung Wärme- und Kältetechnik. Universitätsseitig wurde sie von Professor Peter Stephan an der Technischen Universität Darmstadt betreut.

Bei Herrn Professor Stephan möchte ich herzlich für die die Begutachtung und Betreuung der Promotion bedanken, sowie bei Frau Professorin Luke für die Übernahme der Zweitbegutachtung. Ein großer Dank gilt Lena Schnabel, die die Arbeit vor Ort am Fraunhofer ISE betreut hat, und die mich in allen Phasen der Promotion begleitet, unterstützt und mit konstruktiven Ratschlägen und Denkanstößen versorgt hat. Ebenfalls möchte ich Gerrit Füldner danken, der fachlich und organisatorisch dazu beigetragen hat, diese Arbeit zu ermöglichen.

Bei den experimentellen Arbeiten konnte ich auf viele helfende Hände zurückgreifen: Vorweg ein Dank an die Firma Haver & Boecker OHG für die Bereitstellung der Drahtgewebe und an das Team der Mechanischen Werkstatt am ISE für das Herstellen diverser Bauteile. Danke an Paolo, der die Proben mit großer Sorgfalt und Hingabe gelötet hat, an Franziska für die Probenreinigung und Messvorbereitungen, an Hendrik und Niccolò für die Zusammenarbeit bei der Entwicklung des Messkonzepts und an das Team Technik für Elektro- und sonstige Arbeiten am Teststand.

Nicht minder wichtig war die moralische Unterstützung von diversen Seiten: Die über die Jahre wechselnde Belegschaft von T-301 hat immer für eine angenehme Arbeitsatmosphäre gesorgt, sei es durch fachliche Diskussionen, unkomplizierte Hilfe bei akuten Büroalltagsproblemchen oder durch eine allgemeine Erbauung mittels freitagabendlicher Ratestündchen aus dem Bereich der „klassischen“ Musik (was der Kollege zu verantworten hat, dem Seite 34 gewidmet ist). Auch möchte ich mich bei allen jenseits der Bürotür bedanken – bei der gesamten ISE-Truppe, die für eine einzigartige Arbeitskultur und ein sehr angenehmes Arbeitsumfeld sorgt.

Ein Riesendank geht an Katharina, Annette und Lisa, die mich mit allerlei Care-Paketen kulinarischer und moralischer Art versorgt und motiviert haben. Auch möchte ich mich bei meinen Mitbewohner(inne)n bedanken, die mir insbesondere in Zeiten des Homeoffice-Marathons regelmäßig aufmunternde Schreibtischpausen beschert haben. Dann gibt es noch einen Haufen weiterer toller Menschen, die ich im Laufe der Jahre kennen lernen durfte und die ich nicht missen möchte. Ohne jede(n) einzelne(n) beim Namen zu nennen – danke an euch alle!

Schließlich danke ich von Herzen meiner Familie, die immer für mich da ist. Ich hätte mir keine andere ausgesucht, selbst wenn man mich gefragt hätte…

ABSTRACT

Adsorption heat pumps and chillers can provide thermal energy with a low carbon footprint, therefore, this technology could contribute to a sustainable future heat and cold supply system. Most adsorption modules work with the refrigerant water at sub-atmospheric pressures, which poses a challenge for effective evaporation and requires a customized design concept for the evaporator heat exchanger. The favorable nucleate boiling regime can hardly be reached under the given boundary conditions. Instead, evaporation from extensive thin refrigerant films on capillary structures represents a promising approach.

This work refers to a heat exchanger concept for compact one-chamber adsorption modules, which employs porous capillary structures for cyclic condensation and evaporation without the need of continuous refrigerant supply. Such a concept necessarily involves unsteady evaporation conditions due to a continuous reduction of the refrigerant charge. Since scientific publications in this field are scarce, this work focuses on investigating unsteady evaporation of water from porous structures at sub-atmospheric pressures on the example of copper wire mesh structures. Special attention is paid to the question, how the transforming refrigerant distribution and heat transfer conditions interact, and how this interaction affects the dynamic evaporation performance. In this context, the impact of different structure geometry parameters (i.e. porosity, pore size, structure height, wire orientation angle) and thermodynamic conditions (vapor saturation pressure, heat flux) on the evaporation mechanisms and performance is addressed. Further questions are, if the evaporation dynamics can be reproduced with a simple mathematical model, and if wire mesh evaporators can finally be considered as a promising approach for the envisaged application.

Investigations were pursued via two methodical approaches: Firstly, unsteady evaporation measurements with wire mesh structure samples of different geometry specifications were conducted. Secondly, a simple resistance-capacitance model was developed which includes time-dependent resistance and capacitance definitions representing the presumed heat transfer components. In both measurements and simulations, the overall heat transfer coefficient of the structure (from structure base temperature to vapor saturation temperature) was used as the main evaluation quantity. Additionally, the refrigerant storage capacities of the capillary structures were evaluated.

Measurements and simulations revealed that the pore size of the mesh structure crucially affects the dynamic refrigerant distribution, refrigerant storage capacity, and evaporation performance for the investigated conditions: Large and medium pore sizes (0.8 mm clear mesh width and larger) involve a predominance of gravitational forces as against capillary forces (large Bond number) which leads to the dewetting pattern of a receding evaporation front. The thermal conduction resistance of the refrigerant-filled section represents the performance-limiting factor in a broad refrigerant charge interval for this dewetting type. A small pore size (0.375 mm clear mesh width), in contrast, implicates distinctly different dewetting and evaporation characteristics which presumably originate from a combination of a receding front and a pattern of wet and dry clusters and which can be ascribed to the increasing impact of capillary forces. Besides a potentially higher refrigerant storage capacity, the investigated structure with smallest pore size also reached the highest overall heat transfer coefficients of up to 23…28 kW/(m²K).

Further analyses of geometry impacts indicated that a low porosity and low structure height are beneficial by trend, however, the optimal choice for these geometry factors depends on the envisaged application case.

In the standard version of the resistance-capacitance model the conception of a receding refrigerant front was implemented. Respective simulations show a fairly good qualitative agreement with the measured evaporation dynamics of structures with large and medium pore size (≥ 0.8 mm). The prediction quality for the dynamics of small pore sizes is poor since for these structures the receding front dewetting characteristics do not apply. An alternative model conception ("receding front + static front") implies possible dewetting mechanisms of fine pored structures and yields a better agreement with the respective measurements. Quantitative simulation results from the standard "receding front" approach match the measurement results quite well in several cases, however, the outcomes adumbrate that certain model parameters are imprecise. Despite the necessity for a revision of these definitions, the developed evaporation model is considered as a valuable tool for the prediction of unsteady evaporation processes. Integrated into a model on heat exchanger level it could potentially serve a basis for dimensioning methods.

In order to assess the tested mesh structures with regard to the envisaged application, thermal transmittance (UA) and refrigerant storage capacity were referred to the structure volume which usually represents a critical design factor. On structure level the volume-specific thermal transmittance equals the structure-height-specific overall heat transfer coefficient, which is used as the assessment quantity for heat transfer on structure level. Here, the heat transfer coefficient refers to the temperature difference between structure base and saturation temperature of the vapor atmosphere. Considering the diverging requirements of a power-focused versus efficiency-(COP-)focused adsorption module design, the mesh structure with smallest pore size (0.375 mm clear mesh width) and medium structure height (10 mm) showed the best suitability for both cases (with a structure-volume-specific refrigerant storage capacity of about 850 kg/m^3 and a structure-height-specific optimal mean heat transfer coefficient of 1350… 2500 kW/(m^{3}K), depending on the required refrigerant turnover). A structure type with medium pore size (0.9 mm clear mesh width) and low structure height (5 mm) proved to be the second-best variant.

These two most promising structure types were used for a potential assessment of a hypothetical wire mesh evaporator heat exchanger. A round tube heat exchanger design with external porous structure was assumed. Its geometry was adapted to a specific finned tube heat exchanger for partially flooded continuous operation which is one of the best-performing evaporators among current research activities and which was employed as an ambitious reference. The calculated absolute thermal transmittance values (UA values) reveal that the potential of advanced mesh structures can only be exploited if a sufficiently high fluid-side heat transfer is ensured. As an assessment quantity on heat exchanger level the construction-volume-specific UA value was used, which refers to the temperature difference between heat transfer fluid inside the tube and saturation temperature of the vapor atmosphere, and to the construction volume of the entire heat exchanger. From the estimation results it can be deduced that – depending on the considered conditions – the hypothetical mesh evaporator could reach similar construction-volume-specific UA values (ranging up to 1000 kW/(m^{3}K)) as the highly efficient reference evaporator. An optimization of the structure geometry – such as a reduction of pore size and porosity and modification of the structure height – is expected to allow for-further improvements. For a cyclic operation in one-chamber adsorption modules a mesh evaporator could prove particularly advantageous due to its low required refrigerant mass. Furthermore, it involves a high constructional flexibility. These outcomes suggest that the integration of wire mesh structures in an evaporator in cyclic operation is generally a promising approach for the application in adsorption heat pumps and chillers, and that further investigations are justified.

KURZFASSUNG

Adsorptionswärmepumpen und –kältemaschinen können thermische Energie mit geringem CO_2-Fußabdruck bereitstellen, daher könnte diese Technologie in Zukunft zu einem nachhaltigen Wärme- und Kälteversorgungssystem beitragen. Die meisten Adsorptionsmodule werden mit dem Kältemittel Wasser in einem niedrigem Druckbereich betrieben, was hinsichtlich des Ziels einer effektiven Verdampfung eine Herausforderung darstellt und angepasste Verdampferkonzepte erfordert. Das vorteilhafte Regime des Blasensiedens kann unter den gegebenen Randbedingungen kaum erreicht werden; hingegen stellt die Verdampfung aus ausgedehnten dünnen Kältemittelfilmen auf Kapillarstrukturen einen vielversprechenden Ansatz dar.

Die vorliegende Arbeit bezieht sich auf ein Wärmeübertragerkonzept für kompakte Einkammeradsorptionsmodule, bei dem poröse Kapillarstrukturen für eine zyklische Kondensation und Verdampfung verwendet werden, ohne dass eine kontinuierliche Kältemittelzufuhr nötig ist. Solch ein Konzept ist aufgrund der kontinuierlichen Reduktion der Kältemittelbeladung zwangsläufig mit instationären Verdampfungsbedingungen verbunden. Da kaum wissenschaftliche Veröffentlichungen zu dieser Thematik verfügbar sind, befasst sich diese Arbeit mit der Untersuchung instationärer Verdampfung von Wasser aus porösen Strukturen im subatmosphärischen Druckbereich anhand von Drahtgewebestrukturen aus Kupfer. Ein besonderes Augenmerk ist dabei auf die Frage gerichtet, wie die sich ändernde Kältemittelverteilung und die Wärmeübertragungsverhältnisse sich wechselseitig beeinflussen und wie sich diese Wechselwirkung auf die dynamische Verdampfungseffektivität auswirkt. In diesem Kontext wird auch der Einfluss verschiedener Strukturgeometrieparameter (Porosität, Porengröße, Strukturhöhe, Ausrichtungswinkel der Drähte) und thermodynamischer Parameter (Sättigungsdampfdruck, Wärmestromdichte) auf die Verdampfungsmechanismen und –effektivität betrachtet. Weitere Fragestellungen sind, ob die Verdampfungsdynamik mithilfe eines einfachen Modells abgebildet werden kann und schließlich, ob Drahtgewebeverdampfer als aussichtsreicher Ansatz für die vorgesehene Anwendung betrachtet werden können.

Die Untersuchungen wurden mit zwei methodischen Ansätzen verfolgt: Erstens wurden instationäre Verdampfungsmessungen mit Drahtgewebestrukturen verschiedener Geometriespezifikationen durchgeführt. Zweitens wurde ein einfaches Widerstände-Kapazitäten-Modell entwickelt, dessen Beschreibungen zeitabhängiger Widerstände und Kapazitäten die angenommenen Wärmeübertragungskomponenten repräsentieren. Sowohl für die Messungen als auch für die Simulationen wurde der Wärmedurchgangskoeffizient der porösen Struktur (von der Temperatur der Strukturbasis bis zur Sättigungstemperatur des Dampfraums) als primäre Auswertungsgröße verwendet. Zusätzlich wurden die Kältemittelhaltekapazitäten der Kapillarstrukturen bewertet.

Wie Messungen und Simulationen zeigten, hat die Porengröße unter den betrachteten Bedingungen einen entscheidenden Einfluss auf die dynamische Kältemittelverteilung, das Kältemittelhaltevermögen und die Verdampfungseffektivität: Bei großen und mittleren Porengrößen (0.8 mm lichte Maschenweite und größer) überwiegt die Wirkung von Gravitationskräften gegenüber Kapillarkräften (hohe Bond-Zahl), was zu einer Entnetzungscharakteristik in Form einer absinkenden Verdampfungsfront führt. Der Wärmeleitwiderstand des kältemittelgefüllten Bereiches stellt bei diesem Entnetzungsschema in einem weiten Kältemittelbeladungsbereich den leistungslimitierenden Faktor dar. Eine geringe Porengröße (0.375 mm

lichte Maschenweite) hingegen ist mit einer deutlich abweichenden Entnetzungs- und Verdampfungscharakteristik verbunden, die mutmaßlich von einer Kombination aus absinkender Front und einer Verteilung von gefüllten und trockenen Strukturbereichen herrührt und auf den zunehmenden Einfluss von Kapillarkräften zurückzuführen ist. Neben der potenziell größeren Kältemittelhaltekapazität erreichte die Struktur mit der geringsten Porengröße auch die höchsten Wärmedurchgangskoeffizienten von bis zu 23…28 kW/(m²K).

Die Analyse der Einflüsse weiterer Geometrieparameter ergab, dass eine geringe Porosität sowie eine niedrige Strukturhöhe tendenziell vorteilhaft sind; allerdings hängt die Wahl der optimalen Werte von den Anforderungen des jeweiligen Anwendungsfalls ab.

In der Standardversion des Widerstände-Kapazitäten-Modells wurde die Modellvorstellung einer absinkenden Kältemittelfront implementiert. Entsprechende Simulationen zeigen eine recht gute qualitative Übereinstimmung mit der gemessenen Verdampfungsdynamik von Strukturen mit großen und mittleren Porengrößen (≥ 0.8 mm). Die Abbildungsqualität für die Verdampfungsdynamik kleiner Porengrößen ist dürftig, da für diese Strukturen die Entnetzungscharakteristik einer absinkenden Verdampfungsfront nicht zutrifft. Eine alternative Modellvorstellung („absinkende Front + statische Front“ / “receding front + static front”) basiert auf möglichen Entnetzungsmechanismen feiner Strukturen und führt zu einer besseren Übereinstimmung mit entsprechenden Messungen. Die quantitativen Simulationsergebnisse des standardmäßigen „Absinkende Front“-Ansatzes entsprechen den Messergebnissen in diversen Fällen recht gut, allerdings deuten die Resultate auf eine Ungenauigkeit der Definitionen bestimmter Modellparameter hin. Trotz des Überarbeitungsbedarfs dieser Parameterdefinitionen wird das entwickelte Verdampfungsmodell als nützliches Instrument für die Abbildung instationärer Verdampfungsprozesse beurteilt. Integriert in ein Modell auf Wärmeübertragerebene könnte es potenziell als Basis für Auslegungsmethoden dienen.

Um die vermessenen Gewebestrukturen in Hinblick auf die vorgesehene Anwendung zu bewerten, wurden die Wärmedurchlässigkeit (UA) und die Kältemittelhaltekapazität auf das Strukturvolumen bezogen, das üblicherweise einen kritischen Auslegungsfaktor darstellt. Auf Strukturebene entspricht die volumenspezifische Wärmedurchlässigkeit dem strukturhöhenspezifischen Wärmedurchgangskoeffizienten, der als Bewertungsgröße für die Wärmeübertragung auf Strukturebene verwendet wurde. Dabei bezieht sich der Wärmedurchgangskoeffizient auf die Temperaturdifferenz zwischen Strukturbasis und Sättigungstemperatur des Dampfraums. Unter Berücksichtigung der divergierenden Anforderungen eines wärmeleistungsorientierten versus effizienz-(COP-)orientierten Adsorptionsmodulkonzepts erwies sich die Gewebestruktur mit geringster Porengröße (0.375 mm lichte Maschenweite) und mittlerer Strukturhöhe (10 mm) für beide Fälle als am besten geeignet (mit einer strukturvolumenspezifischen Kältemittelhaltekapazität von ca. 850 kg/m³ und einem strukturhöhenspezifischen optimalen mittleren Wärmedurchgangskoeffizienten von 1350…2500 kW/(m³K), je nach gefordertem Kältemittelumsatz). Als zweitbeste Struktur stellte sich die Variante mit mittlerer Porengröße (0.9 mm lichte Maschenweite) und niedriger Strukturhöhe (5 mm) heraus.

Diese beiden aussichtsreichsten Strukturvarianten wurden für eine Potentialabschätzung eines hypothetischen Drahtgewebewärmeübertragers herangezogen. Es wurde die Bauform eines Rundrohrwärmeübertragers mit äußerlich angebrachter poröser Struktur angenommen. Seine Geometrie wurde angepasst an einen Rippenrohrwärmeübertrager für teilgefluteten, kontinuierlichen Betrieb, dessen Leistungskenngrößen im Vergleich aktueller Forschungsaktivitäten Spitzenwerte erreichen und der hier als ambitionierte Referenz verwendet wurde. Die berechneten Wärmedurchlässigkeitswerte (UA-Werte) machen deutlich, dass das Potenzial effizienter Gewebestrukturen nur ausgenutzt werden kann, wenn ein ausreichend hoher fluidseitiger Wärmeübergang gewährleistet wird. Als Bewertungsgröße auf Wärmeübertragerebene wurde der konstruktionsvolumenspezifische UA-Wert herangezogen, der sich auf die

Temperaturdifferenz zwischen Wärmeträgerfluid im Rohr und Sättigungstemperatur des Dampfraums bezieht, sowie auf das Konstruktionsvolumen des gesamten Wärmeübertragers. Aus den Abschätzungen kann geschlussfolgert werden, dass der hypothetische Gewebeverdampfer – je nach betrachteten Bedingungen – ähnliche konstruktionsvolumenspezifische UA-Werte (von bis zu 1000 kW/(m³K)) erreichen könnte wie der höchsteffiziente Referenzverdampfer. Von einer Optimierung der Strukturgeometrie – beispielsweise in Form einer Reduktion von Porengröße und Porosität sowie einer Anpassung der Strukturhöhe – werden weitere Effizienzsteigerungen erwartet. Für den zyklischen Betrieb in Einkammer-Adsorptionsmodulen könnte sich ein Gewebeverdampfer als besonders vorteilhaft erweisen, da er mit einer sehr geringen Kältemittelmasse auskommt. Zusätzlich erlaubt er ein hohes Maß an baulicher Flexibilität. Diese Ergebnisse lassen darauf schließen, dass die Integration von Drahtgewebestrukturen in einen zyklisch betriebenen Verdampfer grundsätzlich ein vielversprechender Ansatz für den Einsatz in Adsorptionswärmepumpen und –kältemaschinen ist und dass weitere Untersuchungen durchaus gerechtfertigt sind.

TABLE OF CONTENTS

1 INTRODUCTION & MOTIVATION

In this chapter the technological context and envisaged application of the investigations of this work are depicted. The relevance of the field and incorporated challenges are outlined and the motivation for research on the topic is deduced. Finally, a brief overview of the work's structure is given.

Space heating, cooling and domestic hot water supply represent a large fraction of the primary and final energy demand in the European Union (European Commission, Directorate-General for Energy 2016; Pezzutto et al. 2019). Given that the predominant share of energy transformation still relies on the combustion of fossil fuels, heating and cooling applications implicate a considerable contribution to CO_2 emissions and thereby to global warming. A transition to a sustainable energy supply system, which several countries strive for, requires a variety of technological solutions, amongst others in the heating and cooling sector. Thermally driven heat pumps and chillers could make a contribution to that transition by reducing the primary energy demand for domestic heating and cooling (Núñez et al. 2007). As the name implies, this category of heat pumps uses heat instead of electric energy to drive the thermodynamic cycle; heat which can for instance be provided by solar thermal collectors, industrial waste heat or fuel gas. Even if fossil gas is used instead of renewable gas, the energy utilization ratio of the fossil fuel can be increased compared to gas boilers (Meunier 2013; Núñez et al. 2007) due to the integration of low temperature heat, e.g. from a ground-coupled or borehole heat exchanger or from the ambient air. Hence, thermally driven heat pumps might – at least to some extent – replace conventional boilers which currently represent an enormous market share in space heating devices (Meunier 2013).

Thermally driven heat pumps and chillers are usually subdivided into absorption and adsorption heat transformation devices. Their basic functionality and thermodynamic cycle is for instance described in (Kühn and Ziegler 2013), (Critoph and Zhong 2005), (Demir et al. 2008), and (Meunier 2001). For a better readability both the heating and the refrigeration application are summarized with the term "heat pump" in the subsequent text since both are based on the same thermodynamic cycle. In opposition to compression heat pumps, both absorption and adsorption heat pumps do not employ a mechanical compressor but use a so-called "thermal compressor" instead. The concept of thermal compression is based on the absorption or adsorption of refrigerant vapor in / on a liquid (for absorption systems) or solid (for adsorption systems) working medium which provokes the release of heat. In case of the adsorption system – which is the relevant application for this work – the solid adsorbent is connected to a heat exchanger which is operated in a cyclic sequence at a medium and high temperature level. During the medium temperature half-cycle, refrigerant is adsorbed on the heat exchanger and the released heat can be used for domestic heating (in heat pump operation) or it is rejected to a heat sink (in chiller operation). In the high temperature half-cycle, the driving heat source is connected to the heat exchanger which causes desorption of the refrigerant from the adsorbent. In order to complete the thermal compressor concept an evaporator, condenser, and usually an expansion valve are integrated in the system. Heat from the low temperature source (ambient heat source in case of heat pump operation or extracted heat from the air-conditioned room in case of chiller operation) provides the enthalpy of vaporization for the evaporation process. In the condenser the released heat of vaporization is used for heating (heat pump) or rejected to

a heat sink (chiller). Due to the difference in equilibrium temperatures between the adsorption (desorption) and the evaporation (condensation) process at a given system pressure in the pure refrigerant atmosphere, heat can be virtually "pumped" from a lower to a higher temperature level.

Resulting from the necessity for cyclic operation, often two adsorber heat exchangers are included in one adsorption module and operated in shifted adsorption / desorption phases in order to realize a quasi-continuous process (Kühn and Ziegler 2013) (cf. Figure 1, left). The adsorption module then additionally contains an evaporator heat exchanger and a condenser heat exchanger which both run continuously and are by turns connected to the respective adsorber by means of flap valves. A different module concept, consisting of a single chamber, incorporates only one adsorber heat exchanger and one heat exchanger which alternately acts as evaporator and condenser (Wittstadt et al. 2017; Mittelbach and Daßler 2011; Chang et al. 2007) (cf. Figure 1, right). Such a design has the advantages of potentially being very compact (Chang et al. 2007) – which is a crucial factor for the success of the technology on the domestic heating market (Clausse et al. 2011) – and requiring neither valves nor a throttle or refrigerant pump. Drawbacks can be that a) a single module can only provide useful cooling energy in an intermittent manner, that b) the periodic shift of the evaporator-condenser between two temperature levels causes capacitive heat losses which diminish efficiency, and that c) the evaporator-condenser heat exchanger must be suited for both tasks and needs to operate in a dynamic, unsteady way.

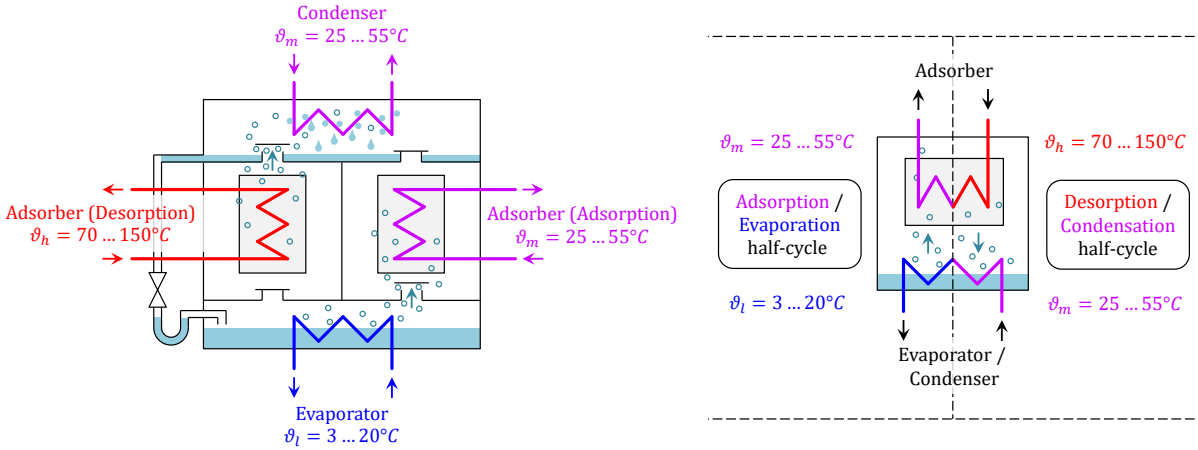

Figure 1: Schematic drawings of different adsorption module concepts with typical temperature ranges for devices with water as refrigerant: four-chamber module with two adsorber heat exchangers and separate evaporator and condenser heat exchanger (left); compact one-chamber module with one adsorber and one evaporator-condenser heat exchanger in alternating operation (right)

The performance of an adsorption heat pump or chiller is usually characterized by its mean useful heating or cooling power and by its efficiency. The latter is typically expressed in form of the coefficient of performance (COP) which is defined as the ratio of useful heat output (heating case) or input (cooling case) to the driving heat input on high temperature level (Kühn and Ziegler 2013). The two performance indicators, power and COP, are generally opposing optimization criteria as they represent a tradeoff: Due to the necessity of operating the adsorption / desorption process in a cyclic manner between two different temperature levels, the capacitive heat flows to or from the adsorber heat exchanger considerably influence the energy balance and lowers the useful energy. In order to reach a high COP it is consequently advisable to run the adsorption and desorption half-cycle until close to equilibrium conditions in order to exploit maximum useful energy per half-cycle in relation to the energy input. On the other hand, adsorption kinetics usually provoke a strongly dynamic power output over time with a maximum in the very beginning and a subsiding characteristic in the later phase. A high-power design target for the adsorption module consequently requires a rather early break-off of the adsorption and desorption

process (short half-cycle times), in order to avoid the low-power conditions close to adsorption equilibrium.

Besides the impact of control strategy, heat recovery concepts etc. the performance of a machine in terms of useful power output and efficiency (COP) is substantially determined by the heat exchanger design and the associated heat and mass transfer characteristics. The suitability of a certain heat exchanger design (for adsorber, evaporator and condenser) can accordingly not be judged universally but it strongly depends on the envisaged design target of the adsorption heat pump or chiller: For a high COP cyclically operated heat exchangers should be able to take up and release a large amount of refrigerant in relation to their sizes and thermal masses to minimize capacitive heat losses. In case a high power is prioritized, minimization of heat and mass transfer resistances within the heat exchangers is an essential factor, and maximization of the absolute thermal transmittance (UA value), respectively.

Various research activities in the last decades were dedicated to the improvement of the adsorber heat exchanger, e.g. by coating or direct crystallization of the adsorbent on an extended heat exchanger surface (Schnabel et al. 2018a; Wittstadt et al. 2015; Kummer et al. 2015). In order to avoid a performance limitation of the module, originating from the condenser's or especially from the evaporator's side, the development of enhanced evaporator concepts is likewise the objective of several research projects, including the activities related to this work.

Most commercial and prototypal adsorption heat pump systems use water (R-718) as refrigerant, in combination with e.g. silica gel or zeolite as adsorbent material (Demir et al. 2008; Critoph 2013; Critoph and Zhong 2005). Water as a refrigerant has several advantages: It has a high specific enthalpy of vaporization, is cheap and abundantly available, it is nontoxic, environmentally friendly (Kühn and Ziegler 2013) and has a global warming potential (GWP) of zero (Dawoud 2013). (The last-mentioned issues have recently gained relevance in the European Union due to the "New F-Gas Regulation 517/2014" which progressively restricts the permitted sales volume for hydrofluorocarbon (HFC) refrigerants in the EU (The European Parliament and the Council of the European Union 4/16/2014).) On the other hand water as refrigerant involves certain challenges: Major drawback is its very low vapor pressure and vapor density in the envisaged temperature range which can make it challenging to provide a sufficient evaporation power. For common target evaporation temperatures of about 3…20°C the corresponding saturation pressures only amount to about 0.76…2.3 kPa and the saturated vapor densities are in the range of 0.006…0.017 kg/m^3. A reasonable evaporation power implies huge vapor volume flow rates which entails the need for large construction volumes. The sub-atmospheric pressure regime requires the utilization of vacuum-tight vessels and components (Kühn and Ziegler 2013). Due to the freezing point at 0°C the feasible evaporation temperatures of water are restricted to the range above 0°C (Kühn and Ziegler 2013). The low pressure conditions further entail some peculiarities for the evaporation of water (cf. chapter 2.2) which make the design of an efficient evaporator more difficult and preclude the usage of some common evaporator concepts. For instance, the favorable nucleate boiling regime can hardly be realized in a reasonable way under the given boundary conditions (Schnabel et al. 2010, 2011; Witte 2016; Schnabel et al. 2018b; Seiler et al. 2019). To overcome these challenges, different evaporation approaches and heat exchanger concepts have been developed (cf. chapter 2.1), for instance based upon the creation of extensive thin refrigerant films which enable efficient evaporation from three-phase contact lines (cf. chapter 2.3). Although some of these approaches are promising, they are often associated with dis-advantages and difficulties for the practical application. Especially for the compact one-chamber module type with a combined evaporator-condenser heat exchanger in cyclic operation most state-of-the-art evaporators are not adequate, amongst others due to their considerable thermal mass.

Against this background, the research activities described in this work were dedicated to the investigation of a novel approach for effective evaporation of water in adsorption heat pumps and chillers with cyclically

operated evaporator-condenser: Its core principle is the usage of a metallic porous structure which can store refrigerant by capillary action in the condensation half-cycle and provides an extensive surface area for the formation of thin refrigerant films which enable efficient evaporation (cf. chapter 2.4). As an exemplary porous structure type, a matrix of parallel vertical copper wire mesh strips was chosen, whose edges are soldered onto the surface of the heat source. This kind of structure promises an excellent thermal conductivity in heat transfer direction, it is easy to process and it is a low-cost material available in various geometric variants. Since the total heat exchanger surface is available for condensation while evaporation is mostly restricted to the contact line regions, the condensation performance is usually not the limiting factor and consequently this work focuses on the evaporation process. A peculiarity of the cyclic operational concept is that evaporation is a dynamic, unsteady process due to the gradual reduction of refrigerant mass. In order to augment the understanding of occurring dewetting phenomena and associated heat transfer mechanisms, experiments were carried out, complemented by the development of a heat transfer model. Methods and results of these research activities are documented in the following chapters:

- **Chapter 2 – Theoretical Background & State of the Art**
  Chapter 2 provides an overview of the state-of-the-art heat exchanger concepts used as evaporators for adsorption heat pumps (2.1). Besides, a literature review on the peculiarities of evaporation at sub-atmospheric pressures (2.2), on evaporation in the vicinity of three-phase contact lines (2.3) and on evaporation from porous structures (2.4) is presented, which are essential fundamentals for the understanding of the evaporation mechanisms investigated in this work. Existing model approaches for relevant evaporation processes are described and compared in terms of level of detail and scope of applicability (2.5). Furthermore, basics on wetting and capillarity, and the particular dewetting behavior of porous structures are addressed (2.6).

- **Chapter 3 – Objectives of the Work**
  Bearing in mind the boundary conditions of the application, the third chapter contrasts existing evaporator designs and knowledge on occurring heat transfer mechanisms with requirements of an efficient and practicable evaporator concept, especially for adsorption modules with a combined evaporator-condenser in cyclic operation. Successful approaches as well as deficiencies and challenges are identified, and a novel approach established in this work – which aims at overcoming those challenges – is presented. From the general goal of understanding the occurring evaporation mechanisms and developing methods for their description, practical objectives for this work are deduced.

- **Chapter 4 – Methods**
  In chapter 4 the employed methods are addressed. Experiments on the evaporation from different wire mesh samples are described, as well as an evaporation model which was designed to reproduce the experiments and to potentially serve as a basis for heat exchanger dimensioning.

- **Chapter 5 – Results & Discussion**
  In chapter 5 measurement and simulation results are presented. Evaporation dynamics are analyzed and related to heat transfer and dewetting mechanisms. The impact of structure geometry parameters and process parameters on the evaporation performance is investigated. By comparing measurement results and simulations for different parameter sets, the quality and scope of validity of the evaporation model is evaluated. Finally, the tested mesh structure variants are assessed in terms of their suitability for the envisaged application and a potential estimation for a hypothetic wire mesh evaporator is presented.

- **Chapter 6 – Summary, Conclusion & Outlook**
  In the last chapter major outcomes and conclusions of the work are summarized. Contrasted with the requirements of the intended application and with the objectives of the work, a review is made on which goals could be achieved and which aspects still involve open questions or challenges. An estimation of the prospects of the evaporation approach for the application in adsorption heat pumps / chillers is given and requirements for further research or development activities are depicted.

- **Appendix**
  Additional information on employed methods is provided in the appendix. This includes information on the experimental setup, procedure and data reduction, as well as data, definitions and calculation methods used for the evaporation model.

2 THEORETICAL BACKGROUND & STATE OF THE ART

This chapter summarizes relevant fundamentals and state of the art of science and technology in the considered field: Firstly, the characteristics of evaporator heat exchangers for adsorption heat pumps and chillers are described and an overview of different evaporator concepts for the said application is given (2.1). Subsequently, the peculiarities of evaporation of the refrigerant water at sub-atmospheric pressures are addressed (2.2). Scientific findings on evaporation in the vicinity of three-phase contact lines (2.3) and from porous structures (2.4) are presented, including respective modeling approaches (2.5). Finally, aspects of capillarity and dewetting dynamics of porous structures are delineated (2.6).

2.1 Evaporators for Adsorption Heat Pumps and Chillers

As mentioned in the introduction, adsorption heat pumps implicate rather unusual boundary conditions for the evaporation process in these devices: In many systems water is used as refrigerant since it has a high specific enthalpy of vaporization, is non-toxic, environmentally friendly and well-suited as a counterpart to the common adsorbents silica gel and zeolites (Critoph and Zhong 2005; Kühn and Ziegler 2013). Depending on the design and requirements of the particular device, evaporation temperatures are typically in the range of 3…20°C (an exemplary overview on applied evaporation temperatures from different research projects can be found in (Demir et al. 2008)) which corresponds to vapor saturation pressures of about 0.76…2.3 kPa (cf. vapor pressure curve in Figure 74 in the appendix). In consideration of this sub-atmospheric pressure range all components within the refrigerant circuit need to comply with vacuum standards, including the evaporator. In addition to leakage, special attention needs to be paid to corrosion prevention since already very small concentrations of non-condensable gases within the refrigerant circuit can severely impede the phase-change processes (Crößmann 2016; Seiler et al. 2020; Wang and Tu 1988) and thereby reduce the module's power output. Besides these direct implications, the sub-atmospheric pressure range in combination with the refrigerant properties substantially affects the evaporation conditions, as described in chapter 2.2. As a result, many conventional evaporator designs and operational modes are not suitable for these conditions but the evaporation concept needs to be adapted to the special circumstances: Due to the low vapor density and vapor pressure of water an open volume must be provided for evaporation. Flow boiling concepts are accordingly not suitable due to their comparably small duct dimensions and large pressure drop. Inducing bubble formation in a pool boiling setup with a plain heated surface in the low pressure range requires very high driving temperature differences (wall superheat) of more than 15 K (Schnabel et al. 2018b; Schnabel et al. 2008b; Giraud et al. 2016), as pointed out in chapter 2.2. In the adsorption module context, though, only rather low driving temperature differences for the evaporation can reasonably be provided in respect of the overall system performance – Schnabel et al. state temperature differences of up to 5 K as feasible (Schnabel et al. 2011, 2010) and Witte specifies a target value of maximum 7 K (Witte 2016). Therefore, the advantageous nucleate boiling regime can hardly be reached (Schnabel et al. 2010, 2011; Witte 2016; Schnabel et al. 2018b; Seiler et al. 2019) and a conventional pool boiling concept is not a reasonable solution. Instead, methods for facilitated bubble formation are required or a different evaporation concept must be

employed like evaporation from thin refrigerant films where the impact of hydrostatic pressure on evaporation is negligible.

Based on the application-related boundary conditions and peculiarities, the major requirements for an evaporator for adsorption heat transformation devices can be summarized as follows:

- High absolute thermal transmittance (UA value) under the given low pressure boundary conditions and under the given constructional constraints (e.g. construction volume, weight, manufacturability, etc.)
- Sufficient refrigerant supply (for cyclic evaporator-condenser heat exchangers with capillary structure: sufficient refrigerant storage capacity)
- Small construction volume
- Void space for vapor flow / low pressure drop (open design on refrigerant side)
- Low thermal mass of heat exchanger and refrigerant (in case of cyclic evaporator -condenser heat exchangers)
- High reliability
- Vacuum tightness
- Corrosion resistance
- Low cost

The first two points of this list are directly linked with the two general and competing optimization targets for adsorption heat pumps and chillers, which were introduced in chapter 1: In case of a high heating or cooling power target, a high UA value of the evaporator is top priority. A high-efficiency (high-COP) machine, on the other hand, primarily requires an evaporator which can reliably provide enough vapor during the complete adsorption half-cycle, even at low driving forces. For the special case of combined evaporator-condenser heat exchangers in cyclic operation without continuous refrigerant supply this means that a sufficient refrigerant mass must be stored in the heat exchanger structure.

Evaporators used in commercially available adsorption heat pumps and scientific works on respective evaporator development pursue various approaches to cope with the special requirements of water evaporation. Basically, the state of the art of water evaporation concepts can be subdivided into five groups: 1. Conventional partially flooded evaporation, 2. Facilitated nucleate boiling, 3. Falling film evaporation, 4. Capillary-assisted partially flooded evaporation and 5. Cyclic evaporation from capillary structures. Particular features and exemplary design configurations from these groups are depicted in separate paragraphs below.

An overview of exemplary performance data from publications on different evaporator concepts is given in Table 1. A direct comparison of the stated values, though, is often hardly possible: Firstly, measurements were mostly made at different thermodynamic conditions which can strongly influence the performance. Secondly, several different assessment quantities are used (refrigerant-side heat transfer coefficient – termed h_{rf} or U_{rf} in Table 1, overall heat transfer coefficient $U_{fl,rf}$ from heat transfer fluid to vapor atmosphere, absolute thermal transmittance UA, construction-volume-specific thermal transmittance UA/V_{cnstr}), and a conversion is not always possible with the available specifications. Moreover, the definitions of the assessment quantities are not always identical: The driving temperature difference $\Delta\vartheta$ can for instance be defined as a wall superheat or as a logarithmic mean temperature difference $\Delta\vartheta_{lm}$, and its respective temperature inputs are occasionally determined differently. The reference area A_{ref} – required for a translation between evaporation power and heat transfer coefficients – can likewise be defined in various ways, especially when heat exchanger geometries become more complex.

Table 1: Literature survey of exemplary performance data of water evaporators for sub-atmospheric pressure applications (approximate values)

Reference	Heat exchanger type	Operational mode	h_{rf} (U_{rf})	$U_{fl,rf}$	UA	UA/V_{cnstr}	p	ϑ_{sat}	$\dot{q}$	$\Delta\vartheta$	Definition of $\Delta\vartheta$	$\vartheta_{fl,in}$	Choice of A_{ref}	Remarks
–	–	–	$\frac{kW}{m^2K}$	$\frac{kW}{m^2K}$	$\frac{kW}{K}$	$\frac{kW}{m^3K}$	kPa	°C	$\frac{kW}{m^2}$	K	–	°C	–	–
(Lanzerath et al. 2016)	horizontal plain Cu tubes	capillary-assisted partially flooded; continuously decreasing filling level	≤ 0.55	≤ 0.5	-	-	-	-	-				enveloping cyl. surf. with outer tube diam.	
	horizontal Cu tube with porous coating		≤ 11.3	≤ 4.1	-	-	-	-	-				enveloping cyl. surface enclosing the coating	h_{rf} and U vary with refr. filling level; flow rate of heat transfer fluid: 16 l/min
	horizontal finned Cu tube (with internal turbulator structure)		≤ 5.7	≤ 3.5	-	-	-	-	-	"a few Kelvin"	$\Delta\vartheta = \Delta\vartheta_{lm}$ (*LMTD*)	15	enveloping cyl. surface enclosing the fins	
	horizontal finned Cu tube with porous coating (with internal turbulator structure)		≤ 13.8	≤ 5.5	-	-	1.71	-	-				enveloping cyl. surface enclosing fins & coating	
(Seiler et al. 2020)	horizontal finned Cu tube (with internal turbulator structure)	capillary-assisted partially flooded; continuously decr. filling level; here: min. filling level	-	6.1…6.5	-	-	1.64	-	-	0.4	$\Delta\vartheta = \Delta\vartheta_{lm}$ (*LMTD*)	15	enveloping cyl. surface enclosing the fins	fluid-side: $Re = 1.53 \cdot 10^4$; flow rate of heat transfer fluid: 7.9 l/min
			-	5.2…6.8	-	-	1.5	-	-	1.25				
(Xia et al. 2008)	horizontal finned Cu tubes (4 variants)	capillary-assisted partially-flooded; steady-state; filling level: 50% of tube diameter	3.0…3.3	-	-	-	-	5	-	5	$\Delta\vartheta = \vartheta_{wall} - \vartheta_{sat}$	-	cyl. surface around diameter of root of fin (core tube diameter)	-
			3.9…4.9	-	-	-	-	5	-	1		-		
			3.6…4.4	-	-	-	-	11	-	3		-		-
		capillary-assisted partially-flooded; steady-state; filling level: 25% of tube diameter	5.8…6.8	-	-	-	-	15	-	4		-		-
(Dang et al. 2017)	horizontal plain Cu tube bundle (3 x 8 tubes)	falling film evaporation	4.8…5.7	-	-	-	2.0	-	-	4.5	$\Delta\vartheta = \overline{\vartheta_{fl}} - \vartheta_{sat}$	22	-	h_{rf} varies with Re of irrigation (19…133); flow rate of heat transfer fluid: 14.7 l/min
			3.2…5.6	-	-	-	2.3	-	-	4.3		24	-	
(Wittstadt et al. 2017)	heat exchanger from sintered Al fiber blocks, brazed between flat Al microchannel tubes	cyclic evaporation from capillary structures (in adsorption module)	-	-	2.05	241	-	15	-	-	$\Delta\vartheta = \Delta\vartheta_{lm}$ (*LMTD*)	19	-	$\boldsymbol{UA}$ averaged over evap. half cycle; half-cycle time: 200 s; $\boldsymbol{UA/V_{cnstr}}$ refers to constr. volume without manifolds
			-	-	1.15	135	-	-	-	-		12	-	
(Schnabel et al. 2018b)	Cu flat tube heat exchanger with corrugated fins	capillary-assisted partially flooded, decr. filling level	-	-	≤ 0.24	≤ 200	-	-	-	-	$\Delta\vartheta = \Delta\vartheta_{lm}$ (*LMTD*)	-	-	heat exchanger volume: 1.2 l
			-	-	≤ 0.29	≤ 240	-	-	-	-		-	-	
	Al flat tube heat exchanger with corrugated fins	cyclic evaporation from capillary structures	-	-	≤ 0.84	≤ 760	-	-	-	-		-	-	heat exchanger volume: 1.1 l
	Cu round tube heat exchanger with knitted Cu fabric		-	-	≤ 0.16	≤ 520	-	-	-	-		-	-	heat exchanger volume: 0.3 l

The symbols used in the headline of Table 1 have the following denotations:

h_{rf} (U_{rf})	refrigerant-side heat transfer coefficient
$U_{fl,rf}$	overall heat transfer coefficient (from heat transfer fluid to vapor atmosphere)
UA	absolute thermal transmittance ($UA = \dot{Q}/\Delta\vartheta$)
UA/V_{cnstr}	absolute thermal transmittance per heat exchanger construction volume
p	system pressure (vapor pressure)
ϑ_{sat}	saturation temperature of vapor atmosphere
$\dot{q}$	(applied) heat flux
$\Delta\vartheta$	(applied) driving temperature difference
$\vartheta_{fl,in}$	inlet temperature of heat transfer fluid
A_{ref}	reference area (used for translation between evaporation power and heat transfer coeff.)

Conventional Partially Flooded Evaporation

In case of conventional partially flooded evaporation a heat exchanger – often a plain tube in coil or meander shape – is partially immersed in a refrigerant pool. Since the nucleate boiling regime is usually not reached (cf. chapter 2.2), evaporation mainly takes place at the three-phase contact lines between tube wall, refrigerant pool and vapor atmosphere (cf. chapter 2.3) and presumably to some extent from the free refrigerant surface. Schnabel, Witte, and colleagues analyzed this evaporation concept as a reference case in (Witte et al. 2009) and (Schnabel et al. 2011). Comparing horizontal plain copper tubes in partially flooded operation with advanced evaporation concepts, the conventional tubes only reached considerably lower evaporation power or absolute thermal transmittance (UA) values for given driving temperature differences. Similarly, Lanzerath et al. and Seiler et al. used horizontal plain copper tubes as a reference in evaporation measurements with continuously falling refrigerant filling level and found poor overall heat transfer coefficients (Lanzerath et al. 2016) (Seiler et al. 2019), e.g. maximum 0.5 kW/(m²K) in (Lanzerath et al. 2016). In (Volmer et al. 2017) evaporation measurements on a coated tube-fin heat exchanger in partially flooded mode with continuously decreasing filling level are described, and again, the achieved absolute thermal transmittance (UA) values are low. The consistently poor performance results for conventional partially flooded evaporation in the aforementioned publications can be attributed to the fact that the contact lines – at which effective evaporation takes place – are very short in relation to the heat exchanger volume and surface area. Judging from the patent application EP1178269A1 (Lang et al. 2001) and from schematic drawings in (Vaillant GmbH n.d.) a partially flooded evaporator concept (in form of a combined evaporator-condenser heat exchanger in alternating operation) was presumably also employed in the gas driven water / zeolite adsorption heat pump zeoTHERM by the German company Vaillant. Clear advantages of the conventional partially flooded evaporation concept are that very simple and low-cost heat exchanger types can be used and that no additional parts or energy for refrigerant supply is required. However, the achieved heat transfer coefficients in relation to heat exchanger volume and mass are usually very low.

Facilitated Nucleate Boiling

The evaporation concept of facilitated nucleate boiling aims at reaching the nucleate boiling regime (cf. Figure 2 and explanations in chapter 2.2) by means of shifting the required driving temperature difference (wall superheat) to lower values which can reasonably be provided in the adsorption module context. One approach is based on the idea of using structured or porous surfaces instead of plain surfaces in order to provide a multitude of potential nucleation sites for bubble formation which can be activated with relatively low wall superheats.

Schnabel et al. conducted pool boiling measurements on smooth, sandblasted and finned copper surfaces with refrigerant filling levels of 22 mm and at system pressures of 1 kPa and 2 kPa (Schnabel et al. 2008a). For the finned surfaces they found required wall superheats of about 3…5 K (depending on pressure) for the initiation of nucleate boiling, while for the sandblasted surfaces about 20 K and for the smooth samples 25…30 K were necessary. Even though the identified required wall superheats for finned surfaces were relatively low, it needs to be taken into account that the heat transfer coefficient and heat flux at the onset of nucleate boiling are usually still rather low (in this case the heat flux amounted to about 2.5…4 kW/m^2 which gives heat transfer coefficients in the range of 0.6…1 kW/(m^{2}K)) and the real benefit of nucleate boiling only becomes evident at higher superheats.

Witte carried out steady-state evaporation measurements with sintered copper fiber structures of different geometric conformations in flooded conditions (Witte 2016). One objective of his work was to find out if the required wall superheat for the onset of nucleate boiling could be reduced to below a target value of 7 K by using the fiber structures. For a system pressure of 1.3 kPa and a refrigerant column height of 12.5 mm above structure surface he found a substantial increase of the transmittable heat flux in the boiling regime at elevated wall superheats for the fiber structures compared to a plain copper surface. However, the required superheat for the onset of nucleate boiling could not be noticeably reduced by using porous structures instead of a plain surface. The required values stayed in the range of 6.5…8 K and could only be slightly reduced to about 6 K by reducing the filling level to 7.5 mm.

Giraud et al. investigated the potential of nucleate boiling in plate heat exchangers for low cooling power sorption units with the refrigerant water (Giraud et al. 2016). In boiling experiments with a narrow vertical gap which is heated from one side they investigated heat transfer and bubble formation characteristics for vapor pressures between 1.2 and 5.0 kPa and different gap widths. Nucleate boiling could be clearly intensified by choosing a beneficial gap width. However, as far as can be concluded from the boiling curves, the effective nucleate boiling regime could only be reached for wall superheats of at least 15 K (referring to the local saturation temperature at the position of bubble formation). With regard to the temperature boundary conditions of the common adsorption heat pump concepts it appears difficult to provide such high driving temperature differences throughout the evaporation half-cycle. Dropping below the required threshold for nucleate boiling, though, would lead to a substantial decline of the evaporation heat transfer coefficient due to transition to the convective boiling regime.

Falling Film Evaporation

The falling film evaporation concept is quite commonly used for absorption heat pumps and chillers (e.g. (W. Baelz & Sohn GmbH & Co. n.d.)) but also in several commercially available adsorption systems this evaporator type is installed: Both the zeolite adsorption chiller AdRef-Noa by Mayekawa Mycom and the gas adsorption heat pump VITOSORP 200-F by Viessmann Deutschland GmbH employ an arrangement of heat exchanger (in case of VITOSORP 200-F a stainless steel helical tube), sprinkling device and refrigerant pump (Mayekawa Mycom n.d.; Viessmann Deutschland GmbH 2013; Franz Meyer 2015). By means of continuously sprinkling small amounts of refrigerant onto the heat exchanger's surface thin refrigerant films can be formed. Evaporation from this thin film is associated with high heat transfer coefficients due to the low thermal resistance of the thin refrigerant film and forced convection. A major drawback – especially for adsorption systems with low nominal power output – is the need of a refrigerant circulation pump which represents an additional investment cost factor, a risk for operational safety due to moving parts inside the vacuum circuit and the requirement of auxiliary energy which can lower the overall device efficiency.

The falling film concept is also of scientific interest in the context of adsorption heat transformation devices. Dang et al. conducted measurements with a falling film evaporator in form of a plain copper tube bundle with the refrigerant water at system pressures of 2.0 kPa and 2.3 kPa, in the context of a sorption

based seasonal thermal storage application (Dang et al. 2017). Depending on sprinkling density and fluid inlet temperature they could achieve refrigerant-side heat transfer coefficients of up to 6 kW/(m²K).

Capillary-Assisted Partially Flooded Evaporation

An evaporation concept which has raised a lot of attention in the academic field is the capillary-assisted partially flooded evaporation. By using heat exchangers with external capillary structures in partially flooded operation, refrigerant from the pool can be distributed over large surface areas by means of capillary forces. Thereby extensive three-phase contact lines can be generated which allow for high heat transfer coefficients (cf. chapter 2.2). A heat exchanger type which has been often chosen for this approach is the finned tube, due to its comparably easy manufacturing process, broad availability and good thermal properties. The performance of capillary-assisted partially flooded evaporators is usually quite sensitive on a precise adjustment of the pool filling level which might become a challenge in practice and therefore represents a risk in regard to operational reliability (Schnabel et al. 2018b).

In 2008 Xia et al. published a detailed study on steady-state capillary-assisted water evaporation with four different horizontal finned copper tubes (Xia et al. 2008). They found that a low driving temperature difference and a low filling level positively influence the evaporation heat transfer. For a saturation temperature of 5°C, a driving temperature difference of 4 K and a filling level of half the tube height they reached refrigerant-side heat transfer coefficients (related to the core tube surface as reference area) in the range of 3.1…3.5 kW/(m²K) which they state to be in the same dimension as those of falling film evaporators in lithium bromide (LiBr) / water absorption machines. Under different conditions values up to 7 kW/(m²K) were achieved.

Schnabel et al. conducted comparable steady-state measurements with partially-flooded finned tubes but they additionally characterized tubes with different kinds of external and also internal structuring, such as external electro-plated micro pins, internal fins and a tube with a dent structure (Schnabel et al. 2011). Moreover, they directly compared the evaporation performance in partially flooded operation to a sprinkled operation. For most tube variants the authors found that in partially flooded mode the achieved evaporation power was nearly as high as in a sprinkled mode. Another central outcome of the study was that fluid-side heat transfer can easily become a limiting factor if the refrigerant-side heat transfer is improved. Internal structures or turbulators could prevent such a limitation but are necessarily associated with a higher pressure drop.

Extensive research on capillary-assisted evaporation in partially flooded mode has been conducted by the group around Lanzerath and Seiler. In (Lanzerath et al. 2016) they investigated the evaporation characteristics of finned copper tubes, tubes with a porous coating and a combination of both under continuously decreasing refrigerant filling level. For a fluid inlet temperature of 15°C they recorded refrigerant-side heat transfer coefficients (reference area: enveloping area around fin tips) of up to 13.8 kW/(m²K) in case of the finned tube with additional porous coating and internal structure. Further detailed experimental results on tubes with porous coating were published in (Seiler et al. 2019). Seiler et al. found that certain porous structure types are prone to dry-out effects at high driving temperature differences. They further state that a high porosity, surface area and roughness of the structure have a positive effect on the heat transfer coefficient.

Schnabel et al. report on evaporation measurements with a copper flat tube heat exchanger with corrugated fins in partially flooded operation with falling filling level (Schnabel et al. 2018b). They found construction-volume-specific UA values of up to 200 kW/(m³ K) and a refrigerant turnover capacity of 0.7 kg which corresponds to a specific value of 580 kg/m³ if referred to the heat exchanger's construction volume.

A collaborative publication by Seiler, Volmer et al. focuses on methodological aspects of capillary-assisted evaporation measurements (Seiler et al. 2020). Based on measurements from two different test rigs with the same type of finned tube the authors deduced that identical results (within measurement uncertainty) can generally be produced with different equipment but that careful consideration of various methodologic issues is essential, such as an exact definition of input conditions and surface properties of the heat exchanger, control of non-condensable gases, and a thorough measurement uncertainty analysis. Overall heat transfer coefficients of up to 6.8 kW/(m²K) could be reached at the minimum refrigerant filling level, for a fluid inlet temperature of 15°C, fluid-side Reynolds number of $1.53 \cdot 10^4$; system pressure range of 1.0…1.33 kPa, and driving temperature difference of about 1.25 K.

Further investigations on capillary-assisted evaporation from finned tubes were conducted by Thimmaiah and coworkers who mainly focus on fin geometry and fluid-side turbulators ((Thimmaiah et al. 2015; Thimmaiah et al. 2016b; Thimmaiah et al. 2016a; Thimmaiah et al. 2017)) and by Pialago and colleagues who studied the impact of composite coatings from copper powder, carbon nanotubes and titanium dioxide (Pialago et al. 2020).

A different concept within the field of capillary-assisted partially flooded evaporators – in this case for application in an absorption refrigeration system – was described by Sabir and Bwalya (Sabir and Bwalya 2002): They applied a capillary groove structure or a porous structure from sintered copper powder on the inner sides of copper tubes and interconnected them to a heat exchanger. Heat was supplied by directly letting air flow through the tube matrix.

Besides these scientific publications, two relevant patents were filed by Vaillant GmbH which refer to capillary-assisted evaporation for sorption heat transformation devices: DE102014223250A1 (Spahn and Szuder 2014) describes a tubular heat exchanger surrounded by metallic mesh which allows refrigerant transport and spreading from a pool while in DE102015213320A1 (Spahn and Szuder 2015) a porous sintered metal structure is applied on the tube surface.

Cyclic Evaporation from Capillary Structures

The last mentioned group of evaporator concepts for adsorption heat pumps and chillers is based on the cyclic evaporation from capillary structures. It is especially adapted to the requirements of compact one-chamber adsorption modules with only one evaporator-condenser heat exchanger in cyclic operation (cf. drawing on the right in Figure 1 in the introduction). Since the evaporator-condenser heat exchanger alternates between two temperature levels, the thermal masses of heat exchanger and refrigerant should be minimized in order to avoid capacitive heat losses. Consequently, the refrigerant mass should be reduced to the amount needed for the vapor turnover of one half-cycle. Following the idea of generating extensive three-phase contact lines to realize high heat transfer coefficients, capillary structures are used. These structures can at the same time serve as a refrigerant storage by condensing directly into the structure during desorption / condensation phase and utilizing the capillary effect. A refrigerant pool is thus not required. Due to the cyclic operational mode without continuous refrigerant feed, the wetting conditions permanently change and evaporation (and condensation) is necessarily an unsteady, dynamic process. This concept in combination with a one-chamber module design potentially allows for an effective thin film evaporation without the need of moving parts – which are required for a conventional four-chamber module (cf. Figure 1, left) – and a simple, compact and low-cost module design (Lang et al. 1999; Chang et al. 2007; Schnabel et al. 2018b). Up to now only a few studies on this evaporator concept have been published:

A patent application DE102011015153A1 by Mittelbach and Daßler (inventors) / SorTech AG (assignee; today: Fahrenheit GmbH) describes an alternating condensation / evaporation heat transfer process on a

heat exchanger surface which aims at storing a small refrigerant mass and generating thin films for efficient evaporation (Mittelbach and Daßler 2011).

Volmer et al. conducted cyclic condensation / evaporation measurements with copper tube-fin heat exchangers in different geometric variants (Volmer et al. 2017). During condensation refrigerant was deposited on the fin surfaces and – depending on the fin distance – in the bottom section of the fin interstices. A strong fluid-side limitation was found under the tested conditions and also a relevant impact of the fin density. Wetting conditions turned out to play a crucial role as well as the contact resistance between tubes and fins. A node model could fairly well reproduce the basic evaporation dynamics, however, the predictions involved quantitative deviations from the measurement results.

In (Schnabel et al. 2018b) three different capillary-active heat exchanger types were used for cyclic evaporation measurements: A conventional aluminum flat tube heat exchanger with corrugated fins, a conventional copper flat tube heat exchanger with corrugated fins and an innovative copper round tube heat exchanger with a knitted fabric from copper wires soldered onto the surfaces. For the aluminum flat tube heat exchanger UA values per construction volume of up to 760 kW/(m³K) could be achieved while maximum values for the copper flat tube heat exchanger of about 250 kW/(m³K) and for the copper round tube / fabric heat exchanger of about 520 kW/(m³K) were recorded. The refrigerant storage densities amounted to 340 kg/m³ (Al flat tube), 200 kg/m³ (Cu flat tube) and 220 kg/m³ (Cu round tube / fabric).

Wittstadt et al. conducted measurements with a one-chamber adsorption module, using an evaporator-condenser heat exchanger in cyclic operation (Wittstadt et al. 2017). The heat exchanger consisted of sintered aluminum fiber blocks brazed between flat microchannel tubes. Due to the fine fibers the porous structure had a high specific surface area of more than 8000 m²/m³. Depending on the temperature boundary conditions mean UA values (averaged over the evaporation half cycle) for evaporation of up to 2 kW/K were achieved which corresponds to a volume-specific mean value of 240 kW/(m³K) if related to the heat exchanger volume.

2.2 Evaporation of Water at Sub-Atmospheric Pressures

Pool Boiling

Evaporation / boiling processes from a solid surface submerged in a liquid which is not subjected to externally induced flow are commonly termed pool boiling (Carey 2008) (Baehr and Stephan 2008). Depending on the applied heat flux or temperature conditions, different boiling mechanisms occur which can be classified in characteristic regimes. The boiling curve, also referred to as Nukiyama curve, depicts the relation of wall superheat $\Delta\vartheta$ (difference between wall / surface temperature ϑ_{wall} and temperature of the saturated vapor ϑ_{sat}) and heat flux $\dot{q}$ in the different boiling regimes, as schematically illustrated in Figure 2. (Formally it only applies if the characteristic dimensions of the setup are large compared to forming vapor bubbles and the surface is well-wetted (Carey 2008).) The actual occurrence of the particular boiling regimes and the nature of their transitions differ for the cases of controlled temperatures vs. controlled heat flux and for the cases of increasing vs. decreasing temperatures / heat flux. The following brief description applies to the case of a controlled increasing wall temperature (at constant saturation temperature) which is marked with solid lines in the diagram of Figure 2. Other cases are indicated by dashed lines in the illustration; details on their specifics can be found in (Carey 2008).

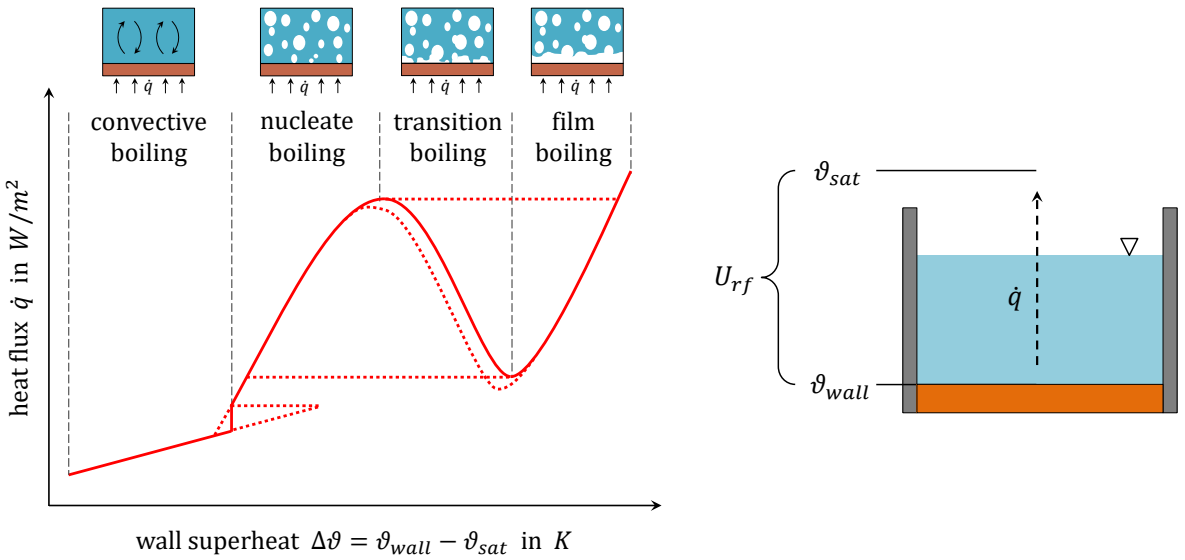

Figure 2: Boiling curve (heat flux $\dot{q}$ vs. wall superheat $\Delta\vartheta$) with characteristic pool boiling regimes (left), on the basis of statements and drawings in (Carey 2008); schematic pool boiling setup with involved quantities (right)

In the range of very low wall superheats (also referred to as the driving temperature difference) heat is transferred from the solid surface through the liquid by means of natural convection, and evaporation takes place at the liquid / vapor interface. The corresponding heat fluxes are comparably low. With rising wall superheat the transferred heat flux increases with a small slope and eventually reaches a characteristic point which is termed onset of nucleate boiling. At this point the wall superheat suffices for the formation, growth and detachment of vapor bubbles which favorably emerge at small inhomogeneities or cavities in the surface, and the heat flux instantaneously jumps to a higher level. The heat flux curve in the nucleate boiling regime shows a steep rise due to the enhanced heat transfer mechanism in combination with an increase in the number of active nucleation sites and frequency of bubble formation (Carey 2008). A further increase of the wall superheat leads to a point where bubbles start to coalesce to vapor columns and slugs which finally accumulate at the solid surface and partially hinders the liquid transport to the surface. Consequently, the transferred heat flux drops in this transition boiling regime. As soon as the vapor forms a stable blanket on the surface the film boiling regime begins. Conductive and convective heat transfer (and radiation where applicable) in the vapor film intensifies with increasing wall superheat and accordingly the heat flux rises again (Carey 2008).

According to the schematic boiling curve, the nucleate boiling regime allows the transfer of large heat fluxes, and considering equation (2-1) also high heat transfer coefficients U_{rf} can usually be reached. Consequently, operation in the pool boiling regime is often envisaged for evaporation applications.

$$U_{rf} = \frac{\dot{q}}{\Delta\vartheta} = \frac{\dot{q}}{\vartheta_{wall} - \vartheta_{sat}} \tag{2-1}$$

However, the occurring thermophysical mechanisms, the particular shape and position of the curve, and correspondingly the efficiency of heat transfer for a given wall temperature or heat flux, depend on several factors, such as wall topology, thermophysical properties of the liquid, and saturation temperature / pressure of the vapor (Baehr and Stephan 2008). For the application context of adsorption heat transformation devices, which is considered in this work, the particularities of water evaporation at sub-atmospheric pressures is of interest. An overview of scientific findings on this topic is given in the following paragraph.

Pool Boiling Characteristics of Water at Sub-Atmospheric Pressures

Numerous authors observed distinctly diverging boiling phenomena at low pressures in comparison to atmospheric pressure, such as a shift of the boiling curve ($\dot{q}$ vs. $\Delta\vartheta$) towards higher wall superheats (Raben et al. 1965; McGillis et al. 1990) – which means a considerably decreased heat transfer performance for a certain wall superheat (Raben et al. 1965; McGillis et al. 1990) – and different bubble appearance (Giraud 2015a; McGillis et al. 1990). These particularities of sub-atmospheric pressure evaporation of water are associated with the specific thermophysical properties of water in the low pressure range. Among these are a very low vapor density and a high surface tension in saturated conditions and a small slope of the vapor pressure curve (cf. Figure 74 in the appendix).

A major aspect leading to a decreased heat transfer performance is the impact of pressure on the bubble formation mechanism in the nucleate boiling regime. As bubble formation in pool boiling settings usually occurs in form of heterogeneous nucleation (Stephan 1988), the number and conformation of imperfections or cavities on the heated solid surface, which can serve as nucleation sites, plays a crucial role. In order to be activated for bubble initiation, a nucleation site needs to have critical site radius. This critical site radius depends on vapor density and saturation temperature and thus it increases with reduced pressure (Giraud 2015a). Consequently, a fewer number of potential nucleation sites can be activated at low pressures for a given wall superheat (Raben et al. 1965).

Also the bubble growth mechanisms at low pressures differ from those at elevated pressures. The low vapor density and high surface tension contribute to a changed balance of forces during bubble growth which affects bubble size, shape and formation process. As a result, very large bubble diameters could be observed by several authors (McGillis et al. 1990; Raben et al. 1965; Giraud 2015a; Giraud et al. 2015b; van Stralen et al. 1975). Raben et al. recorded departure diameters of up to 15 mm for a pressure of 2.7 kPa (Raben et al. 1965); Giraud et al. even observed departure diameters of up to 150 mm at 1.2 kPa (Giraud et al. 2016). According to van Stralen et al., bubbles only have a hemispherical shape during the first milliseconds of growth (van Stralen et al. 1975). For the subsequent growth time the schematic bubble profiles in (van Stralen et al. 1975) show a strong constriction in the vicinity of the heated wall. Shortly after departure of the bubble van Stralen et al. found a high-velocity liquid jet being formed, often followed by a secondary vapor column (for pressures of 2…8 kPa) which then enter the bottom of the original bubble. Giraud et al. accordingly refer to the bubble shape as a “mushroom” shape (Giraud et al. 2015b). Due to their large vapor volume departing bubbles create a large wake which causes vigorous mixing and thereby displaces overheated liquid from the heated surface (McGillis et al. 1990). This loss of overheated liquid at the solid surface is one cause for long waiting times between the formation of two consecutive bubbles (low bubble frequency) under low pressure conditions (McGillis et al. 1990), which were reported in several publications. Van Stralen et al. for instance found waiting time values in the dimension of 10…100 s for pressures of 2 kPa and 4 kPa (van Stralen et al. 1975).

As Raben et al. and McGillis and al. state, the large critical site radius or the resulting small number of active nucleation sites increases the required wall superheat for initiation of bubble formation at low pressures (McGillis 1990). Another factor which is relevant in the context of wall superheat is the shape of the vapor pressure curve (which is depicted in Figure 74 in the appendix): Raben et al. mention that with decreasing pressure the boiling curve is shifted towards higher wall superheats due to the smaller slope of the vapor pressure curve of water at low pressures (Raben et al. 1965). An explanation for such a causal relationship between high wall superheats and small slope is comprehensively given by Giraud et al. (Giraud et al. 2015b, 2016). Their essential reasoning will be explained with aid of a comparative example which is illustrated in Figure 3:

At atmospheric pressure ($p = 101.3\ kPa$) the slope of the vapor pressure curve is relatively large, as can be learned from Figure 74 in the appendix (and from the small graph at the top of the left side of Figure 3).

A small pressure difference therefore corresponds to a rather small difference in saturation temperature. Considering the pool boiling settings, the hydrostatic pressure caused by the liquid column represents such a pressure difference. Consequently, the local saturation temperature within the liquid $\vartheta_{sat}(z)$ increases slightly as it approaches the heated wall which is located at the height coordinate $z = 0$ (cf. left diagram in Figure 3). An exemplary liquid height of 100 mm is now assumed, which corresponds to a hydrostatic pressure difference of approximately 1 kPa. Further, a global wall superheat $\Delta\vartheta$ of 10 K is assumed which equals the difference of wall temperature ϑ_{wall} and vapor saturation temperature ϑ_{sat} at the pool surface. (The small difference between vapor and liquid saturation temperature at the liquid / vapor phase interface is neglected here, therefore the liquid saturation temperature $\vartheta_{sat}(z = 100mm)$ is used for $\Delta\vartheta$ in Figure 3.) Under these conditions the local saturation temperature at the wall surface $\vartheta_{sat}(z = 0)$ would only be about 0.27 K higher than at the liquid surface. The useful wall superheat for bubble formation thus amounts to 9.73 K which can be roughly considered equal to the original 10 K. Regarding the exemplary vertical temperature profile in the liquid pool $\vartheta_l(z)$ for the case of convective boiling – which is schematically depicted in Figure 3, pursuant to (Baehr and Stephan 2008) – the local liquid temperature exceeds the local saturation temperature at all height positions which means that the liquid is uniformly at superheated conditions.

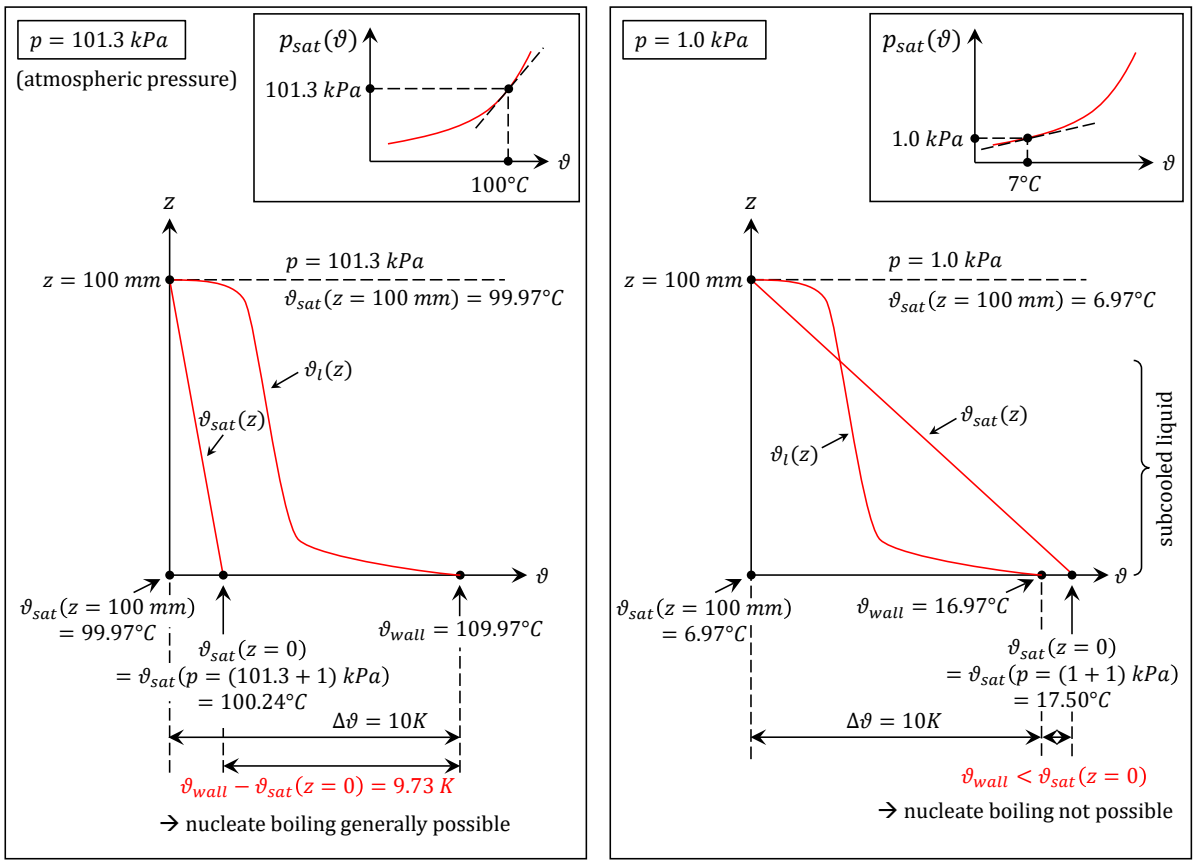

Figure 3: Visualization of the impact of hydrostatic pressure on pool boiling conditions at atmospheric vapor pressure (left), and sub-atmospheric vapor pressure (right); liquid temperature profile $\vartheta_l(z)$ for convective boiling pursuant to (Baehr and Stephan 2008)

Now considering the same settings (liquid height of 100 mm, wall superheat $\Delta\vartheta$ of 10 K) at sub-atmospheric vapor pressure conditions of 1.0 kPa (cf. right diagram in Figure 3), the corresponding saturation temperature at the liquid / vapor phase interface amounts to about 6.97°C. In this point the vapor pressure curve of water has a distinctly lower slope and the same hydrostatic pressure difference of approx. 1 kPa of the liquid column leads to a difference in the local saturation temperatures of about

10.53 K (cf. Figure 3, right). The local saturation temperature at the wall surface $\vartheta_{sat}(z = 0)$ is thus 17.50°C which is above the wall temperature ϑ_{wall} of 16.97°C ($\vartheta_{sat}(z = 100mm) + \Delta\vartheta = 6.97°C + 10K$). Under these conditions the local liquid temperatures of the lower section of the liquid pool is below the local saturation temperature which means that the liquid is subcooled in this region. At the wall surface a "negative local superheat" exists, so to say, which per se excludes evaporation.

In order to emphasize the varying pressure and subcooling conditions within the liquid pool at sub-atmospheric pressure boiling, Giraud et al. generally speak of a "non-homogeneity of the boiling environment" (Giraud et al. 2016, 2015b). Considering the large bubble sizes, a single bubble might therefore be exposed to a strongly spatially-varying environment at the same time. According to their understanding, this non-homogeneity is a major cause of the particular boiling phenomena at low pressures, including bubble size and shape – with as much impact as the particular thermophysical properties.

Regarding the heat transport in pool boiling, three mechanisms are distinguished: free convection, vapor-liquid exchange and latent heat transport (Raben et al. 1965). At elevated pressures the latent heat transport – the energy transferred by phase change – dominates due to the relatively high vapor density. At low pressures, where the vapor density is low, the vapor-liquid exchange prevails. This mechanism refers to the reflux of cold liquid to the heated wall after bubble detachment. Due to the large bubble size at low pressures this effect is then intensified (Raben et al. 1965).

In literature, several correlations for the heat transfer coefficient in nucleate boiling conditions can be found. An overview is for instance given by Witte (Witte 2016) who especially investigated their validity for evaporation of water from porous fiber structures at sub-atmospheric pressures.

2.3 Evaporation in the Vicinity of a Three-Phase Contact Line

Characteristic Regions of an Evaporating Meniscus

Multiple scientific studies demonstrated that evaporation in the vicinity of three-phase contact lines – which refers to contact areas between a heated solid, a liquid volume and vapor atmosphere – is often associated with very high heat transfer coefficients despite the absence of nucleate boiling. The region in which the wetting liquid meniscus approaches the solid wall, is commonly termed (triple) interline region (Wayner and Coccio 1971) or contact line region (Wayner 1982). Wayner and many other researchers after him subdivided the interline region into three characteristic sections which are illustrated in Figure 4:

(I) The "intrinsic meniscus" (Potash and Wayner 1972; Wayner 1999; Wang et al. 2007), (also referred to as "macroscopic meniscus" (Batzdorf 2015; Crößmann 2016), "bulk meniscus" (Wee 2004), "meniscus region" (Ma and Peterson 1997), or "macro region" (Höhmann and Stephan 2002)

(II) The "evaporating thin film" (Potash and Wayner 1972; Wayner 1999; Ma and Peterson 1997) (also referred to as "transition film region" (Wee 2004; Wang et al. 2007), "thin-film region" (Wang et al. 2007), or "micro region" (Höhmann and Stephan 2002; Crößmann 2016)

(III) The "equilibrium (flat) thin film region" (Potash and Wayner 1972; Wayner 1999) (also referred to as "adsorbed film region" (Wee 2004; Crößmann 2016; Höhmann and Stephan 2002; Stephan and Busse 1992), "non-evaporating region" (Wang et al. 2007; Ma and Peterson 1997))

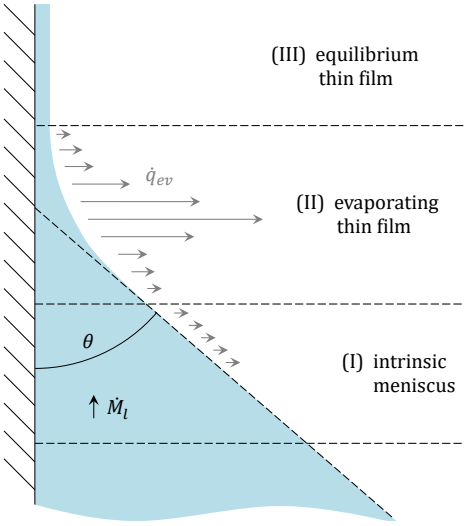

Figure 4: Schematic drawing of an evaporating meniscus in the interline region, including the three characteristic regions (I) intrinsic meniscus, (II) evaporating thin film, (III) equilibrium thin film

In the intrinsic meniscus (I) the liquid film has a large thickness and pressure conditions are governed by capillary forces (Wayner 1999). Due to the considerable thermal resistance of the liquid film, evaporation at the liquid / vapor interface is restricted and the liquid temperature at the interface virtually equals the saturation temperature of the vapor atmosphere (Stephan 1992). The slope of the liquid / vapor interface in relation to the wall is constant in the intrinsic meniscus region (Stephan 1992).

The equilibrium thin film region (III) is located at the outmost part of the meniscus. Here, the liquid film only has the thickness of a few molecular layers and its curvature approximates zero (Stephan 1992). Attractive intermolecular forces at the solid / liquid interface cause a reduction of the local liquid pressure which is termed disjoining pressure (Wayner et al. 1976). Due to the strong impact of disjoining pressure the liquid in the equilibrium thin film region does not evaporate, even if the interface temperature practically equals the wall temperature and thus distinctly exceeds the saturation temperature of the vapor phase (Stephan 1992; Potash and Wayner 1972).

The evaporating thin film region (II) represents the transition between the two aforementioned lateral regions and also a transition between the impacts of capillary pressure and disjoining pressure (Wayner 1999): While the film thickness is large enough to diminish the adhesive effect of intermolecular forces on the fluid molecules at the phase interface (Potash and Wayner 1972), it is at the same time small enough to ensure a low conduction resistance of the film (Wang et al. 2007). Consequently, a high local evaporative heat flux ($\dot{q}_{ev}$) occurs in the region of the evaporating thin film in form of a narrow peak in the heat flux distribution (Wang et al. 2007; Stephan 1992). The dimension of evaporative heat flux is governed by thermal conduction through the liquid film and the molecular kinetic thermal resistance at the liquid / vapor interface (Potash and Wayner 1972; Stephan 1992). While in earlier model conceptions the liquid temperature at the liquid / vapor interface in the evaporating thin film region was equated with the saturation temperature of the vapor phase, Wayner (Wayner 1982) and Stephan and Busse (Stephan and Busse 1992; Stephan 1992) demonstrated that this assumption does not apply but that the temperature distinctly exceeds the vapor saturation temperature. Since a sharp maximum of curvature occurs in the evaporating thin film region the meniscus appears to approach the wall in a constant angle from a macroscopic view (Stephan 1992). The respective angle is consequently termed apparent contact angle (θ). The change in curvature (or film thickness) of the meniscus profile and the resulting pressure gradient cause a continuous liquid flow ($\dot{M}_l$) from the intrinsic meniscus towards the evaporating thin film (Wayner et al. 1976; Potash and Wayner 1972) which counterbalances the evaporative mass flux.

For non-spreading systems (finite apparent contact angle $0 < \theta < 90°$) Wayner defined the narrow equilibrium thin film region (III) of constant film thickness as the position of the "contact line" or "interline", while for spreading systems (zero apparent contact angle $\theta = 0$) he referred these terms to the junction between the broader equilibrium thin film (III) and the evaporating thin film (II) (Wayner 1982).

Although researchers engaged in the field basically agree on the general characteristic features of the interline region and of its three characteristic sub-regions, the employed definitions for the transition points between the regions are not always identical:

The transition point between equilibrium thin film (III) and evaporating thin film (II) is defined consistently by most authors as the point at which the film thickness starts to increase (coming from the constant value in the equilibrium thin film region (III)) and evaporation heat flux is not zero anymore (Stephan 1992; Wang et al. 2007).

For the transition from evaporating thin film region (II) to intrinsic meniscus region (I), though, the definitions are quite diverse: Potash and Wayner chose the point at which the disjoining pressure eventually has a negligible effect on heat flux (Potash and Wayner 1972) but they do not specify a criterion for negligibility. According to Crößmann's definition for the transition between regions (II) and (I), the evaporating thin film region (II) (which he terms micro region) ends when the thermal conduction resistance of the thin film exceeds the molecular kinetic resistance of the liquid / vapor interface and when additionally the difference between interface temperature and vapor saturation temperature is negligible (Crößmann 2016). Wang et al. use two different classification levels for characteristic meniscus regions which partly overlap (Wang et al. 2007): On one hand they differentiate between a micro region, which includes the part close to the wall until the point where the film thickness has grown to 1 µm, and a macro region, which starts at this points and includes the rest of the bulk meniscus. On the other hand they distinguish between the three characteristic regions (I), (II), (III), and define the transition from evaporating thin film (II) to intrinsic meniscus (I) as the point where the disjoining pressure has diminished to $1/5000^{th}$ of its value in the equilibrium thin film region. Stephan specifies the transition between evaporating thin film region (II) ("micro region") and intrinsic meniscus region (I) ("macro region") as the point from which on the assumptions of a constant curvature and of the equality of liquid / vapor interface temperature and saturation temperature of vapor are justified, which means that the impact of adhesive forces and curvature vanish (Stephan 1992).

Considering this broad variety of classifications and definitions for the different regions in the vicinity of the three-phase-contact line, a global determination of the width (or "length") and film thickness range in the particular regions for certain conditions is hardly possible. Similarly, specifications of the percentage of evaporation heat flow transferred in the evaporating thin film region compared to the total heat flow in the meniscus (or in the complete interline region, including (I), (II), (III), compared to the total heat flow) are mostly not comparable even if the same boundary conditions were set.

In simulations of an evaporating water meniscus in copper re-entrant channels and microchannels Crößmann found length values for the evaporating thin film region (II) ("micro region length") which continuously increase with decreasing wall superheat; e.g. a length of approx. 10 µm / 16 µm / 27 µm for wall superheats of 20 K / 5 K / 1 K (Crößmann 2016). The corresponding shares of the total heat flow are not specified, though. From the results of high-resolution temperature measurements of an evaporating water meniscus in a capillary slot by Höhmann and Stephan a width of the evaporating thin film region (II) ("micro region") about 50 µm can be deduced (Höhmann and Stephan 2002), however, the specific boundary conditions and definition criteria are unclear. Ma and Peterson calculated the characteristics of an evaporating water meniscus in tilted triangular copper grooves and defined a "micro region" which starts at the transition from equilibrium film (III) to evaporating film (II) and has a constant length of 1 µm (see above), independent of the respective boundary conditions (Ma and Peterson 1997). They found a

percentage of 19…42% of the total heat flow being transferred in this area and a maximum film thickness of about 0.5…1 µm, depending on the axial position in the groove and the corresponding driving temperature difference. Stephan and Busse found a percentage of heat flux in the "micro region" (which is similarly defined as in (Stephan 1992)) of 45% from evaporation simulations for ammonia in an aluminum channel (Stephan and Busse 1992). In (Stephan 1992) Stephan reports a portion of 55% for ammonia in an aluminum channel for the investigated boundary conditions. Crößmann found a share of up to 70% being transferred in the evaporating thin film region (II) for methanol in re-entrant channels at low superheats. Wang et al. report percentages of 50…97% being transferred in the "micro region" (according to their above-mentioned definition) for octane in micro-channels of different width for exemplary conditions and they state that the resulting values strongly depend on channel width and wall superheat (Wang et al. 2007).

Impact of Thermodynamic Conditions on Evaporation from Menisci

Many authors noticed distinct effects of the employed thermodynamic boundary conditions on the resulting profile of the evaporating meniscus and the corresponding heat and mass transfer characteristics. Among these influencing factors are the applied driving temperature difference (or heat flux) and the vapor saturation temperature (or vapor pressure). In several publications a decreasing heat transfer coefficient of evaporation with rising driving temperature difference or heat flux is reported. In some cases the origin of this effect is ascribed to an influence on the meniscus shape, while in others it is traced back to dryout effects:

From measurements of methanol evaporating from re-entrant channels and additional microchannels at a saturation temperature of 20°C and for heat flux variations within a range of about 0.5…13 kW/m² Crößmann found a non-linear decrease of the heat transfer coefficient with increasing applied heat flux for all channel geometries (Crößmann 2016). As a reason for this dependence Crößmann identified the increasing film thickness of the refrigerant in the evaporating thin film region with increasing heat flux due to an increased inward flow of refrigerant under steady-state conditions. A larger film thickness represents a larger thermal resistance and a local decrease of the heat transfer coefficient. While at low heat fluxes a large share of the total heat is transferred in the evaporating thin film region, the relative heat flux ratio in evaporating thin film vs. macroscopic meniscus is consequently shifted towards a larger share in the macroscopic meniscus in case of higher heat fluxes. Crößmann further names the thermophysical properties of the refrigerant as an important influencing factor for the local heat transfer characteristics. The dimension of applied heat flux strongly affects absolute temperatures and potentially temperature distributions within the meniscus. Consequently, thermophysical properties are altered which might affect heat transfer characteristics.

Similar general relations were found by Ma and Peterson (Ma and Peterson 1997): Simulations of evaporation from a tilted triangular groove with fluid supply on the lower side and a constant heat flux input yielded a distinct change of the local superheat along the groove axis. Associated with the superheat increase in axial upward direction they noticed a changed meniscus profile with increased film thickness and apparent contact angle and a reduction of the heat transfer coefficient.

Wong and Chen conducted measurements with a groove wick and groove-powder wick evaporator in a flat-plate heat pipe setup with water, acetone and methanol and with different heat flux levels (Wong and Chen 2013). For all tested refrigerants they noticed an increasing evaporator resistance – which corresponds to a decreasing overall heat transfer coefficient – with increasing heat flux and attribute this behavior to an expansion of dryout regions.

In experimental investigations on the capillary-assisted evaporation of water from partially flooded copper finned tubes Xia et al. found a decreasing overall heat transfer coefficient with increasing superheat

(in the range from 0.5 K to 5 K, referring to the difference between mean tube wall temperature and vapor saturation temperature) (Xia et al. 2008). They attribute this behavior to the increased heat flux share transferred in the macroscopic meniscus (as against the evaporating thin film region) for elevated heat fluxes, and to the corresponding deteriorated heat transfer in that region. It cannot be clearly deduced from the publication, though, if dryout effects play a role as well.

Seiler et al. conducted measurements on partially flooded copper tubes with porous coating, using water as refrigerant with dynamically decreasing refrigerant filling level (Seiler et al. 2019). Tests with different driving temperature differences were carried out while keeping the heat transfer fluid inlet temperature constant at 20°C / 15°C / 10°C. Results showed a decrease of the overall heat transfer coefficient (which includes fluid side heat transfer and conduction through the wall besides evaporation) with increasing superheat in the interval of low refrigerant levels. The authors attribute this observation to dryout effects due to the long required length for capillary transport and support their statement with respective photographs. In the range of higher refrigerant flooding levels, where the capillary supply is less challenging, no distinct impact of superheat on overall heat transfer coefficient can be observed in their results. This apparent absence of an impact at high refrigerant levels, though, might possibly originate from a superimposition by other limiting factors.

The impact of vapor saturation temperature (or vapor pressure) on the heat transfer from evaporating menisci is addressed by Crößmann, Seiler et al. and Xia et al.:

From his measurements of methanol evaporation from microchannels Crößmann found a virtually linear increase of the mean heat transfer coefficient with increasing saturation temperature (in the range from 10°C to 40°C) for all channel variants (Crößmann 2016). He attributes this behavior to the temperature dependence of the thermophysical properties of the refrigerant (vapor density, enthalpy of vaporization, condensation coefficient) which in sum cause a reduction of the thermal resistance with increasing temperature. Crößmann especially emphasizes the impact of increasing vapor density as a relevant factor.

Seiler et al. come to similar qualitative results in their evaporation measurements with water and copper tubes with porous coatings (Seiler et al. 2019). By varying the heat transfer fluid inlet temperature and comparing the resulting UA values in relation to their respective driving temperature difference the impact of saturation temperature can be deduced. For higher fluid inlet temperatures (and correspondingly higher saturation temperatures) distinctly higher maximum absolute thermal transmittance (UA) values were observed. Seiler et al. ascribe this dependency to an improved fluid-side heat transfer on one hand, but also to an improvement of the refrigerant side due to temperature-dependent thermophysical properties such as vapor density and liquid viscosity.

Xia et al. also noticed an increased refrigerant-side heat transfer coefficient for elevated saturation temperatures for the case of water evaporation from partially flooded finned tubes (Xia et al. 2008). As an explanation they state the increase of liquid thermal conductivity and decrease of viscosity and surface tension with increasing temperature which might lead to an increased evaporation mass flux and improved liquid refrigerant flow conditions in the meniscus.

Impact of Material Properties on Evaporation from Menisci

Another relevant factor influencing the heat transfer characteristics of an evaporating meniscus is the wall / fluid material combination and the associated material properties. Stephan generally states that the relevance of evaporation from the interline region is especially pronounced if the thermal conductivity of the fluid is much lower than that of the wall material (Stephan 1992). He reasons that the fluid film thickness becomes a limiting factor then and the heat flux consequentially intensifies in the interline region where film thickness and accordingly thermal resistance are lowest. In the context of heat pipes

Stephan further points out that the choice of a fluid with good wetting characteristics is crucial in order to avoid dryout effects.

The impact of fluid properties was also investigated by Crößmann who compared evaporation characteristics of methanol and acetone (Crößmann 2016). For all driving temperature differences he found higher heat transfer coefficients for methanol compared to acetone. Comparing the ratio of heat transfer coefficients of the two fluids with the ratio of their Merit numbers – which includes liquid density, surface tension, enthalpy of vaporization and liquid viscosity – he does not find a distinct correlation. Instead, he mainly attributes the different outcomes for the fluids to the lower film thickness and higher liquid thermal conductivity of methanol and the resulting higher relevance of heat transfer in the interline region. As another important fluid property Crößmann identifies the condensation coefficient, since it directly influences the molecular kinetic thermal resistance of the phase interface. He refers to Marek and Straub who state that already minimal contaminations of the fluid can tremendously change its condensation and evaporation coefficient due to accumulation at the interface (Marek and Straub 2001).

Wee concludes from his investigations that the polarity of a working fluid needs to be considered. He states that the polarity of water leads to an extension of the evaporating thin film region (II) but on the other hand provokes a more pronounced adhesive effect of intermolecular forces which hinders evaporation (Wee 2004).

Impact of Geometry Parameters on Evaporation from Menisci

If evaporation in the vicinity of a three-phase contact line is investigated on the level of a three-dimensional evaporator structure, geometry aspects need to be taken into account.

Wang et al. evaluated the impact of channel size on the evaporation from microchannels for the special case that the channel radius is in the range of the asymptotic intrinsic meniscus radius, which is specified as 200 nm to 210 µm. While channel size apparently had a negligible impact on evaporation characteristics in the evaporating thin film region (II) (which they define as ranging to the point where disjoining pressure drops to $1/5000^{th}$ of its value in the equilibrium thin film region (III)) they report that evaporation from the intrinsic meniscus (I) was notably influenced by channel width. With decreasing channel size the contribution of the evaporating thin film region (II) to total heat flux increased (Wang et al. 2007).

In terms of geometry impact Crößmann analyzed the interrelation of contact line length and phase interface area with the total heat transfer coefficient for evaporator plates with parallel re-entrant channels and additional microchannels. His results showed that the heat transfer coefficient was positively correlated both with contact line length and phase interface area. However, while the impact of the interface area on the heat transfer coefficient was rather small, the heat transfer coefficient appeared nearly proportional to the contact line length (Crößmann 2016). This outcome suggests that a large portion of the phase interface area only made a negligible contribution to heat transfer for the investigated channel geometries.

Xia et al. compared finned tubes with different fin heights and widths in partially flooded mode. As a characteristic quantity they chose the quotient of fin height to fin width and they noticed that a large height/width value was beneficial for mostly all conditions (Xia et al. 2008). Considering their results, it moreover appears that the fin width is the governing factor for this behavior since a small fin width is most probably associated with an increased total contact line length for a given tube length. An increased fin height might also increase the contact line length due to a larger diameter of the arc-shaped contact line but its impact is presumably smaller and besides it would involve an increased heat transfer path length through the fin.

Impact of Contact Line Motion on Evaporation from Menisci

Evaporation characteristics of moving three-phase contact lines compared to static ones were studied by several researchers. Fischer experimentally analyzed the heat flux profile along the meniscus cross section for the case of receding and advancing contact lines at various velocities (Fischer 2015). For receding contact lines he did not notice any influence of contact line velocity on the heat flux distribution. However, under certain conditions (especially at elevated interface velocities) a thin evaporating film was deposited on the solid surface due to the relative velocity of the meniscus to the solid which represents an additional evaporation site to the contact line. For advancing contact lines Fischer found an increase of the heat flux maximum in the evaporating thin film region (II) with increasing contact line velocity.

Similar to Fischer's work, Kunkelmann et al. investigated the impact of contact line velocity on heat transfer in the contact line region and could not detect an interdependence for receding contact lines but a distinct rise of the local heat flux maximum with increasing velocity for advancing contact lines (Kunkelmann et al. 2012).

2.4 Thin Film Evaporation from Porous Structures

According to the findings of various authors, the overall evaporation performance of a thin film evaporator structure can be considerably enhanced by increasing the total length of three-phase contact lines per surface area (e.g. (Ma and Peterson 1997; Hanlon and Ma 2003; Crößmann 2016; Bodla et al. 2013; Wong and Chen 2013)). In the case of capillary grooves or channels this can be realized by decreasing the channel width and increasing the channel density (e.g. (Crößmann 2016)). However, the possibilities of increasing the channel density are limited from manufacturing side (Hanlon and Ma 2003), therefore the utilization of porous structures, such as sintered metal powders or metallic meshes, have gained attention. A large portion of the research activities on evaporation from porous structures are conducted in the context of heat pipes and capillary pumped loops for electronics cooling purposes which is often associated with high heat transfer requirements (Wen et al. 2018; Crößmann 2016; Ranjan et al. 2012). In these applications the porous wick structure must allow for high evaporation heat transfer coefficients while at the same time ensuring the capillary-induced flow of the working fluid to maintain steady-state evaporation without early dry-out (Wen et al. 2018; Ranjan et al. 2012). Consequently, the geometry parameters of the porous structure need to be chosen in accordance with both heat transfer and fluid flow requirements. Unsteady evaporation processes from porous structures – in which a continuous liquid feed through the structure is not necessarily required – are uncommon in the named application area, and accordingly respective publications are scarce.

Hanlon and Ma consider steady-state evaporation from a porous structure from sintered copper particles at atmospheric pressure (Hanlon and Ma 2003). The structure is intended to be completely saturated with liquid working fluid (water) by means of capillary action, so that evaporation only takes place at the three-phase contact lines at the top surface of the structure while heat is supplied from the bottom. By means of a mathematical model – which will be roughly described in chapter 2.5 – and experiments the authors investigate the impact of geometric structure parameters as particle size, porosity and thickness of the wick structure. They report increasing heat transfer coefficients with decreasing particle radius (which was varied between 0.01 mm and 0.635 mm in the simulations) and with decreasing structure thickness (varied between 1.9 mm and 5.7 mm in the experiments). However, a low structure thickness could also lead to a reduced dry-out heat flux limit for certain conditions, due to insufficient capillary pumping and / or due to onset of bubble formation. The optimum wick thickness in terms of a maximum dry-out heat flux turned out to depend on geometry parameters such as porosity and particle size.

Bodla et al. investigate the evaporation from sintered copper wick structures as well by developing an evaporation model for digitized 3D images of real structures (shortly described in chapter 2.5) (Bodla et al. 2013). From simulations for the considered structures they conclude that the evaporation heat transfer coefficient can be increased by reducing the particle size (which is linked to a reduced pore size) since this measure leads to a larger total meniscus area and extended three-phase contact regions.

Li, Peterson and coworkers carried out steady-state evaporation measurements of water at atmospheric pressure with porous copper mesh structures and studied the effects of wick thickness, porosity and mesh size on the evaporation heat transfer coefficient and the critical heat flux (Li et al. 2006; Li and Peterson 2006). An optimized sintering process ensured low contact resistances between mesh layers and at the mesh / heater interface. In the experimental setup the horizontal mesh structure samples were heated from the bottom and constant capillary flow of refrigerant into the porous structure was enabled by adjusting the structure position at the surface of a refrigerant reservoir. According to the authors, the thickness of all investigated structure samples was chosen very thin (between 0.21 mm and 0.82 mm) in order to stay below the bubble departure diameter of about 1 mm (Li et al. 2006). In that way they assume that nucleation on the heater surface can occur but that no bubble flow through the porous structure will occur and thus blocking of the capillary-induced liquid supply might be avoided. In (Li et al. 2006) the authors state that heat transfer coefficients of up to 245.5 kW/(m²K) were achieved. However, in the calculation of the heat transfer coefficient they define the liquid refrigerant temperature in the reservoir as the saturation temperature. Even if they state that the measurement chamber is kept at saturation conditions by means of auxiliary heaters, it appears questionable if the liquid temperature is identical with the saturation temperature of the vapor above the structure surface. With increasing heat flux (which was varied between 0 and about 3700 kW/m²) Li et al. observed the heat transfer coefficient to increase at first and then decrease again after passing a maximum. The initial increase seems to oppose the findings of other authors (cf. chapter 2.3) but probably originates from the occurrence of nucleate boiling (in contrast to pure convective thin film evaporation) which intensifies heat transfer with increasing driving force (cf. chapter 2.2). The decreasing course of the coefficient at high heat fluxes is ascribed to a partial dryout of the structure by the authors. The measurement results further indicate that the heat transfer coefficient is influenced by the exposed surface area but not by the structure thickness whereas an increasing structure thickness strongly raises the critical heat flux for the investigated thickness values. In the second part of their study (Li and Peterson 2006) Li and Peterson discuss the impact of mesh width (pore size), porosity and wire diameter on heat transfer coefficients and critical heat flux. They found a strongly increasing critical heat flux with increasing pore size (varied between 119 µm and 233 µm) and with increasing wire diameter (varied between 56 µm and 191 µm). For the porosity (varied between 41% and 69%) they noticed an optimum value at medium porosities which leads to the maximum critical heat flux. In terms of heat transfer coefficients the authors report a positive effect of small pore sizes which they attribute to a larger exposed surface area. A reduced porosity led to slightly increased heat transfer coefficients which – according to Li and Peterson – might have been caused by a minor increase of the effective thermal conductivity of the structure and a correspondingly promoted nucleation.

Besides evaporator structures with re-entrant channels and additional microchannels – which were already mentioned in chapter 2.3 – Crößmann also investigated a sample which exhibits a porous structure instead of microchannels (Crößmann 2016). The porous structure consists of a 0.5 mm layer of sintered copper powder with an average particle diameter of 150 µm. Measurement results at a saturation temperature of 20°C with methanol as refrigerant showed considerably higher heat transfer coefficients for the evaporator sample with porous structure compared to the microchannel variants. For an exemplary effective imposed heat flux of 10 kW/m² a heat transfer coefficient of 2 kW/(m²K) could be reached with the porous evaporator surface while the best microchannel surface only reached about 1 kW/(m²K). This performance advantage of the porous structure can be ascribed to its increased contact line length and extended areas of thin refrigerant films.

Khrustalev and Faghri describe an "inverted meniscus" evaporator design which consists of a porous structure in thermal contact with a heater and vapor channels in between and which is operated in steady-state conditions (Khrustalev and Faghri 1995). At low heat fluxes evaporation takes place at the border of the liquid-saturated porous structure to the heater and vapor directly flows into the vapor channel while liquid refrigerant is constantly provided by capillary flow in the structure. At high heat fluxes a vapor blanket forms in the porous structure around the contact to the heat source which represents a local dryout region. In that case evaporation takes place at the border between this dry area and the liquid-saturated part which means that the heat flow must pass the thermal resistance of the vapor-filled "dry" area before reaching the point of evaporation. Khrustalev and Faghri report that a third unstable regime can occur in form of vapor bubbles which travel through the porous structure towards the vapor channels. Simulation results predict effective heat transfer coefficients (referring to the temperature difference between heater wall and vapor temperature) of 80…150 kW/(m²K) with the described evaporation setup for the refrigerant water at atmospheric pressures, depending on applied heat flux (varied between approx. 700 and 2300 kW/m²) and permeability of the porous structure. The authors do not state, though, if these simulated values were validated in any way. The simulation results further show a distinct decrease of the effective heat transfer coefficient with increasing applied heat flux.

Zhao and Liao present experimental and modeling results of a similar evaporator concept where a porous structure is heated from the top and vapor is released through channels in the heating surface while refrigerant is continuously replenished by capillary action (Zhao and Liao 2000). The concept is especially envisaged for the application in capillary pumped loops and loop heat pipes where high heat transfer rates are required. In their experiments with water in a matrix of spherical glass beads Zhao and Liao consequently apply heat fluxes in the range of 13…260 kW/m² and apparently work around atmospheric pressure. Similar to the statements of Khrustalev and Faghri, Zhao and Liao found that at low heat fluxes (here: below 177.2 kW/m²) the porous structure stayed completely saturated with refrigerant and they recorded increasing heat transfer coefficients of 6…10 kW/(m²K) with increasing heat flux. At higher heat fluxes they found that a two-phase zone forms close to the heated surface where a certain share of the pores stays saturated with refrigerant and the rest falls dry. In this regime (at heat fluxes between 177.2 kW/m² and 259.58 kW/m²) the measured heat transfer coefficients stagnate and eventually decline strongly down to 8 kW/(m²K) with increasing heat flux. At the highest imposed heat flux of 264.81 kW/m² the heat transfer coefficient dropped to 7 kW/(m²K) which the authors attribute to the formation of a vapor blanket.

Further studies on thin film evaporation from porous structures related to heat pipe and capillary pumped loop applications are for instance presented in (Ranjan et al. 2009; Ranjan et al. 2012; Iverson et al. 2007; Wen et al. 2018; Wong and Chen 2013; Boubaker et al. 2015).

In the context of adsorption and absorption heat transformation devices Witte presents comprehensive experimental results on evaporation of water at sub-atmospheric pressures (0.9…1.5 kPa) with porous structures made of sintered copper fibers (Witte 2016). Besides pool boiling experiments he conducted measurements in a partially-flooded and capillary-fed operational mode. For the capillary-fed mode he found – among other results – that the wettability of the structures plays a crucial role for the achievable heat transfer coefficients and that a low structure height is beneficial. Comparing the results of the different evaporation modes Witte could achieve the highest heat transfer coefficients in the capillary-fed operational mode. Depending on the particular sample structure (with structure heights of 8 mm and 12 mm) he measured heat fluxes in the range of 4…8 kW/m² for a wall superheat of 2 K and of about 5…20 kW/m² at 5 K, which corresponds to heat transfer coefficients in the range of 2…4 kW/(m²K) for 2 K superheat and 1…4 kW/(m²K) for 5 K (both at a system pressure of 1.3 kPa). He further assumes that the achievable heat transfer coefficients might still be considerably enhanced by optimizing the fiber structures and extending the provided three-phase contact line length.

On a heat exchanger level Lanzerath, Seiler and colleagues compare the evaporation performance of horizontal copper heat exchanger tubes with porous coatings to that of regular finned tubes and plain tubes in a partially flooded operation. Lanzerath et al. report in (Lanzerath et al. 2016) that the overall heat transfer coefficient (related to the temperature difference between heat transfer fluid and vapor saturation temperature) could be enhanced by a factor of up to 11 for the investigated conditions by using finned tubes with porous coating instead of plain tubes. While they measured a maximum overall heat transfer coefficient of 0.5 kW/(m²K) for plain tubes, the maximum value for uncoated finned tubes (with internal turbulence structure) was 3.5 kW/(m²K), for plain tubes with porous coating 4.1 kW/(m²K) and for finned tubes with porous coating (with internal turbulence structure) 5.5 kW/(m²K). In (Seiler et al. 2019) Seiler and coworkers state that the structural properties of a porous coating on evaporator tubes substantially affect its performance: Based on their measurement results they conclude that a high porosity, specific surface area and roughness have a positive effect on evaporation performance. They attribute the advantage of a high porosity to an increased cross-sectional area available for capillary-induced refrigerant flow. As a cause for the positive effect of a high specific surface area and roughness they mention the increased available surface area for the heat transfer process. The authors further report that suitable pore structure characteristics can considerably increase the critical driving force level associated to the onset of dry-out effects.

Pialago et al. present experimental results of similar horizontal evaporator tubes but instead of a pure copper coating they use a porous composite coating of copper particles, carbon nanotubes and titanium dioxide (Pialago et al. 2020). The authors noticed an improved wettability for the composite coating compared to a pure copper porous coating. Evaporation measurements in partially flooded operation with externally structured tubes with composite coating showed an increased external and overall heat transfer coefficient compared to evaporator tubes with a pure copper coating. Pialago et al. ascribe this finding to the enhanced hydrophilicity and higher porosity of the surface and an assumed corresponding extension of thin-film regions.

2.5 Evaporation Modeling for Menisci and Capillary Structures

A lot of different model approaches have been developed with the aim of predicting the characteristics of evaporation from thin liquid films and of corresponding evaporator structures. These approaches differ considerably in terms of their level of detail, methodological concept and scope of applicability.

The group around Wayner established a two-dimensional model for the description of heat and mass transport mechanisms in a steady-state evaporating meniscus (Potash and Wayner 1972). The model includes the occurring heat transfer mechanisms as well as the different pressure contributions which provoke the liquid flow compensating the evaporation mass flux. Depending on respective boundary conditions the two-dimensional meniscus profile and heat flux distribution along the liquid / vapor phase interface can be calculated.

Wayner's approach served as a fruitful basis for several modifications and extensions which were later elaborated by other researchers involved in the field. As an example, Stephan used Wayner's model conception as a starting point for the development of a two-dimensional model for steady-state evaporation from trapezoidal capillary grooves for heat pipe applications (Stephan 1992). He described the heat and mass transfer in the evaporating thin film region (II) ("micro region") using a differential equation system and coupled it with a mathematical description for the "macro region" in the groove structure. By means of an iterative computation method the radial overall heat transfer coefficient for evaporation from the groove could be calculated. A comparison of the employed "micro region" model with earlier model

variants furthermore revealed that the assumptions of a) the liquid / vapor interface temperature in the evaporating film region equaling the vapor saturation temperature and of b) a constant curvature of the meniscus profile do not hold. The model approach was also presented in (Stephan and Busse 1992) and further developed and applied to different evaporation problems by Batzdorf (Batzdorf 2015) and Crößmann (Crößmann 2016).

Ma and Peterson state in (Ma and Peterson 1997) that the assumption of a constant temperature distribution and heat transfer coefficient along the axis of heat pipe grooves is not justified. For this reason they elaborated a detailed mathematical model on the basis of Wayner's concept, which not only considers the heat and mass transfer mechanisms in the two-dimensional cross section of a groove but also those occurring in axial direction.

The relatively simple geometries of the aforementioned modeling examples generally allow a comprehensive and precise description of the governing heat and mass transfer mechanisms with aid of differential equations of manageable number and complexity. Once the considered geometries become more complicated, such an approach is usually not feasible anymore. Instead, often two basic modeling strategies are pursued, which are occasionally combined: A first possibility is the development of three-dimensional spatially resolved numerical models of the wetted capillary structure and the respective heat and mass transfer mechanisms including evaporation, often solved by using the finite element method or finite volume method. Simulations with such a model can potentially yield precise predictions and allow valuable insights. However, a major drawback of these comprehensive models is that they require detailed knowledge of the structure geometry and that they consequently have a very restricted scope of applicability. A transfer to different structure geometries is not per se possible but requires individual modelling. Besides, the computational effort is extensive which in sum makes this model type unfavorable for dimensioning purposes. The second basic approach for dealing with evaporation from capillary structures is the concept of a simplified model which reduces the structure geometry to its basic characteristic quantities and which replaces the complex spatially-resolved mechanisms by effective relations and lumped parameters. A common method for such a simplification is a thermal resistance model (lumped-parameter model / node model). Clear benefits of this model type are its simplicity and low computational effort, ideally a broad transferability to different structure morphologies and boundary conditions and possibly the usability as a dimensioning tool. These advantages, though, usually come at the cost of a reduced model accuracy which can vary from a marginal to a severe effect on the simulation results.

In the field of spatially-resolved three-dimensional modelling of heat transfer and evaporation from porous structures extensive research was done by the group around Garimella. In order to identify effective thermal conductivity, permeability and interfacial heat transfer coefficients of real fluid-saturated wick structures they performed computer tomography scans of sintered copper wick samples and implemented the generated morphology data in a heat transfer model, as for example presented in (Bodla et al. 2012).

A numerical model which describes steady-state evaporation of water from common porous copper wick structures for heat pipes – namely wire mesh, rectangular grooves, sintered wicks and vertical microwires – is presented in (Ranjan et al. 2011). Equilibrium meniscus shapes for the different structure types are calculated with the software SURFACE EVOLVER based on the Young-Laplace equation. These interface shapes are transferred to a computational fluid dynamics software in which mass, momentum and energy equations are solved for the liquid domain of an elementary cell and evaporation is modeled with aid of the kinetic theory. The model is based on two assumptions: Firstly, the meniscus shape under evaporation conditions is taken to be identical as in thermal equilibrium conditions. The authors state that only low superheats are considered in their simulations and therefore they consider the assumption as justified. Accordingly, it may be suspected that the model is not valid for elevated superheats. Secondly, the effects

of disjoining pressure and capillary pressure on evaporation in the vicinity of the three-phase contact lines are neglected. Ranjan et al. argue that these impacts are marginal for the considered length scales of the pore structures of more than 100 µm. They refer to respective investigations by Wang et al. whose results indicated that the thin-film region only makes a very small contribution to the total heat transfer in case of relatively large channel widths. A similar modelling approach of the group is presented in (Bodla et al. 2013). As opposed to idealized structures considered by Ranjan et al., Bodla et al. focused on realistic sintered wick structures which were characterized from samples by X-ray microtomography.

In an earlier publication (Ranjan et al. 2009) the work group presents a model which merges the approach of a three-dimensional space-resolution with that of a simple resistance network. For different idealized wick structures for heat pipes (parallel rectangular ribs, horizontal parallel cylinders, vertically aligned cylinders, packed spheres) and different filling levels they first calculate the three-dimensional equilibrium meniscus shapes with the software SURFACE EVOLVER. From these interface shape data functional relations for three non-dimensional characteristic geometric quantities are deduced, which are the area-averaged minimum meniscus distance (between the solid surface and the liquid-vapor interface), the meniscus area, and the thin-film percentage area. The thin film region is defined in a pragmatic way as the area in which the liquid film thickness is below 10% of a characteristic length (which is the diameter of the sphere or cylinder). The authors state that the model is not very sensitive on the exact definition of the thin film region and alternatively apply 5% and 15% of the characteristic length for comparison reasons. Based on characteristic geometry data Ranjan et al. created a thermal resistance network – depicted in Figure 5 – which includes heat conduction through the liquid-saturated bottom section of the wick (calculated with an effective thermal conductivity) and two parallel resistance pathways for evaporation in the thin film region and in the intrinsic meniscus. Each evaporation pathway is composed of a heat conduction resistance of the respective film thickness and a resistance representing the evaporation phase change. The latter resistance type is defined with aid of the "convective heat transfer coefficient accounting for evaporation from the meniscus" (Ranjan et al. 2009) which the authors set to a constant value of 10^6 W/(m² K) and refer to (Wang et al. 2007) as the source of this value. Contact resistances between the spheres are not considered in the model.

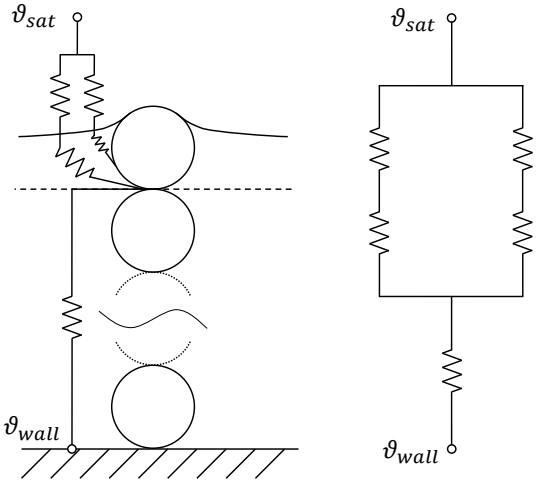

Figure 5: Schematic of a thermal resistance network by Ranjan et al. for heat transfer and evaporation from a porous wick structure; drawing on the basis of (Ranjan et al. 2009)

Hanlon and Ma also combined a relatively detailed description of the meniscus shape with simplified definitions for the heat transfer through the structure: They developed a model for steady-state evaporation from the thin films in the top region of a saturated sintered wick structure of spherical particles (Hanlon and Ma 2003). Apparently based on the model of Ma and Peterson, Hanlon and Ma implicitly calculate a thermal resistance for the evaporation from the thin films on top of the particles by integrating

over the local film conduction resistance (depending on the film thickness profile) along the meniscus profile direction. The contact line length per particle is obviously assumed to be the maximum circumference of the spherical particle. To account for the thermal resistance of heat conduction through the liquid-saturated porous structure an effective thermal conductivity is calculated. The thermal resistance of phase transition at the liquid / vapor interface was apparently neglected. The modalities of liquid flow are considered by determining the capillary pressure and permeability of the wick structure, and the driving temperature difference for the onset of nucleate boiling was calculated to account for dry-out effects. By means of the different resistance contributions the total heat transfer coefficient was calculated in dependence of wick thickness. A comparison with experimental data, though, showed a deviation of the simulated heat transfer coefficients of about one order of magnitude. It is not quite clear to the reader whether this discrepancy only originates from nucleate boiling in the experiments which is not considered in the simulations or if it is also caused by general deficiencies of the model conception.

An example for a simple thermal resistance model for an evaporation process from a capillary structure can be found in a publication from Kim et al. (Kim et al. 2003). The authors designed a resistance network for steady-state evaporation from the cross-section of a meniscus in a groove structure – which is schematically depicted in Figure 6 – as a part of a comprehensive thermal resistance model characterizing the overall thermal resistance of a miniature copper / water heat pipe. The trapezoidal groove shape is simplified to a rectangular cross section and the temperature of the liquid / vapor interface is assumed to be identical with the vapor temperature. For the arrangement of the resistance network of the evaporator section an assumption from Chi (Chi 1976) was adopted which comprises that heat flow through a meniscus in a groove follows two parallel pathways: One through the groove fin and subsequently through the evaporating thin film region of the meniscus and another one through the bulk liquid. While the thermal resistances of the fin and the bulk meniscus are calculated by means of a simple conduction approach, the resistance of the evaporating thin film region is described with aid of an effective heat transfer coefficient, as suggested by Chi. Kim et al. compared simulation results for the complete heat pipe resistance with measurement results for working temperatures of 40°C to 70°C and found a relatively good agreement with deviations of 12…16%.

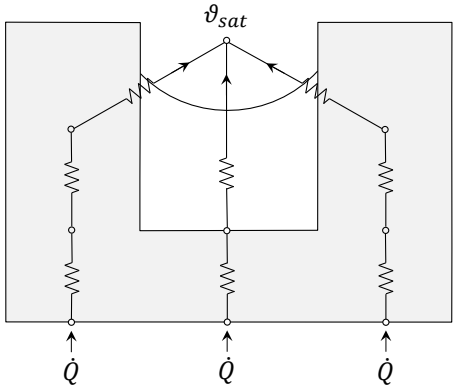

Figure 6: Schematic of a thermal resistance network by Kim et al., modeling the evaporation from a groove structure in a copper / water heat pipe; drawing on the basis of (Kim et al. 2003)

Another straightforward resistance model for heat pipes with capillary wicks, which can be utilized for performance estimations and dimensioning, is presented in the VDI Heat Atlas (Stephan 2013) and schematically depicted in Figure 7. Disregarding the heat transfer between heat pipe wall and ambient, the evaporator section is modeled as a serial connection of resistances which represent the radial arrangement of the evaporator: A conduction resistance of the wall, a conduction resistance of the liquid-saturated capillary structure and a resistance representing the evaporation phase change at the surface of the capillary structure. Depending of the particular capillary structure type (parallel or serial arrangement

of matrix and fluid, rectangular or triangular axial grooves, mesh structure, sintered wick structure) different equations for the effective thermal conductivity of the saturated capillary structure are listed up which can be used for calculating the conduction resistance of the fluid-saturated capillary structure. (Detailed information on effective thermal conductivities of wick structures can be found in (Chi 1976).) The resistance of evaporation phase change is described by an equation for the molecular kinetic resistance of the phase interface. However, the phase change resistance is stated to be usually negligible because its magnitude is marginal compared to the resistance of the liquid-saturated capillary structure.

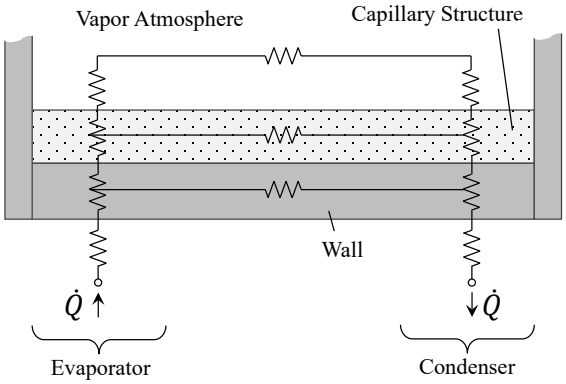

Figure 7: Schematic of a thermal resistance network by Stephan / VDI Heat Atlas, representing the basic heat transfer mechanisms in a wick heat pipe; drawing on the basis of (Stephan 2013)

2.6 Capillarity and Dewetting Dynamics of Porous Structures

Wetting and Contact Angle

The equilibrium shape of a liquid which is brought in contact with a solid surface is usually characterized by the contact angle, which basically depends on the interfacial tensions between the involved solid, liquid and surrounding gas phase (Yuan and Lee 2013). If referred to a flat inflexible surface this relationship is described by the Young equation which is depicted in Figure 8 and which reads (Gennes et al. 2004):

$$\gamma_{lg} \cdot cos(\theta) = \gamma_{sg} - \gamma_{sl} \tag{2-2}$$

In this equation γ represents the interfacial tension between two phases (solid s, liquid l, gas g) and θ the contact angle between solid surface and liquid / gas interface.

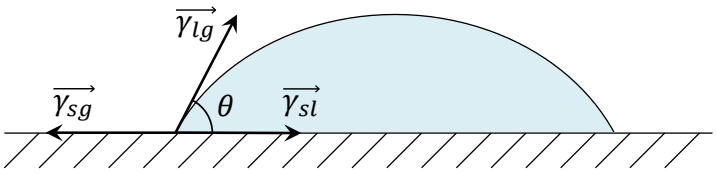

Figure 8: Visualization of the involved interfacial tensions and contact angle of a liquid partially wetting a solid surface

Generally, two characteristic types of wetting are distinguished: If a liquid completely spreads on a solid surface and the contact angle is zero the wetting behavior is called “total wetting”. If a liquid drop does not totally spread on the solid but forms a certain contact angle ($\theta > 0$) it is referred to as “partial wetting”. The partial wetting behavior can again be subdivided in “mostly wetting” for contact angles $\theta \leq 90°$ and

"mostly non-wetting" for $\theta > 90°$. A particular characteristic of a "mostly wetting" liquid / solid combination is that the liquid will spontaneously infiltrate into a capillary or porous medium (Gennes et al. 2004; Yuan and Lee 2013).

The interfacial tension at a phase boundary depends on the strength relation of intermolecular forces acting on the respective phases and are thus governed by material properties. "High-energy surfaces" (e.g. metals and glass) which are subjected to covalent, ionic or metallic bonding provoke spreading of virtually all liquids (Gennes et al. 2004) due to the effort of the system to minimize surface energy (Yuan and Lee 2013). "Low-energy surfaces" on the other hand which are bound by van-der-Waals forces or hydrogen bonds are usually hardly wettable, such as plastics (Gennes 1985). It can further be stated that a liquid will completely spread on a solid surface if the polarizability of the solid is higher than that of the liquid (Gennes et al. 2004). Surface chemistry and topology are governing factors as well in terms of wettability. For the case of copper and aluminum surfaces in combination with water and different organic fluids Hong et al. for instance found that roughness and oxidation of the solid surfaces lead to a decreasing contact angle (Hong et al. 1994).

Capillary Effect

In narrow spaces, tubes with small diameter and porous structures the relation of interfacial tensions can provoke intrusion of liquid into the structure against gravity, which is known as the capillary effect. As mentioned before, a spontaneous infiltration of liquid into the capillary space only occurs in case of a contact angle smaller than 90° while in case of larger contact angles the liquid does not enter the structure without the exertion of external forces (Gennes et al. 2004; Yuan and Lee 2013). Due to the forces associated with the interfacial tensions of solid, liquid and gas phase (or more general solid and two immiscible fluids), a pressure difference between the wetting fluid and the non-wetting fluid will occur, which is termed the capillary pressure (Yuan and Lee 2013).

For a cylindrical vertical tube with sufficiently small radius r_{tb} – in which the meniscus forms a section of a sphere – the relationship between capillary pressure Δp_c, fluid / fluid interfacial tension γ_{lg}, contact angle θ and tube radius r_{tb} can be described by the following equation which is derived from the Young-Laplace equation (Gennes 1985):

$$\Delta p_c = \frac{2 \cdot \gamma_{lg} \cdot cos(\theta)}{r_{tb}} \tag{2-3}$$

The balance between capillary pressure and gravitational force causes the meniscus to rise to a certain equilibrium height (capillary height) h_c (cf. Figure 9) which can be calculated by means of Jurin's law (Yuan and Lee 2013):

$$h_c = \frac{2 \cdot \gamma_{lg} \cdot cos(\theta)}{\Delta\rho_{lg} \cdot g \cdot r_{tb}} \left(= \frac{\Delta p_c}{\Delta\rho_{lg} \cdot g} \right) \tag{2-4}$$

In this equation $\Delta\rho_{lg}$ represents the density difference between liquid and gas (or between the two fluids) and g the gravitational acceleration.

In porous structures of practical relevance the pore diameter is usually not constant but scatters within a certain range. White (White 1982) therefore defined an effective capillary radius for powder beds with aid of the volume fraction of the solid ϕ, the density of the solid ρ_s and the mass-specific surface area of the solid a_s, which allows a modification of equation (2-3) to

$$\Delta p_c = \frac{\gamma_{lg} \cdot cos(\theta) \cdot \phi \cdot a_s \cdot \rho_s}{1 - \phi} \tag{2-5}$$

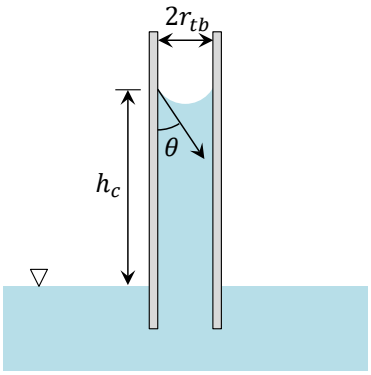

Figure 9: Visualization of the capillary rise in a vertical cylindrical tube (Jurin's law)

Dynamic Dewetting Behavior of Porous Structures

Comprehensive research on fluid distribution and dynamic dewetting processes in porous media is done in the field of drying technologies. In drying, evaporation of a liquid does usually not take place in a one-fluid system at saturation conditions (evaporation according to the saturation pressure curve) as considered within this work. Instead, mostly air is used to absorb the vapor of the drying process which makes it a two-fluid system. Evaporation is then driven by the difference between fluid temperature and saturation temperature of the vapor partial pressure in the surrounding air. For the analysis of drying processes even isothermal conditions are often assumed and evaporation is only driven by a concentration gradient. Despite these differences, the occurring mechanisms in drying processes might to some extent be transferrable to the dynamic evaporation of a one-fluid system from a porous structure.

Virtually all porous structures of practical relevance do not have a uniform pore size but are characterized by a pore size distribution. Besides, the pore shape mostly features a certain variation as well (Irawan 2006). Since pore size strongly influences capillary pressure, vapor diffusion and viscous forces, transport phenomena and liquid distribution inside a porous structure are essentially governed by the pore size distribution (Irawan 2006). In isothermal drying processes the evaporation or drying dynamics depend on the interrelation of capillary forces, friction forces and evaporation rate. In a fluid-saturated matrix the largest pores at the structure's surface to the ambient will empty at first due to their lowest capillary pressure. The subsequently emerging pattern of dry, saturated or partially saturated pore domains decisively depends on geometry and material properties of the structure and the corresponding force relations. These drying dynamics are often described by means of pore network models in which the void volume of the structure is considered as a network of nodes (pores) which are interconnected by bonds (throats) (Irawan 2006).

The impact of gravity on drying dynamics of a pore network has been investigated by Laurindo and Prat (Laurindo and Prat 1996), by using the Bond number Bo (which is also often used synonymous with the Eötvös number Eo) as an indicator for the relation of gravitational to capillary forces:

$$Bo = Eo = \frac{\Delta\rho_{lg} \cdot g \cdot L^2}{\gamma_{lg}} \tag{2-6}$$

where $\Delta\rho_{lg}$ is the density difference between liquid and gas, g the gravity vector, L a characteristic length of the pores (for which they use the distance between two pore nodes), and γ_{lg} the interfacial tension between liquid and gas. The authors consider three different cases (cf. Figure 10): Firstly, a flat porous structure is arranged horizontally so that the impact of gravity can be neglected ($Bo = 0$); secondly, its

side open for vapor mass flow is oriented upwards ($Bo > 0$) and thirdly, its open side is oriented downwards ($Bo < 0$). From experimental and simulation results Laurindo and Prat found for the horizontal case ($Bo = 0$) that during the drying process a section towards the open side was completely dry while the rest of the structure exhibited dry and wet clusters. For the case with the open side upwards ($Bo > 0$) a relatively sharp receding front between a dry section at the top and a liquid-saturated section at the bottom formed. In the case of the open edge pointing downwards ($Bo < 0$) the pore matrix close to the opening at the bottom was mostly still saturated with liquid except some channel-like partially dry cluster which was connected to a more extended partially dry area in the upper section.

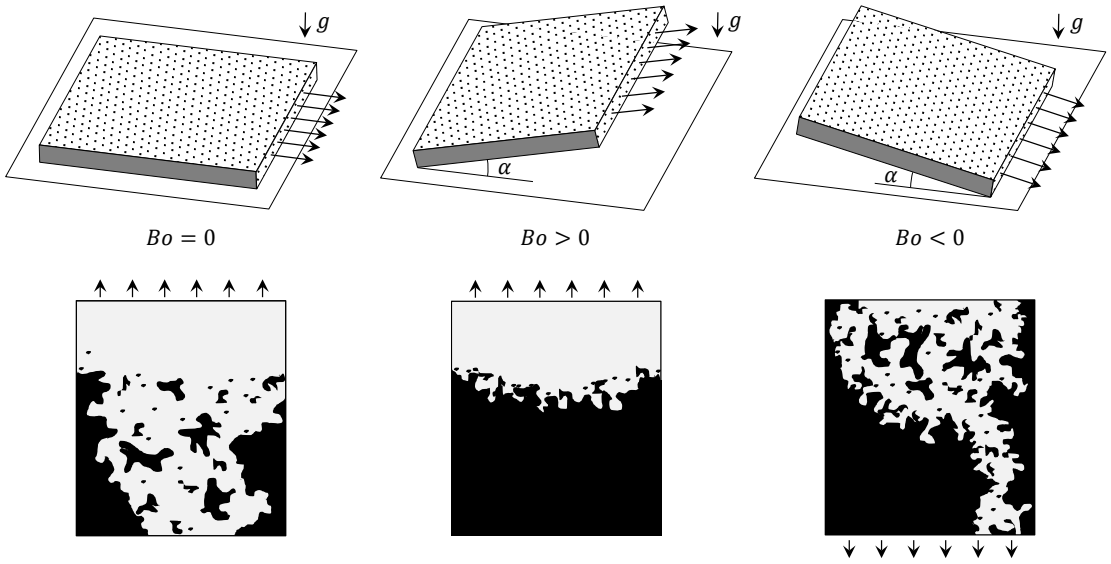

Figure 10: Impact of gravity on drying dynamics: Spatial arrangement of pore structure (top) and schematic drying patterns (bottom; liquid phase black, gas phase white) for different Bond number ranges, after investigations of Laurindo and Prat; reproduced from (Laurindo and Prat 1996)

Another phenomenon influencing the liquid distribution in drying processes is film flow (Laurindo and Prat 1998). According to Laurindo and Prat, the occurrence of film flow is associated with the capillary number of the considered system which describes the relation of viscous drag forces (represented by the dynamic viscosity of the liquid (or more general fluid) μ_l and a characteristic velocity v) to surface tension forces (represented by the interfacial tension of the two fluids or of liquid and gas γ_{lg}):

$$Ca = \frac{\mu_l \cdot v}{\gamma_{lg}} \tag{2-7}$$

At very low capillary numbers ($Ca < 10^{-8}$) liquid is prone to flow within the roughness of the pore walls while at low to intermediate capillary numbers ($10^{-8} < Ca < 10^{-4}$) liquids tends to flow in films formed in the corners of angular pores (cf. Figure 11, right). The formation of such liquid films can provoke a third characteristic wetting state in a porous structure besides completely dry and completely wet clusters. For case of a drying process with the open side of the structure pointing upwards (strong impact of gravitation, $Bo > 0$) Laurindo and Prat state that, instead of a sharp front between a fluid-saturated section at the bottom and a dry section at the top (Figure 11, left), an intermediate layer can exist in which most of the pore volume is dry but a liquid film still covers parts of the pore walls (Figure 11, center). In that way the evaporation front is closer to the open edge of the structure than without formation of a film region. The authors suspect this phenomenon as the cause for higher experimental drying rates compared to simulation results which do not consider the formation of liquid films. Film flow phenomena in drying processes were also investigated by Yiotis and colleagues, and addressed for instance in (Yiotis et al. 2004; Yiotis et al. 2005). Besides the field of drying processes, the occurrence of film flow is also discussed in the

context of drainage scenarios of groundwater flow and oil recovery from porous soils, as for example in (Tuller and Or 2001).

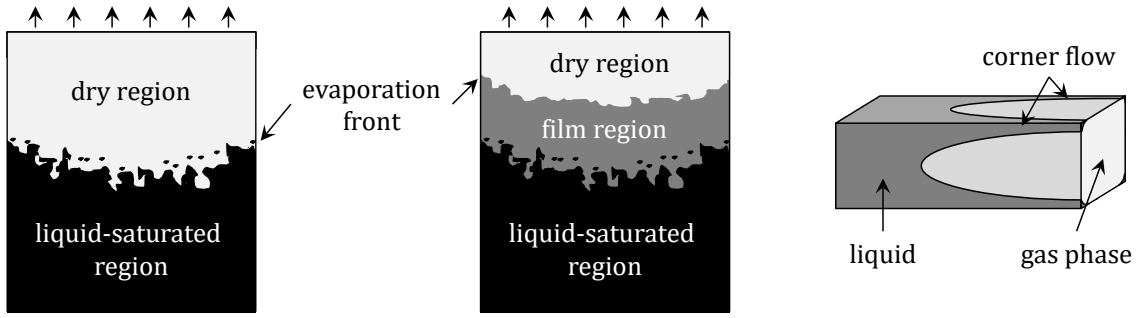

Figure 11: Schematic drying patterns of porous structures without (left) and with (center) consideration of film flow; schematic of corner flow in angular duct (right); according to Laurindo and Prat; reproduced from (Laurindo and Prat 1998)

Considering that the particular balance of capillary, viscous and gravitational forces determines the liquid distribution dynamics of a slow drying process, the group around Prat, Bouleux, Plourde suggest to predict the characteristic distribution pattern with aid of three characteristic lengths (Prat and Bouleux 1999) and a corresponding phenomenological map (Plourde and Prat 2003). The characteristic length of the gravity front L_g is defined as (Prat and Bouleux 1999)

$$L_g \approx \frac{L}{Bo} \tag{2-8}$$

using a characteristic length L for the average pore size and a formulation variant for the Bond number Bo:

$$Bo = \frac{\rho_l \cdot g \cdot L^2}{2 \cdot \gamma_{lg} \cdot cos(\theta)} \tag{2-9}$$

The characteristic length of the viscous front L_{cap} is defined as

$$L_{cap} \approx \frac{k_p}{L \cdot Ca} \tag{2-10}$$

with the permeability k_p and a formulation of the capillary number Ca

$$Ca = \frac{\mu_l \cdot v}{2 \cdot \gamma_{lg} \cdot cos(\theta)} \tag{2-11}$$

which involves a characteristic liquid filtration velocity v that is defined as

$$v = e/\rho_l \tag{2-12}$$

using the evaporation flux density e and the liquid density ρ_l.

By comparing the characteristic length values L_g and L_{cap} with the characteristic length (height) of the porous structure sample L_{str} the strength relations of the different forces can be estimated (Prat and Bouleux 1999). The applicable liquid distribution pattern can then be determined from a map (Plourde and Prat 2003) which is schematically depicted in Figure 12. In case gravitational and / or viscous forces exceed capillary forces, L_g and / or L_{cap} are small compared to L_{str} (large quotients L_{str}/L_g and L_{str}/L_{cap})

and a receding front pattern applies. If capillary forces dominate over gravitational or viscous forces, L_g and L_{cap} are larger than L_{str} (small quotients L_{str}/L_g and L_{str}/L_{cap}) and a so-called "capillary-fingering" pattern (invasion percolation) will form.

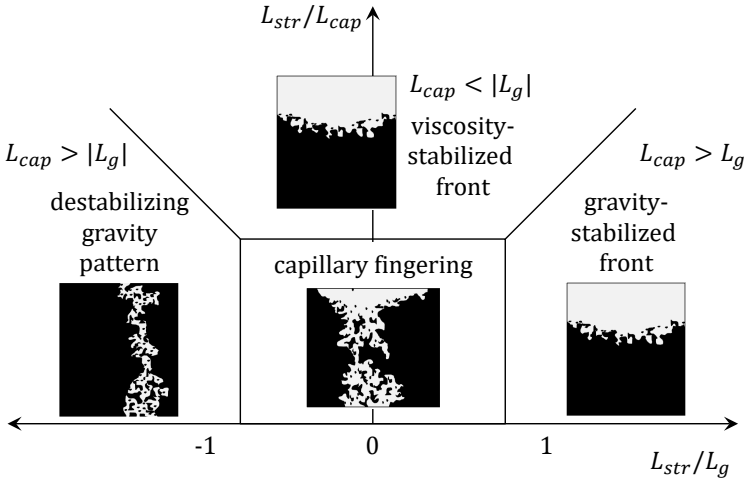

Figure 12: Phenomenological map of characteristic liquid distribution patterns for porous structures in a slow drying process, developed by Plourde and Prat; simplified reproduction from (Plourde and Prat 2003)

3 OBJECTIVES OF THE WORK

In this chapter the current state of the art of evaporator concepts are contrasted with the application-related boundary conditions, and deficiencies of existing solutions are specified. The technological approach which is pursued in this work is motivated and the respective research focus is described. Under consideration of existing and lacking knowledge, the particular objectives for this work are defined by means of three scientific questions.

As described in chapters 1 and 2.1, adsorption heat pumps and chillers can make a valuable contribution to a stable, efficient and sustainable energy supply system. Given that considerable research efforts are spent on the improvement of adsorber heat exchangers, the availability of efficient evaporators becomes increasingly crucial to ensure a satisfying overall adsorption module performance (Schnabel et al. 2011). The usage of water as refrigerant– which is employed for most adsorption heat pumps – in combination with the required sub-atmospheric pressure range of about 0.76…2.3 kPa, however, involves rather unusual evaporation characteristics (cf. chapter 2.2) which necessitates a systematic customization of heat exchanger design and operation mode to the boundary conditions. Existing evaporator concepts, as pointed out in chapter 2.1, are often associated with either a low heat transfer performance, high constructional complexity or insufficient operational reliability. Especially for compact one-chamber adsorption modules with only one evaporator-condenser heat exchanger in cyclic operation (cf. chapter 1, Figure 1 right) most of these designs are not particularly suitable since this module type requires a very simple and low-cost evaporator design and it is reliant on a minimization of the refrigerant mass in order to avoid thermal losses.

A promising solution for these compact modules is a combined evaporator-condenser heat exchanger with porous metal structures on its surface, which allows storage of refrigerant in the condensation phase and efficient evaporation from extensive three-phase contact lines. For this work a vertically-arranged wire mesh structure was chosen as an exemplary porous structure type. Due to the cyclic operation, evaporation and condensation are not steady-state processes but have a dynamic, unsteady character, and the evaporation performance is strongly interrelated with the wetting state of the structure. For designing an efficient evaporator of that type it is crucial to have a profound knowledge of the occurring heat transfer mechanisms and of the effect of the different impact factors on the evaporation dynamics. To date, only few experiments with non-optimized evaporators were conducted (cf. chapter 2.1). The interrelations of occurring heat transfer and wetting dynamics are hardly understood and consequently, there are no design guidelines which allow a straightforward dimensioning procedure based on the particular requirements and boundary conditions.

Valuable insights on evaporation from three-phase-contact lines and porous structures can be obtained from numerous publications in the context of wicked heat pipes and electronics cooling, as chapters 2.3 and 2.4 reveal. However, they mainly refer to different boundary conditions: Often only very simple capillary geometries such as channels / grooves are considered. Also, most investigations refer to steady-state conditions in which a continuous refrigerant feed compensates for the evaporation mass flow.

Investigations on unsteady evaporation processes from porous structures – which are relevant for the envisaged application of this work – could hardly be found in the course of a literature research. Also the (dynamic) interaction of refrigerant distribution and evaporation mechanisms is virtually not addressed.

Against this background, the basic objective of this work is to contribute to a better understanding of the unsteady evaporation mechanisms of the refrigerant water in evaporators with porous structures and to provide a foundation for the development of dimensioning methods. From this goal, the following scientific questions were derived:

1. **Which heat transfer mechanisms occur in the unsteady evaporation of water from porous structures and how are they interrelated with dewetting dynamics? How do geometric parameters of the porous structure and process parameters influence these mechanisms?**

   Due to the absence of a continuous refrigerant feed the decreasing refrigerant mass will continuously change its distribution during the evaporation process. At each point of time the distribution change depends on previous wetting conditions, on the current spatial distribution of evaporative mass flow and on the local balance of capillary, gravitational and potentially viscous forces. Evaporation will preferentially occur at places which are in good thermal contact to the heat source while refrigerant will preferentially accumulate at places which are energetically favorable in terms of interfacial tension. Obviously, there are strong interrelations between dewetting characteristics and evaporation dynamics. The first scientific question aims at investigating these interrelations and their effect on the evaporation performance. With aid of an overall heat transfer coefficient the evaporation performance of the porous structure should be quantified and its dynamic course over time should be analyzed and related to the refrigerant charge state of the structure. Since heat transfer and capillary action are essentially governed by the structure's geometry and by thermodynamic conditions, the impact of these factors on the evaporation process is supposed to be analyzed.
   This scientific question is addressed by means of experiments on the evaporation from porous structures and additionally by model analysis. Respective results can mainly be found in chapters 5.1-5.4.

2. **Can a simple model describe the dynamic evaporation process for different structure geometries and process conditions with a satisfactory precision?**

   To allow for a comprehensive analysis of the different heat transfer mechanisms and dewetting dynamics, the development of a mathematical model is envisaged in this work. By means of comparisons with experimental results the simulations could enable a better understanding of the occurring mechanisms and the identification of limiting parameters. The model is intended to be simple and feature a broad applicability while ensuring a sufficient prediction accuracy. Provided that it proves reliable, the evaporation model is prospectively intended to serve as a basis for a model on heat exchanger level and thereby as a basis for design and dimensioning guidelines for respective cyclic evaporators for adsorption heat pumps and chillers.
   A detailed description of the evaporation model is provided in chapter 4.2. Simulation results are presented in chapters 5.1-5.4.

3. **Which structure geometries are suitable for the envisaged application and which potential can be expected from an evaporator-condenser heat exchanger with wire mesh structure?**

   The last scientific question addresses the assessment of geometric structure properties and of the general concept of an evaporator-condenser with porous structures (especially wire mesh structures) for cyclic operation. Within this task the evaporation heat transfer of the structure should

not be considered as an independent characteristic but it should be related to the boundary conditions and requirements of an evaporator heat exchanger and of the operating conditions in an adsorption module. An intended outcome is the identification of limiting parameters and deduction of design suggestions.

In order to judge the general reasonability of the concept of an evaporator-condenser with porous structure in cyclic operation, a potential estimation should be carried out which roughly estimates the achievable performance range. A comparison with a state-of-the-art reference concept can reveal whether or not further development activities on the examined evaporator type are promising.

This third scientific question is primarily addressed in chapters 5.4.5 and 5.5.

4 METHODS

This chapter specifies the methodical approaches employed in this work, which mainly consist of an experimental part (4.1) and an associated mathematical model (4.2). As respects the experiments, the measuring task and concept are explained (4.1.1), followed by a description of the experimental setup (4.1.2), samples (4.1.3), and the measuring procedure (4.1.4). Additional remarks on the measuring concept motivate the choice of particular implementation aspects (4.1.5). Subsequently, the selected measurement parameters are listed (4.1.6), methods for data reduction (4.1.7) and measurement uncertainty analysis (4.1.8) are explicated, and assessment methods for the investigated samples are derived (4.1.9). On the part of the model, at first objectives and concept are presented (4.2.1), followed by a description of the developed resistance-capacitance network of the peripheral setup components (4.2.2). The model implementation of the dewetting dynamics and heat transfer conditions during evaporation from the porous structures is delineated (4.2.3), and finally, the computational algorithm used for determining the simulation results is described (4.2.4).

4.1 Evaporation Measurements

4.1.1 Measuring Task and Concept

As stated in the objectives of the work in chapter 3, a series of measurements was scheduled in order to provide the data base for an analysis of the characteristics of unsteady water evaporation from porous wire mesh structures. In order to ensure a straightforward evaluation of the measurements, one-dimensional heat transfer conditions on the macroscopic level were envisaged. Therefore the porous structure sample was supposed to be heated homogeneously from one side, as schematically illustrated in Figure 13 (left). The overall heat transfer coefficient of evaporation U_{ev} should serve as the main evaluation quantity, characterizing the efficiency of evaporative heat transfer. According to equation (4-1), U_{ev} can be calculated from the heat flux $\dot{q}_{ev}$ through the structure and the driving temperature difference $\Delta\vartheta$:

$$U_{ev} = \frac{\dot{q}_{ev}}{\Delta\vartheta} = \frac{\dot{q}_{ev}}{\vartheta_{strb} - \vartheta_{sat}} \tag{4-1}$$

The driving temperature difference $\Delta\vartheta$ represents the global driving force of the evaporation process and is defined as the difference between the temperature at the base of the porous structure ϑ_{strb} and the saturation temperature ϑ_{sat} of the vapor above the structure surface. By definition, the overall heat transfer coefficient U_{ev} does not consider the individual heat transfer processes within the structure volume but only its net heat transfer capability. With aid of the heat flux through the structure ($\dot{q}_{ev}$) also the vapor mass flow rate $\dot{M}_{vap}$ and the refrigerant mass M_{rf} inside the pore structure can be determined, which allows for an analysis of the relation between dewetting dynamics and evaporation performance. With the cross-sectional area A_{str} of the sample structure and the specific enthalpy of vaporization Δh_v the equation for the vapor mass flow rate $\dot{M}_{vap}$ reads:

$$\dot{M}_{vap} = \frac{\dot{q}_{ev} \cdot A_{str}}{\Delta h_v} \tag{4-2}$$

The current refrigerant mass charge M_{rf} of the sample structure at time t can be derived by integrating the vapor mass flow rate $\dot{M}_{vap}$ from time t until the end time t_n of the evaporation process, which corresponds to the dryout:

$$M_{rf}(t) = \int_{t}^{t_n} \dot{M}_{vap}(\tau)\, d\tau \tag{4-3}$$

A detailed description of data reduction methods is given in chapter 4.1.7.

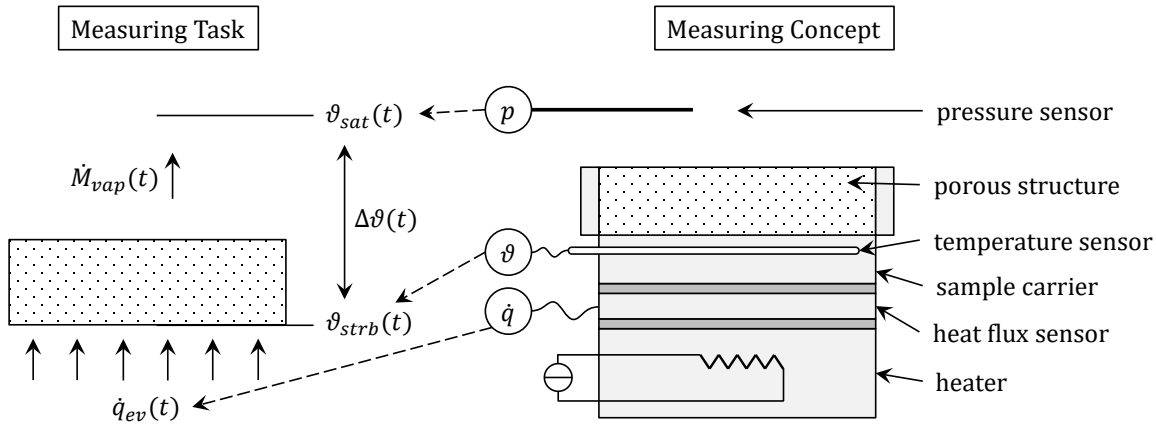

Figure 13: Schematic visualization of the measuring task (left) with relevant measuring and evaluation quantities, and of the implemented measuring concept (right); drawings not true to scale

Considering the general measurement task and the objective of the first scientific question in chapter 3, the following major requirements for the measurement concept can be defined:

- Experimental setup:
  - The experimental setup should allow for one-dimensional heat transfer on a macroscopic level; edge effects should be minimized
  - Vapor saturation pressure and either heat flux or driving temperature difference should be well-defined and time-constant during the whole measurement
  - Setup and data acquisition chain must be suitable for transient heat transfer conditions (time resolution, response time, thermal capacities need to be taken into account)
  - A satisfactory measurement precision of all direct and indirect measuring quantities should be ensured for all measuring conditions. The choice of sensors and setup design should strive for a minimization of measurement uncertainties.
- Sample geometry:
  - The topology of the porous mesh structure should be well-defined, simple and homogeneous in order to allow for a clear attribution of measurement characteristics to certain geometric structure properties. Considering the requirement from application side for efficient heat transfer, the porous structure should have a high thermal conductivity in heat flow direction.
  - Samples with varied geometry parameters should be investigated. The parameters to be varied are porosity, pore size, structure height, and orientation angle of the wire mesh. The choice of parameter values should consider effective thermal conductivity, potential

refrigerant storage capacity, capillarity, specific weight, manufacturability, and commercial availability of the mesh material. Besides, the chosen parameter variants should be sufficiently different so that a distinct effect on wetting and evaporation behavior can be expected

- Operational parameters:
    - The choice of thermodynamic operating points should be made under consideration of application-related boundary conditions (reasonable conditions for an adsorption heat pump / chiller) and setup-related boundary conditions (device restrictions, operational safety, measuring ranges, measurement uncertainties)

The most important features of the realized measuring concept will briefly be summarized in the next paragraphs. Details on the constructional implementation will follow in chapters 4.1.2 (experimental setup) and 4.1.3 (sample structures), a description of the measurement procedure in 4.1.4, and specifications of chosen measurement parameters in 4.1.6. In chapter 4.1.5 several presumptions, justifications and restrictions regarding the implementation of the measurement concept are discussed. Data reduction, measurement uncertainties and assessment methods are addressed in chapters 4.1.7-4.1.9.

In the implemented measuring concept – which is schematically depicted in Figure 13 on the right – the porous structure samples were decided to have a cylindrical shape of 40 mm diameter and a variable height. One circular and planar side of the porous structure is mechanically and thermally connected to a flat cylindrical copper carrier of the same diameter. Heat is supplied to the carrier by means of an electric heating element in a copper block. The outer cylindrical surface of the structure sample is blocked by an encircling ring in order to prevent lateral escape of water vapor. The symmetric design of the setup, the one-sided heat supply, the high thermal conductivity of the copper components, and the lateral vapor blocking aim at meeting the requirement of one-dimensional heat transfer.

With the choice of an electric heat supply the driving force which triggers the evaporation process is provided in form of a defined heat flux instead of a fixed temperature difference boundary condition. The driving temperature difference $\Delta\vartheta$ will accordingly adapt to the prevailing heat transfer coefficient U_{ev} of the evaporating structure under the respective conditions. Considering the unsteady character of the measurements and the thermal capacity of the heater block, the heat flux entering the porous structure $\dot{q}_{ev}$ might temporarily deviate from the heat flux applied by the heater. In order to determine the heat flux into the structure with highest possible dynamic accuracy, it is measured directly below the sample carrier. The carrier height is reduced to a constructional minimum of 4 mm to keep the thermal capacity between structure base and measuring position as small as possible. Heat flux measurement is implemented with a flat thermopile-type heat flux sensor.

The temperature at the structure base ϑ_{strb} is determined with aid of a rod-shaped Pt100 resistance thermometer with 1.6 mm diameter and low response time which is positioned in a horizontal drill hole inside the carrier material. The hole is applied at the smallest feasible distance below the structure base (1.5 mm from bore axis to carrier surface) in order to minimize the thermal resistance and capacitance between structure base and measuring position.

The vapor saturation temperature ϑ_{sat} is determined from a pressure measurement and conversion with aid of the vapor pressure curve of water (cf. Figure 74 in the appendix) since temperature measurement of low-density gaseous atmospheres is often not reliable. To ensure saturated conditions and thus the validity of the vapor pressure curve translation, careful evacuation of the system is required in order to reduce the amount of non-condensable gases to a negligible amount.

4.1.2 Experimental Setup

Test Rig

For the scheduled measurements of this work a pre-existing test rig was utilized as a basis. Originally it was built for steady-state evaporation measurements with porous structures in flooded and partially flooded mode (see details in (Witte 2016)). In order to accommodate the different requirements of unsteady measurements the setup was modified in the course of this work.

The general setup of the test rig is depicted in a simplified piping and instrumentation diagram in Figure 14. Specifications of the installed devices and parts are listed in the appendix in Table 9.

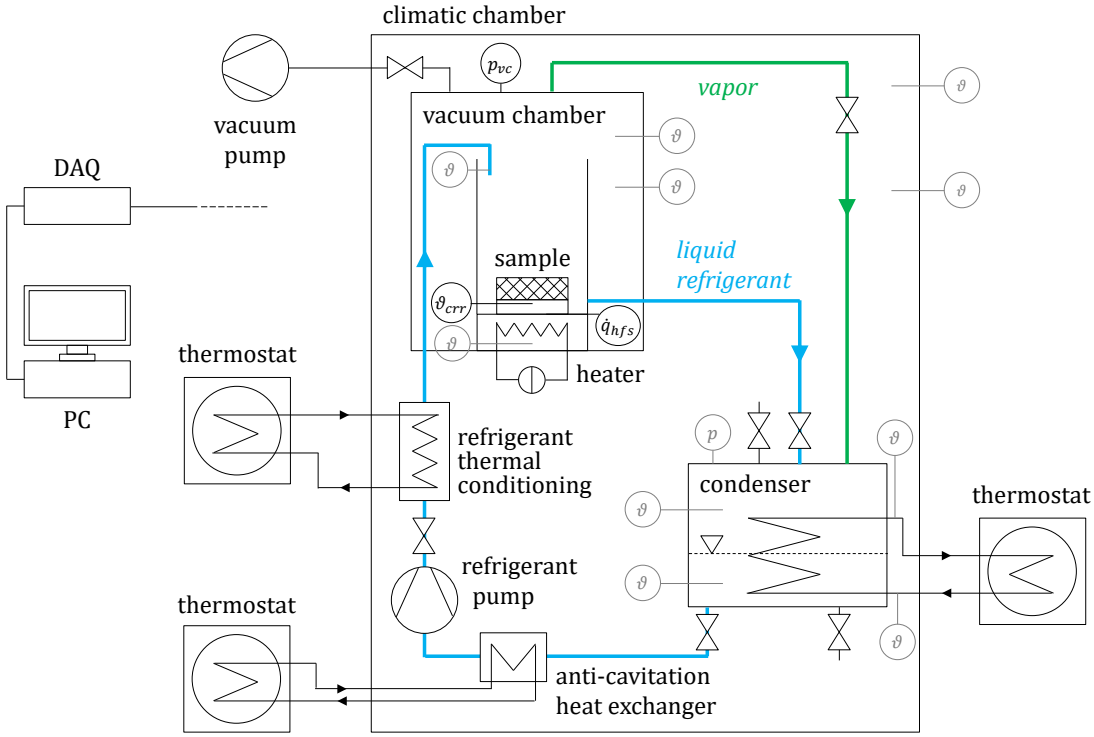

Figure 14: Piping and instrumentation diagram of the test rig

Since a pure water atmosphere at sub-atmospheric pressure is required for the measurements, all components of the refrigerant circuit comply with vacuum standards. Connection lines and parts are therefore equipped with ISO-KF vacuum flanges. In order to quantify the achievable level of vacuum-tightness a pressure rise test was conducted which is described in chapter B.6 in the appendix. The identified leak rate of the complete vacuum system amounts to $5.3 \cdot 10^{-6}$ mbar l/s which is assessed as an acceptable value for the scheduled measurement conditions.

Central component of the test rig is the vacuum chamber in which evaporation on the porous structure sample takes place. It has a lid on the upper side covering the whole diameter which allows to open the chamber and install / uninstall the evaporation assembly. The lid is sealed against the chamber body with a large O-ring which can be compressed by applying clamps on the flange edges. Via a manual ball valve the vacuum chamber can be connected to a scroll type vacuum pump (Edwards nXDS 6iC, cf. Table 9) for evacuation.

Continuous evaporation is enabled by simultaneous liquefaction of refrigerant vapor on a condenser which consists of a stainless steel tube-fin heat exchanger inside a stainless steel chamber (cf. Table 9 for specifications). Being permanently partially flooded, the condenser also acts as a refrigerant reservoir. Its filling level can be monitored by means of a glass viewport. System pressure (and therewith saturation / evaporation temperature) can be controlled by the set temperature of a thermostat which is connected to the condenser heat exchanger. To allow for direct evacuation the condenser exhibits a flange connecting branch which can be linked to the vacuum pump.

The refrigerant vapor produced inside the vacuum chamber can travel to the condenser through a DN-50 flexible stainless steel hose, passing an electropneumatic bellows angle valve which allows to close this connection. Liquid refrigerant can be fed into the vacuum chamber via a lead-through in the chamber wall. Excess refrigerant can be drained to the condenser through another tube connection which can be closed with a manual valve.

For refrigerant supply to the sample setup refrigerant can be pumped from the condenser sump to the vacuum chamber by a peristaltic pump (cf. Table 9 for specifications). To avoid the risk of cavitation inside the pump – which might arise due to operation close to saturation state of the water – the refrigerant is cooled down before it enters the peristaltic pump. This cooling is realized by piping the refrigerant through a water-ethylene-glycol bath which additionally contains a tube-fin heat exchanger fed by a thermostat (set temperature: 0.5°C). In order to have the refrigerant entering the vacuum chamber at a defined temperature, a counterflow coaxial tube heat exchanger is installed between peristaltic pump and vacuum chamber, connected to a third thermostat.

All devices affiliated to the refrigerant circuit are placed within a climatic chamber. Setting the temperature of the climatic chamber to a temperature slightly above evaporation temperature permits minimization of heat gains into the system and avoids condensation of refrigerant vapor on the chamber walls.

Evaporation Assembly

The vacuum chamber contains an assembly in which the evaporation process takes place, mainly consisting of sample, heater block, PMMA (polymethyl methacrylate) container and sensors (cf. Figure 15 and Figure 16).

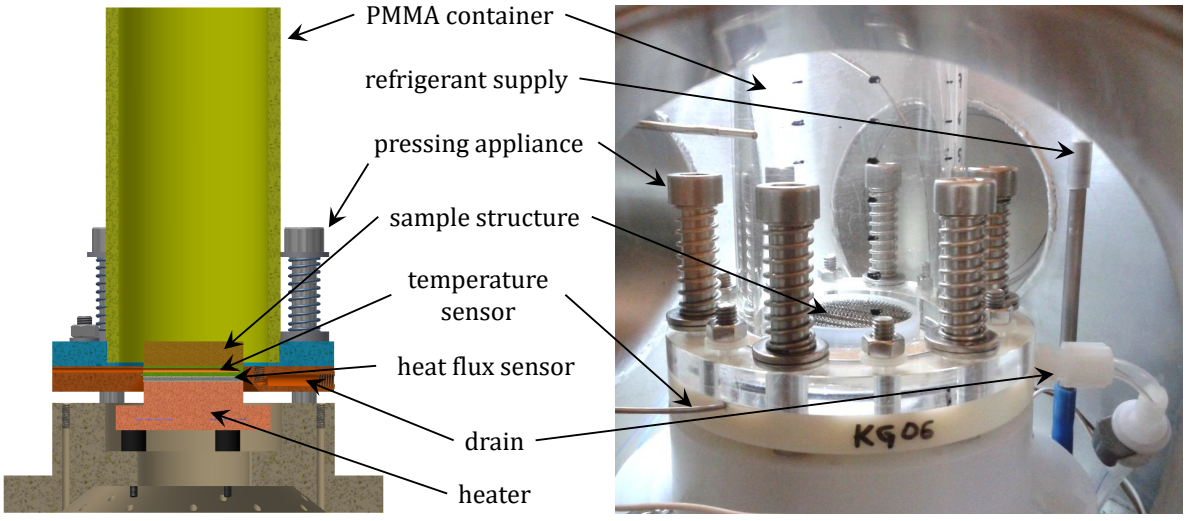

Figure 15: Sectional drawing (left) and side view photograph (right) of the evaporation setup inside the vacuum chamber

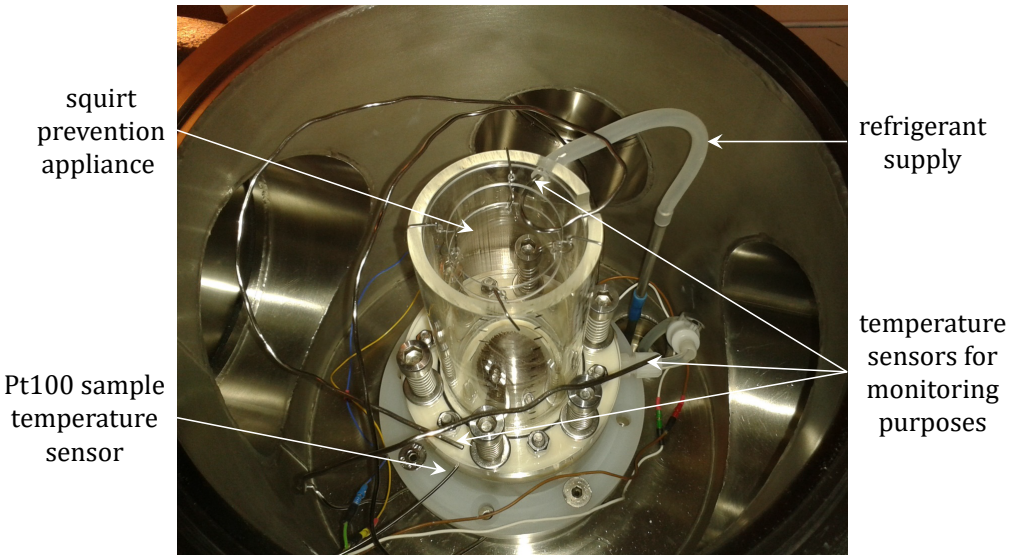

Figure 16: Top view photograph of the evaporation setup inside the vacuum chamber

On the base of the vacuum chamber a PVDF (polyvinylidene fluoride) heater support part is mounted as the foundation of the setup. The heater block is fixed to the support by means of four PVDF dowel pins which prevent major conductive heat losses from the heater to the support part and to the chamber walls due to their low thermal conductivity.

The heater block represents the heat source for the evaporation process. It is made from copper of ETP grade ("Electrolytic-Tough-Pitch") and consists of a top part and a bottom part. A negative relief of the spiral heating element was milled into the lower side of the upper heater part into which the heating element is placed in order to achieve a good thermal coupling to the surrounding copper. The diameter of the upper section of the upper part was adapted to the main diameter of the sample (40 mm) in order to provide a homogeneous one-dimensional heat flow into the sample. All surfaces of the copper parts are galvanically gold plated for corrosion prevention. The heating element itself is composed of a nickel/ chromium heating wire covered with a stainless steel jacket and an insulating magnesium oxide layer in between. Its maximum power output is 140 W and its nominal electrical resistance is 86 Ω. A defined voltage can be applied to the heater by a DC power supply unit. In order to prevent overheating of the setup the power supply is automatically switched off at a predefined threshold temperature by means of a hardware controller and a Pt100 temperature sensor inside the heater block.

The sample is placed concentrically on top of the heater block, separated by a stack of the heat flux sensor and connecting foils. As depicted in Figure 17, each sample consists of a porous metallic structure, a sample carrier, and a support ring. While generally all kinds of porous structures and morphologies can be applied, a copper mesh structure type was used in this work, which is described in chapter 4.1.3. The porous structure has a cylindrical shape with 40 mm diameter and variable height. On one plane side it is soldered to a sample carrier of Cu-ETP. Just like the structure's diameter, the main diameter of the sample carrier is 40 mm, whereas on its lower edge it exhibits a 1 mm wide and 1 mm high outward shoulder which is intended to take up mechanical forces produced by the pressing appliance described below. The carrier has a height of 4.0 mm. Above the shoulder a radial blind hole of 1.8 mm diameter for the sample temperature sensor is applied in parallel to the flat surface of the carrier. The drill hole has a depth of 38 mm and its axis is located in 1.5 mm distance from the upper surface of the carrier. To allow for installation of the sample in the evaporation setup and ensure watertightness the sample carrier is glued into a support ring made from ABS (acrylonitrile butadiene styrene) (cf. Figure 17). Like the sample carrier the support ring also features a radial hole on one side which enables the sample temperature sensor to

be inserted through the ring into the carrier. A partially circumferential groove is milled into the upper surface of the ABS support ring which is supposed to promote refrigerant drainage. From the groove to the cylindrical surface two orthogonal holes form a drainage channel. Stainless steel wire pieces are placed in the groove and conducted through the holes and attached hose to further facilitate drainage. Vertical through holes allow the support ring to be screwed to the flange of the PMMA container (small holes) and are used for the pressing appliance, respectively (large holes).

For the measurements a polypropylene ring is placed around the porous structure so that it covers most of the structure's cylindrical surface (cf. Figure 17). As stated in chapter 4.1.4, the intention of this blocking is to prevent lateral vapor flow at the circumference of the structure. On the level of the structure base a height of 1 mm of the structure must be left uncovered to allow drainage of the refrigerant column at the end of the measurement preparation phase.

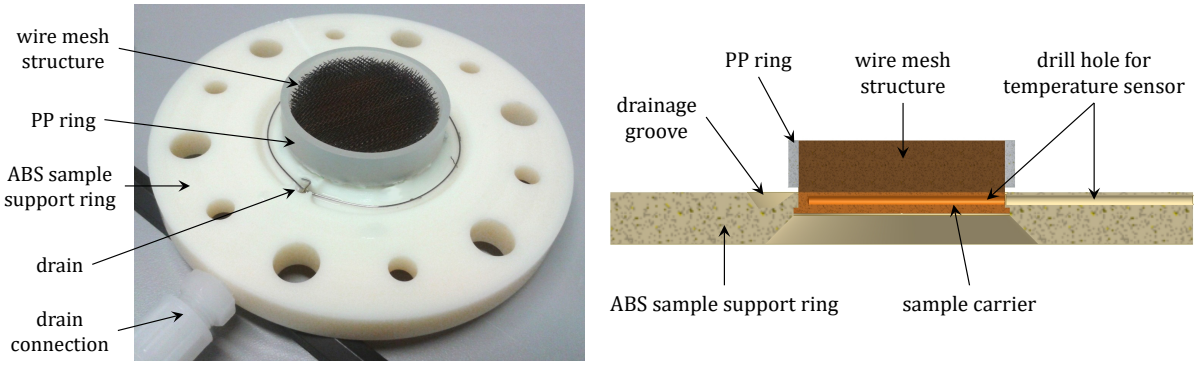

Figure 17: Photograph (left) and sectional drawing (right) of an exemplary sample

Between heater block and sample carrier the heat flux sensor is installed which measures the heat flux entering the sample (cf. schematic drawing in Figure 13 (right) in chapter 4.1.4). With 40 mm the circular sensor has the same diameter as the upper part of the heater and the main diameter of the sample structure. The sensor is permanently attached to the heater block by means of a temperature-resistant adhesive foil. In the course of every sample installation a fresh thermally conductive foil (3M 5590H, thickness: 0.5 mm, $\lambda_{tcf} = 3.0\ W/(mK)$) is placed on the surface of the heat flux sensor which that way thermally couples the heat flux sensor with the sample carrier.

On top of the sample assembly a transparent PMMA container is installed which allows flooding of the sample with refrigerant. A PMMA flange part with holes for the pressing appliance is glued on the lower side of a tubular section. The flange is placed flush on top of the ABS sample support ring, sealed by an O-ring in a groove. At the top edge of the tubular section two cut-outs are applied: Into one of them the refrigerant feed hose is positioned, the other one serves as a lead-through for a refrigerant feed temperature sensor.

In order to assure a good and homogeneous thermal contact of the sample carrier with the heater and heat flux sensor, a pressing appliance was implemented in the construction. It consists of six distance bolts with compression springs and washers which connect the flanges of PMMA container and sample support ring to the heater support. By screwing the bolts to a mechanical stop the springs apply a defined and reproducible downward pressure to the flanges of the PMMA container and sample support ring which presses the sample carrier onto the conductive foil and heat flux sensor.

A "squirt prevention appliance" is mounted on top of the PMMA container (cf. Figure 16) which avoids major losses of liquid refrigerant during nucleate boiling phases. The appliance is composed of a PMMA

inner disc and outer ring which are horizontally adjusted in 10 mm distance and such form a closed projected surface.

Refrigerant feed into the PMMA container and thus to the sample structure is enabled by a silicone hose which connects the refrigerant supply pipe end at the base of the vacuum chamber with the top edge of the PMMA container (cf. Figure 16). For refrigerant drainage another silicone hose is connected to the drain channel inside the sample support ring and to the drainage pipe end inside the vacuum chamber.

Sensors and Data Acquisition

According to the measurement concept presented in chapter 4.1.4, there are three sensors whose signals are directly used for evaluation of the evaporation process: a sample temperature sensor, a pressure sensor and a heat flux sensor. Their arrangement in the experimental setup is schematically depicted in Figure 13 (4.1.4). Apart from these primary sensors, several other sensors are installed which are not directly related to the evaluation quantities but contribute to monitoring the system state. Specifications of the sensors are listed up in Table 10 in the appendix.

For measuring the temperature inside the sample carrier a rod-shaped Pt100 resistance temperature sensor (RTD) with 1.6 mm diameter in four-wire configuration is used. To enhance its accuracy a calibration with subsequent derivation of characteristic coefficients was performed shortly before the measurement series. The calibration procedure is described in the appendix, chapter B.2.

The pressure inside the vacuum chamber is measured with a capacitive absolute pressure sensor (MKS a-Baratron®) with a range of 0…100 mbar which is inherently heated to 100°C to avoid condensation on sensor components. The sensor is installed vertically on the lid of the vacuum chamber.

The heat flux sensor (Captec Entreprise) between heater block and sample carrier has a diameter of 40 mm and a total thickness of approx. 0.75 mm. It is composed of 0.3 mm copper foils on its outer sides and a resin filling in between in which a thermopile is embedded. The thermopile is a serial connection of miniature thermocouples which – according to the Seebeck effect – convert temperature differences into a voltage signal proportional to the heat flux through the sensor (Childs et al. 1999; Hukseflux Thermal Sensors B.V. 2016).

Several rod-shaped Pt100 temperature sensors (four-wire configuration) are installed for monitoring reasons: inside the vacuum chamber there are two sensors positioned in the vapor atmosphere outside the PMMA container. Despite the uncertainty in temperature measurement in low-density phases these temperature signals can be useful indicators. Another sensor is placed with its tip inside the refrigerant supply hose, measuring the temperature of the refrigerant feed. Four Pt100 are installed in the condenser: One in the vapor phase, one in the liquid refrigerant sump and one each in the heat transfer fluid inlet and outlet. Two sensors record the air temperature inside the climatic chamber in proximity to the vacuum chamber.

Another pressure sensor – a piezo-resistive sensor type – is installed at the top of the condenser. In combination with the refrigerant temperature sensors it allows to estimate the amount of non-condensable gases inside the system by comparing the saturation pressure of the measured temperatures with the indicated pressure in steady-state conditions.

All sensor signals are recorded and processed by a data acquisition unit (Keysight 34972A) with integrated digital multimeter (DMM), multiplexer modules and analog / digital converter. Control and configuration of data acquisition as well as writing to data files is realized by a LabVIEW (National Instruments) program installed on a PC.

4.1.3 Sample Structures

Material and Topology

In this paragraph the utilized porous mesh structures are described. The complete sample construction and its integration into the experimental setup are addressed in chapter 4.1.2, section "Evaporation Assembly".

As mentioned before, a wire mesh structure with parallel mesh planes aligned in heat flux direction was used as an exemplary porous structure type for the investigations on dynamic evaporation within this work. This structure topology has not been utilized in any of the publications presented in chapter 2, but it appears promising due to its presumable high effective thermal conductivity in heat flux direction and its low-cost raw material.

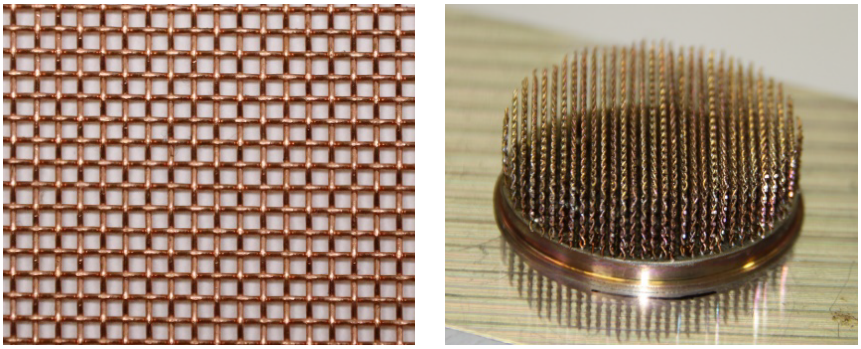

Figure 18: Exemplary copper mesh raw material (left); sample KG05-850-400 after soldering onto the carrier (right)

All samples consist of several strips of copper square wire mesh of plain weave type (cf. Figure 18, left) made from Cu-ETP (E-Cu58, material no. 2.0065) and provided by Haver & Boecker OHG. The strips are arranged in parallel in form of a cylindrical body and they are soldered to a copper sample carrier (ETP grade) with their edges (cf. Figure 18, right). Presuming a horizontal orientation of the carrier, the planes of the mesh strips thus have a vertical orientation. By default, the orientation of the wires in relation to the surface of the sample carrier (α_{wire}) is ± 45° (cf. Figure 19, left) in order to maximize the share of wires which are in direct soldering contact with the carrier (cf. Figure 21). The vertical orientation of the mesh strips and the 45° orientation of the wires aim at complying with the requirement of a high thermal conductivity in heat flow direction, stated in chapter 4.1.1. As opposed to a stack of horizontal wire layers, the described arrangement ensures that the wire axes at least partially point in the direction of heat flow and that the wires are in good thermal contact to the heat source. Due to the circular surface of the sample carrier and the cylindrical shape of the structure, the lengths of the strips vary according to their respective position on the carrier. Instead of a dense arrangement of mesh strips, a gap is left between all neighboring mesh layers. The target gap width is generally defined by equalizing the strip spacing l_{strp} (distance between centers of two neighboring mesh layers) with the mesh spacing l_{mesh} (distance between the axes of two neighboring wires within one piece of mesh) of the respective sample, as illustrated in the schematic on the right in Figure 19. Due to manufacturing restrictions a perfect equality of the nominal l_{strp} and l_{mesh} could not be realized, therefore the respective values slightly differ. By using these nearly equal distances a cubic pore morphology can be approximated, which satisfies the requirement of homogenous structure properties noted in chapter 4.1.1. This virtual geometric homogeneity of the pore in all three dimensions is especially valuable because it enables the definition of a characteristic pore size and potentially the attribution of capillary phenomena to that pore size. Accordingly, the clear mesh width w_{mesh} (void distance between two adjacent parallel wires within a mesh layer) is used as the characteristic pore size within this work.

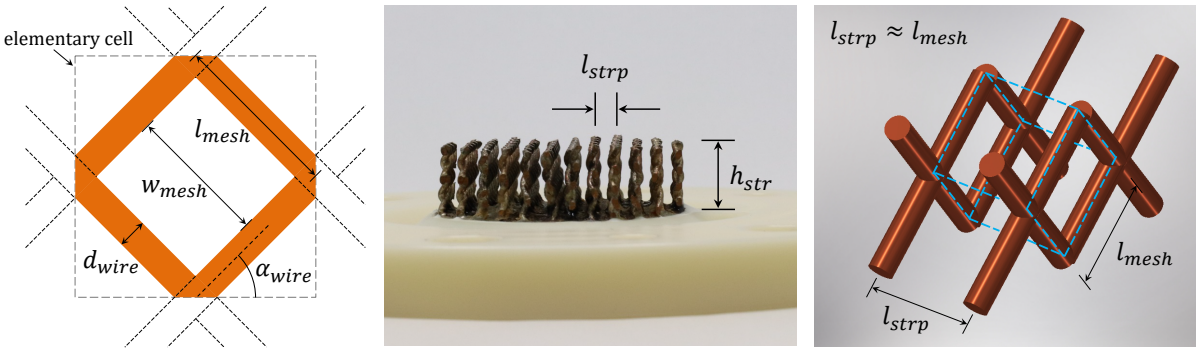

Figure 19: Visualizations of the characteristic geometric quantities of the wire mesh structures

All samples were soldered with the solder paste type "SC BLF021" by Solder Chemistry which has a composition of 97% tin, 3% copper and rosin flux (DIN: L-Sn97/Cu3/1.2.2.C/88-3). Since a thermal conductivity value of the solder was not specified by the manufacturer, the value was estimated to 61 W/(m K) based on specifications from a material properties database (MakeItFrom.com 2009) for the same solder composition. The applied solder mass per sample amounts to 2.5…4.5 g.

Geometric Variants

In order to allow for an analysis of the impact of geometry of the porous structure on dewetting and evaporation dynamics – as scheduled in the objectives in chapter 3, first scientific question – several samples with different structure properties were investigated.

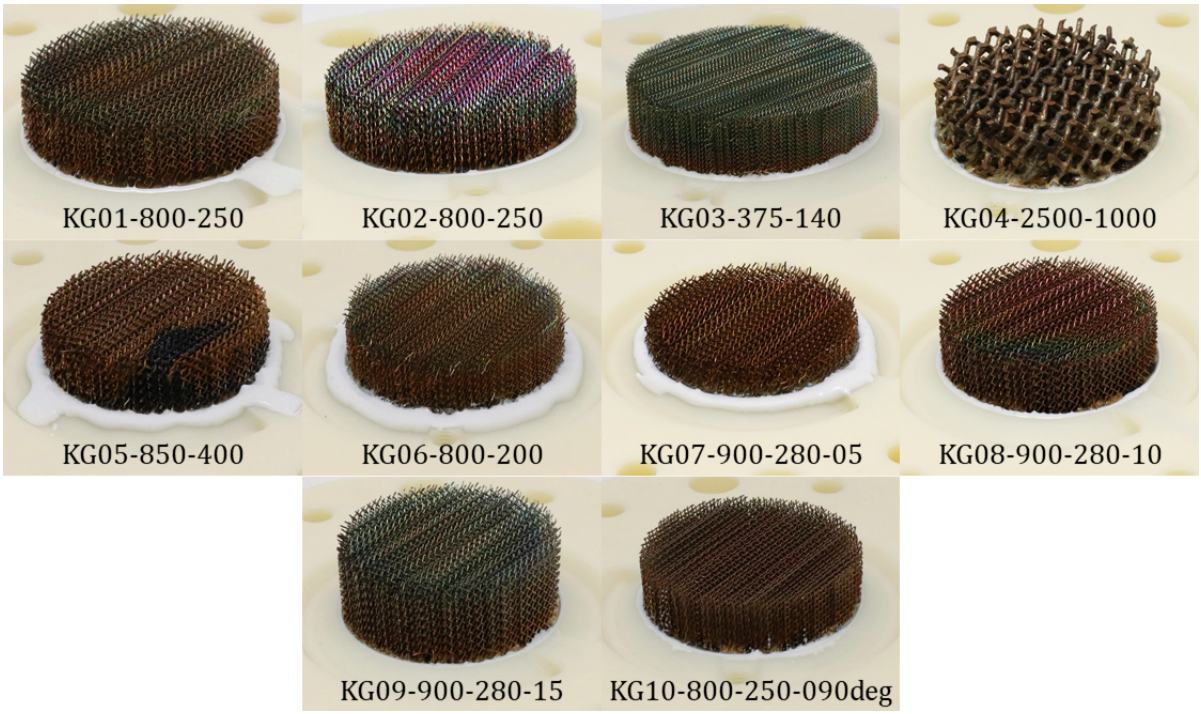

Figure 20: Photographs of the different porous structure samples

The sample names generally consist of three or four parts, separated by a hyphen: a consecutive number from KG01 to KG10, the clear mesh width (w_{mesh}) of the employed mesh structure in micrometers, the wire diameter (d_{wire}) in micrometers and for some samples additionally the structure height in millimeters or information on the wire orientation angle. For the standard sample (KG01-800-250: clear mesh

width of 800 µm, wire diameter of 250 µm), a structure configuration was chosen whose specifications are mostly in the middle of the varied parameter ranges. Based on this standard parameter set different geometry parameters are separately varied, namely porosity ψ, pore size (which is defined as the clear mesh width w_{mesh}), structure height h_{str} and the wires' orientation angle α_{wire} in relation to the carrier surface. Major geometric characteristics of all samples are listed in Table 2. The meaning of the geometric quantities is visualized in Figure 19. Photographs of the samples are shown in Figure 20.

Table 2: Geometry specifications of the porous structure samples (the sample name consists of a consecutive number, the clear mesh width in µm, the wire diameter in µm, and if applicable additional geometry information)

Sample name	Clear mesh width	Wire diameter	Mesh spacing	Strip spacing	Structure height	Wire orientation angle	Porosity
	w_{mesh}	d_{wire}	l_{mesh}	l_{strp}	h_{str}	α_{wire}	ψ
	mm	mm	mm	mm	mm	°	%
KG01-800-250	0.8	0.25	1.05	1.0	10	45	90.7
KG02-800-250	0.8	0.25	1.05	1.0	10	45	90.7
KG03-375-140	0.375	0.14	0.515	0.53	10	45	88.7
KG04-2500-1000	2.5	1	3.5	3.5	10	45	87.2
KG05-850-400	0.85	0.4	1.25	1.3	10	45	84.5
KG06-800-200	0.8	0.2	1	1.01	10	45	93.8
KG07-900-280-05	0.9	0.28	1.18	1.17	5	45	91.1
KG08-900-280-10	0.9	0.28	1.18	1.17	10	45	91.1
KG09-900-280-15	0.9	0.28	1.18	1.17	15	45	91.1
KG10-800-250-090deg	0.8	0.25	1.05	1.0	10	0/90	90.7

Values for clear mesh width (w_{mesh}) and wire diameter (d_{wire}) in Table 2 are nominal values specified by the manufacturer. Values for mesh strip spacing (l_{strp}), structure height (h_{str}) and wire orientation angle (α_{wire}) are nominal values for sample manufacturing. Values for mesh spacing (l_{mesh}) and porosity (ψ) were calculated from other geometric quantities. In case of porosity, the calculation bases on the clear mesh width, wire diameter and strip spacing. The slight tilt of the wires in relation to the mesh plane due to the weaving principle is neglected in that calculation.

Generally, the choice of parameter variants was made in a way that significant effects on wetting and evaporation behavior could be expected. A variation of porosity was realized by means of different wire diameters at a nearly constant mesh spacing and strip spacing, which applies to the samples KG05-850-400 ($\psi = 84.5\%$), KG01-800-250 ($\psi = 90.7\%$) and KG06-800-200 ($\psi = 93.8\%$). With regard to the requirement of a high effective thermal conductivity (cf. measuring task in chapter 4.1.1) also lower porosities would have been desirable. An associated increased pressure drop of the structure would presumably not have been relevant since – in contrast to the cases of steady-state evaporation presented in chapter 2 – operation without a continuous refrigerant supply is envisaged in this work and only vapor needs to travel through the structure. However, the range of realizable porosity variants was restricted by the availability of respective mesh types.

The variation of pore size was implemented by using different clear mesh widths (w_{mesh}), wire diameters (d_{wire}) and respective strip spacing (l_{strp}) while the porosity (ψ) was kept preferably constant. As

mentioned before, the clear mesh width w_{mesh} is used as a definition for the characteristic pore size and the pores can be regarded as having a cubic shape due to the strip spacing l_{strp} equaling the mesh spacing l_{mesh}. For the samples KG03-375-140, KG01-800-250 and KG04-2500-1000 the pore size amounts to 375 µm, 800 µm and 2500 µm and thus covers a quite broad range. The porosity values of the samples could not be kept perfectly constant, varying between 87.2% and 90.7%. However, this porosity difference is assumed to have a much smaller impact on the measurement results than the pore size. Due to its large mesh width and wire diameter sample KG04-2500-1000 was subjected to a special pretreatment: Prior to cutting the strips the mesh material was covered with solder paste and the crossing wires were soldered to each other in order to prevent the mesh strips from falling apart. This solder coating (estimated to a mass of 1.6 g) certainly influences porosity, thermal conductivity and surface properties of the structure, which needs to be considered in measurement evaluation.

In terms of manufacturability and refrigerant storage capacity, structure heights of 5 mm (KG07-900-280-05), 10 mm (KG08-900-280-10) and 15 mm (KG09-900-280-15) were considered reasonable. For all three samples the same type of wire mesh was used.

Besides the standard wire orientation angle of 45° a sample with a wire orientation of 0°/90° (KG10-800-250-090deg) was built from the same mesh type as KG01-800-250. The wire orientation has a direct impact on their thermal contact to the carrier: With a 45° orientation, most wires have a solder contact with the carrier, except some wire sections in the top-outer regions of the structure, as Figure 21 illustrates. The 0°/90° angles implicate that half of the wires are arranged perpendicular to the carrier surface and have a solder contact to the carrier while the other half is arranged in parallel to the carrier surface and does not have a direct thermal contact to the carrier.

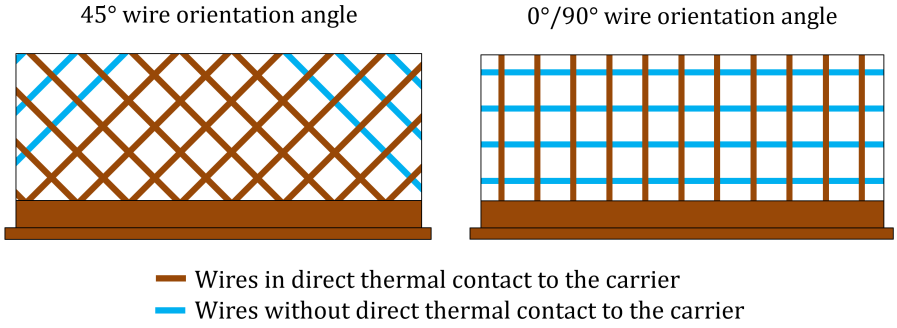

Figure 21: Illustration of the thermal contact conditions of the wires to the sample carrier; for mesh structures with 45° wire orientation angle (left) and 0°/90° wire orientation angle (right); drawing not true to scale

In one case two specimens with identical geometric parameters were manufactured (KG01-800-250 and KG02-800-250) in order to evaluate the reproducibility of manufacturing and exclude a major influence of small non-uniformities originating from mesh inhomogeneities or manufacturing inaccuracy.

Pretreatment of Sample Structures

In order to ensure comparable and well-defined surface properties and provide for reproducible measurements, all samples were subjected to a two-step pretreatment process before being glued into the ABS support ring.

In the first step the metallic assemblies of sample carrier and mesh structure were cleaned by boiling them in isopropanol at 90°C for one hour. This procedure aimed at removing possible grease contamination from the mesh production process and rosin flux residues from the soldering process.

The second step was a heat treatment whose purpose was to prevent an uncontrolled long-term surface oxidation or other change of chemical, physical or morphological surface properties during storage and measurements with the sample. Since surface properties can crucially affect the wetting behavior, an undefined surface could lead to an arbitrary and non-retraceable influence on the evaporation characteristics. Basic idea of the heat treatment was to create a well-defined and stable oxide layer on the mesh surface which passivates the surface and thus impedes further reactions. A second aspect was that an oxidation was expected to decrease the water contact angle and thus lead to a better spreading behavior, thinner refrigerant films, a larger surface coverage with refrigerant and thereby possibly to an improved evaporation performance. Procedure and parameters of the conducted heat treatment were derived from a literature review on the formation of different copper oxide compounds on copper surfaces in dependence of applied heat treatment modalities and their effect on wettability. A summary of the literature review can be found in chapter B.3 in the appendix. Resulting from its findings, the sample structures were placed in a furnace and were kept at 180°C for 4 days (96 h) under exposure to air.

A special cleaning treatment was carried out with sample KG05-850-400 after the first measurements. The cleaning turned out necessary because a crack in the ABS support ring had presumably provoked a contamination of the mesh structure with ingredients of the thermally conductive paste inside the drill hole of the temperature sensor (cf. discussion in chapter 5.2.3). The aforementioned initial cleaning procedure with isopropanol could not be repeated since the sample structure was already glued into the ABS support ring which might not have been chemically stable to this treatment. For the cleaning procedure the sample was placed in a stirred aqueous solution of sodium dodecyl sulfate (2.5 g/l) at 80°C for 4 hours. Afterwards it was carefully rinsed with deionized water and finally dried under ambient conditions.

4.1.4 Measuring Procedure

Sample Installation

In order to provide for comparable measurement conditions the respective sample was newly installed in the setup before each measurement (except for one test run without reinstallation). The assembly of sample and PMMA container is firstly built together outside the test rig before mounting it in the vacuum chamber.

A detailed description of the sample installation workflow is given in chapter B.4 in the appendix.

Preparatory Phase

Before the actual evaporation measurement can start, several preparations are required:

After the sample installation the vacuum chamber is evacuated with a scroll vacuum pump while disconnected from the rest of the refrigerant system. Evacuation is continued for at least 15 hours, until a pressure of maximum $2.5 \cdot 10^{-3}$ kPa (during evacuation) is reached. In order to minimize parasitic heat gains from the ambient into the setup during measurement, the complete test rig inside the climatic chamber is cooled down until steady-state conditions are reached. The nominal temperature is usually set approximately 2 K above the envisaged saturation temperature of the vapor to prevent condensation of vapor on the chamber walls. The ethylene-glycol-water bath for the anti-cavitation cooling of the refrigerant is also cooled down to steady-state conditions with a thermostat set temperature of 0.5°C. The thermostat conditioning of the refrigerant feed in the counterflow heat exchanger is started. For a first rough adjustment of the scheduled system pressure the thermostat supplying the condenser heat

exchanger is started and its nominal temperature is set slightly lower than saturation temperature of the aspired system pressure.

As soon as steady-state conditions are reached and the vacuum chamber pressure has reached a stable minimum value, the evacuation of the vacuum chamber is terminated. The condenser chamber is then evacuated twice for a duration of 3 minutes each and a waiting time of 5 minutes in between in order to remove non-condensable gases from the gas phase and dissolved gases from the liquid refrigerant pool. A comparison of the saturation temperature to the measured condenser pressure with the condenser's temperature signals allows for an estimation of the amount of non-condensable gases in the system. Afterwards the valve between vacuum chamber and condenser is opened which allows vapor to flow into the vacuum chamber. After opening the two hand valves at the refrigerant feed line the peristaltic pump is switched on in order to fill the PMMA container with refrigerant. Since the valve in the refrigerant drainage line is kept closed the accumulating refrigerant in the PMMA container forms a refrigerant column above the sample structure whose hydrostatic pressure presses refrigerant into the pore volume (cf. Figure 22, left). Refrigerant feed is continued until a filling level of 60 mm from structure base is reached; then the pump is stopped and the level is held for a dwell time of 5 minutes. After the dwell time, the level of the refrigerant column is reduced to a height of 10 mm above the structure's surface by opening the drainage valve.

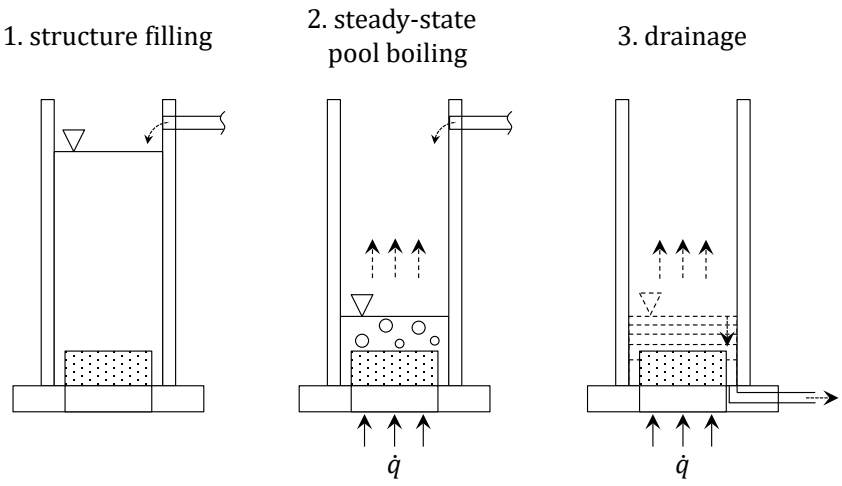

Figure 22: Steps of the preparatory phase prior to the evaporation measurement

Subsequently, the steady-state pool boiling phase is initiated (cf. Figure 22, center) by switching on the power supply for the heater and adjusting it to the scheduled constant heating power value of the respective measurement. In order to reach steady-state boiling conditions at a constant filling level, refrigerant is continuously fed into the PMMA container. A threshold temperature value (usually 20…40°C) for the safety shutdown mechanism is specified in the control program. It triggers a heater switch-off in case the sample temperature reaches the threshold temperature in order to prevent the setup components from overheating. (An additional hardware safety mechanism provokes a heater shutdown if the heater block temperature rises above 120°C.) For a last time the complete vacuum system is evacuated for 5 minutes to remove non-condensable gases which might have remained in the system and especially in the refrigerant lines. The set temperature of the condenser is now re-adjusted until the scheduled system pressure is reached within an accuracy of approximately ±0.05 kPa (including peaks from nucleate boiling). The setup is then left to stabilize for at least 10 min but at most until 30 min after termination of the last evacuation. At the end of the preparatory phase the continuous refrigerant feed into the PMMA container is stopped and the refrigerant column is drained (cf. Figure 22, right).

Measurement Phase

After drainage of the refrigerant column evaporation only takes place from the capillary-stored refrigerant inside the pore volume which represents the intended evaporation mode of this work. The starting point for measurement evaluation is defined as the point when drainage is completed, which is usually the case 15…40 s after opening the drainage valve.

During evaporation from the porous structure, all settings – including heating power and condenser temperature which determines the system pressure – are kept constant. All sensor signals are processed and recorded by the data acquisition system and the LabVIEW measurement control program with a sampling interval of about 2 s. As soon as the sample structure falls dry, the sample temperature rises immediately and rapidly due to the lack of evaporative heat removal. As soon as the temperature reaches the predefined safety shutdown threshold the heater is automatically switched off which represents the end of the measurement and termination point for data evaluation.

Remarks on the Identification of the Starting Point of Evaluation

In some of the conducted measurements the drainage process at the end of measurement preparation did not instantaneously proceed to completion. Instead, a residual refrigerant column of up to 10 mm above structure base level remained and provoked an unwanted partial flooding of the sample structure. This partially flooded period usually terminated after a few minutes of evaporation. Since only evaporation from capillary-stored refrigerant should be considered in this work, the partially flooded period was excluded from measurement evaluation and the point of time when the unintended partial flooding ended was defined as the beginning for evaluation. The termination point of partial flooding was identified by means of visual observations of the experimental setup or by means of clear indications in the measurement results. (In unclear cases the respective graphs in chapter 5 are accordingly marked with parentheses.) Comparisons of measurements with spontaneous complete drainage and an unwanted partially flooded phase showed that the partially flooded phase did not noticeably change the further course of wetting behavior and evaporation dynamics. Therefore, the utilization of the evaluated data after exclusion of the partially flooded phase is considered legitimate.

4.1.5 Remarks on the Measuring Concept

In the following paragraph the choices for certain solutions in the implementation of the measurement concept – regarding construction, instrumentation, and procedure – are motivated. The discussed aspects are relevant in terms of compliance with the requirements of the measuring task (chapter 4.1.1), validity of presumptions and evaluation methods, and measurement accuracy.

For measurement of the temperature close to the structure base a rod-shaped Pt100 resistance thermometer in four-wire configuration was chosen, which is positioned in a drill hole inside the sample carrier. Despite its faster response behavior a chip-type Pt100 sensor was not selected due to its lack of mechanical robustness and the need of frequent (de-)installation. However, simulations presented in (Boertz 2017) showed that a thin rod-shaped Pt100 sensor with 1.6 mm diameter also allows for a tolerable response time.

As an alternative to the chosen thermopile-type heat flux sensor, the heat flux entering the sample structure also could have been determined by means of a temperature sensor cascade using the heat conduction approach. As simulations and calculations from Boertz (Boertz 2017) revealed, both solutions involve relatively high measurement uncertainties (as shown in chapter 4.1.8 and in the appendix B.7.2 for the heat flux sensor). The estimated uncertainties of the thermopile heat flux sensor, though, were

lower than those of a temperature sensor cascade within the considered parameter range, which motivated the choice for the thermopile-type sensor.

In order to minimize the distorting effects of capacitive heat flows on measurement in unsteady conditions (cf. requirement specified in chapter 4.1.1), all thermal masses between sensors and positions of interest were kept as small as possible. This effort firstly applies to the sample carrier which is located between heat flux sensor and structure base and whose height was fixed to a constructionally feasible minimum of 4 mm. Secondly, the temperature sensor in the sample carrier was positioned as close to the structure base as possible, resulting in a distance of 1.5 mm from its horizontal axis to the top surface of the carrier (which equals the structure base). The remaining material thickness of 0.6 mm was assessed as necessary to guarantee mechanical stability.

The lateral sensor hole inside the sample carrier as well as the shoulder on the lower edge of the carrier represent sources of disturbance for the demanded uniform, one-dimensional heat flow. 3D simulations described in (Boertz 2017) with a blind hole of 2.2 mm diameter and conservative assumptions, however, revealed that the impact of the discontinuity from the drill hole on the temperature field is relatively small for the scheduled parameter ranges. Simulations in the impact of the shoulder also showed a marginal impact. Based on these results, the error associated to the assumption of a homogeneous heat flux distribution is considered tolerable.

The depth of the blind hole for the temperature sensor was fixed to 38 mm in a 40 mm diameter sample carrier. This maximum feasible depth was chosen in order to minimize measurement uncertainties due to heat dissipation or gains to / from the ambient, induced by heat conduction through the sensor material. Considering the ratio of immersion depth to sensor diameter of about 24 and applying it to a respective error estimation method from Nicholas and White (Nicholas and White 2001) the uncertainty due to heat dissipation or gains can be neglected.

In order to ensure a good thermal coupling of the temperature sensor to the sample carrier, thermally conductive paste is inserted into the hole. Ideally, the paste completely fills the gap between bore wall and sensor. Though, in practice it cannot be excluded that a certain volume of the gap is not filled. To find out if the quality of thermal coupling significantly influences the measured temperature signal, test measurements with and without thermally conductive paste were conducted. Similar tests were conducted on the thermal contact between sample carrier and heat flux sensor by applying a complete thermally conductive foil, a foil section which only covers half of the interface or no foil at all. In both cases the measurement results did not show any pronounced differences beyond the usual random scattering effects, therefore potential minor differences in the distribution of thermally conductive paste and in the constitution of the thermally conductive foil are regarded as uncritical.

Heat losses from the evaporation assembly to the ambient can potentially distort measurement results and impede one-dimensional heat transfer (cf. requirement in chapter 4.1.1). Due to the low density vapor atmosphere in the vacuum chamber, heat losses by thermal conduction and convection can be assumed to be considerably lower compared to atmospheric pressure conditions. Since the dimension of heat losses by conduction, convection and radiation depends on the temperature difference between the respective part of the setup and the ambient temperature, the highest heat losses can be expected to occur from the heater block. This heat loss component provokes that only a reduced fraction of the applied heat flow reaches the heat flux sensor. Heat losses from the sample carrier and ABS support ring to the ambient will be much smaller since the sample temperature is only moderately higher than the ambient temperature. This heat loss component, however, leads to a difference between heat flow through the heat flux sensor and heat flow entering the porous structure – additionally to a potential capacitive effect of the sample carrier. Based on simulations by Boertz (Boertz 2017) for virtually the same experimental setup and temperature conditions similar to those of the standard parameters used in this work, the radial heat

losses from the sample are estimated to less than 0.2% of the heat flow through the sensor. Considering the distinctly higher uncertainty of the heat flux sensor (cf. chapters 4.1.8 and B.7.2), this heat loss component is regarded as negligible.

Another aspect relevant for the requirement of one-dimensional heat transfer is homogeneity of evaporation from the porous structure. As stated in chapter 4.1.2, a polypropylene ring around the lateral cylindrical surface of the mesh structure is applied in order to prevent lateral vapor flow and thus minimize edge effects.

The "squirt prevention appliance" which is placed on the upper side of the PMMA container is intended to impede the loss of refrigerant during the preparatory pool boiling phase in case of nucleate boiling. Since it partially blocks the passage between PMMA container and outer vacuum chamber, the vapor flow might cause a pressure drop between place of evaporation and place of pressure measurement. This could potentially invalidate the assumption that the measured pressure equals the pressure above the structure's surface. Though, a rough calculative estimation for the maximum possible occurring pressure drop indicated that due to the low vapor density and relatively low velocities the pressure drop is negligibly small. Therefore, the assumption that the measured pressure in the vacuum chamber equals the pressure above the structure's surface is considered as valid.

By means of a refrigerant column above the sample a maximum-possible filling degree of its pore volume is aspired in the preparatory phase. In order to ensure that the scheduled column height and dwell time suffice for maximum filling, pretests with different conditions were performed. The results showed that a column height of 60 mm and a dwell time of 5 minutes fully meet the requirements.

Objective of the pool boiling phase prior to the thin film evaporation measurement was to establish steady-state conditions as a defined starting point for the measurement. Starting the heater during evaporation from the porous structure would have entailed large capacitive heat flows and unsteady thermodynamic conditions which would have complicated measurement evaluation. The height of the refrigerant column during the pool boiling phase was intentionally set to a rather low value of 10 mm above structure surface in order to allow for regular bubble formation (steady conditions) and to prevent refrigerant loss due to squirting in case of nucleate boiling.

Nucleate boiling conditions were sometimes observed to change arbitrarily during the steady-state pool boiling phase, e.g. in form of an abrupt change of bubble formation frequency. Accordingly, the varying heat transfer coefficient leads to a different sample temperature. Results from pretests showed that the initial sample temperature does not have a noticeable impact on the further evaporation characteristics. Therefore it was not considered necessary to guarantee perfectly identical boiling conditions and sample temperature at the beginning of thin film evaporation from the capillary-stored refrigerant.

According to the measuring task (cf. chapter 4.1.1), maintenance of a constant system pressure is envisaged during the evaporation measurement. Since pressure is adjusted by means of the condenser's fluid inlet temperature – which is kept constant throughout the measurement – instead of an active control, the system pressure slightly changes in dependence of the current heat transfer capability of the sample structure. Given that the absolute thermal transmittance (UA value) of the condenser is considerably higher compared to that of the sample structure, the system pressure is mostly governed by the condenser. Thus, the occurring pressure variations of maximum 0.02 kPa (including peaks from nucleate boiling events) are rather small compared to the nominal pressure difference of 0.3 kPa which is used for investigations on the impact of system pressure (cf. chapter 4.1.6). Therefore, the pressure variations within a measurement are assessed as tolerable.

4.1.6 Measuring Parameters

As defined in the first scientific question (cf. chapter 3), one objective of this work is to analyze the impact of geometric parameters of the porous structure and of thermodynamic parameters on the dewetting dynamics and evaporation heat transfer. The scheduled parameter sets for all evaporation measurements are listed in Table 3. (Remark on sample denomination: KGXY – "clear mesh width in µm" – "wire diameter in µm" – "structure height in mm / wire orientation angle [optional]"; sample geometry specifications in Table 2, p. 49) In order to allow for a rough assessment of measurement reproducibility and the impact of random differences in the dewetting characteristics, two measurements were conducted with each parameter set.

The standard sample structure KG01-800-250 was used for measurements at different thermodynamic conditions. The nominal system pressure p_{nom} was varied between 1.0 / 1.3 / 1.6 kPa – which corresponds to saturation temperatures of 6.97 / 10.85 / 14.01°C, as emanates from the vapor pressure curve of water in Figure 74, appendix A.1 – and the nominal heat flux $\dot{q}_{nom}$ between 10 / 20 / 30 / 40 kW/m². Only one parameter was varied at a time and the other was set to standard conditions. These standard conditions were defined as $p_{nom} = 1.3\ kPa$ – corresponding to a saturation temperature of 10.85°C – and $\dot{q}_{nom} = 30\ kW/m^2$. Complying with the requirements in chapter 4.1.1, the range of tested vapor pressures was chosen according to frequently used evaporation temperatures of about 3…20°C. The employed heat flux range was determined on the basis of application-related and experiment-related considerations: According to a rough estimation, heat fluxes of up to 100 kW/m² might potentially occur in an evaporator heat exchanger until the fluid side limits the overall heat transfer, if calculating with best-case assumptions for the fluid-side heat transfer. However, heat fluxes in these dimensions cannot be realized with the utilized setup due to temperature restrictions of the components. The maximum allowable heat flux for safe operation amounts to about 40 kW/m², therefore this value was used as the maximum employed heat flux for the measurements. The minimum value was fixed to 10 kW/m² because measurement uncertainty reaches unacceptable dimensions for lower heat fluxes.

In order to study the impact of structure geometry all mesh structure variants presented in chapter 4.1.3 were measured at standard conditions ($p_{nom} = 1.3\ kPa,\ \ \dot{q}_{nom} = 30\ kW/m^2$). As described in 4.1.3, the varied geometric parameters are porosity, pore size, structure height and wire orientation angle.

Additional to the investigation of geometry and process parameters, an analysis of a possible impact of sample aging was considered in the measurement schedule by conducting repeated measurements with the standard sample KG01-800-250 at standard conditions with a time lag of several weeks in between. Time relations can be deduced from the column "Measurement day" in Table 3 which refers to the elapsed days since the first regular measurement of the series. (As an exception, measurement M21 was conducted before starting the regular series, therefore it is labeled with a negative number of days.)

To study the impact of manufacturing reproducibility measurements with sample KG02-800-250 were scheduled which features the same nominal structure geometry parameters as the standard sample KG01-800-250.

Table 3: Measuring parameters

Measure-ment no.	Sample	Nominal system pressure	Nominal heat flux	Investigated impact	Measure-ment day	Remarks
		p_{nom}	$\dot{q}_{nom}$			
–	–	kPa	kW/m^2	–	d	–
M01	KG01-800-250	1.3	30	standard conditions	15	—
M02	KG01-800-250	1.3	30	standard conditions	33	sample not newly installed
M03	KG01-800-250	1.3	30	standard conditions	74	—
M04	KG01-800-250	1.3	30	standard conditions	106	—
M05	KG01-800-250	1.3	10	heat flux	20	—
M06	KG01-800-250	1.3	10	heat flux	75	—
M07	KG01-800-250	1.3	20	heat flux	27	—
M08	KG01-800-250	1.3	20	heat flux	76	—
M09	KG01-800-250	1.3	40	heat flux	21	—
M10	KG01-800-250	1.3	40	heat flux	77	—
M11	KG01-800-250	1.0	30	pressure	22	—
M12	KG01-800-250	1.0	30	pressure	109	—
M13	KG01-800-250	1.6	30	pressure	26	—
M14	KG01-800-250	1.6	30	pressure	104	—
M15	KG02-800-250	1.3	30	reproducibility of manufacturing	12	—
M16	KG02-800-250	1.3	30	reproducibility of manufacturing	14	—
M17	KG03-375-140	1.3	30	pore size	40	—
M18	KG03-375-140	1.3	30	pore size	41	—
M19	KG04-2500-1000	1.3	30	pore size	34	—
M20	KG04-2500-1000	1.3	30	pore size	69	—
M21	KG05-850-400	1.3	30	porosity, surface properties	-217	original state
M22	KG05-850-400	1.3	30	porosity, surface properties	1	presumably contaminated state
M23	KG05-850-400	1.3	30	porosity, surface properties	8	presumably contaminated state
M24	KG05-850-400	1.3	30	porosity, surface properties	112	after special cleaning
M25	KG05-850-400	1.3	30	porosity, surface properties	113	after special cleaning
M26	KG06-800-200	1.3	30	porosity	54	—
M27	KG06-800-200	1.3	30	porosity	116	—
M28	KG07-900-280-05	1.3	30	structure height	56	—
M29	KG07-900-280-05	1.3	30	structure height	117	—
M30	KG08-900-280-10	1.3	30	structure height	57	—
M31	KG08-900-280-10	1.3	30	structure height	61	—
M32	KG09-900-280-15	1.3	30	structure height	70	—
M33	KG09-900-280-15	1.3	30	structure height	71	—
M34	KG10-800-250-090deg	1.3	30	wire orientation	110	—
M35	KG10-800-250-090deg	1.3	30	wire orientation	111	—

4.1.7 Data Reduction

Overall Evaporation Heat Transfer Coefficient U_{ev}

As stated in the measuring task (chapter 4.1.1), the overall heat transfer coefficient U_{ev} is used as the main evaluation quantity for the presented measurements, characterizing the effectiveness of evaporation from the porous wire mesh structures. U_{ev} comprises the net heat transfer capability of the structure between structure base and saturation temperature of the vapor atmosphere, as schematically depicted in Figure 23. Individual heat and mass transfer mechanisms within the reference volume are not considered, according to this "black box" conception.

The evaporation heat transfer coefficient U_{ev} can be calculated from the effective evaporation heat flux $\dot{q}_{ev}$ of the structure and the driving temperature difference $\Delta\vartheta$, which is the difference between the temperature at the structure base ϑ_{strb} and saturation temperature ϑ_{sat} of the vapor atmosphere above the sample surface:

$$U_{ev}(t_i) = \frac{\dot{q}_{ev}(t_i)}{\Delta\vartheta(t_i)} = \frac{\dot{q}_{ev}(t_i)}{\vartheta_{strb}(t_i) - \vartheta_{sat}(t_i)} \tag{4-4}$$

Just like U_{ev}, its input quantities $\dot{q}_{ev}$, ϑ_{strb}, and ϑ_{sat} are not measured directly but they are derived from directly measured quantities, auxiliary quantities, and corrective terms via functional relations. The deduction of these corrections and functional relations of the input quantities $\dot{q}_{ev}$, ϑ_{strb}, and ϑ_{sat} are presented in the following paragraphs. Additionally, the definition of the experimental refrigerant storage capacity $M_{rf,cap}$ is specified, which is another key evaluation quantity of this work.

Positions in the experimental setup corresponding to the discussed quantities are illustrated in Figure 23. Since all measurements have an unsteady character, evaluation of all relevant quantities is conducted for each time step t_i of data acquisition during the measurement.

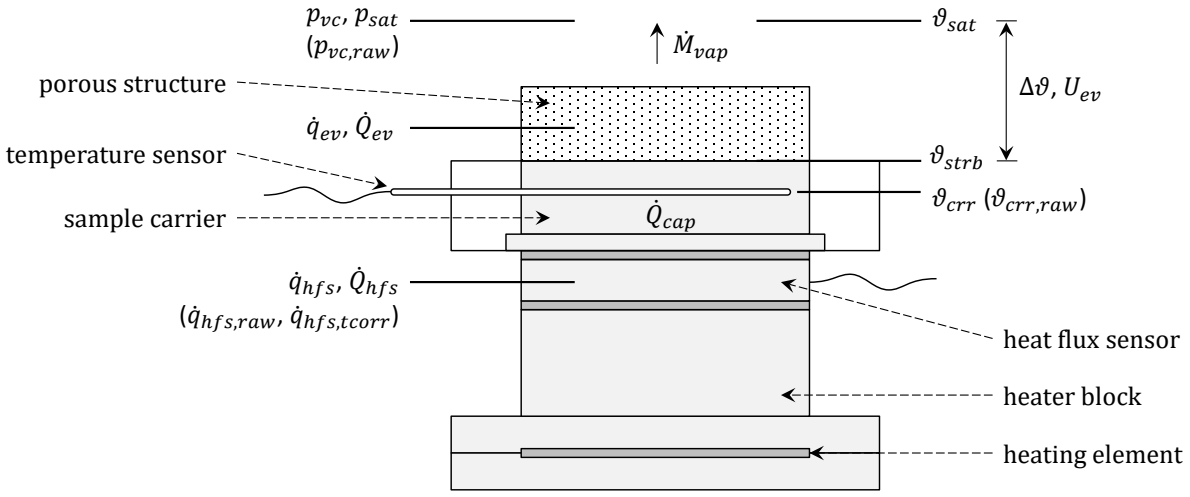

Figure 23: Visualization of the measurement and evaluation quantities at their corresponding positions in the experimental setup (drawing not true to scale)

Corrections of Directly Measured Quantities

In accordance with GUM (Joint Committee for Guides in Metrology 2008) systematic effects which cause deviations of the measurands are eliminated in the data reduction wherever possible, as documented within this chapter. Uncertainties due to random effects are likewise treated according to GUM. Given that they cannot be corrected, the applied methods are addressed separately in chapter 4.1.8.

Directly measured quantities which are the basis for the calculation of U_{ev} are the temperature $\vartheta_{crr,raw}$ which is measured by the Pt100 sensor inside the sample carrier, the heat flux $\dot{q}_{hfs,raw}$ through the heat flux sensor below the sample carrier, and the absolute pressure $p_{vc,raw}$ inside the vacuum chamber. (Specifications of sensors etc. are given in chapter 4.1.2.) These direct measurands are subjected to certain distorting systematic effects, namely a time delay in the data acquisition process, inaccuracy of the heat flux sensor's nominal characteristic curve, and the response time of the sensors:

Since the data acquisition system requires some time to scan all sensor channels within one sweep, the point of time of a scan does not perfectly match the time stamp which is defined at the beginning of each sweep. This time delay $\Delta t_{delay,x}$ causes a systematic measurement deviation of the measurand x if its value is assigned to the time stamp of the current sweep. However, it is necessary for data evaluation to assign different sensor signals to identical time stamps. Therefore a correction of the measured "raw" values $x_{raw}(t_i)$ is applied to the three measurands $\vartheta_{crr,raw}(t_i)$, $\dot{q}_{hfs,raw}(t_i)$ and $p_{vc,raw}(t_i)$ in terms of a linear interpolation of two consecutive data values:

$$x(t_i) = x_{raw}(t_i) - \frac{x_{raw}(t_i) - x_{raw}(t_{i-1})}{t_i - t_{i-1}} \cdot \Delta t_{delay,x}(t_i) \tag{4-5}$$

Given that delay times are rather small (approximately 0.2 s for ϑ_{crr}, 0.35 s for p_{vc} and 0.67 s for $\dot{q}_{hfs}$), also the differences between raw data and corrected data are little. The inaccuracy due to the assumption of linearity can thus be considered as very small compared to other uncertainties of the measurement chain and is consequently neglected in the measurement uncertainty analysis in chapters 4.1.8 and B.7 (appendix).

A comparison of the measured heat flow output signal with the applied heating power in steady-state conditions revealed that the nominal characteristic curve of the heat flux sensor is subjected to a certain deviation. Therefore, a correction function was derived which reads:

$$\dot{q}_{hfs}(t_i) = 0.91 \cdot \dot{q}_{hfs,tcorr}(t_i) \tag{4-6}$$

In the equation $\dot{q}_{hfs,tcorr}$ denominates the heat flux values after correction for the scanning time delay described above. The derivation of the correction function from a calibration measurement is explained in detail in the appendix, chapter B.5.

Another systematic effect which influences the measured values is the response time of the particular sensor which originates from the sensor's thermal capacitances and resistances. Since the "real" values of the measurands are not known and the specified response times of the sensors can rather be understood as maximum values than exact values, a systematic correction of measurement values is not possible. Instead, the effect of response time is handled as a source of uncertainty within this work and is explained in more detail in the appendix B.7.

The corrected values of the directly measured quantities are in the following named ϑ_{crr} (temperature of sample carrier), $\dot{q}_{hfs}$ (heat flux through heat flux sensor), and p_{vc} (pressure in vacuum chamber).

Temperature at the Structure Base ϑ_{strb}

For the calculation of the effective heat transfer coefficient U_{ev} the temperature ϑ_{strb} at the interface of sample carrier and porous structure (= base of porous structure) is required. It can be assumed that ϑ_{strb} is fairly close to the temperature ϑ_{crr} measured inside the sample carrier due to the high thermal conductivity of the copper sample carrier and the small distance between structure base and measuring point of $\Delta z_{strb,mp} = 1.5\ mm$; however, there will be a certain temperature gradient. ϑ_{strb} is calculated by means of Fourier's law (and the thermal conductivity of the sample carrier material λ_{crr}), assuming a linear temperature gradient:

$$\vartheta_{strb}(t_i) = \vartheta_{crr}(t_i) - \frac{\Delta z_{strb,mp}}{\lambda_{crr}} \cdot \dot{q}_{hfs}(t_i) \tag{4-7}$$

The assumption of a linear temperature gradient in the sample carrier in heat flow direction implies a certain inaccuracy due to the transient character of the measurements. A calculative assessment – described in the uncertainty analysis in chapter B.7.4 (appendix) – though led to the conclusion that this inaccuracy is negligible for the presented measurements.

In principle heat losses from the sample carrier to the ambient systematically influence the relation of ϑ_{strb} and ϑ_{crr} in equation (4-7). Simulations by Boertz prior to this work (Boertz 2017, p. 62) revealed, though, that heat losses for the realized experimental setup are very small compared to the applied heat flux. According to his calculations, total heat losses (from heater block and from sample) amount to approximately 1.3 W for a heating power of 40 W under the assumption of pool boiling conditions with an evaporation heat transfer coefficient of 2500 W/(m²K). The respective total heat loss value for a theoretical setup with sample carrier height of 20 mm instead of 4 mm is only 0.26 W higher. This suggests that the share from the sample carrier – which is the only one with impact on equation (4-7) – to the total heat loss is even less than 0.26 W which is 0,65% of the applied heating power. In addition, heat transfer coefficients of evaporation from capillary-held refrigerant are usually considerably higher than for pool boiling which leads to lower temperatures of heater block and sample and consequently to even lower heat losses. Taking all these factors into account, the impact of heat losses on the relation of ϑ_{strb} and ϑ_{crr} (equation (4-7)) is assessed as negligible.

Effective Evaporation Heat Flux $\dot{q}_{ev}$

The heat flow through the heat flux sensor $\dot{Q}_{hfs}$ can be calculated from the heat flux $\dot{q}_{hfs}$ with the cross-sectional area of the sensor A_{hfs}– assuming a homogeneous heat flux within the sensor area:

$$\dot{Q}_{hfs}(t_i) = \dot{q}_{hfs}(t_i) \cdot A_{hfs} \tag{4-8}$$

The heat flow entering the sample structure is considered to be identical with the heat flow of evaporation $\dot{Q}_{ev}$ since heat losses from the porous structure are neglected and capacitive effects within the structure are not considered according to the "black box" approach. $\dot{Q}_{ev}$, however, is not identical with the heat flow $\dot{Q}_{hfs}$ through the heat flux sensor but it is also affected by a capacitive heat flow $\dot{Q}_{cap}$ in the sample carrier due to changes in its temperature field, by radial heat losses from the sample carrier to the ambient and by heat gains from the LED device which illuminates the sample from the top. As pointed out before, heat losses from the carrier were estimated as extremely small and are thus neglected. Heat gains by LED illumination were estimated by evaluation of the heat flux signal after switching on the LED device. The measured steady-state heat flux amounted to maximum 0.01 kW/m² which is negligible compared to the applied heating heat flux of 10…40 kW/m². Consequently, the evaporation heat flow $\dot{Q}_{ev}$ is described as:

$$\dot{Q}_{ev}(t_i) = \dot{Q}_{hfs}(t_i) - \dot{Q}_{cap}(t_i) \tag{4-9}$$

The capacitive heat flow $\dot{Q}_{cap}$ can only be approximated since no information on the spatial and time-dependent temperature distribution within the sample carrier is available. For this purpose the carrier is regarded as a discrete temperature node at the measured carrier temperature ϑ_{crr} which is associated with a thermal capacitance defined by the mass of the carrier M_{crr} and its specific heat capacity c_{crr}. In differential notation the capacitive heat flow can be written as:

$$\dot{Q}_{cap}(t) = M_{crr} \cdot c_{crr} \cdot \frac{d\vartheta_{crr}(t)}{dt} \tag{4-10}$$

For the calculation of a time series based on discrete measurement data the differential quotient is converted to a central difference quotient:

$$\dot{Q}_{cap}(t_i) = M_{crr} \cdot c_{crr} \cdot \frac{\vartheta_{crr}(t_{i+1}) - \vartheta_{crr}(t_{i-1})}{t_{i+1} - t_{i-1}} \tag{4-11}$$

The approximation of the capacitive heat flow implies a certain inaccuracy due to the one-node-simplification. This inaccuracy, however, is considered negligible as pointed out in the uncertainty analysis in chapter B.7.5.

The evaporation heat flow $\dot{Q}_{ev}$ can be related to the cross-sectional area of the sample structure A_{str}, yielding the effective evaporation heat flux $\dot{q}_{ev}$:

$$\dot{q}_{ev}(t_i) = \frac{\dot{Q}_{ev}(t_i)}{A_{str}} \tag{4-12}$$

Saturation Temperature of the Vapor Atmosphere ϑ_{sat}

The absolute pressure p_{vc} measured inside the vacuum chamber is not equal to the saturation vapor pressure p_{sat} above the sample surface – the latter being the relevant quantity for evaluation: Due to inevitable leakage small amounts of non-condensable gases enter the vacuum system during measurement and are included in pressure measurement. Additionally, a certain pressure drop caused by the vapor flow through the PMMA container and the "squirt prevention appliance" must be expected.

In order to compensate for the partial pressure of non-condensable gases p_{ncg}, a pressure correction is carried out, based on the previously determined pressure rise rate of the total vacuum system $(\Delta p/\Delta t)_{leak}$ (cf. chapter B.6 in the appendix) and the elapsed time Δt_{leak} since end of the last evacuation.

$$p_{sat}(t_i) = p_{vc}(t_i) - p_{ncg}(t_i) = p_{vc}(t_i) - \left(\frac{\Delta p}{\Delta t}\right)_{leak} \cdot \Delta t_{leak}(t_i) \tag{4-13}$$

The correction implies the assumption that at the end of the evacuation procedure the vacuum system contains a pure water atmosphere, free of non-condensable gases. Assuming moreover, that the vapor above the sample structure is in saturation state, the validity of this assumption can be checked in each measurement by comparing the condenser pressure with the saturation pressure of the liquid refrigerant temperature inside the condenser. Furthermore, equation (4-13) presumes a linear pressure rise (or a constant leak rate, respectively) inside the vacuum system. Since the pressure difference to the ambient – which is the driving force for leakage – diminishes only slightly during the measurement, the assumption of a linear pressure rise is considered to be legitimate.

A coarse assessment of the expected vapor pressure drop in PMMA container and the "squirt prevention appliance" yielded values in the dimension of 10^{-2} Pa which is about factor 100 smaller than the measurement uncertainty of pressure measurement. Consequently, the impact of pressure drop on the vapor pressure is neglected.

As saturation conditions in the vapor atmosphere are assumed, the saturation temperature ϑ_{sat} of the vapor above the sample structure can be calculated from the vapor pressure p_{sat} by using the vapor pressure curve of water (cf. Figure 74 in the appendix). The „International Association for the Properties of Water and Steam" (IAPWS) provides a definition of the saturation pressure curve (and its inverted form – the saturation temperature curve or "backward equation") of water in their standard IAPWS IF-97 (The International Association for the Properties of Water and Steam 2007). This standard is used for evaluation of the presented measurements in the form of the freeware script „XSteam.R"(Holmgren n.d.) which implements correlations for various physical properties of water according to the IAPWS IF-97 standard in the interpreter language R (R Core Team n.d.). The complex functional relations of the saturation curves are not presented here; instead, the saturation temperature equation is only described in the generalized form:

$$\vartheta_{sat}(t_i) = f(p_{sat}(t_i)) \tag{4-14}$$

Refrigerant Mass M_{rf} and Experimental Refrigerant Storage Capacity $M_{rf,cap}$

Another relevant quantity for the assessment of dynamic evaporation from the porous structures is the total refrigerant mass inside the structure, M_{rf}. For the derivation of M_{rf} firstly the vapor mass flow rate $\dot{M}_{vap}$ is calculated from the evaporation heat flow $\dot{Q}_{ev}$, using the specific enthalpy of vaporization Δh_v (from IAPWS IF-97 (The International Association for the Properties of Water and Steam 2007) via XSteam.R (Holmgren n.d.)):

$$\dot{M}_{vap}(t_i) = \frac{\dot{Q}_{ev}(t_i)}{\Delta h_v\big(p_{sat}(t_i)\big)} \tag{4-15}$$

Using the counter value $i = 1$ for the first and $i = n$ for the last data point, the cumulated evaporated refrigerant mass M_{cum} can be calculated by numerical integration of the vapor mass flow rate

$$M_{cum}(t_i) = \sum_{j=2}^{i} \dot{M}_{vap}\big(t_j\big) \cdot \big(t_j - t_{j-1}\big) \qquad for\ 2 \leq\ i \leq n \tag{4-16}$$

with the initial condition $M_{cum}(t_1 = 0) = 0$.

The refrigerant mass inside the structure M_{rf} at time t_i is then determined as the difference between the total evaporated refrigerant mass $M_{cum}(t_n)$ and the cumulated mass at the current time step $M_{cum}(t_i)$:

$$M_{rf}(t_i) = M_{cum}(t_n) - M_{cum}(t_i) = \sum_{j=i+1}^{n} \dot{M}_{vap}\big(t_j\big) \cdot \big(t_j - t_{j-1}\big) \qquad for\ 1 \leq i \leq (n-1) \tag{4-17}$$

The final refrigerant mass value is set to $M_{rf}(t_n) = 0$.

Equation (4-17) is based on the assumption that any change of refrigerant mass inside the structure originates from evaporation ($dM_{rf}/dt = -dM_{cum}/dt = -\dot{M}_{vap}$). This relation is in fact not always true because small amounts of refrigerant are sometimes squirted out of the structure if vapor bubbles form

within the refrigerant-filled porous matrix. It is further suggested that the sample structure is completely dry at the end of measurement evaluation ($M_{rf}(t_n) = 0$). This does not necessarily have to be the case because the evaluation is deliberately terminated when the carrier temperature exceeds a certain security limit. Anyway, the determined evaporation heat flow approaches zero when the heater is switched off which indicates that hardly any refrigerant is left in the structure. Both simplifying assumptions lead to the statement that $M_{rf}(t_1 = 0) = M_{cum}(t_n)$ which is involves a potential inaccuracy. However, there is no possibility of quantifying the ejected and the residual refrigerant masses, therefore, a correction or uncertainty estimation cannot be done. Instead, this source of inaccuracy must be considered in the interpretation of the measurement data.

The maximum cumulated refrigerant mass $M_{rf}(t_1 = 0) = M_{cum}(t_n)$ is used as an estimation for the actual refrigerant storage capacity $M_{rf,cap}$ of a mesh structure in the considered measurement, which refers to the refrigerant mass which can be held inside the pore volume by means of capillary forces. As pointed out above, this value can only serve as a rough estimation since it may deviate from the real storage capacity due to squirting and refrigerant residues. In some measurements the cumulated refrigerant value is furthermore subject to uncertainty due to an unintended incomplete drainage of the refrigerant column at the end of the measurement preparation (cf. chapter 4.1.4) which prohibits an exact determination of the measurement start.

4.1.8 Measurement Uncertainty Analysis

Measurement uncertainties of the evaluated quantities in this work are determined according to the "Guide to the expression of uncertainty in measurement" (GUM) in its version from 2008 ("GUM 1995 with minor corrections") (Joint Committee for Guides in Metrology 2008). The following methodology is completely based on GUM, therefore the individual statements are not individually marked with references. The presented methods were applied to the complete chain of data reduction from the directly measured quantities to the different evaluation quantities. A detailed description of the involved uncertainty components and of the derivation of the combined standard uncertainty for each quantity is given in the appendix B.7.

Since all measurements of physical quantities are subjected to disturbing effects, several observations of a constant quantity may lead to different results – the measurement results comprise a certain deviation from the real value, which is traditionally termed "error". Given that "real value" and "error" are quantities which are usually unknown in practical measurement, GUM suggests to rather employ the concept of uncertainty in measurement. This concept focuses on the observed values of a measurand and quantifies their reliability with associated uncertainty values. In accordance with this approach, the reliability of measurement results within this work is expressed in form of uncertainties.

Generally, disturbance effects on a measurement are differentiated into two categories: random effects and systematic effects. Systematic effects influence every measurement observation in the same way and cause a bias in the result. Therefore, their impact on the measurement result can be reduced or eliminated by means of a correction term in the functional relation, which is included in the data reduction at several occasions, as described in chapter 4.1.7. Systematic effects themselves do not contribute to the measurement uncertainty but only the inaccuracy of the correction must be considered in the uncertainty analysis.

Random effects have a statistical character and lead to an arbitrary spreading of repeated observations around the real value. The expectation of these deviations (and its estimate, which is denoted as Δx within this work) is zero. However, since usually only a finite number of observations is available, the estimate of the measured quantity still incorporates an uncertainty which is denoted as $u(\Delta x)$ in the uncertainty analysis of this work.

According to GUM uncertainty components can be attributed to either of two different categories, A or B:

If several independent observations X_k of a randomly varying quantity X are available, a "type A evaluation" can be applied. This method was used to quantify the noise impact on temperature, heat flux and pressure measurement, as documented in B.7.1, B.7.2, and B.7.3. The type A evaluation is based on statistical methods: The "estimate of the measurand X" – denoted as x – yields an estimation for the expected value μ_X and is usually described by the arithmetic mean $\bar{X}$ of the n observations:

$$x = \bar{X} = \frac{1}{n}\sum_{k=1}^{n} X_k \tag{4-18}$$

The experimental variance $s^2(X_k)$, characterizing the dispersion of the observed values around their mean, is an estimation of the variance of the probability distribution σ^2 and can be calculated as follows:

$$s^2(X_k) = \frac{1}{n-1}\sum_{k=1}^{n}(X_k - \bar{X})^2 \tag{4-19}$$

The positive square root of the experimental variance is called the experimental standard deviation s. Indicators for how good the arithmetic mean $\bar{X}$ of a measurand matches its expectation μ_X are the "experimental variance of the mean" $s^2(\bar{X})$ and its positive square root which is termed the "experimental standard deviation of the mean" $s(\bar{X})$. Since $\bar{X}$ is used for the estimate x, $s(\bar{X})$ describes the uncertainty of the estimate $u(x)$ and is accordingly termed "type A standard uncertainty". It is defined as:

$$u(x) = s(\bar{X}) = \frac{s(X_k)}{\sqrt{n}} = \sqrt{\frac{1}{n\cdot(n-1)}\sum_{k=1}^{n}(X_k - \bar{X})^2} \tag{4-20}$$

The standard deviation σ characterizes an interval around the expectation of a measurand μ_X which covers a certain percentage of the probability density function. For a normal probability distribution approximately 68% of the observed values are in the interval $[\mu_X - \sigma,\ \mu_X + \sigma]$; for a rectangular probability distribution it is approx. 58%. Analogously, the standard uncertainty $u(x)$ is also subjected to these levels of confidence. If higher certainty standards are required, the expanded uncertainty $U(x)$ can be used which increases the percentage of covered observations at the cost of a broadened interval of possible values. Usually, an integer multiple of $u(x)$ is used, employing the coverage factor k:

$$U(x) = k \cdot u(x) \tag{4-21}$$

For a normal distribution a coverage factor of $k = 2$ for example yields a level of confidence of approx. 95% while doubling the interval to $[\mu_X - 2\sigma,\ \mu_X + 2\sigma]$ or $[x - 2u,\ x + 2u]$.

If no data for statistical evaluation is available a "type B evaluation" of an uncertainty component can be done. In this case the standard uncertainty of the estimate $u(x)$ – then termed "type B standard uncertainty" – is determined "by scientific judgement based on all of the available information on the possible variability" (Joint Committee for Guides in Metrology 2008) of the quantity X. This information can origin from "- previous measurement data; - experience with or general knowledge of the behaviour and properties of relevant materials and instruments; - manufacturer's specifications; - data provided in calibration and other certificates; - uncertainties assigned to reference data taken from handbooks" (Joint Committee for Guides in Metrology 2008). For this work uncertainty information for type B evaluations are usually taken from manufacturers' datasheets and calibration certificates for the different sensors, as

described B.7 for the different evaluation quantities. The provided information is not necessarily given in the form of a standard uncertainty but can also be stated as an expanded uncertainty value (as for instance in case of the DAQ unit or the reference sensor for temperature calibration) or an uncertainty with a level of confidence of a specified percentage. If not otherwise stated, a normal distribution of probabilities can be presumed and the standard uncertainty can be calculated accordingly – in case of an expanded uncertainty specification according to equation (4-21). Uncertainty information is occasionally also provided in form of an interval $[a_-, a_+]$ which includes all observed values X_k with a probability of one, often termed as "error limits". This applies for example to the calibration inaccuracy of the heat flux sensor, cf. B.7.2. If no information on the probability distribution is given, a rectangular distribution can be assumed and the estimate x is defined as the center point of the interval. If the distance between a_- and a_+ is denoted as $2a$, the standard uncertainty $u(x)$ is – derived from the definition of variance and standard uncertainty:

$$u(x) = \frac{a}{\sqrt{3}} \tag{4-22}$$

For most evaluation quantities used in this work – such as the evaporation heat transfer coefficient U_{ev} – the measurand Y is not evaluated directly but results from a mathematical model which is expressed as a functional relationship $Y = f(X_1, X_2, \dots, X_N)$, including N different input quantities X_i. The uncertainty of Y depends on the uncertainties of the input quantities and on the characteristics of the functional relation. Provided that all input quantities X_i are uncorrelated and the input uncertainties $u(x_i)$ are small, the combined standard uncertainty of the output quantity's estimate y, denoted as $u_c(y)$, can be calculated according to the law of propagation of uncertainty:

$$u_c(y) = +\sqrt{\sum_{i=1}^{N}\left(\frac{\partial f}{\partial x_i}\cdot u(x_i)\right)^2} \tag{4-23}$$

Equation (4-23) is derived from a first-order Taylor series approximation of the functional relation f. If f shows relevant nonlinearities, higher-order terms of the Taylor series have to be included in the uncertainty calculation. The partial derivatives $\partial f/\partial x_i$ are also called sensitivity coefficients in this context since they determine how strongly the uncertainties of the input quantities affect the combined uncertainty of the output y. In practice, the partial derivatives are deduced from the functional relation of the physical quantities X_i and evaluated at their estimates x_i:

$$\frac{\partial f}{\partial x_i} = \left.\frac{\partial f}{\partial X_i}\right|_{x_1, x_2, \dots, x_N} \tag{4-24}$$

If some of the input quantities are considerably correlated (here: X_i and X_j), equation (4-23) is not valid and the respective covariances $u(x_i, x_j)$ must be considered in the calculation of the combined standard uncertainty. Correlation must be expected if, for example, the same measuring device or the same physical measurement standard is used for two input quantities. $u_c(y)$ can then be described as:

$$u_c(y) = +\sqrt{\sum_{i=1}^{N}\sum_{j=1}^{N}\frac{\partial f}{\partial x_i}\frac{\partial f}{\partial x_j}u(x_i, x_j)} = +\sqrt{\sum_{i=1}^{N}\left(\frac{\partial f}{\partial x_i}\cdot u(x_i)\right)^2 + 2\cdot\sum_{i=1}^{N-1}\sum_{j=i+1}^{N}\frac{\partial f}{\partial x_i}\frac{\partial f}{\partial x_j}\cdot u(x_i, x_j)} \tag{4-25}$$

In the special case of a maximum correlation of all input quantities (correlation coefficient of +1) and sensitivity coefficients of identical algebraic signs, equation (4-31) simplifies to:

$$u_c(y) = \sum_{i=1}^{N} \left| \frac{\partial f}{\partial x_i} \cdot u(x_i) \right| \tag{4-26}$$

Due to the sum of linear terms, this approach prevents a partial extinction of uncertainty from interrelation of the uncertainty components, and consequently yields a worst-case assumption for the combined uncertainty.

Due to the unsteady character of the evaporation measurements of this work, the uncertainty calculation was conducted for each time step and the uncertainty quantities are consequently time-dependent themselves. In the diagrams in chapter 5 they thus appear in form of a shaded area adjacent to the measurement curves. In order to provide a rough overview on the resulting uncertainty ranges, exemplary values are shown in Table 4. The table lists up values of the measurement and evaluation quantities (denominated with x in the column names) with their associated absolute uncertainties ($u(x)$) and relative uncertainties ($u_{rel}(x)$) for different exemplary measurement conditions. Conditions of the standard parameter set with medium applied heat flux of about 30 kW/m² (measurement M01, cf. Table 3, p. 57) are confronted with a "worst case" parameter set with the minimum applied heat flux of 10 kW/m² (measurement M05) which leads to highest uncertainties of the heat transfer coefficient U_{ev}. To account for the dynamic character of the measurements characteristic values are calculated, firstly for the initial period of moderate evaporation heat transfer coefficients U_{ev} for which average values $\bar{x}$, $\overline{u(x)}$, and $\overline{u_{rel}(x)}$ of minute 2-3 are calculated, and secondly for the point of maximum heat transfer coefficient U_{ev}.

As the table reveals, the relative uncertainties of the temperature of the sample carrier ϑ_{crr} and vacuum chamber pressure p_{vc} are well below 1% for all conditions. The relative uncertainty of heat flux measurement $\dot{q}_{hfs}$ is 3% for all conditions, mostly due to the comparably large calibration uncertainty. For the driving temperature difference $\Delta\vartheta$ between base of the porous structure and vapor the relative uncertainty values strongly vary for the different conditions: While for medium applied heat flux (standard parameter set) at a moderate U_{ev} it only amounts to 1.5%, it reaches 26% for the case of small applied heat flux and maximum U_{ev}. This dramatic difference can be attributed to the decreasing temperature difference $\Delta\vartheta$ with increasing heat transfer capability of the sample and with decreasing applied heat flux, and to the associated large proportion of the absolute uncertainty $u(\Delta\vartheta)$ in relation to the temperature difference $\Delta\vartheta$ itself. The same effects act on the uncertainty of the evaporation heat transfer coefficient U_{ev}. While under high heat flux and moderate heat transfer capability conditions the relative uncertainty of U_{ev} is 6.2%, it rises to a very large value of 32% for a low applied heat flux and maximum heat transfer capability of the sample.

The relative uncertainty of the refrigerant mass M_{rf} both increases with decreasing applied heat flux and increasing U_{ev}. The absolute uncertainties are much smaller for maximum U_{ev} than for moderate since the U_{ev} maximum occurs later in the measurement and is therefore closer to the reference point of zero refrigerant mass. However, since the refrigerant mass continuously diminishes during the measurement, the relative uncertainty is anyway higher for the high heat transfer coefficient. The increase of the relative uncertainty of M_{rf} for the lower applied heat flux can be attributed to the higher uncertainty of the evaporation heat flow $\dot{Q}_{ev}$ which is included in its calculation. For a comprehensive assessment of the uncertainty of the refrigerant mass M_{rf} it must further be considered that additional uncertainty can arise from mass losses due to squirting and a potential refrigerant residual at the end of the measurement, which can both not be quantified.

Table 4: Measurement values (x), absolute measurement uncertainties ($u(x)$) and relative measurement uncertainties ($u_{rel}(x)$) for various evaluation quantities; for medium applied heat flux (measurement M01) and for low applied heat flux (measurement M05), both evaluated in a period of moderate heat transfer capability and at the point of maximum heat transfer capability

		Medium heat flux (M01), moderate U_{ev}			Medium heat flux (M01), maximum U_{ev}			Low heat flux (M05), moderate U_{ev}			Low heat flux (M05), maximum U_{ev}		
		$\bar{x}$	$\overline{u(x)}$	$\overline{u_{rel}(x)}$	x	$u(x)$	$u_{rel}(x)$	$\bar{x}$	$\overline{u(x)}$	$\overline{u_{rel}(x)}$	x	$u(x)$	$u_{rel}(x)$
ϑ_{crr}	$°C$	17.3	0.072	0.42%	12.8	0.072	0.56%	15.5	0.072	0.46%	11.3	0.071	0.63%
$\dot{q}_{hfs}$	kW/m^2	29.2	0.86	3.0%	30.5	0.9	3.0%	10.2	0.3	3.0%	10.2	0.3	3.0%
p_{vc}	kPa	1.3	0.0057	0.43%	1.3	0.0057	0.43%	1.3	0.0058	0.45%	1.3	0.0058	0.45%
ϑ_{strb}	$°C$	17.2	0.072	0.42%	12.7	0.072	0.57%	15.4	0.072	0.46%	11.2	0.072	0.64%
$\dot{Q}_{hfs}$	W	36.7	1.2	3.3%	38.3	1.2	3.3%	12.8	0.42	3.3%	12.8	0.42	3.3%
$\dot{Q}_{cap}$	W	0.0085	0.68	8000%	-0.046	0.66	1400%	-0.063	0.65	1000%	-0.0013	0.64	50000%
$\dot{Q}_{ev}$	W	36.7	1.4	3.7%	38.4	1.4	3.7%	12.9	0.77	6.0%	12.8	0.77	6.0%
$\dot{q}_{ev}$	kW/m^2	29.2	1.4	4.7%	30.5	1.4	4.6%	10.3	0.68	6.6%	10.2	0.67	6.6%
p_{sat}	kPa	1.3	0.0057	0.44%	1.3	0.0057	0.44%	1.3	0.0059	0.45%	1.3	0.0059	0.46%
ϑ_{sat}	$°C$	10.8	0.066	0.61%	10.9	0.066	0.61%	10.8	0.068	0.63%	10.8	0.069	0.63%
$\Delta\vartheta$	K	6.3	0.098	1.5%	1.8	0.098	5.4%	4.6	0.099	2.2%	0.39	0.099	26%
U_{ev}	$kW/(m^2K)$	4.6	0.29	6.2%	17	1.7	10.0%	2.2	0.2	8.7%	26	8.5	32%
$\dot{M}_{vap}$	g/s	0.015	0.00056	3.7%	0.016	0.00057	3.7%	0.0052	0.00031	6.0%	0.0052	0.00031	6.0%
M_{cum}	g	1.3	0.064	4.8%	9.1	0.35	3.9%	0.5	0.13	27%	11	0.74	7.0%
M_{rf}	g	8.3	0.32	3.9%	0.56	0.034	6.1%	11	0.68	6.4%	0.46	0.07	15%

4.1.9 Assessment of Sample Structures

Based on the requirements for an evaporator heat exchanger which were explained in chapter 2.1, two methods for the assessment of porous structures regarding their suitability for the evaporation of water at sub-atmospheric pressures were developed. The first method derives characteristic performance values from the complete dynamic evaporation process (from maximum saturation of the pores with refrigerant to dryout) which delineates the general field of possible performance values. In contrast, the second method considers the option of running the envisaged cyclic evaporation-condensation process only in a favorable refrigerant charge interval. Thereby it illustrates the realizable options in the tradeoff between maximization of the adsorption module's power output versus maximization of its COP and it enables an application-oriented assessment.

As mentioned in chapters 1 and 2.1, a high thermal power output and a high efficiency in terms of COP are generally opposing targets for the conceptual design of an adsorption heat pump or chiller. A high power output requires high mean absolute thermal transmittances (UA values) of all involved heat exchangers, which usually entails the choice of a short half-cycle time (due to the power maximum in the beginning of the process) and relatively small transferred refrigerant masses per half-cycle. For a high COP, on the other hand, relatively large refrigerant masses need to be stored and released by the cyclically operated heat exchangers in relation to their thermal masses, in order to minimize capacitive heat losses. Referred to an evaporator-condenser heat exchanger with capillary structures in cyclic operation this means that a high

average absolute thermal transmittance (UA value) is the main requirement in case of a high-power design focus of the machine, while the refrigerant storage capacity of the capillary structure, $M_{rf,cap}$, becomes increasingly relevant in case of a high-COP focus.

For deriving the structure assessment quantities of the first method, both of the above-mentioned critical quantities for an evaporator, UA and $M_{rf,cap}$, are referred to the requirement of a small construction volume. Since only the porous structure is meant to be assessed, the effective heat transfer coefficient of the structure, U_{ev}, is used instead of an overall heat transfer coefficient of the heat exchanger, $U_{fl,rf}$ (which would additionally include the heat transfer on the fluid duct side). Analogously, only the structure volume V_{str} is considered instead of the construction volume of the heat exchanger. Due to the dynamic character of the evaporation process, the mean heat transfer coefficient of the complete evaporation process ($\overline{U_{ev}}$), the heat transfer coefficient of the starting phase (first minute) ($U_{ev,start}$) and the maximum heat transfer coefficient ($U_{ev,max}$) of the process are used as characteristic heat transfer values. Referring the absolute thermal transmittance $U_{ev}A$ to the structure volume, this leads to the assessment quantity of the mean (start / maximum) heat transfer coefficient of evaporation per structure height, $\overline{U_{ev}} \cdot A_{str}/V_{str} = \overline{U_{ev}}/h_{str}$. Referring the refrigerant storage capacity to the structure volume leads to the second assessment quantity of the first method, $M_{rf,cap}/V_{str}$. It characterizes the refrigerant mass which can be held inside a certain porous structure volume by capillary action and therefore quantifies the maximum refrigerant mass turnover per half cycle. To allow for an assessment of the actual storage capacity, a theoretical refrigerant storage capacity $M_{rf,th}$ is calculated for comparison. This quantity is determined from structure geometry data and represents the hypothetical refrigerant mass which could be stored inside the structure if its total pore volume was saturated with refrigerant.

The first assessment method marks out the field of possible working points, however, it does not allow for a detailed assessment since it refers to the whole refrigerant charge interval of the dynamic measurement, from maximum saturation to complete dryout. Due to the usually pronounced dependence of the heat transfer coefficient on the refrigerant filling conditions (cf. results in chapter 5), though, it can be beneficial to run the evaporation / condensation cycles only in a limited advantageous refrigerant charge interval and thereby increase the mean heat transfer coefficient, at the cost of a diminished refrigerant mass turnover per half-cycle. These interrelations are illustrated in the right diagram in Figure 24. The choice of the interval width is directly linked with the tradeoff between a high power output or a high COP of the adsorption module: In case of a high-power focus a restriction of the evaporation process to a narrow refrigerant charge interval around the maximum heat transfer coefficient ($M_{rf,to}/V_{str}$ (I) in Figure 24, right) is advisable to achieve a high mean heat transfer coefficient. In contrast, for a high COP a wider interval ($M_{rf,to}/V_{str}$ (II) in Figure 24, right) might be favorable in order to increase the refrigerant mass turnover.

These interrelations are considered in the second assessment method by defining nine exemplary specific refrigerant turnover values ($M_{rf,to}/V_{str}$) from 100 kg/m³ to 900 kg/m³ in steps of 100 kg/m³. For each of these values the optimal refrigerant charge interval in terms of the highest achievable mean specific heat transfer coefficient $\overline{U_{ev,opt}}/h_{str}(M_{rf,to}/V_{str})$ is identified, and the corresponding mean heat transfer coefficient of this interval is determined (cf. Figure 24). As a necessary consequence of this method, $\overline{U_{ev,opt}}/h_{str}$ decreases with increasing refrigerant turnover demand since also the less efficient phases of the U_{ev} curve need to be included in the calculation of the mean. This second method allows to directly display the impact of a prioritization of either power output or efficiency (COP) of the adsorption / evaporation half cycle from the evaporator side on structure level.

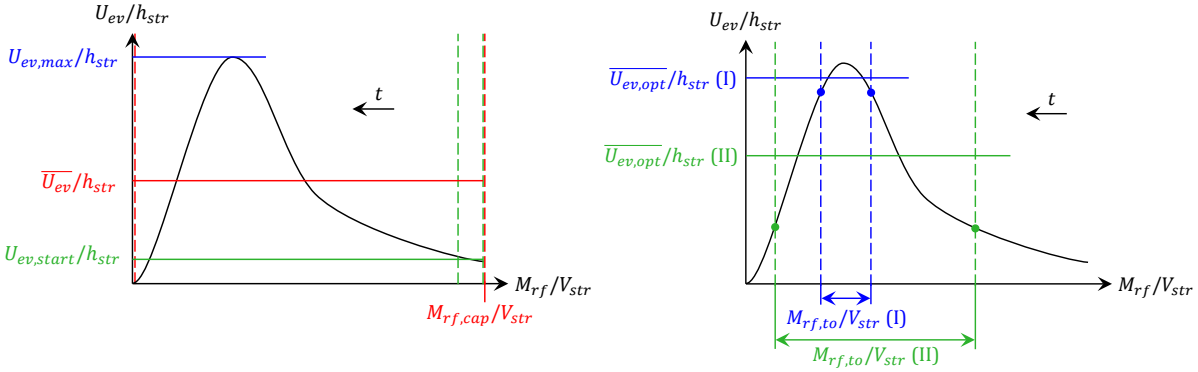

Figure 24: Visualization of the determination of the characteristic quantities for the two assessments methods for structure samples; left: method 1: structure-volume-specific refrigerant storage capacity $M_{rf,cap}$ and structure-height-specific mean (start, maximum) evaporation heat transfer coefficient $\overline{U_{ev}}/h_{str}$ ($U_{ev,start}/h_{str}$, $U_{ev,max}/h_{str}$); right: method 2: structure-height-specific optimal mean heat transfer coefficients $\overline{U_{ev,opt}}/h_{str}$ for predefined structure-volume-specific refrigerant mass turnover demands $M_{rf,to}/V_{str}$

4.2 Evaporation Model

4.2.1 Model Objectives and Concept

As a complementary element to the experimental investigations of this work, an evaporation model was developed. According to chapter 3, the main objective of the modeling activities was to create a simple mathematical tool which allows a calculative reproduction of the dynamic evaporation behavior of the experiments with a satisfactory precision. A comparison with experimental results was expected to contribute to a better understanding of evaporation and dewetting dynamics, geometry impacts and limiting factors. The targeted scope in terms of operating conditions and sample geometries was defined equal to the parameter ranges covered by the experiments, which were chosen according to the intended application (cf. chapter 4.1.1). Ideally, the model should also be applicable for structures with other pore morphologies than the employed wire mesh, as for example metal foams, sintered fiber structures, knitted wire fabrics etc. In order to reach a maximum scope of applicability, the model was supposed to be preferably based on physical relations instead of empirically derived correlations. On the condition that its prediction accuracy is assessed as sufficient, the model might be integrated in a subsequent model describing evaporation on heat exchanger level and thus contribute to establishing dimensioning methods.

To comply with the requirement of simplicity, the model was realized in form of a lumped-parameter model. The continuous temperature field and thermal capacity distribution of a certain setup domain are reduced to a discrete node associated with a temperature value ϑ and a thermal capacitance C, as depicted in Figure 25. Heat transfer between two neighboring nodes is described by means of a scalar thermal resistance R. The connection of these elements for adjacent structure domains results in a resistance-capacitance (RC) network. Due to the unsteady character of the process, some of the thermal resistances and capacitances are time-dependent quantities. Accordingly, a time discretization to points of time t_i is implemented besides the lumped spatial discretization. By setting up energy balances with the involved heat flow contributions $\dot{Q}$ for each node (equation (4-27)), each resistance (equation (4-28)) and each

capacitance (equation (4-29)) and including boundary conditions, a linear equation system (LES) can be derived which fully defines the system.

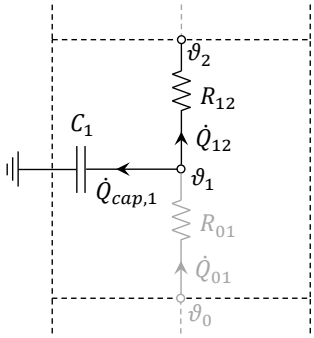

Figure 25: Schematic of an exemplary resistance-capacitance scheme for a defined reference volume (associated energy balance equations are given in (4-27), (4-28), (4-29))

$$\dot{Q}_{01}(t_i) - \dot{Q}_{12}(t_i) - \dot{Q}_{cap,1}(t_i) = 0 \tag{4-27}$$

$$\vartheta_2(t_i) - \vartheta_1(t_i) = R_{12}(t_i) \cdot \dot{Q}_{12}(t_i) \tag{4-28}$$

$$\dot{Q}_{cap,1}(t_i) = C_1 \cdot \frac{\vartheta_1(t_i) - \vartheta_1(t_{i-1})}{t_i - t_{i-1}} \tag{4-29}$$

In order to allow for a comparison of the simulation results with measurements, not only the porous structure is incorporated in the model but the whole experimental setup, including heater block, sample carrier etc. The sample structure is not spatially resolved according to its topology but instead described by effective geometric values and properties such as porosity, characteristic pore size and material data. Besides these geometric specifications, thermodynamic parameters, i.e. vapor saturation pressure of the system and applied heat flux, are employed as input quantities. Main output quantity is the time series of the overall heat transfer coefficient of evaporation of the porous structure, denoted by U_{ev}. Analog to its definition in the experimental context, it refers to the temperature difference between structure base and saturation temperature. Individual thermal resistances in between – which will be addressed later – can be summarized to a total thermal resistance $R_{tot,str}$ of the porous structure, and using the cross-sectional area A_{str} of the structure the heat transfer coefficient of evaporation can be described as:

$$U_{ev}(t) = \frac{1}{R_{tot,str}(t) \cdot A_{str}} \tag{4-30}$$

Further output quantities are time series of the node temperatures, heat flux components, time-dependent resistances, refrigerant masses and other auxiliary quantities. Implementation of the model description and calculation of the output quantities for discrete time steps was done with the programming language "R" (R Core Team n.d.).

For minimizing the model complexity, several simplifying assumptions were made: First of all, a one-dimensional heat-transfer in vertical direction from the heating element through the sample structure up to the vapor atmosphere was assumed. This implies a temperature constancy within every horizontal plane of the setup. Heat losses to the ambient by heat conduction, convection and/or radiation – which might cause a temperature gradient in horizontal direction and distort the calculated heat flows – are neglected. Considering an estimation by Boertz (Boertz 2017) which revealed that heat losses of the setup are very small compared to the applied heat flow for the relevant operating range (cf. chapter 4.1.5), this simplification is regarded as acceptable. In accordance with the assumption of one-dimensional heat

transfer, potential edge effects at the structure's circumference are not considered by the model. Furthermore, the thermal capacitance of heat flux sensor and adjacent foils are treated as negligible.

While the thermal resistances and capacitances of the peripheral setup components – which are specified in chapter 4.2.2 – are constant and determined from geometry and material of their components, the description of the structure section in terms of resistances and capacitances is less obvious since it depends on the assumed model conception of the dewetting behavior during the evaporation process. The initial refrigerant mass and the final mass of zero is fixed but the dynamic refrigerant distribution in between is influenced by a complex interaction of capillary forces, gravitational forces, viscous forces etc. which are in turn affected by structure geometry, material and surface properties, process parameters etc. Since space-resolved simulations of wetting equilibria are beyond the scope of this work, different model conceptions for the dewetting dynamics were developed and translated into resistance-capacitance arrangements; amongst them the "receding front" approach which was chosen as the standard approach for this work. Modelling approaches and implementation of dewetting dynamics are presented in chapter 4.2.3. Finally, in chapter 4.2.4 the computational algorithm for the calculation of the time-dependent quantities is described.

4.2.2 Resistance-Capacitance Network for the Peripheral Setup Components

The resistance-capacitance network for the peripheral setup components – which are heater block, heat flux sensor unit, and sample carrier – is depicted in Figure 26. Due to the assumption of one-dimensional heat transfer, the temperature nodes of the network are arranged in one line in direction of heat transfer. Nodes are placed at each outer boundary of the setup, which is the temperature of the heating element ϑ_{he} and the saturation temperature of the vapor atmosphere ϑ_{sat}. Further temperature nodes are placed at interfaces between major structural and/or material domains, which is $\vartheta_{htr,hfs}$ at the interface between the heater block and the heat flux sensor unit, $\vartheta_{hfs,crr}$ between heat flux sensor unit and sample carrier, and $\vartheta_{crr,sldr}$ between sample carrier and solder contacts which connect the mesh strips of the porous structure to the carrier. Additional nodes are placed in the centers of those structure domains to which a thermal capacitance is allocated, which yields a node in the center of the heater block ϑ_{htr} and one in the center of the sample carrier ϑ_{crr}.

The constant resistances for the respective domains of the experimental setup were calculated according to the general equation for (absolute) thermal resistances R for the case of a cartesian system

$$R = \frac{d}{\lambda \cdot A} \tag{4-31}$$

which comprises the length d of the domain in heat flow direction, its thermal conductivity λ and its cross-sectional area A. In this way the resistance R_{htr} of the heater block, the resistance R_{hfs} of the heat flux sensor unit and the resistance R_{crr} of the sample carrier were determined. All required geometry and material data for the model were taken from technical drawings and data sheets of the respective parts and are listed up in Table 20 in the appendix. Any temperature dependences of the solids' thermal conductivities were neglected. For domains with a temperature node in their center – which is the heater block and the sample carrier – the thermal resistances were split into halves and placed before and after the node in the resistance network (cf. Figure 26).

In case of the heater block only the height of its upper part – which is located above the heating element – was taken into account for its resistance. Since the upper part of the heater features a shoulder with larger diameter at its bottom end, the presumption of one-dimensional heat transfer is certainly not realistic within the heater block. Still, for simplicity reasons the total resistance of the heater block R_{htr} is treated

as a serial connection of the resistance contributions of the two sections with different diameter. As R_{htr} is rather small compared to other resistance contributions and not directly included in the calculation of the evaporation heat transfer coefficient U_{ev}, this simplification is considered acceptable.

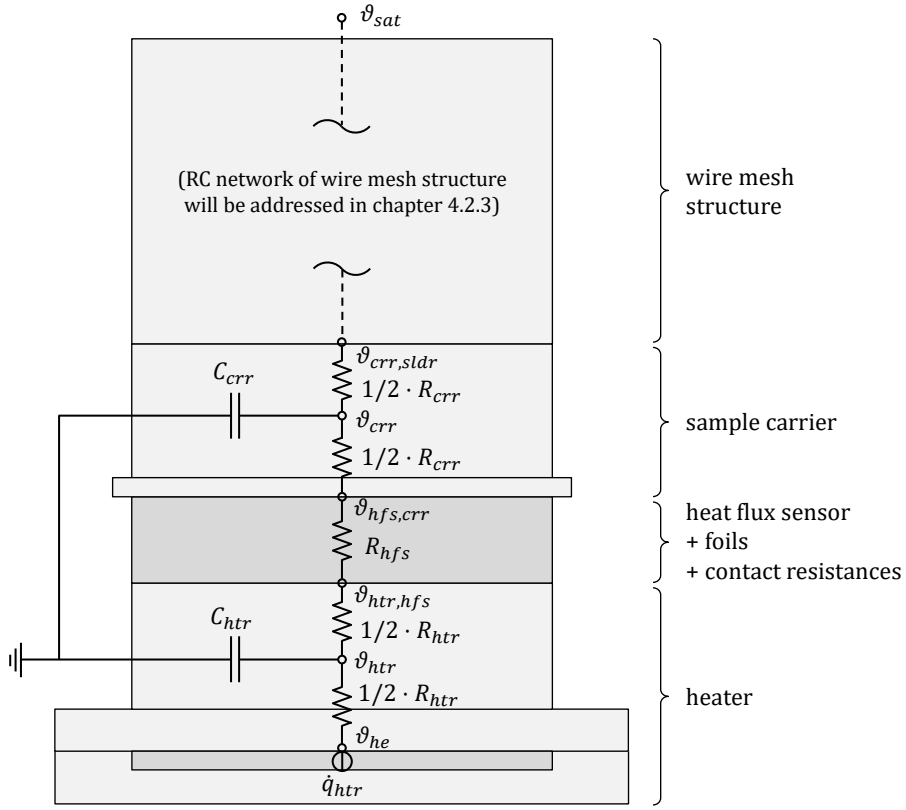

Figure 26: Resistance-capacitance network of the peripheral setup components (schematic of the setup not true to scale)

The resistance of the heat flux sensor unit R_{hfs} is modeled as a serial connection of resistance contributions of the sensor (which basically consists of two copper sheets with an epoxy layer in between), adhesive foil, thermally conductive foil and contact resistances at the four interfaces between heater block, foils, sensor and sample carrier. The contact resistance was estimated empirically in consideration of measured heater temperatures which yielded a value of 0.135 K/W per single contact face.

In the calculation of the thermal resistance of the sample carrier R_{crr} the small shoulder at the carrier's bottom was neglected. Earlier 3D simulations during development of the measurement concept had proven that the impact of the shoulder on the course of heat flow lines is negligible, therefore this simplification is considered legitimate.

Thermal capacitances C are determined from their mass M and the specific heat capacity c of the respective material:

$$C = M \cdot c \tag{4-32}$$

In the resistance-capacitance network of the peripheral setup components only the capacitances of the heater block C_{htr} and of the sample carrier C_{crr} are respected. The thermal capacitance of the heat flux sensor unit is neglected due to its small mass and relatively low mean specific heat capacity. For the capacitance of the heater block also the mass of its lower part (below the heating element) is considered.

4.2.3 Modeling of the Dewetting Dynamics

As addressed in chapter 4.2.1 in the context of the model concept, the dewetting process of the porous structure and its associated dynamic refrigerant distribution could potentially follow various characteristic patterns, depending on the interrelation of acting forces and heat transfer mechanisms. Major relevant forces for the wetting behavior of porous structures are gravitational forces, capillary forces, and viscous forces. Viscous forces are assumed to play only a minor role for the considered conditions of this work since liquid water has a relatively low viscosity. Additionally, the envisaged evaporation process does not include a continuous refrigerant feed, therefore, the liquid refrigerant in the pore volume is not expected to reach high flow velocities. The ratio of the two remaining forces – gravitational force and capillary force– can be expressed by means of the dimensionless Bond number Bo (or Eötvös number Eo) which is defined in equation (2-6) (p. 32). A large Bond number implies the predominance of gravitational forces over capillary forces. Accordingly, it can be supposed that liquid in a porous structure accumulates in the lower part and forms a horizontal front between the filled and dry section which moves downwards as the liquid mass is reduced ("receding front"). Small Bond numbers, on the other hand, correspond to a predominance of capillary forces which might rather lead to a distribution of wet and dry clusters within the porous structure with the refrigerant accumulating at places of high capillary pressure. As presented in chapter 2.6, Laurindo and Prat used the Bond number for the prediction of liquid distribution patterns of porous structures for the case of drying processes (Laurindo and Prat 1996). Their drying experiments confirmed the occurrence of a receding front drying pattern for positive Bond numbers and a cluster-like pattern for a Bond number of zero, as illustrated in Figure 10 (p. 33).

The range of Bond numbers calculated for the wire mesh structures used in this work (for a pressure of 1.3 kPa and with the mesh spacing l_{mesh} as the characteristic length L) are listed up in Table 5, including the smallest and largest value and that of the standard sample KG01-800-250. All calculated Bond numbers naturally increase with increasing pore size, indicating the growing relevance of gravitation in relation to capillary forces. Samples with larger pore size should thus have a stronger affinity to form a receding front pattern. However, absolute relations are unknown and depend on the particular choice for the characteristic length L, and also the pattern categories by Laurindo and Prat are not associated to absolute Bond numbers. Predictions on the actually formed refrigerant distribution patterns are consequently not possible.

Table 5: Bond numbers (Bo) and clear mesh widths (w_{mesh}) of exemplary samples KG03-375-140, KG01-800-250, and KG04-2500-1000 (for a pressure of 1.3 kPa)

		KG03-375-140	KG01-800-250	KG04-2500-1000
w_{mesh}	mm	0.375	0.8	2.5
Bo	$-$	0.035	0.15	1.6

Based on these considerations, and since at least the Bond number of sample KG04-2500-1000 is larger than one, the model conception of a receding liquid front was chosen as the standard approach to describe the dewetting dynamics within this work. Its appropriateness for the different sample structures and conditions is discussed in chapter 5.

Besides this standard approach, three alternative model conceptions for the dewetting dynamics were developed and discussed in the context of pore size in chapter 5.4.2. The basic ideas of the four different model conceptions will be described in the subsequent paragraphs, followed by the translation of the standard model conception ("receding front") into a resistance-capacitance scheme and the definitions of the relevant resistances and capacitances.

Model Conception no. 1: "Receding Front" (Standard Approach)

The "receding front" model conception is based upon the presumption that a horizontal evaporation front moves through the porous structure in a downward direction, as illustrated in Figure 27. Evaporation is assumed to take place at the three-phase contact lines which are arranged in a horizontal zone that forms the evaporation front. Starting from a predefined filling level (which by default equals the structure height, cf. 0. in Figure 27), the section below the front is always completely saturated with refrigerant, while the section above is completely dry (1.). The speed of the front height position h_{front} is consequentially determined by the mass flow rate $\dot{M}_{vap}$ of evaporated refrigerant and by the structure's porosity.

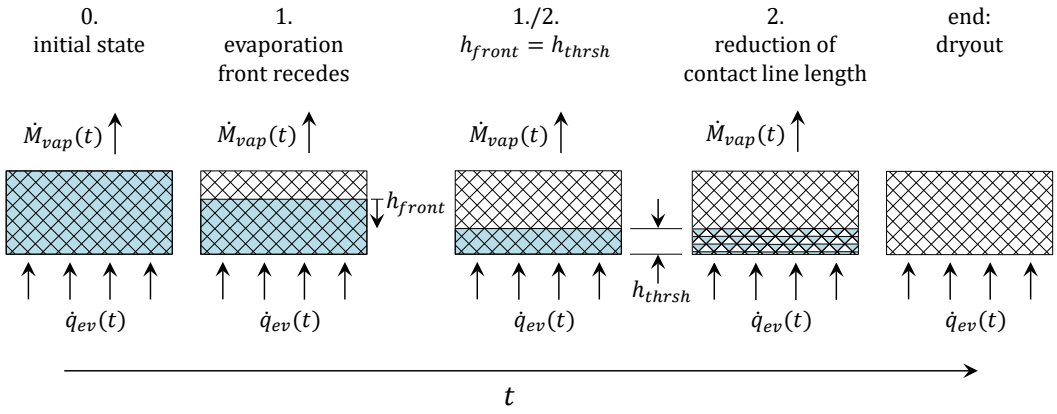

Figure 27: Visualization of the dewetting process according to the "receding front" model conception

Due to interfacial tensions and the formation of menisci at energetically favorable places, it is physically unrealistic that the refrigerant-filled layer below the front becomes infinitesimally thin. Therefore, a threshold height h_{thrsh} for the evaporation front is defined, below which the dewetting mechanism is assumed to change: As soon as the evaporation front reaches the threshold height (cf. 1./2. in Figure 27), the evaporation mass flow does not entail a further reduction of the front height h_{front} anymore but instead causes a reduction of the filling degree of the pore volume below the front (2.). The contact line length is assumed to decrease proportionally with the pore filling degree from this point on.

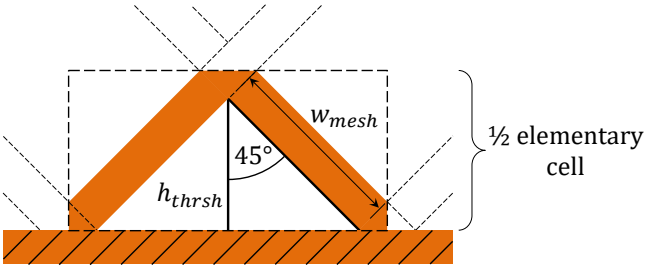

Figure 28: Definition of the threshold height h_{thrsh} for the receding front model approach, exemplary for mesh structure with 45° wire orientation

The value of the threshold height h_{thrsh} is deduced from the particular structure geometry and defined as the average clear height of half an elementary cell layer, as illustrated in Figure 28 for the case of a 45° wire orientation. This definition is based on the conception that contact lines always form along the wires within one layer of elementary cells – as supposed in definition variants (II) and (III) for the contact line length which will be presented later in this chapter. Since on average half of the (clear) height of an elementary cell layer is required to allow the maximum extent of the contact lines, a lower height of the

evaporation front would result in a reduction of the total contact line length. The threshold height h_{thrsh} is accordingly calculated as follows, using the clear mesh width w_{mesh}:

$$h_{thrsh} = w_{mesh} \cdot \cos(45°) \qquad \text{for 45° wire orientation} \qquad (4\text{-}33)$$

$$h_{thrsh} = w_{mesh} \cdot 0.5 \qquad \text{for 0°/90° wire orientation} \qquad (4\text{-}34)$$

Evaporation with reducing contact line length continues at the threshold height position until the porous structure falls dry, as depicted in the last drawing of Figure 27.

Alternative Model Conceptions for the Dewetting Dynamics

- **Model Conception no. 2: "0D Static Contact Lines"**
  This model conception is based on the idea that evaporation does not take place at a confined front but homogeneously distributed in the whole structure volume (cf. Figure 29). Consequently, the reduction of refrigerant mass leads to a uniform decrease of the filling degree of the pores with time (1. in Figure 29). For spatial discretization the mean position of evaporation is allocated to the center of the structure where it stays during the whole process. The contact line length is assumed to be dependent on the filling degree of the pores, being zero for completely full and empty pores and reaching the maximum length at a filling fraction of 0.5 while increasing or decreasing linearly in between.

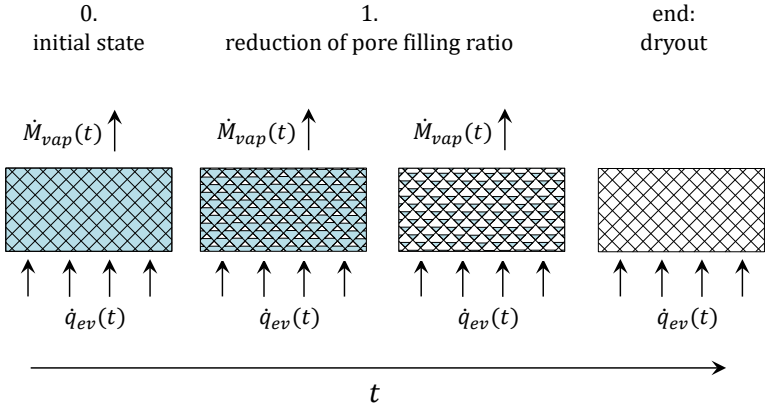

Figure 29: Visualization of the dewetting process according to model conception no. 2 "0D Static Contact Lines"

- **Model Conception no. 3: "Receding Front + Rising Front"**
  The third model conception is similar to the standard "receding front" approach in terms of presuming a moving evaporation front. Though, in contrast to the standard approach the section above the front is not completely dry but a certain fraction of the refrigerant remains in the pores (cf. 1. in Figure 30). As soon as the front reaches the structure base (1./2.), it switches directions and pursues moving upwards (2.). During this second phase refrigerant from the partially filled pores evaporates at the rising front which leaves a dry section of the structure.

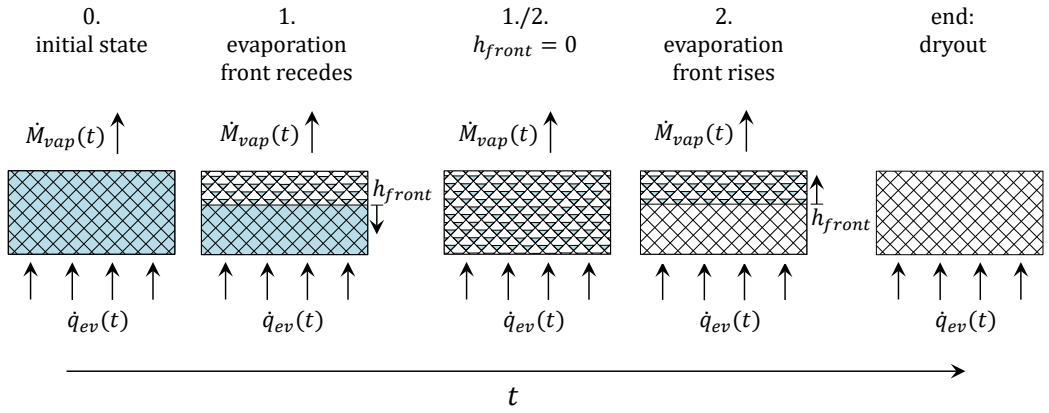

Figure 30: Visualization of the dewetting process according to model conception no. 3 "Receding Front + Rising Front"

- **Model Conception no. 4: "Receding Front + Static Front"**
  Also in this model conception a downward-moving front is presumed, which separates a fully saturated section below from a partially filled section above in a first phase (cf. 1. in Figure 31). When the front reaches a threshold height (1./2.), a second phase starts: The refrigerant of the partially wetted section above the front is assumed to evaporate at the constant threshold height position h_{thrsh} by means of a continuous transport to the front by capillary action and gravity (2.). The remaining refrigerant below the threshold height finally evaporates at the threshold height position in the third phase (3.) until the porous structure is completely dry (end).

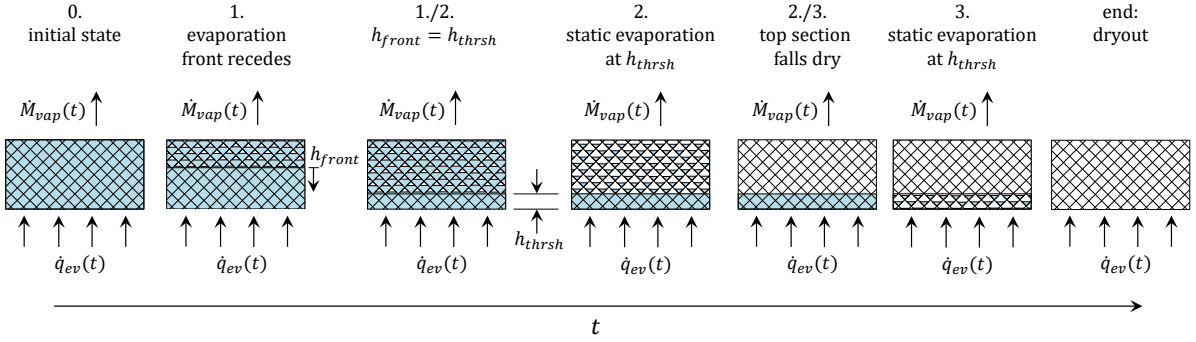

Figure 31: Visualization of the dewetting process according to model conception no. 4 "Receding Front + Static Front"

Resistance-Capacitance Scheme of the Standard "Receding Front" Model Conception

The translation of the "receding front" model conception into a resistance-capacitance scheme is illustrated in the upper section of Figure 32: In order to consider the moving front in the scheme, a temperature node ϑ_{front} is defined as the temperature of the mesh at the current position of the evaporation front (h_{front}) and consequently, the node moves through the structure with time. A resistance R_{ev} represents the evaporation mechanism between ϑ_{front} and the saturation temperature of the vapor atmosphere, ϑ_{sat}. The refrigerant-filled section of the porous structure is characterized by the resistance R_{rfs} which is split into two parts in the network and separated by a moving temperature node ϑ_{rfs}. Between mesh structure and sample carrier a thermal resistance R_{sldr} is placed which represents the resistance of the solder

contacts fixing the wire ends on the carrier. R_{sldr} connects the respective temperature nodes at the interface between carrier and solder material, $\vartheta_{crr,sldr}$, and at the interface between solder and mesh structure, $\vartheta_{sldr,str}$. The thermal capacitances of the structure matrix and refrigerant in the refrigerant-filled section are represented by $C_{rfs,str}$ and $C_{rfs,rf}$. The capacity of the solder material is neglected due to its relatively small mass.

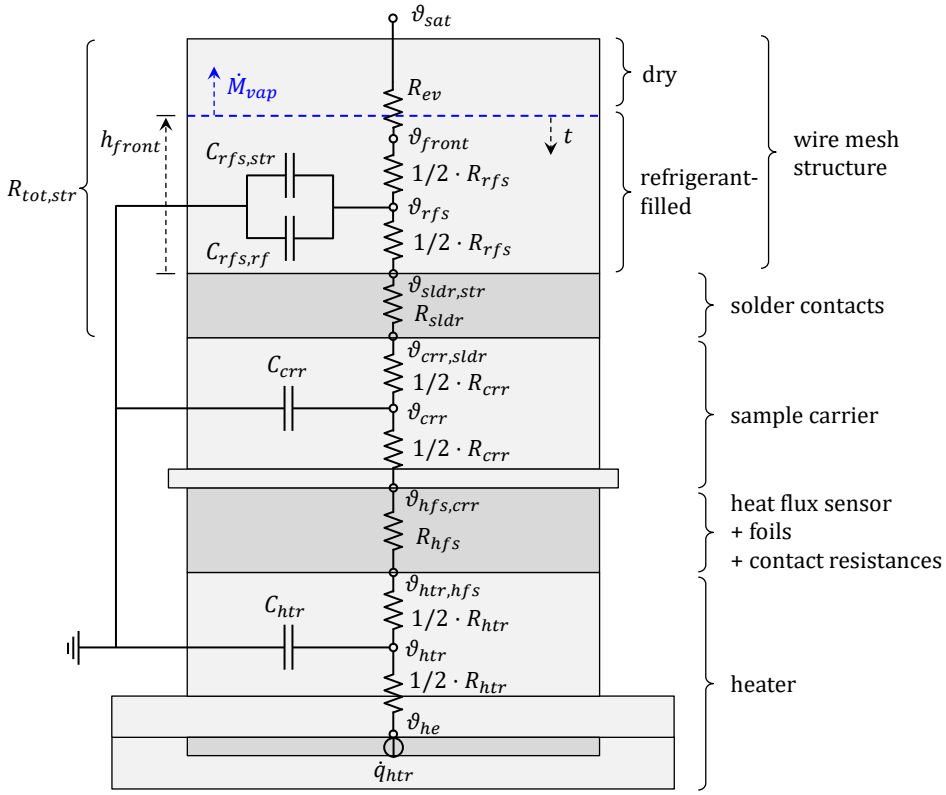

Figure 32: Resistance-capacitance network of the "receding front" model conception (schematic of the setup not true to scale)

Calculative estimations revealed that the vapor which flows through the dry section of the porous structure is not subjected to a considerable pressure drop, due to its low density and relatively low velocity. Consequently, a possible pressure drop resistance was not included in the model. Besides, any thermal interaction between dry mesh matrix and vapor is neglected. It is assumed that the resistance of conduction through the wires plus convection at the dry mesh surface is considerably higher than the small resistance of evaporation at the front (R_{ev}). Consequently, the complete heat flux can be regarded to flow through the evaporation branch and the dry mesh section is taken to be close to saturation temperature. Given that the saturation temperature stays constant throughout the evaporation process as a boundary condition and R_{ev} is nearly constant for front positions $h_{front} > h_{thrsh}$, the temperature of the dry mesh section will also virtually stay constant. A capacitive heat flux in the dry section can accordingly be neglected and a thermal capacitance for the dry section is not included in the RC network.

For the "receding front" approach the total resistance $R_{tot,str}$ of the porous structure – which is used for the calculation of the evaporation heat transfer coefficient U_{ev} in equation (4-30) – thus results from a serial connection of solder resistance R_{sldr}, resistance of the refrigerant-filled section R_{rfs}, and evaporation resistance R_{ev}:

$$R_{tot,str}(t) = R_{sldr} + R_{rfs}(t) + R_{ev}(t) \tag{4-35}$$

Resistance of the Solder Contacts R_{sldr}

For the calculation of the solder contacts' resistance R_{sldr} a simplifying geometric model conception was developed: Due to mechanical cutting of the wire mesh strips in the sample manufacturing process, wedge-shaped cutting edges are assumed for the wire ends instead of plane ends. Since the wire ends are cut in parallel to the strip edges, the wire ends are assumed to have a line-contact with the carrier after soldering, as illustrated in Figure 33 for the case of a 45° wire orientation angle α_{wire}. The tilted planes of the wedge are supposed to be arranged in a 90° angle; length and width of the wedge are set equal to the wire diameter d_{wire} and its height to half a wire diameter.

The wedge-shaped section of the wire is surrounded by solder in a conical shape. The height of the conus is taken as identical to the wedge's height and its broadening angle is fixed to 45°. Its top circular circumference is assumed to coincide with the corners of upper wedge plane, and has consequently a diameter of $\sqrt{2} \cdot d_{wire}$.

As a simplification, the wire and solder material are considered as parallel resistances, which in turn are composed of a serial connection of horizontal layers of varying cross-sectional areas. The total solder resistance R_{sldr} is derived from a parallel connection of all individual solder contact points of the wire mesh sample. Even if the solder contacts are certainly exposed to the refrigerant in the measurement setup, they are not regarded as such in the model for simplicity reasons. Instead, the resistance of solder contacts is considered to be serially connected to the resistance-capacitance unit of the refrigerant-filled structure section, as depicted in Figure 32.

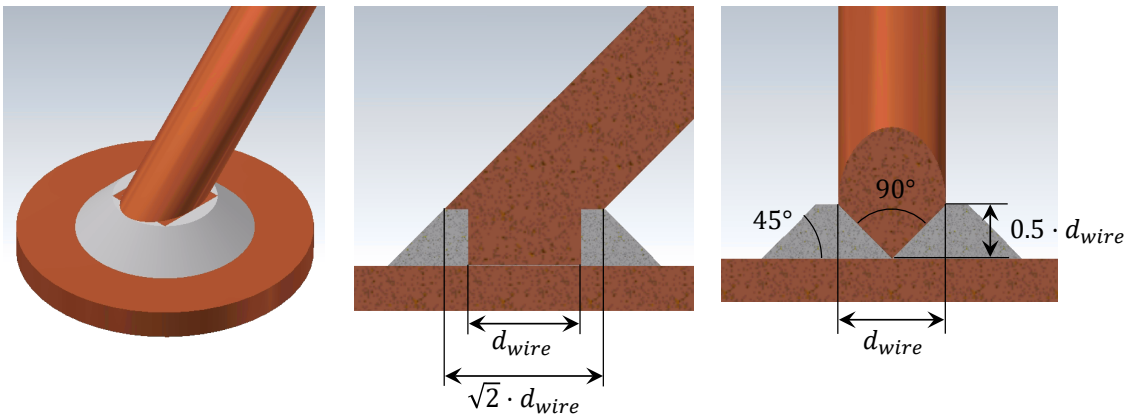

Figure 33: 3D-Visualization (left) and half-sections (center, right) of the assumed solder contact geometry between wire and sample carrier for the modeled resistance R_{sldr}; illustrations exemplary for a wire orientation angle α_{wire} of 45°

Heat Conduction Resistance R_{rfs} and Capacitances of the Refrigerant-Filled Section

In the refrigerant-filled section of the porous structure heat transfer is assumed to occur only in form of heat conduction. According to equation (4-31) and analogue to the modelling approach for heat pipe evaporator sections from (Stephan 2013) portrayed in chapter 2.5, the thermal resistance R_{rfs} of this section is defined as

$$R_{rfs}(t) = \frac{h_{front}(t)}{\lambda_{rfs,eff}(t) \cdot A_{str}} \tag{4-36}$$

The length of the refrigerant-filled section in heat flow direction equals the front height h_{front} which decreases with time. Consequently, R_{rfs} is a time-dependent quantity. The cross-sectional area of the heat flow equals the projected cross-sectional area of the sample structure, A_{str}. $\lambda_{rfs,eff}$ represents the effective thermal conductivity of the section which includes conduction through matrix and refrigerant. As pointed out in chapter 2.5 the topology of the capillary structure needs to be taken into account for the calculation of $\lambda_{rfs,eff}$. For a parallel connection of a solid and a fluid – which would be the case e.g. in an arrangement of parallel vertical wires –the effective thermal conductivity λ_{eff} can be calculated with the following equation which was adapted from (Stephan 2013) and which includes the thermal conductivities of the fluid λ_{fl} and of the solid λ_s and the porosity of the structure ψ:

$$\lambda_{eff} = \lambda_{fl} \cdot \psi + \lambda_s \cdot (1 - \psi) \tag{4-37}$$

In case of the wire mesh structures employed in this work, the samples do not exhibit such a parallel connection in heat flow direction but in most of them the wires are oriented in a 45° angle ($\alpha_{wire} = \pm 45°$) to the carrier surface (cf. chapter 4.1.3). Considering the longer heat conduction path through the wires, equation (4-37) is modified for those samples:

$$\lambda_{rfs,eff} = \lambda_{rf,l} \cdot \psi + \lambda_{CuETP} \cdot (1 - \psi) \cdot \sin(45°) \qquad \text{for } \alpha_{wire} = \pm 45° \tag{4-38}$$

Here, $\lambda_{rf,l}$ and λ_{CuETP} denote the thermal conductivities of the liquid refrigerant water and of the copper mesh material. Taking into account that necessarily a fraction of the wires in the upper outer region of the cylindrical structure does not possess a direct solder contact to the sample carrier (cf. Figure 21 in chapter 4.1.3), equation (4-38) implies a certain inaccuracy and might overestimate the thermal conductivity. However, since there is no obvious method for correction, this inaccuracy is tolerated.

One sample (KG10-800-250-090deg) has a wire orientation of 0°/90° which means that half of the wires have their axes in direction of heat flow while the other half is arranged perpendicularly to the heat flow direction. As a first estimate the horizontal wires (perpendicular to the heat flow direction) are assumed not to contribute in heat conduction. Accordingly, equation (4-37) is modified for this sample:

$$\lambda_{rfs,eff} = \lambda_{rf,l} \cdot \psi + \lambda_{CuETP} \cdot (1 - \psi) \cdot 0.5 \qquad \text{for } \alpha_{wire} = 0°/90° \tag{4-39}$$

If the model was applied to different structure topologies, respective definitions for the effective thermal conductivity were required. Definitions for groove structures, sintered structures and wire mesh structures consisting of a stack in heat flow direction are given in the VDI Heat Atlas (Stephan 2013) and in (Chi 1976), in the context of thermal resistance calculation of heat pipe wicks.

The thermal capacitances of the matrix volume and the refrigerant volume within the refrigerant-filled section are represented by the quantities $C_{rfs,str}$ and $C_{rfs,rf}$ in the RC network, which are connected to the temperature node ϑ_{rfs}. Due to the movement of the evaporation front these capacitances are also time-dependent quantities and they are defined as

$$C_{rfs,str}(t) = \frac{M_{str}}{h_{str}} \cdot h_{front}(t) \cdot c_{CuETP} \tag{4-40}$$

$$C_{rfs,rf}(t) = M_{rf}(t) \cdot c_{rf}(\vartheta_{rfs}(t)) \tag{4-41}$$

with the total mass and height of the wire mesh structure, M_{str} and h_{str}, the refrigerant mass M_{rf}, and the specific heat capacities of copper and of the liquid refrigerant, c_{CuETP} and c_{rf}.

Evaporation Resistance R_{ev}

For modelling the heat transfer mechanisms at the evaporation front, a thermal resistance R_{ev} is included in the network. This resistance represents the heat transfer between the wire positions at the upper edge of the refrigerant-saturated region (h_{front}) and the vapor atmosphere, and consequently includes heat transfer through the thin refrigerant films in the menisci at the wetting front and the molecular kinetic resistance at the liquid / vapor phase interface. As confirmed by the literature cited in chapters 2.3 and 2.4, the local heat flux, thermal resistance and meniscus shape / film thickness in the vicinity of three-phase contact lines are highly interrelated and they vary dramatically with position and boundary conditions due to the delicate balance between disjoining pressure and capillary pressure. Deriving a simple straightforward non-empirical resistance definition from these complex circumstances is therefore hardly possible. The definition of a certain thin film area with a characteristic film thickness in which evaporation heat transfer occurs is not feasible since film thickness and heat flux have a continuous distribution. Furthermore, the spatial definitions for the evaporating film area or "micro region" and their corresponding contribution percentages to the total heat transfer diverge considerably among different authors.

As a consequence and in order to comply with the objective of a simple resistance model, a simplified resistance description for evaporation from a meniscus was adopted from a thermal resistance model for grooved wick heat pipes by Chi (Chi 1976) which was taken up by Kim et al. in (Kim et al. 2003). A schematic of the resistance network is given in Figure 34.

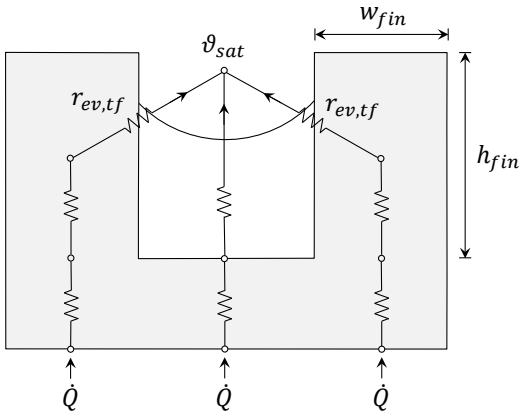

Figure 34: Resistance network for evaporation from a meniscus in a groove, suggested by Kim (Kim et al. 2003) on the basis of works by Chi (Chi 1976), including the resistance for evaporation in the vicinity of the contact line which was employed for the model of this work; drawing on the basis of (Kim et al. 2003)

As already mentioned in chapter 2.5, Chi presumed that the total heat flow through one groove element of the evaporator section can be divided into a pathway from the bottom of the groove through the bulk refrigerant and another parallel pathway through the groove fin and the thin film region in the vicinity of the three-phase contact line. For the heat transfer through the evaporating thin film region – from the middle of the groove fin (on meniscus height) to the vapor atmosphere – which is mainly responsible for evaporation, he defined a length-specific thermal resistance with the unit "m K/W" (named $r_{ev,tf}$ here) which refers to the cross-section through the groove and meniscus:

$$r_{ev,tf} = \frac{1}{h_{eff,tf} \cdot h_{fin}} \tag{4-42}$$

The equation comprises the height of the groove and fin h_{fin} and an effective heat transfer coefficient $h_{eff,tf}$ which he specifies as

$$h_{eff,tf} = \frac{\lambda_l}{0.185 \cdot w_{fin}} \tag{4-43}$$

employing the thermal conductivity of the liquid λ_l and the fin width w_{fin}.

The stated definitions for resistance and heat transfer coefficient of the evaporating thin film region by Chi and Kim (equations (4-42) and (4-43)) apply to evaporation from a groove structure, as illustrated in Figure 34. Accordingly, it cannot generally be presumed that the equations are likewise valid for different capillary geometries. However, as a tentative approach the resistance definition was transferred to the wire mesh geometry of this work. For this purpose the parameters of Chi's resistance definition were translated to their supposed analogs: The fin height h_{fin} was replaced by the clear mesh width w_{mesh}, the fin width w_{fin} by the wire diameter d_{wire}, the thermal conductivity of the liquid λ_l by $\lambda_{rf,l}$. For conversion into an absolute resistance the length-specific resistance is divided by the total contact line length l_{cl} whose definition will be discussed below. The resulting equation for the evaporation resistance of the model thus becomes:

$$R_{ev}(t) = \frac{0.185 \cdot d_{wire}}{\lambda_{rf,l}(t) \cdot w_{mesh} \cdot l_{cl}(t)} \tag{4-44}$$

In case of the groove structure considered by Chi and Kim et al. a conversion from the line-specific into an absolute resistance can easily be done: Since the meniscus uniformly stretches along the groove wall the sum of the groove length on both sides represents the total contact line length. A division of the line-specific resistance by this total contact line length leads to the absolute resistance. For complex pore morphologies as the employed mesh structures, however, the spatial course of the contact lines is not that obvious. Due to the more complex geometry of a porous structure and a potential variability in pore size and pore shape within the same structure, the local conditions influencing capillarity and wetting are non-uniform. Since the effect of the interaction of forces on the local interface shape at the evaporation front is unknown, different contact line arrangements are imaginable. As a consequence, three alternative approaches for possible contact line courses with corresponding contact line lengths l_{cl} were derived from the structure geometry. They are schematically depicted in Figure 35 for the case of a 45° wire orientation (top row) and a 0°/90° wire orientation (bottom row). The appropriate equations for the contact line length per elementary cell, $l_{cl,ec}$, are listed up in Table 6. (The definitions of an elementary cell for $\alpha_{wire} = \pm 45°$ and $\alpha_{wire} = 0°/90°$ are depicted in Figure 35.)

The first definition (I) is based on the idea that a contact line is formed at each circumference of the structure matrix which is created by a horizontal cut through the structure. For a wire mesh structure with 45° wire orientation the intersection line is an ellipse. For 0°/90° wire orientation it equals the circumference of all vertical wires plus in average a share of the outer lines of the horizontal wires. The enlarging effect of the refrigerant film thickness on the circumference is neglected since the film thickness in the evaporating film region or in the "micro region" is usually quantified to maximum 1 µm by many researchers (as mentioned in chapter 2.3) which is much less than the wire diameter of 140 µm to 1000 µm. In the second definition of l_{cl} (II) it is assumed that contact lines always form on top of horizontal or tilted wires, in parallel to their axes (cf. Figure 35, central column) and as the refrigerant mass reduces the contact line jumps to the next lower wires. The third variant (III, Figure 35, right column) similarly presumes contact lines along the wires but here the meniscus is positioned at the middle of the vertical wire extent which produces two contact lines on each wire, one on each side.

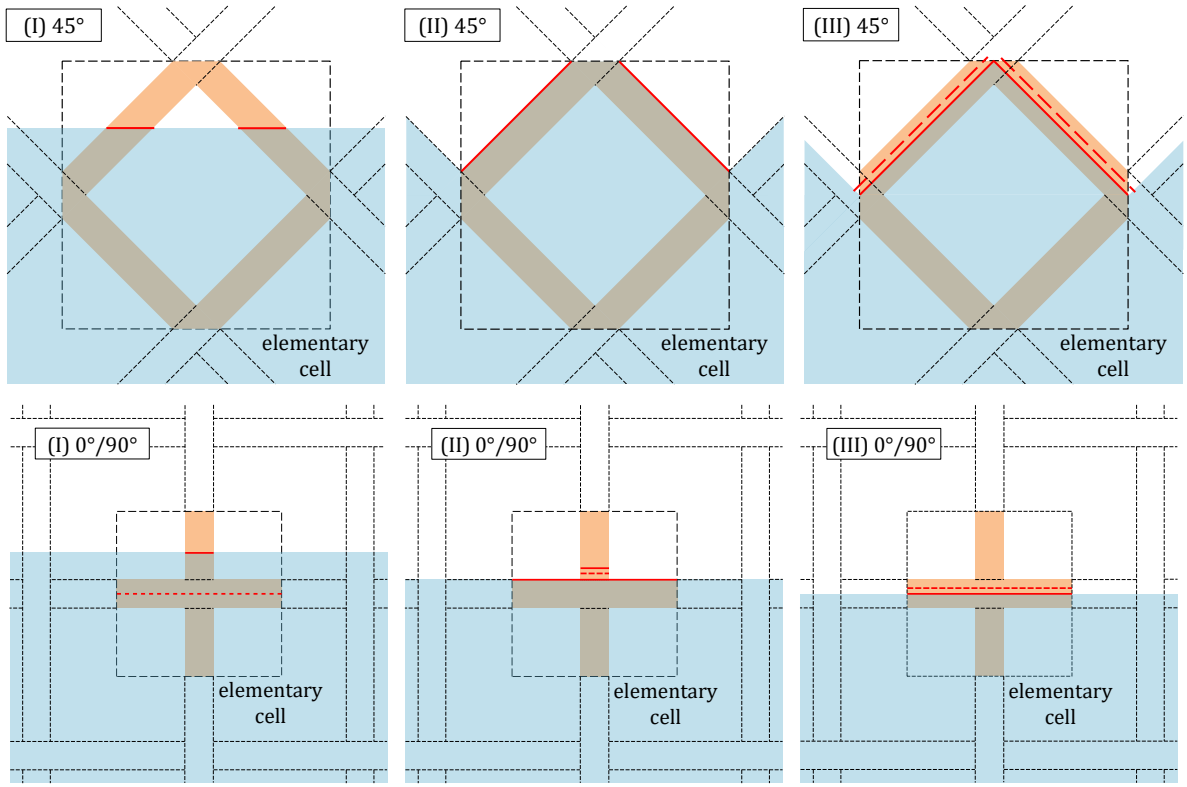

Figure 35: Schematic of the different definitions for the formation of contact lines in the wire mesh structure: (I) horizontal circumference of wires (left), (II) one contact line on top of each wire (center), (III) contact lines along both sides of each wire (right); for 45° wire orientation (top) and for 0°/90° wire orientation (bottom)

Table 6: Equations for the contact line length of an elementary cell for three different approaches

Approach (I):		
Intersection lines of horizontal cut		
45° wire orientation	$l_{cl,ec} = 2 \cdot \frac{\pi}{2} \cdot d_{wire} \cdot \left(1 + \frac{1}{cos\left(\frac{\pi}{4}\right)}\right)$	(4-45)
0°/90° wire orientation	$l_{cl,ec} = \pi \cdot d_{wire} + 2 \cdot l_{mesh} \cdot \frac{d_{wire}}{l_{mesh}}$	(4-46)
Approach (II):		
One contact line along each wire		
45° wire orientation	$l_{cl,ec} = 2 \cdot l_{mesh}$	(4-47)
0°/90° wire orientation	$l_{cl,ec} = l_{mesh} + \pi \cdot d_{wire}$	(4-48)
Approach (III):		
Two contact lines along each wire		
45° wire orientation	$l_{cl,ec} = 4 \cdot l_{mesh}$	(4-49)
0°/90° wire orientation	$l_{cl,ec} = 2 \cdot l_{mesh} + \pi \cdot d_{wire}$	(4-50)

Since the evaporation front is presumed to form a horizontal plane in the "receding front" approach, the number of elementary cells in one horizontal layer contribute to the total contact line length l_{cl}, which can thus be calculated as

$$l_{cl}(t) = l_{cl,ec}(t) \cdot \frac{n_{ec}}{h_{str}} \cdot h_{ec} \tag{4-51}$$

with the total number of elementary cells in the sample structure, n_{ec}, the total height of the structure h_{str} and the height of an elementary cell h_{ec}.

Given that resistance definition by Chi and Kim refers to a uniform meniscus in a groove structure in steady-state conditions, its transferability to a wire mesh structure with probably irregular meniscus shapes in an unsteady evaporation process is not per se ensured. For simplification, it was further assumed that only a negligible heat flux share passes through the central pathway of the meniscus and the respective resistances were consequently not included in the model. Moreover, it is unclear if any of the presented model conceptions for the contact line arrangement and length matches the actual circumstances. However, the diverging factors between the mesh structure and the groove might potentially be of little impact. The impact of motion of the meniscus, for instance, might be negligible, as the findings of (Fischer 2015) and (Kunkelmann et al. 2012) for receding contact angles at low velocities (cf. chapter 2.3) adumbrate. Nevertheless, the suitability of the definition for the evaporation resistance R_{ev} in equation (4-44) needs to be critically assessed in the discussion of the simulation results.

4.2.4 Computational Algorithm

All simulations based on the described evaporation model were carried out by means of a computational algorithm which will be described in this chapter. Figure 36 shows a flowchart which depicts all major steps of the algorithm.

As a first step several kinds of input data are loaded: A geometry data file of a specified real or hypothetical sample structure contains values for porosity ψ, mean pore diameter (w_{mesh} per definition for the mesh structures), matrix and carrier material, masses of matrix, carrier and solder, structure height h_{str}, and a morphology specification, which – in the case of mesh structures – can be a 45° wire orientation or a 0°/90° orientation. For the mesh structures also the wire diameter d_{wire}, mesh spacing l_{mesh}, and strip spacing l_{strp} of the mesh are quantified. A second parameter file contains thermodynamic boundary conditions of the process, which are the (constant) saturation pressure of the vapor atmosphere, p_{sat}, the heat flux applied by the heating element, $\dot{q}_{htr}$ (the applied heating power is related to the sample cross section), the initial refrigerant mass inside the porous structure, $M_{rf,init}$, and a value for the initial effective heat transfer coefficient of the structure $U_{ev,init}$. $U_{ev,init}$ was derived from measurement results and was by default set to 4 kW/(m²K). Since simulation tests revealed that the choice of this initial value did not have a significant impact on the course of the simulated quantities, setting the quantity to a standard value was considered as adequate. Further input data include material properties of sample, setup components and of the refrigerant water and geometry specifications of setup components.

With aid of the material properties and setup geometry input the constant resistances of heater block (R_{htr}), heat flux sensor unit (R_{hfs}), sample carrier (R_{crr}) and solder contacts (R_{sldr}) are calculated. Afterwards a linear equation system (LES) describing the initial steady-state of pool boiling is defined with aid of the constant resistances, the initial value for the overall heat transfer coefficient of the structure, $U_{ev,init}$, and the saturation pressure p_{sat}. The solution of the LES is a temperature vector representing the steady-state temperatures at the respective nodes. From these temperatures and Kirchhoff's circuit laws

the heat flow components of the RC network, the refrigerant mass flow, refrigerant mass, front height and refrigerant material properties for the initial time step are deduced.

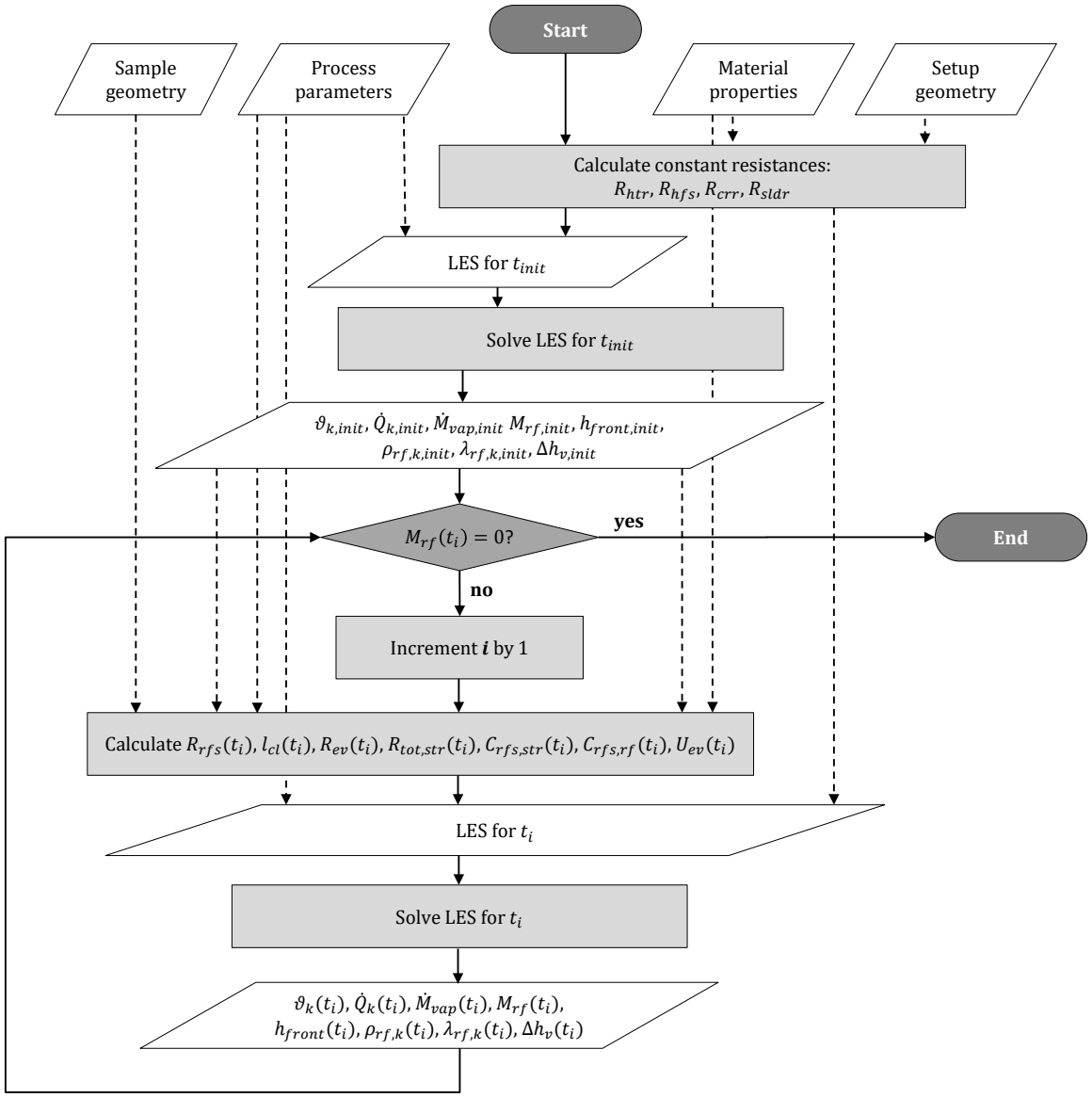

Figure 36: Flowchart of the computational algorithm of the "receding front" evaporation model

Starting from this initial state, the algorithm enters a condition-controlled loop in which the quantities of interest are calculated for all following time steps t_i. The time step size can be arbitrarily defined and is usually set to 1 s. The loop starts with a verification of the loop condition, which is the existence of refrigerant in the structure ($M_{rf}(t_i) = 0$?). In case there is refrigerant left in the structure ("no") the counter for the time step, i, is incremented by one. Subsequently, the time-dependent thermal resistances and capacitances and the overall heat transfer coefficient of the structure, U_{ev}, for the new time step are calculated, using results of the previous time step, sample geometry and material inputs. The resistance and capacitance values are then included in a linear equation system (LES) which characterizes the resistance-capacitance network for the dynamic evaporation process. Solving the LES yields the node temperatures ϑ_k and heat flow components $\dot{Q}_k$ (with index k denominating the different nodes or connections) of the current time step t_i and deduced quantities as vapor mass flow rate $\dot{M}_{vap}$, refrigerant

mass M_{rf}, front position h_{front} and material properties of the refrigerant. Having reached the end of the current loop cycle, the algorithm leads to the verification of the loop condition again and the refrigerant mass is checked. As long as there is refrigerant left in the porous structure (“no”) the algorithm will rerun the loop. As soon as the structure is completely dry (“yes”) the loop condition is not fulfilled anymore which leads to exiting the loop and termination of the algorithm.

5 RESULTS & DISCUSSION

In this chapter measurement and simulation results are presented. In chapter 5.1 the general evaporation and dewetting dynamics are analyzed by comparing measurement and simulation results, using the example of the standard sample and parameter set. Chapter 5.2 addresses several issues related to measurement reliability, which is the repeatability of measurements (5.2.1), reproducibility of sample manufacturing (5.2.2) and the impact of surface properties and sample aging (5.2.3). In chapter 5.3 the impact of process parameters (applied heat flux (5.3.1), system pressure (5.3.2) on evaporation is analyzed; while chapter 5.4 focuses on the impact of structure geometry parameters (porosity (5.4.1), pore size (5.4.2), structure height (5.4.3), wire mesh orientation (5.4.4)). In 5.4.5 an application-related assessment of the different structure geometries is carried out. Finally, in chapter 5.5 the potential of a hypothetical evaporation heat exchanger with wire mesh structure is assessed and compared to a reference evaporator concept.

5.1 Analysis of Evaporation Dynamics for the Standard Parameter Set

In the following paragraph the standard sample (KG01-800-250) and standard conditions ($p_{nom} = 1.3\ kPa$, $\dot{q}_{nom} = 30\ kW/m^2$; cf. Table 3) are used for a general analysis of the measured and simulated evaporation dynamics and of the occurring heat transfer mechanisms and dewetting dynamics. Moreover, the impact of different model parameters and presumptions are discussed. From the available measurement data of the standard parameters, measurement M01 was chosen exemplarily. For a better visualization all time series are depicted as continuous curves in the diagrams, even if the data sets consist of discrete points. Measurement uncertainties are plotted as vertical lines in positive and negative direction for each value which usually appears as shaded areas due to the high density of measurement values.

Figure 37 shows the time series of the vacuum chamber pressure p_{vc} (left) and heat flux through the heat flux sensor $\dot{q}_{hfs}$ (right) which are directly measured quantities. The pressure signal shows a fairly constant course with only minor fluctuations and it matches the nominal system pressure of the parameter set of 1.3 kPa very well. Only at the very end of the measurement the pressure slightly drops by about 0.01 kPa due to dryout of the structure. Overall, the pressure conditions can be considered as constant with sufficient accuracy. The heat flux signal on the right matches the nominal value of 30 kW/m² relatively good as well. During the first ten minutes of the measurement it slightly rises due to the changing heat transfer capability of the sample structure and associated capacitive heat flows in the setup. At the very end the heat flux drops to about 23 kW/m². Also in the case of heat flux, the boundary condition is regarded as sufficiently constant to allow for a comparison of different heat flux settings. The uncertainty values are relatively constant with time and correspond to the exemplary values in Table 4 (chapter 4.1.8, p. 67).

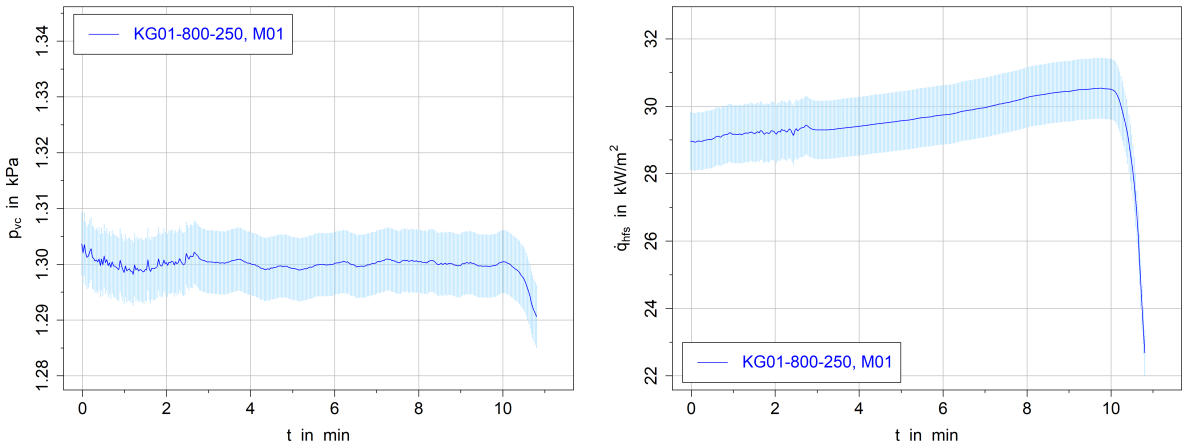

Figure 37: Measured vacuum chamber pressure p_{vc} (left) and heat flux through heat flux sensor $\dot{q}_{hfs}$ (right) of measurement M01 (standard parameter set: sample KG01-800-250, $p_{nom} = 1.3\ kPa$, $\dot{q}_{nom} = 30\ kW/m^2$)

The evaporation heat transfer coefficient of the porous structure U_{ev} – which is a major evaluation quantity of this work – is plotted against time (left) and against the refrigerant mass in the structure, M_{rf}, (right) in Figure 38 for measurement M01. Apart from the mirror inverted appearance which arises from the refrigerant mass decreasing with time, both representations of U_{ev} are obviously very similar and do not exhibit any considerable extension or compression of certain periods. This circumstance is caused by the relatively constant evaporation heat flux which is associated with a relatively constant vapor mass flow rate, and thus a virtual proportionality of t and M_{rf}.

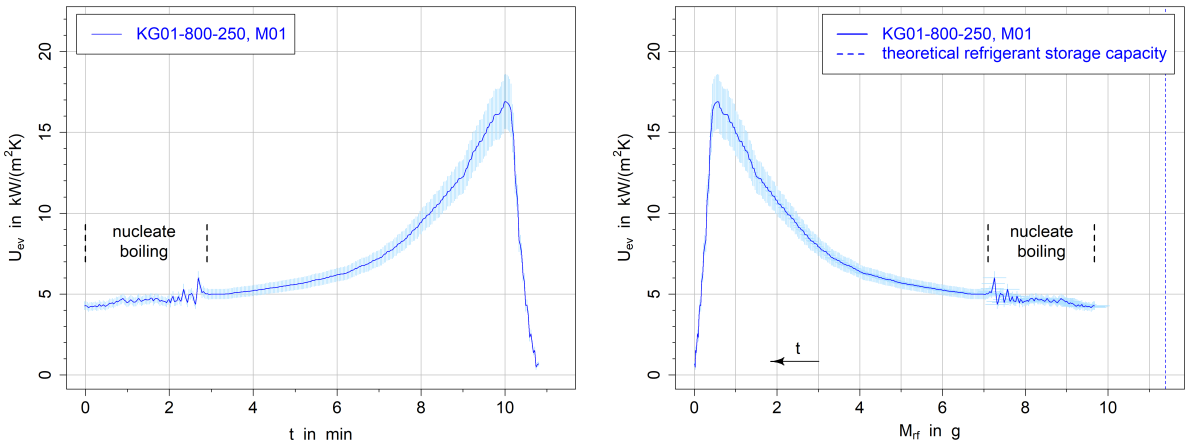

Figure 38: Heat transfer coefficient vs. time (left) and vs. refrigerant mass (right) of measurement M01 (standard parameter set: sample KG01-800-250, $p_{nom} = 1.3\ kPa$, $\dot{q}_{nom} = 30\ kW/m^2$)

In the first about three minutes of evaporation the measured heat transfer coefficient U_{ev} stays on a nearly constant level of 4...5 kW/(m²K) and fluctuates with a small amplitude. In visual observations of the experimental setup the occurrence of nucleate boiling within the porous structure was recorded in this first phase. Periodic oscillations of heat transfer are typical for nucleate boiling due to varying heat transfer during bubble formation, growth and detachment (Giraud et al. 2016). The observed oscillations – which can also be found in the pressure signal in Figure 37 – are therefore attributed to nucleate boiling. Figure 39 depicts the driving temperature difference $\Delta\vartheta$ (= superheat) between the temperature ϑ_{strb} at the structure base and the saturation temperature ϑ_{sat} of the vapor pressure. The first minutes of fluctuating heat transfer take place at a temperature difference of about 6-7 K which obviously suffices to fulfill the

local energetic requirement for bubble formation (cf. chapter 2.2) under the given conditions. This range is in accordance with findings of Witte who observed an onset of nucleate boiling in capillary-assisted evaporation from fiber structures at similar superheats of 3…8 K for the same system pressure (Witte 2016), however, the results are of course not fully comparable due to different conditions. Approximately 3 minutes after the beginning of the experiment the heat transfer coefficient and pressure curves become smooth which indicates that the temperature difference does not meet the demand for nucleate boiling under current conditions anymore but evaporation only takes place in form of convective evaporation from thin films. Simultaneously, U_{ev} starts to rise with increasing slope until after 10 minutes it reaches its maximum of 16.9 kW/(m²K). After the maximum U_{ev} drops abruptly and approaches zero within less than 30 seconds.

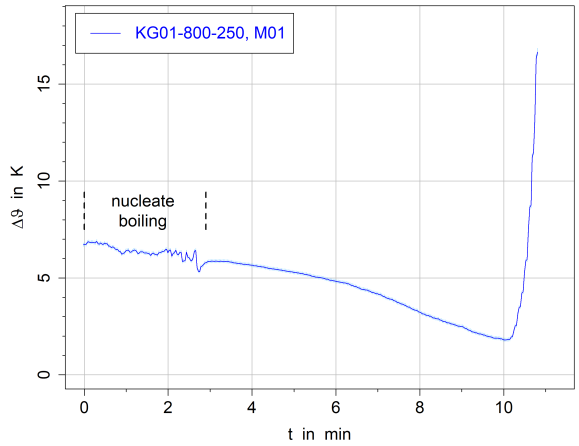

Figure 39: Driving temperature difference $\Delta\vartheta$ of measurement M01 (standard parameter set: sample KG01-800-250, $p_{nom} = 1.3\ kPa$, $\dot{q}_{nom} = 30\ kW/m^2$)

In order to understand the governing heat transfer mechanisms and wetting dynamics of the evaporation process, the simulation results for the parameters of measurement M01 are analyzed in comparison with the measurement. Simulations were carried out with the standard dewetting model conception of a "receding front" and with the three different approaches for the contact line length l_{cl}, according to Figure 35 and Table 6 in chapter 4.2.3. Figure 40 shows the resulting graphs of the evaporation heat transfer coefficient U_{ev} against the refrigerant mass M_{rf}.

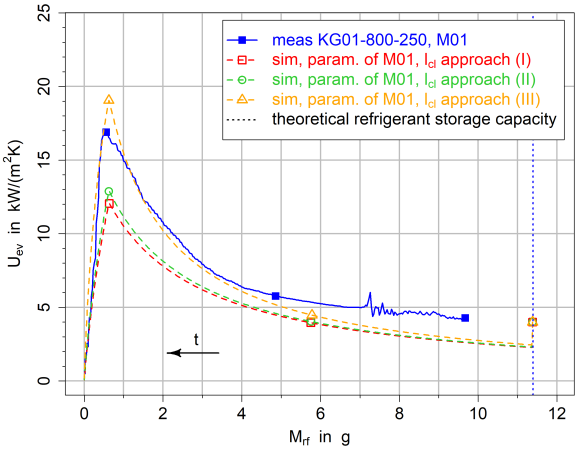

Figure 40: Measured and simulated evaporation heat transfer coefficient vs. refrigerant mass of measurement M01 (sample KG01-800-250; standard conditions: $p_{nom} = 1.3\ kPa$, $\dot{q}_{nom} = 30\ kW/m^2$); receding front model conception; contact line approaches (I), (II), and (III)

Considering the simulated U_{ev} curves, it appears that their general curve shape and quantitative dimensions match the measured data relatively well. This outcome indicates that the actual dewetting phenomena of the experiment might indeed resemble a receding front with a relatively sharp transition between saturated and dry structure section. The standard "receding front" model conception thus appears to be an appropriate approach for sample KG01-800-250 and the considered conditions. However, the agreement quality of the three simulation variants with the measurement differs (which will be discussed later) and there are also some characteristic deviations from the measurement which all simulations have in common: Firstly, the maximum refrigerant mass – which represents the refrigerant storage capacity of the sample – from the measurement (9.7 g) is considerably lower than the simulated ones (11.4 g). While the model presumes a complete saturation of the porous structure with refrigerant as the standard initial state, the structure might have been incompletely filled with refrigerant in the beginning due to insufficient capillary forces. However, another potential factor for the refrigerant mass discrepancy is the observed nucleate boiling during the first minutes of the experiment: Due to bubble formation inside the porous structure it is likely that a certain amount of liquid refrigerant is squirted out of the structure by the emitted vapor. Since this refrigerant mass leaves the structure without being evaporated, it is not covered by the energy balance and causes an error to the plotted relation of U_{ev} vs. M_{rf}. As a consequence, the evaluated maximum refrigerant mass does not necessarily represent the actual refrigerant storage capacity of the sample.

Figure 40 further reveals a considerably lower simulated U_{ev} for all definition approaches of l_{cl} at high refrigerant masses compared to the measurement. The very first data point of the simulations (maximum M_{rf}) is still on a similar level as the measurement's, since it represents the initial condition $U_{ev,init}$ which was fixed to an empiric value of 4 kW/(m²K) (cf. chapter 4.2.4). After this initial value, though, the simulated U_{ev} curves immediately drop to a lower level of about 2.5 kW/(m²K) while the measured curve stays at about 4…5 kW/(m²K) in its initial phase. The presumed reason for this discrepancy at high refrigerant masses is that nucleate boiling increases the heat transfer in this initial period of the measurement while in the model only evaporation from thin refrigerant films is implemented and nucleate boiling is not.

Insight on the heat transfer mechanisms and the dewetting process and on the relevance of the definition of the contact line length can be gained from an analysis of the individual thermal resistances. Figure 41 depicts the resistance contributions of the simulations with approach (I) for the contact line length (intersection lines of horizontal cut – left) and approach (III) (two contact lines along each wire – right). At high and medium refrigerant filling degrees M_{rf} the total thermal resistance of the structure $R_{tot,str}$ (which is directly determines U_{ev} – cf. equation (4-30)) is in both cases clearly dominated by the thermal conduction resistance of the refrigerant-filled structure section R_{rfs} while the resistance of the solder contact R_{sldr} and the resistance of evaporation at the refrigerant front R_{ev} only play a marginal role. Since R_{sldr} is calculated on the basis of certain geometric assumptions and simplifications – as explained in chapter 4.2.3 – its dimension might be subject to inaccuracy. However, the absolute value of R_{sldr} of $4.6 \cdot 10^{-3}$ K/W is very small in relation to $R_{tot,str}$ values in the range of 0.042 K/W to 0.35 K/W (in the linear interval), so that the impact of a potential inaccuracy could probably only become noticeable at relatively low refrigerant masses M_{rf}.

The resistance relations reveal the cause for the increasing slope of the U_{ev} curve with time or with decreasing refrigerant mass: Since the conduction resistance of the refrigerant-filled section, R_{rfs}, is directly proportional to the position of the front h_{front} (cf. equation (4-36), p. 78) and h_{front} in turn to the refrigerant mass M_{rf}, R_{rfs} decreases linearly with decreasing refrigerant mass. The total resistance of the structure, $R_{tot,str}$, follows a similar linear course due to the constant values of R_{sldr} and R_{ev} at elevated

M_{rf} and the dominance of R_{rfs}. Given that the heat transfer coefficient U_{ev} is reciprocal to $R_{tot,str}$ (cf. equation (4-30)), the U_{ev} curve follows a "1/x" shape as long as R_{rfs} predominates heat transfer.

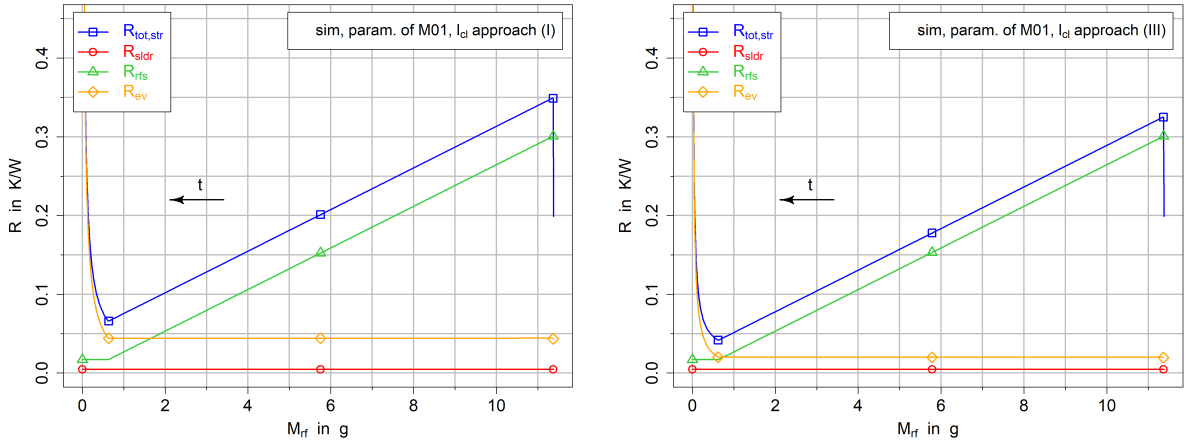

Figure 41: Thermal resistance contributions for parameter set of measurement M01 (geometry of sample KG01-800-250; standard conditions: $p_{nom} = 1.3\ kPa$, $\dot{q}_{nom} = 30\ kW/m^2$); receding front model conception; approach (I) (intersection lines of horizontal cut – left) and approach (III) (two contact lines along each wire – right) for the contact line length

As Figure 40 depicts, both measurement and simulations show a narrow U_{ev} maximum at a refrigerant mass of about 0.6 g and a sharp drop towards zero as the refrigerant mass further decreases. In the model this effect is caused by the presumption that the position of the refrigerant front h_{front} does not continuously decrease to zero but when reaching a threshold height h_{thrsh} it stays constant. The refrigerant mass loss is now assumed to result in a reduction of the filling degree of the pores and an associated proportional shrinkage of the contact line length l_{cl}. According to equation (4-44)) that provokes the evaporation resistance R_{ev} to rise rapidly which can be observed in Figure 41. R_{ev} becomes the governing quantity which causes U_{ev} to drop strongly until all refrigerant is evaporated and U_{ev} approaches zero. This model conception of a transition from a uniformly sinking refrigerant front to a reduction of the contact line length is based on the idea that a refrigerant layer on the sample carrier will not become infinitesimally thin due to surface tension effects. The refrigerant spatially arranges in a way that its free surface energy is minimized which entails that at some point certain parts of the sample's base area fall dry and refrigerant remains only at the energetically favorable places (e.g. intersections of two wires) until the structure dries out completely.

The sharp transition from a moving evaporation front to a reduction of contact line length in the model approach is certainly a simplification of a more complex realistic process. Due to a lack of knowledge on the exact arrangement of menisci and three-phase contact lines in the porous structure, the validity of the threshold height definition as half the clear height of an elementary cell (cf. chapter 4.2.3, equations (4-33) and (4-34)) can generally be questioned. Figure 42 demonstrates that the definition of h_{thrsh} considerably influences the maximum simulated heat transfer coefficient and its corresponding refrigerant mass value. Exemplary alternative definitions for h_{thrsh} of one or a quarter of the clear height of an elementary cell lead to U_{ev} maxima of 13.6 kW(m²K) and 23.8 kW(m²K) compared to 19.1 kW(m²K) for the standard definition. However, as Figure 40 shows, the simulated refrigerant mass at the transition (U_{ev} maximum) based on the standard definition of h_{thrsh} ($M_{rf}(U_{ev,\max}) = 0.62 \ldots 0.64\ g$ for the different l_{cl} approaches) are in fairly good agreement with the measurement ($M_{rf}(U_{ev,max}) = 0.56\ g$). The alternative definitions for h_{thrsh} in contrast lead to less realistic values of $M_{rf}(U_{ev,max}) = 1.27g$ (1 x clear height of elementary cell) and $M_{rf}(U_{ev,max}) = 0.32g$ (0.25 x clear height of elementary cell). Thus, the model implementation of the dryout process with its associated standard definition for the threshold height h_{thrsh} appears to be

a reasonable approach for the standard sample and conditions. Its suitability for different structure geometries and measurement conditions certainly needs to be assessed individually.

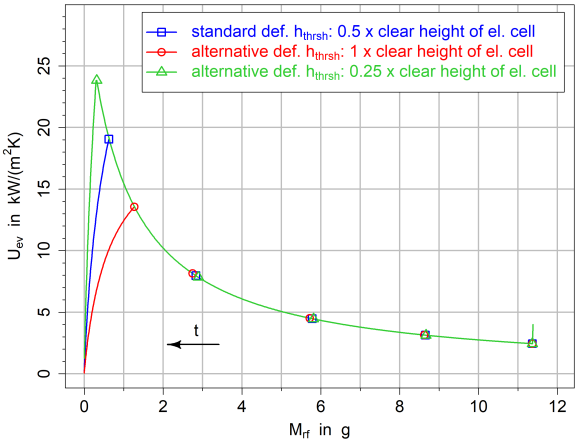

Figure 42: Impact of the definition of the threshold height h_{thrsh} on simulations of the evaporation heat transfer coefficient with parameter set of measurement M01 (geometry of sample KG01-800-250; standard conditions: $p_{nom} = 1.3\ kPa$, $\dot{q}_{nom} = 30\ kW/m^2$); receding front model conception; approach (III) for the contact line length (two contact lines along each wire)

Coming now to the evaluation of the different definitions of the contact line length l_{cl}, Figure 40 and Figure 41 reveal that the simulated heat transfer coefficient is in general quite sensitive on the definition of l_{cl} and that the thermal resistance R_{ev} is not per se negligible, according to the standard model settings. At high refrigerant masses the dominance of the conduction resistance of the refrigerant-filled section R_{rfs} is so pronounced that R_{ev} only plays a marginal role, which leads to a virtual congruence of the simulated U_{ev} curves (Figure 40) despite their different contact line length definitions. At lower refrigerant masses, though, the impact of R_{rfs} decreases with declining height of the evaporation front and the different l_{cl} definitions significantly affect the heat transfer coefficient. For refrigerant masses larger than 0.63 g (front above threshold height h_{thrsh}) the evaporation resistance amounts to 0.044 K/W for approach (I) for the contact line length l_{cl} (intersection lines of horizontal cut), 0.040 K/W for approach (II) (one contact line along each wire), and 0.020 K/W for approach (III) (two contact lines along each wire), as depicted in Figure 41 for (I) and (III). As a result, (I) and (II) produce similar U_{ev} curves with maxima of 12.1 kW/(m²K) and 12.9 kW/(m²K) which are distinctly lower than that of approach (III) with a maximum of 19.1 kW/(m²K). As Figure 40 demonstrates, the simulation with approach (III) for l_{cl} shows the best agreement with the measurement. Except for the nucleate boiling phase at high refrigerant masses and the maximum, its curve nearly coincides with the measured curve, while approach (I) and (II) underestimate U_{ev}. Thus, the model conception (III) for the contact lines (contact lines on both sides of a wire in parallel to its axis) in combination with the simplified resistance definition for R_{ev} (which was adapted from Kim and Chi, as described in chapter 4.2.3, equation (4-44)) appears to be a suitable approach for the considered conditions. However, despite the good accordance it cannot be taken for granted that the model conception for the contact line arrangement exactly mirrors the real circumstances. A different contact line arrangement might lead to the same results and inaccuracies of the resistance definition and contact line definition might potentially compensate for each other. Further analyses on the assessment of the contact line definitions will be presented in chapters 5.4.1 and 5.4.2 in the context of mesh geometry impacts. Still, contact line approach (III) is employed as the tentative standard definition for the simulations in the following chapters.

5.2 Assessment of Measurement Reliability

Aspects of measurement reliability which cannot be easily expressed in form of measurement uncertainties are the repeatability of measurements, the reproducibility of sample manufacturing and the impact of surface properties and sample aging. The repeatability of measurements might be influenced by the uniformity of sample installation and by random variations in the dewetting process. The manual manufacturing process might lead to certain imprecisions of the sample geometry. Despite the pretreatment of the samples, aging effects or other changes of surface properties could alter their evaporation characteristics. In order to assess the relevance of these factors, respective measurement results are evaluated in the following sub-chapters. Measurement uncertainties are not analyzed at this point since they have already been discussed in chapter 4.1.8.

5.2.1 Repeatability of Measurements

Figure 43 shows repeated measurements with the same parameters for sample KG01-800-250 (top-left), KG02-800-250 (top-right), KG09-900-280-15 (bottom-left) and KG10-800-250-090deg (bottom-right).

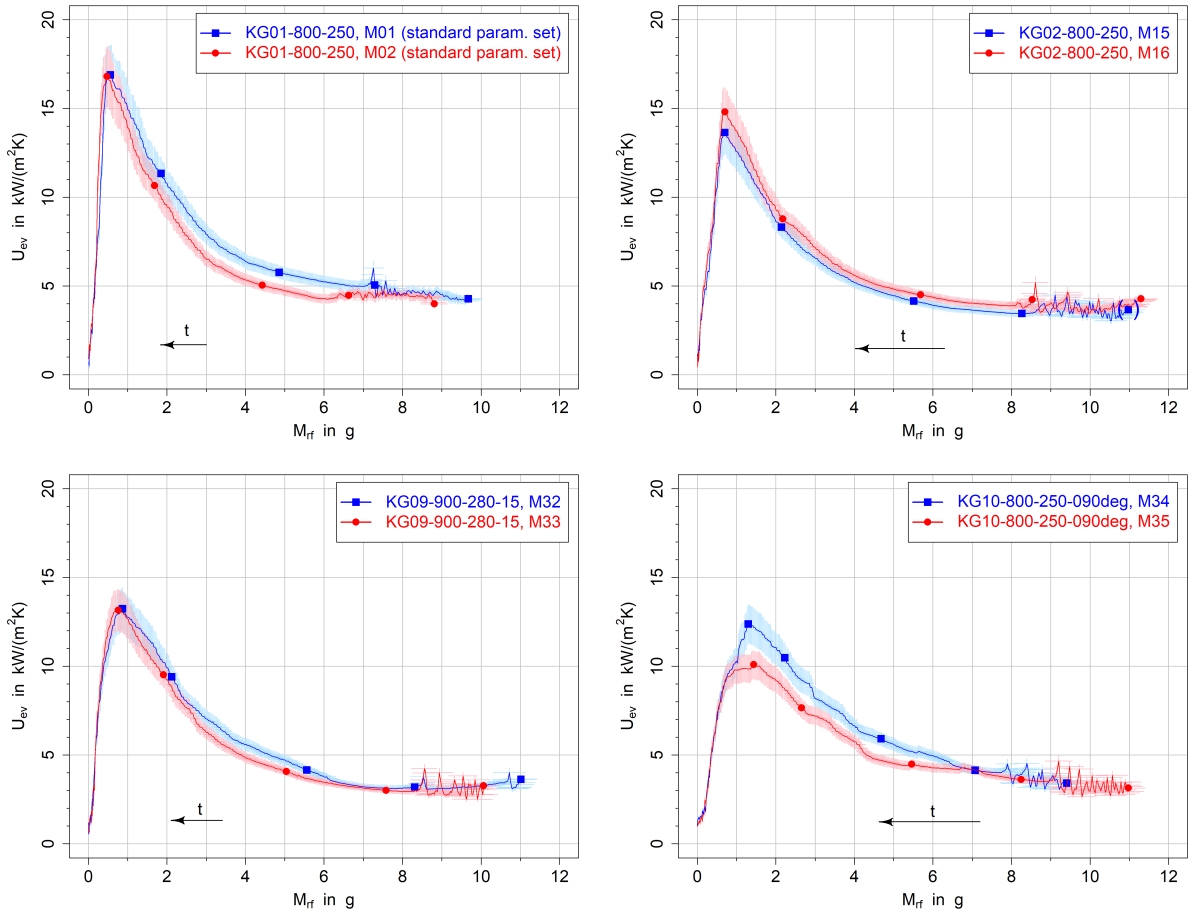

Figure 43: Repeatability of Measurements – Heat transfer coefficient vs. refrigerant mass for repeated measurements with KG01-800-250 (top-left; no re-installation of sample), KG02-800-250 (top-right; re-installation of sample); KG09-900-280-15 (bottom-left; re-installation of sample) and KG10-800-250-090deg (bottom-right; re-installation of sample); standard conditions: $p_{nom} = 1.3\ kPa$, $\dot{q}_{nom} = 30\ kW/m^2$

While the measurements with KG01-800-250 have been carried out successively without new installation of the sample, the sample has been re-installed before each measurement repetition for all other measurements. In case of sample KG01-800-250 the time lag between both measurements was 18 days; for the other measurement pairs only 2 days maximum. A potential impact of sample aging can therefore be widely excluded for samples KG02, KG09 and KG10, whereas for KG01 there might be a certain effect.

As the diagrams illustrate, the uncertainty ranges of the measurements with KG02-800-250 and KG09-900-280-15 overlap throughout the measurement which means that the results are identical within measurement uncertainty, despite the re-installation of the sample before the second measurement. In the measurements with KG10-800-250-090deg the uncertainty ranges of both measurements do mostly not overlap and the maximum heat transfer coefficient of the second measurement (M35) for instance deviates from that of the first (M34) by about -19%. This discrepancy might origin from random effects on the dewetting behavior. However, it cannot be completely excluded either that some kind of unnoticed contamination affected the wettability of the structure in one of the measurements. Aging effects are not very likely since the time lag between both measurements was only one day. Differences in installation conditions are not regarded as a likely reason either since for the samples KG02 and KG09 no such effect has been observed. In the case of sample KG01-800-250 – where the sample was not re-installed before the repeated measurement – both curves coincide within measurement uncertainty at low refrigerant masses but deviate at higher masses. Obviously, the repeatability is not generally better if the installation conditions stay the same.

From the overall picture it can be concluded that the course of the heat transfer coefficient curve can obviously be affected by random differences of the dewetting dynamics to some extent. The intensity of the variations differs, though, and in some cases measurements can be reproduced within measurement uncertainty. Possible minor differences in sample installation conditions do not seem to noticeably influence the measurement.

5.2.2 Reproducibility of Sample Manufacturing

Samples nos. KG01-800-250 (standard sample) and KG02-800-250 were made from identical wire mesh material (cf. Table 2) in order to analyze the potential effect of manufacturing irregularities. In Figure 44 measurement results from both sample specimens under standard conditions ($p_{nom} = 1.3\ kPa$, $\dot{q}_{nom} = 30\ kW/m^2$) are compared. As the diagram shows, all heat transfer coefficient curves lie within a relatively uniform band. Their uncertainty ranges partially overlap for most refrigerant masses and there is no clear trend of a closer agreement of two measurements from one sample specimen than from different specimens. A slightly different behavior of the two samples seems to occur at very low refrigerant masses, shortly before dryout: While the U_{ev} curves of sample KG02 reach their maxima already at a refrigerant mass of about 0.70 g (M15) and 0.71 g (M16), the curves of KG01 only continue down to a refrigerant mass of 0.56 g (M01) and 0.47 g (M02) before they drop towards zero. The evaluated U_{ev} maxima of KG02 are lower with 13.7 kW/(m²K) (M15) and 14.8 kW/(m²K) (M16) compared to 16.9 kW/(m²K) (M01) and 16.8 kW/(m²K) (M01) and the slope of their final drop is smaller. These observations resemble the effect of the modeled threshold height which was discussed in chapter 5.1. According to this conception a transition from the receding front to a reduction of contact line length occurs at a certain threshold height. In the considered measurements a poorer wettability of sample KG02-800-250 might have caused a higher threshold height and consequently an earlier decline of the contact line length and of the heat transfer coefficient. A possible reason for such a difference in wettability might for instance be solder flux residuals at the structure base which could not be removed by the cleaning procedure. The observed differences between the samples at low refrigerant masses are relatively small, though. Therefore the applicability of the suggested hypothesis cannot be regarded as definite.

The actual refrigerant storage capacity ($M_{rf,cap}$) of the samples seems to be another slightly differing factor. The measurements with KG02-800-250 nearly reach the theoretical storage capacity ($M_{rf,th}$) of 11.4 g (even if the exact starting point of M15 is unsure, as marked with brackets), while the curves of KG01-800-250 show maximum refrigerant masses of less than 10 g or even 9 g. This difference might be caused by a varying wettability of the samples but as pointed out before, the accuracy of the storage capacity values can be affected by squirting of refrigerant during nucleate boiling.

Generally, it is deduced from these results that minor differences in sample manufacturing might have a certain effect on the measurement results but the dimensions of this effect seem to be about in the same range as the scattering effect of random dewetting variations.

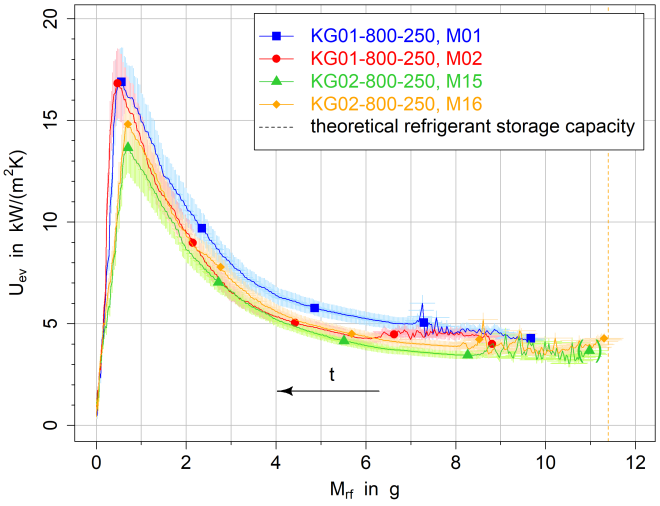

Figure 44: Reproducibility of Sample Manufacturing – Heat transfer coefficient vs. refrigerant mass for samples with identical wire mesh material: KG01-800-250 (M01 & M02) vs. KG02-800-250 (M15 & M16); standard conditions: $p_{nom} = 1.3\ kPa$, $\dot{q}_{nom} = 30\ kW/m^2$

5.2.3 Impact of Surface Properties and Sample Aging

In order to investigate the impact of surface properties and sample aging, several measurements with the standard sample KG01-800-250 were carried out with a time lag of up to 91 days. Figure 45 shows the achieved heat transfer coefficients versus refrigerant charge for measurements no. M01, M02, M03, and M04.

The evaluated refrigerant storage capacities vary between 8.8 g (M02) and 11.2 g (M04) without showing a clear trend. Moreover, the values of M03 and M04 are uncertain due to incomplete drainage at the end of the preparation phase and squirting of refrigerant during nucleate boiling can affect the values. Therefore, the existence of a correlation between storage capacity and sample age cannot be stated.

At high refrigerant filling degrees nucleate boiling – indicated by oscillations in U_{ev} – occurs in all measurements and leads to a virtually congruent plateau value of U_{ev} of approximately 4.5 kW/(m²K). In the last measurement (M04) nucleate boiling continues down to a refrigerant charge of about 5.5 g while it stops earlier in the other measurements. However, this difference might be covered by random variability.

At lower refrigerant filling degrees, in the region of rising U_{ev}, measurements M01 (day 15), M03 (day 74), and M04 (day 106) suggest a slightly subsiding heat transfer coefficient with increasing sample age. However, the differences are mostly within the uncertainty of measurement. Additionally, the uncertainty of the refrigerant mass due to "squirting losses" from nucleate boiling cannot be quantified in the evaluation but needs to be considered as well in this context. Furthermore, measurement M02 (day 33) does not comply with the trend and exhibits a relatively low U_{ev} despite its low sample age. Its slightly different behavior might be caused by the fact that the sample was not newly reinstalled before this measurement as opposed to all other measurements. Anyway, for the reasons stated above no clear trend for the relation of sample age and heat transfer coefficient can be observed for the approximate refrigerant mass range between 1 g and 7 g.

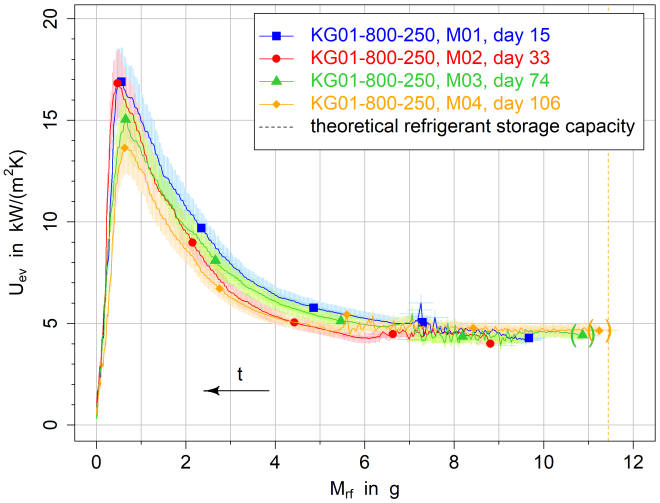

Figure 45: Impact of sample aging – heat transfer coefficient vs. refrigerant mass for sample KG01-800-250 (measurements nos. M01, M02, M03, M04); standard conditions: $p_{nom} = 1.3\ kPa$, $\dot{q}_{nom} = 30\ kW/m^2$

At refrigerant masses of roughly 0.5 g all measurements reach their maximum U_{ev} values. While in the earlier measurements the highest values of 16.9 kW/(m²K) (M01) and 16.8 kW/(m²K) (M02) are reached, a decrease of the maximum value with rising sample age can be found, as the identified maximum for measurement M03 is only 15.0 kW/(m²K) and for M04 only 13.6 kW/(m²K). Taking into account that the drawn error bars in the diagram are partially overlapping, this trend cannot be regarded as totally significant. However, a certain negative impact of sample age on the maximum heat transfer coefficient seems likely which suggests a deterioration of wettability with sample age.

There are several possible causes for a surface change with time: Firstly, the sample's exposure to oxygen and/or water vapor in the ambient air during storage or its contact with water during measurements might have provoked a further oxidation of the copper surface layer or a transformation to a different copper oxide phase – assuming that the surface had not reached a stable oxidation state by the heat treatment. However, according to the information in chapter 4.1.3 and B.3, oxidation should provoke an improved wettability rather than a deteriorated as observed. Another explanation might be the occurrence of other chemical reactions on the copper surface such as formation of copper salt compounds, e.g. in form of sulfates, carbonates or chlorides (Deutsches Kupferinstitut Berufsverband e.V. 2019). Furthermore, the adsorption of gaseous substances on the structure surface and/or its contamination with liquid or solid material might cause an alteration of the surface properties. As an example, volatile organic compounds (VOC) might be emitted by the polymeric sample containers or by construction parts inside the experimental setup and be deposited on the sample surface. Any alteration of chemical or physical surface properties can potentially lead to changes in the interfacial tension with the refrigerant. The consequence

can be changes of the contact line length and the contact angle which affects the constitution of the evaporating film region and thus the evaporation resistance.

The impression that the impact of sample age on heat transfer becomes stronger with decreasing refrigerant filling degree is in accordance with the model conceptions: As discussed in chapter 5.1, the thermal resistance of evaporation does not play a significant role at relatively high refrigerant filling degrees because heat conduction through the refrigerant-filled matrix to the point of evaporation dominates the heat transfer process. Only at very low refrigerant masses the evaporation resistance becomes relevant which includes by definition the wetting characteristics or contact line length. The effect of a modelled reduction of the total contact line length can be seen in Figure 40 which obviously resembles the measured findings on sample aging in Figure 45 in a qualitative way.

Another indication for an effect of surface properties on evaporation characteristics can be found in measurements with sample KG05-850-400: As Figure 46 illustrates, in the first measurement M21 (which was conducted before the actual measurement series) the sample shows a virtually full saturation with refrigerant in the beginning (theoretical refrigerant storage capacity: $M_{rf,th} = 10.5g$), a heat transfer coefficient of around 4 kW/(m²K) in the early phase with nucleate boiling, a strongly increasing slope of U_{ev} with decreasing refrigerant mass and a maximum U_{ev} of approximately 15.8 kW/(m²K).

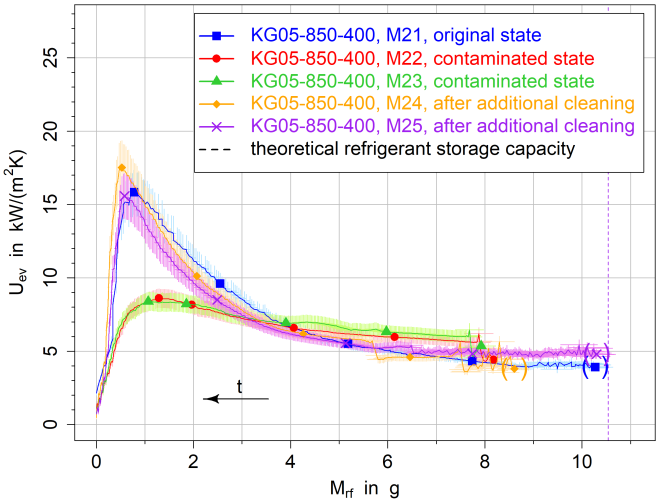

Figure 46: Hypothesized impact of surface contamination – heat transfer coefficient vs. refrigerant mass for sample KG05-850-400 in original state (M21), after crack formation – presumably in contaminated state (M22, M23) and after additional cleaning and sealing (M24, M25); standard conditions: $p_{nom} = 1.3\ kPa$, $\dot{q}_{nom} = 30\ kW/m^2$

After this measurement, a crack formed in the ABS support ring around the sample carrier, which opened up a connection between the drill hole for the sample temperature sensor and the wire mesh structure. Subsequent measurements showed a dramatically different evaporation behavior: The determined refrigerant storage capacities of measurements M22 and M23 of about 8 g were considerably smaller than before. Furthermore, the heat transfer coefficients in the beginning were larger than in the earlier measurements at respective refrigerant filling states but their maxima reached only about factor 2 smaller values than before (8.6 kW/(m²K) for M22, 8.4 kW/(m²K) for M23). This radical change of evaporation dynamics might hypothetically originate from a change of wetting properties caused by a contamination of the mesh surface: Due to the crack in the ABS support ring, oily compounds of the thermally conductive paste in the sensor drill hole might have deposited on the wire mesh structure. The hydrophobic character of the oily paste could thus have deteriorated the wettability of the structure by increasing the macroscopic contact angle, which possibly led to the incomplete saturation with refrigerant. Also, the

declined wettability could have caused a reduction of the contact line length and could thus be responsible for the low heat transfer coefficients. Intrusion of refrigerant into the sensor drill hole and a corresponding distortion of the measurement conditions by means of unscheduled evaporation inside the drill hole is not considered as a likely explanation for the deviating measurement results. Since the temperature sensor is covered with hydrophobic thermally conductive paste, the refrigerant water would probably not be able to enter the drill hole from the crack.

After the altered evaporation dynamics of the possibly contaminated sample KG05-850-400 was confirmed by repeated measurements, the sample was subjected to a cleaning procedure, as described in chapter 4.1.3 and the crack was sealed. Subsequent measurements (M24, M25) mostly yielded identical results to those before the crack formation within uncertainty of measurement (cf. Figure 46). This observation supports the hypothesis of contamination: Presumably, the chosen cleaning procedure succeeded in removing deposited contaminant and could roughly restore the original surface properties of the mesh structure.

From the presented measurement results it can be concluded that surface properties and wettability of the porous structure represent a crucial factor for evaporation dynamics. The suggested thermal pretreatment process can probably not guarantee perfectly stable surface conditions but surface changes might also be caused by ambient conditions during storage. Contamination of the structure needs to be carefully prohibited in order to maintain comparable sample conditions.

5.3 Impact of Process Parameters

5.3.1 Impact of Heat Flux

The impact of applied heat flux $\dot{q}_{nom}$ on the measured evaporation heat transfer coefficient curves is depicted in Figure 47 for two measurement cycles with the same sample (KG01-800-250) at a nominal pressure of 1.3 kPa. At relatively high refrigerant filling degrees the U_{ev} curves with an applied heat flux of 20, 30 and 40 kW/m² show oscillations in both measurement cycles while in the measurements with 10 kW/m² no oscillations can be observed. These oscillations can again be attributed to nucleate boiling which accords with visual observations of the evaporation process. In the very beginning of the experiments (high refrigerant masses) the oscillations in the curves have a very small amplitude or they are not visible at all even if nucleate boiling was visually observed already in the experimental setup. An explanation for these seemingly contradicting observations is the thermal capacity of the sample carrier and mesh structure which acts as a low-pass filter. Supposedly, in the very beginning of the experiment the frequency of bubble formation is rather high so that the temperature fluctuations from bubble formation and detachment are damped by the thermal capacity between structure and temperature sensor. Later on, the frequency decreases which causes the oscillations to be recorded by the temperature sensor. Figure 48 shows the curves of the driving temperature difference between structure base and saturation temperature for both measurement cycles. Similar to Figure 39 in chapter 5.1 nucleate boiling seems to occur above driving temperature differences around 5-6 K, while it fades or does not arise at all below this range. These values are of a comparable dimension as results from Witte (Witte 2016). For sintered copper fiber structures in continuously capillary-assisted evaporation mode, Witte identified required superheat values for the onset of nucleate boiling about 3…8 K for different sample geometries at the same system pressure of 1.3 kPa. The distinctly larger pore sizes of the mesh structures investigated in this work compared to the ones by Witte obviously does not lead to a general increase of the required temperature difference for the onset of nucleate boiling.

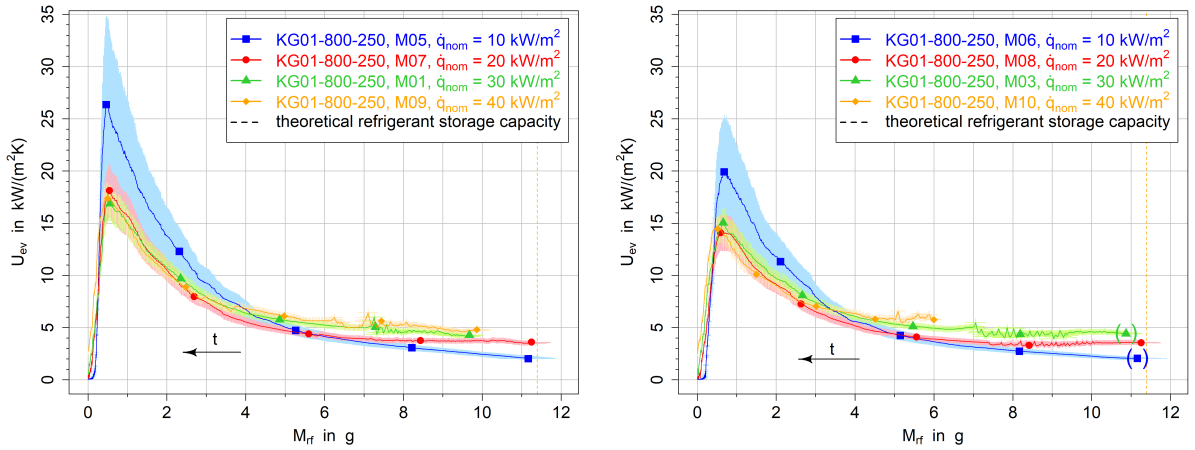

Figure 47: Impact of applied heat flux – heat transfer coefficient vs. refrigerant mass for sample KG01-800-250 at $p_{nom} = 1.3\ kPa$ and varied nominal heat fluxes of $\dot{q}_{nom} = 10/20/30/40\ kW/m^2$; first (left) and second (right) measurement cycle

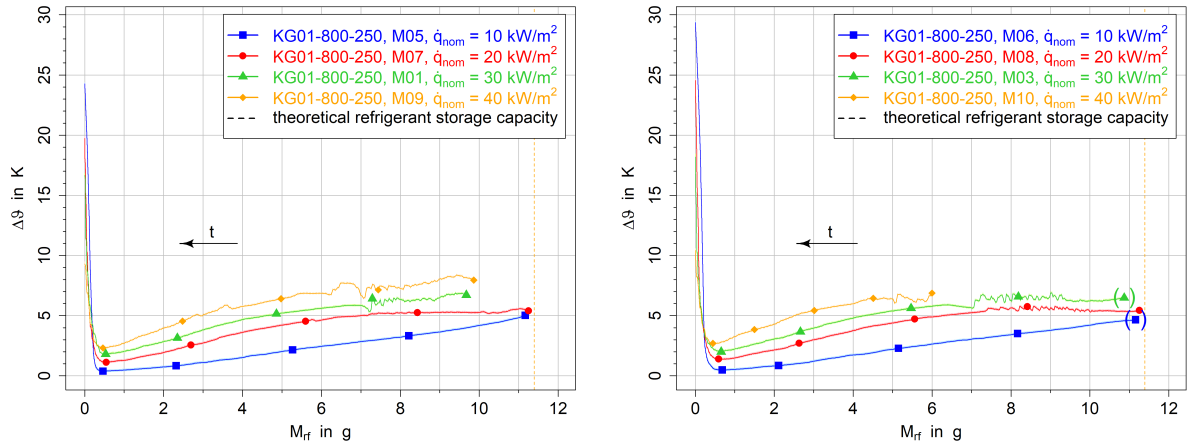

Figure 48: Impact of applied heat flux – driving temperature difference vs. refrigerant mass for sample KG01-800-250 at $p_{nom} = 1.3\ kPa$ and varied nominal heat fluxes of $\dot{q}_{nom} = 10/20/30/40\ kW/m^2$; first (left) and second (right) measurement cycle

The magnitude of U_{ev} during nucleate boiling visibly increases with rising heat flux, as both diagrams in Figure 47 reveal. This observation matches the fundamentals of boiling (cf. chapter 2.2) which state that in the nucleate boiling regime the heat transfer coefficient strongly rises with increasing driving temperature difference or "wall superheat" (Carey 2008).

Figure 47 further suggests an overall trend of decreasing total refrigerant mass with increasing heat flux. While the measurements with a nominal heat flux of 10 kW/m² and 20 kW/m² reach a maximum refrigerant mass of 11.1 g (M05 and M06) and 11.3 g (M07 and M08) which is close to the theoretical storage capacity ($M_{rf,th}$) of 11.4 g, maximum masses of the measurements at higher heat fluxes are mostly considerably lower (except for M03 but this value is unsecure due to incomplete drainage). This effect is ascribed to mass losses due to refrigerant squirting which is more pronounced at elevated heat fluxes due to vigorous nucleate boiling.

Considering the measurement phase at low refrigerant filling degrees, where only evaporation from thin refrigerant films take place, all U_{ev} curves feature the typical shape of increasing slope with decreasing refrigerant mass and a final sudden drop as the mass approaches zero. As pointed out in chapter 5.1, this

shape indicates that wetting and evaporation dynamics mostly comply with the model conception of a receding front. This result adumbrates that the applied heat flux does not have a considerable influence on the general mechanisms of dewetting dynamics.

Despite the similar shape of the curves, their absolute values differ in some points: Firstly, the U_{ev} values of the second measurement cycle are consistently about 2…6 kW/(m²K) lower than in the first measurement cycle. This finding is attributed to deteriorated wetting conditions due to sample aging, as discussed in chapter 5.2.3. Secondly, while at heat fluxes of 20, 30 and 40 kW/m² the curves are congruent within measurement uncertainty and reach a U_{ev} maximum of approx. 17…18 kW/(m²K) (first measurement cycle) and 14...15 kW/(m²K) (second measurement cycle), the evaluated U_{ev} curves for the 10 kW/m² measurements are occasionally more than 50% higher, having their maxima at 26.4 kW/(m²K) (first measurement cycle) and 19.9 kW/(m²K) (second measurement cycle). In the discussion of this observation it must be taken into account that measurement uncertainties for a nominal heat flux of 10 kW/m² are very large, as marked in the diagrams. (Main reason for the large uncertainties is the small temperature difference $\Delta\vartheta$ (cf. Figure 48) which yields high temperature uncertainties relative to the absolute temperature difference. This uncertainty component adds up to the uncertainty of evaporation heat flux $\dot{q}_{ev}$ and both propagate to a relative uncertainty of U_{ev} of up to 32%, as summarized in Table 4, p. 67.) The uncertainty intervals of the 10 kW/m² measurements overlap with those of the other measurements which means that the deviating behavior of the 10 kW/m² measurements can generally not be considered as significant. However, the recorded higher values of the 10 kW/m² measurements might also have a physical origin:

As pointed out in chapter 2.3, several authors observed a dependence of the heat transfer coefficient from the applied heat flux in thin film evaporation experiments. Wong and Chen found a decreasing heat transfer coefficient with increasing heat flux in experiments with groove-wicked flat-plate heat pipes (Wong and Chen 2013). Similarly, experimental results of Seiler et al. on evaporation from partially flooded copper tubes with porous coating reveal a decreasing heat transfer coefficient with increasing heat flux (Seiler et al. 2019). In both cases, this behavior is attributed to the occurrence of partial dryout effects at high heat fluxes, as the high vapor mass flow rates cannot be compensated by continuous capillary pumping anymore due to increasing pressure drop in the porous structure.

The presented measurement results in Figure 47 do not suggest the occurrence of any dryout phenomena until the evaporation front reaches a critical height and the U_{ev} maximum is reached. Due to the unsteady character of the measurements and the absence of a continuous refrigerant supply, flow limitations within the porous structure are not to be expected. As discussed in the analysis of evaporation and wetting dynamics in chapter 5.1, the whole cross-sectional area of the sample is assumed to be wetted and the contact line length at the evaporation front is supposed to be constant for all refrigerant masses above $M_{rf}(U_{ev,max})$. Still, a difference in U_{ev} curve of the measurements with a heat flux of 10 kW/m² already occurs in this interval. Therefore, a partial dryout is not a satisfying explanation for the apparent impact of heat flux on heat transfer coefficient within this work.

As mentioned in chapter 2.3, Xia et al. conducted steady-state evaporation measurements with partially-flooded finned tubes and refrigerant water (Xia et al. 2008). They also found a decrease of the overall evaporation heat transfer coefficient with increasing driving temperature difference which corresponds to an increasing heat flux. As an explanation for this dependence they argue that with increasing heat flux the share of the heat flux which is transferred via the macroscopic meniscus (in contrast to the evaporating thin film region) increases and that this heat transfer through the macroscopic part of the meniscus is less efficient. Comparable observations were made by Crößmann (Crößmann 2016): His thin-film evaporation measurements from different microchannel geometries suggest a decreasing heat transfer coefficient with increasing heat flux as well. Crößmann ascribes this finding to an increase of the film thickness in the

evaporating thin film region, caused by the intensified inward liquid flow. Correspondingly, the conduction resistance of the thin film is increased and the local heat transfer coefficient decreases. Besides film thickness, Crößmann states the dependence of thermophysical properties on heat flux conditions as a potential origin of the effect.

Interestingly, both Xia et al. and Crößmann report a non-linear relation of heat flux (driving temperature difference) and heat transfer coefficient, and a gradual fading of the heat flux impact with increasing heat flux. This finding is in accordance with the adumbrated trend in Figure 47: For higher heat fluxes (20 / 30 / 40 kW/m²) no significant difference in U_{ev} can be detected but for the lowest heat flux of 10 kW/m² a higher heat transfer coefficient becomes noticeable. Converting the presented driving temperature differences from Xia et al. to heat flux values, it can be deduced that for most tube specimens the dependence of heat transfer coefficient from heat flux becomes negligible for heat fluxes greater than approximately 15-20 kW/m². Even if the different sample geometries, configurations, process conditions and definitions of the evaluated quantities impede a direct comparison, this apparent threshold matches very well the detectability threshold of a heat flux dependence in this work which might be an indicator for a universal relation.

In terms of transferability of the investigations of Wong and Chen (Wong and Chen 2013), Seiler et al. (Seiler et al. 2019), Xia et al. (Xia et al. 2008) and Crößmann (Crößmann 2016) to this work, it must be taken into account that the experiments of the aforementioned authors are all conducted under steady-state conditions, and all except Seiler et al. address menisci in channel-shaped structures instead of porous structures. In their setups a continuous feed flow of liquid refrigerant counterbalances the evaporating mass flow which allows a stable evaporation process (except for oscillations observed in (Wong and Chen 2013) and except for dryout incidents). In contrast, the experiments described in this work refer to menisci in porous structures under dynamic conditions without a continuous refrigerant feed. The shape of the menisci will be irregular due to the non-homogeneous "wall" morphology and it will change dynamically. As a consequence, the heat transfer mechanisms described by the abovementioned authors are not per se transferable to the experiments of this work. However, the described findings might still be applicable to this work to some extent since the sensitivity of the evaporation process to morphology and dynamics is unsettled. Overall, a change of meniscus shape with a thinner refrigerant film in the evaporating thin film region and the impact of altered thermophysical properties of the refrigerant are considered as a plausible reason for the increased heat transfer coefficients of the measurements with lowest applied heat flux within this work.

As regards the evaporation model, the definitions of thermal resistances do not include any heat-flux-dependent or directly temperature-dependent quantities, such as meniscus shape, dry-out effects etc., except for the minor temperature impact on thermophysical properties (density, thermal conductivity) of the refrigerant. Consequently, simulations for different heat flux settings do not reflect any noticeable impact of heat flux on the evaporation heat transfer coefficient and the respective curves virtually coincide.

5.3.2 Impact of Vapor Pressure

With the standard sample KG01-800-250 measurements at three different vapor pressure levels of 1.0, 1.3 and 1.6 kPa – which corresponds to saturation temperatures of approx. 7.0°C, 10.9°C, and 14.0°C – were conducted at a constant nominal heat flux of 30 kW/m² (cf. measurement parameters in Table 3). Figure 49 illustrates the dynamic heat transfer coefficient U_{ev} against the refrigerant mass charge of the sample M_{rf} for two measurement cycles.

As in the measurements discussed before, the typical oscillations on a stable U_{ev} plateau caused by nucleate boiling can be observed again in the range of higher refrigerant masses. Following a consistent trend, the level of the plateau increases with pressure. The magnitude of the differences between the U_{ev} levels is partially within measurement uncertainty. However, the perceived trend is regarded as significant as it accords with the thermodynamic principles of nucleate boiling and experimental results of numerous publications: As explained in chapter 2.2, pressure conditions affect several thermophysical properties of the refrigerant water which are relevant for the evaporation process, as vapor density, surface tension and the slope of the vapor pressure curve. These properties for instance influence the bubble formation mechanism in the nucleate boiling regime: According to Giraud and Raben et al., the critical site radius required for bubble formation increases with reduced pressure (Giraud 2015a) which means that at a given wall superheat the number of active nucleation sites is reduced as the system pressure decreases (Raben et al. 1965). Since the frequency of bubble departure is directly related to the heat transfer coefficient as a fact of boiling fundamentals (Carey 2008), the heat transfer coefficient rises as the system pressure rises in the nucleate boiling regime under low pressure conditions. Giraud additionally emphasizes the relevance of the slope of the vapor pressure curve which gradually reduces with decreasing pressure (cf. Figure 74 in the appendix). The small slope at low pressures involves that the hydrostatic pressure of a small refrigerant column can already provoke a relevant increase of the local saturation temperature within the refrigerant bulk which can lead to subcooled conditions in certain vertical sections of the liquid. In effect a low pressure again hinders bubble formation and thus negatively influences the heat transfer coefficient. A more detailed explanation of these circumstances can be found in chapter 2.2.

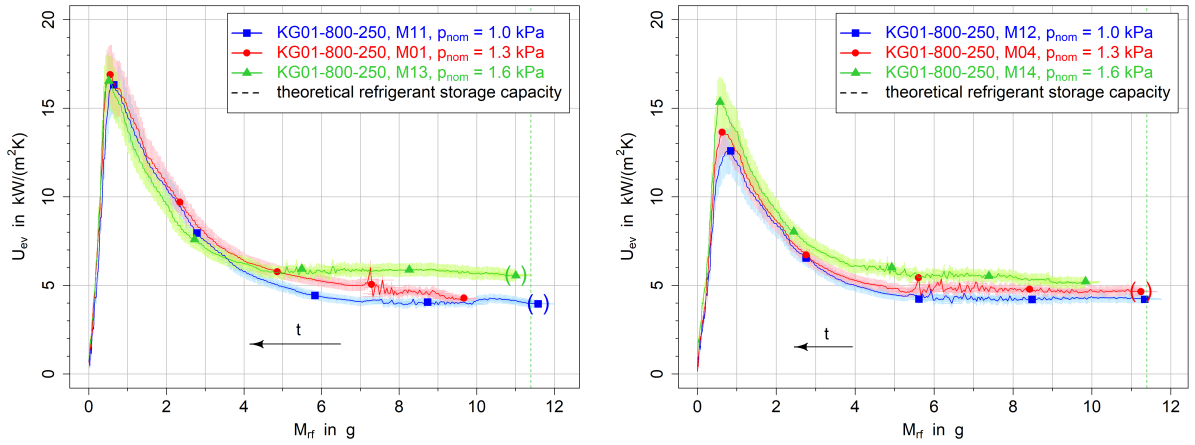

Figure 49: Impact of vapor pressure – heat transfer coefficient vs. refrigerant mass for sample KG01-800-250 at $\dot{q}_{nom} = 30\ kW/m^2$ and varied nominal pressures of $p_{nom} = 1.0/1.3/1.6\ kPa$; first (left) and second (right) measurement cycle

At refrigerant masses about 5-7 g in the first cycle and about 4-5.5 g in the second cycle the oscillations fade and with reducing mass the U_{ev} curves turn into an increasing course. The slope of the curves becomes bigger in direction of a reducing mass until the U_{ev} maximum is reached at a refrigerant mass of approximately 0.5-1.0 g. In this period of thin-film evaporation the curves of different pressures converge into an identical course within uncertainty of measurement. Only in a small interval around the maximum and only in the second measurement cycle the curves diverge again (with overlapping uncertainty intervals), reaching a higher maximum U_{ev} with increasing system pressure.

Considering the congruence of U_{ev} in most of the thin-film evaporation period, the system pressure does apparently not have a significant impact on the heat transfer coefficient during this phase. Several authors who conducted experiments on evaporation from thin films or menisci, however, did notice a positive

impact of an increased pressure (saturation temperature) on heat transfer, as pointed out in chapter 2.3. Xia et al. (Xia et al. 2008), Crößmann (Crößmann 2016) and Seiler et al (Seiler et al. 2019) similarly found an increase of the refrigerant-side or overall heat transfer coefficient for a rising saturation temperature or system pressure for different evaporator types, refrigerants and parameter settings. They all ascribe these observations to an alteration of thermophysical properties of the refrigerant (and if applicable also those of the heat transfer fluid), especially to the increase of vapor density and liquid thermal conductivity, and the decrease of viscosity, surface tension and enthalpy of vaporization with increasing (saturation) temperature. Xia et al. for instance presume this change of thermophysical properties to cause a promoted evaporation mass flux and improved refrigerant flow conditions in the meniscus.

The suggested reason why a dependence from system pressure cannot distinctly be observed in the thin-film evaporation period within this work – in seeming contradiction to literature statements – is that heat conduction through the refrigerant-filled porous structure section (R_{rfs} in the model) dominates this period: Just like the standard measurement discussed in chapter 5.1, the measurements at higher and lower pressure show the same typical U_{ev} curve shape which suggest wetting dynamics that are primarily determined by a downward-moving refrigerant front. As pointed out in chapter 5.1, the thermal resistance of heat conduction through the refrigerant-filled structure matrix is the limiting factor of heat transfer in most of the time of this kind of evaporation process. Only as the evaporation front approaches the structure base and the refrigerant mass approaches zero, the resistance of evaporation from the meniscus becomes more relevant. Consequently, only in this last period of the measurements, at small refrigerant masses, the pressure dependence – which affects the refrigerant in the meniscus but not the thermal conductivity of the structure – can have an impact on the heat transfer coefficient. In the second measurement cycle such a pressure dependence actually seems to become manifest in the U_{ev} maxima which decrease with reducing pressure. This effect could be explained by the altered thermophysical properties of the refrigerant as pointed out above. In the first cycle, though, no pressure dependence can be observed for the U_{ev} maxima. An explanation for this discrepancy between the two cycles might be a change of surface properties: All measurements of the second cycle were done roughly three months after the first cycle (cf. Table 3), and as discussed in chapter 5.2.3 alteration of surface properties due to sample aging can have a noticeable effect on the overall heat transfer coefficient. Since U_{ev} maxima generally decreased from first to second cycle, it is assumed that sample aging provoked a deterioration of wettability. Such an impaired wettability might be associated with a changed meniscus shape in terms of an increased contact angle and larger film thickness in the evaporating thin film region and also with an earlier reduction of contact line length or earlier dryout, respectively. A reduction of system pressure is expected to increase the contact angle and deteriorate general wetting conditions as well since surface tension increases. As a consequence, possibly the hydrophilic character of the surface in the first measurement cycle leads to low contact angles and extended evaporating thin film regions, so that a small rise of contact angle for low pressures does not cause a relevant effect. In the second cycle an increased contact angle due to sample aging could make the system more sensitive to a further contact angle rise caused by a low pressure. This superposition of both effects might explain why a pressure dependence of the heat transfer coefficient can only be observed for the aged samples in the second measurement cycle.

Despite the hypothesized deterioration of wettability with decreasing system pressure, a systematic reduction of the refrigerant storage capacity cannot be deduced from Figure 49. All calculated capacity values are within 85…100% of the theoretical storage capacity ($M_{rf,th}$) but due to incomplete drainage in the preparation phase of some measurements, their respective capacity values (marked with brackets in the diagram) are not reliable. Consequently, no trend for a pressure impact on storage capacity can be determined.

Except the minor pressure influence on thermophysical properties (liquid refrigerant density, liquid thermal conductivity, enthalpy of vaporization, specific heat capacity), the model does not include a direct

dependence on pressure in any resistance definitions. A description for nucleate boiling is not implemented in the model either, therefore the measured differences of the heat transfer coefficient at high refrigerant masses cannot be reproduced by the model. Given that the sensitivity of the resistance definitions on the temperature-dependence of thermophysical properties is very small, simulations at different pressure levels yield virtually identical U_{ev} curves.

5.4 Impact of Structure Geometry

5.4.1 Impact of Porosity

Measurement Results

To study the impact of structure porosity on evaporation dynamics, three samples with different porosities of 84.5% (KG05-850-400), 90.7% (KG01-800-250) and 93.8% (KG06-800-200) and similar pore sizes (clear mesh widths of 0.85 mm for KG05, 0.80 mm for KG01 and KG06; cf. Table 2) are compared by means of the measurements no. M24, M01, M26, M25, M03, M27 (cf. Table 3). All measurements were conducted at standard conditions ($p_{nom} = 1.3\ kPa$, $\dot{q}_{nom} = 30\ kW/m^2$). As mentioned in chapter 4.1.3, the porosity values were not measured but calculated from the geometry specifications of the wire mesh. The resulting dynamic evaporation heat transfer coefficient U_{ev} is plotted against the time-dependent refrigerant mass charge M_{rf} in Figure 50 for the first (left) and second (right) measurement cycle.

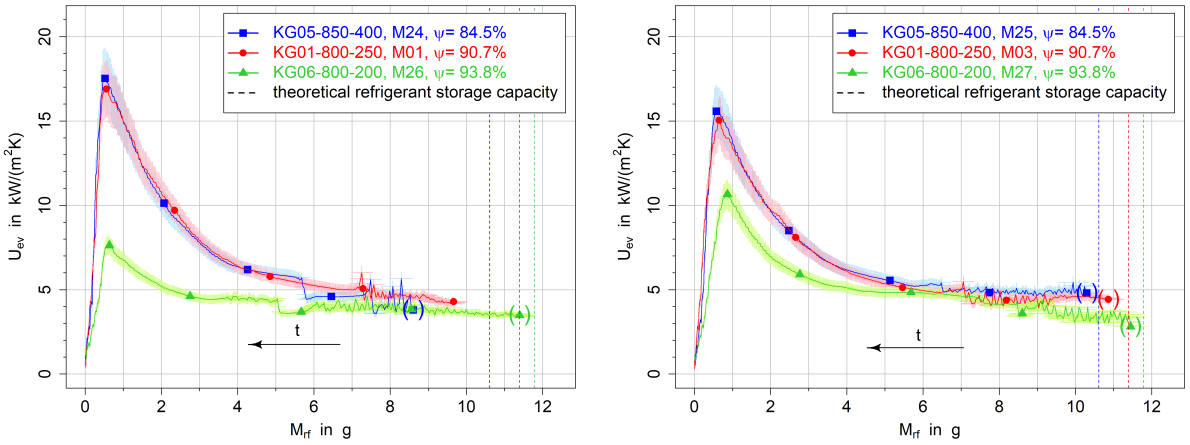

Figure 50: Impact of porosity – measured heat transfer coefficient vs. refrigerant mass for samples KG05-850-400 ($\psi = 84.5\%$), KG01-800-250 ($\psi = 90.7\%$), and KG06-800-200 ($\psi = 93.8\%$); standard conditions: $p_{nom} = 1.3\ kPa$, $\dot{q}_{nom} = 30\ kW/m^2$; first (left) and second (right) measurement cycle

In the nucleate boiling phase at higher refrigerant masses – recognizable by the oscillations – the U_{ev} plateau appears to increase slightly with decreasing porosity in the second cycle. However, this trend is mostly within the uncertainty of measurement, furthermore it cannot be observed in the first cycle. Therefore, porosity is not considered to have a significant effect in the nucleate boiling phase for the investigated porosity range.

In the thin-film evaporation period (at lower refrigerant masses) the U_{ev} curves of the sample with 84.5% (KG05-850-400) and 90.7% (KG01-800-250) porosity are congruent within measurement uncertainty in

both cycles, including their maximum values of approx. 17-18 kW/(m²K) (first cycle) and 15-16 kW/(m²K) (second cycle). In the interpretation of these measurements, it should be considered that sample KG05-850-400 was presumably subjected to contamination which caused an alteration of surface properties, as pointed out in chapter 5.2.3. However the presented measurements of KG05 in Figure 50 are supposedly not affected by this alteration, since measurements M24 and M25 were conducted after the cleaning procedure which evidentially allowed a restoration of the original surface properties of the sample. The sample KG06-800-200 with the highest porosity value of 93.8% only achieves considerably lower U_{ev} values than the samples with lower porosities. In the first measurement cycle a maximum U_{ev} of about 7.6 kW/(m²K) is reached, in the second cycle 10.6 kW/(m²K). These small values and especially their large difference cannot be completely attributed to the low porosity but are partially ascribed to a negative impact of surface contamination on wettability. In retrospect it turned out that the hardening process of the adhesive between sample carrier and ABS support ring had obviously not taken place properly so that during or before the first measurement the adhesive swelled which damaged its sealing function. Either the adhesive itself or leaking thermally conductive paste from the temperature sensor's hole seemed to have contaminated the surface of the mesh structure. It is presumed that the contamination lead to a reduction of contact line length and / or to an unfavorable meniscus shape in the evaporating thin film region which contributed to a diminished heat transfer coefficient. The impact share of contamination and of high porosity on the low U_{ev}, however, cannot be specified. The increased U_{ev} curve in the second measurement cycle suggests that the effect of contamination was reduced in the second cycle.

In the measurements with KG05 and KG01 a clear decrease of the maximum heat transfer coefficient from the first to the second measurement cycle can be observed. This finding matches the supposed negative impact of sample aging on surface wettability of the structure and on evaporation performance, as discussed in chapter 5.2.3.

Simulation Results

Simulated heat transfer coefficient curves are displayed against the measurement results in Figure 51. The simulations are based on the "receding front" model approach, approach (III) for the definition of the contact line length (two contact lines along each wire, cf. Figure 35) and on the respective parameters of measurements M24, M01, M26, M25, M03, M27.

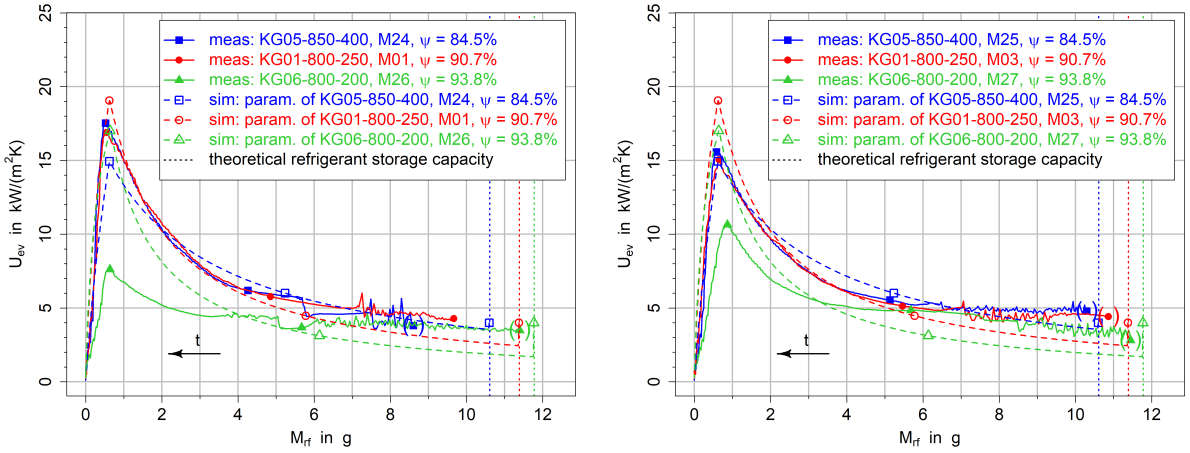

Figure 51: Impact of porosity – comparison of measured and simulated heat transfer coefficient vs. refrigerant mass for samples KG05-850-400 ($\psi = 84.5\%$), KG01-800-250 ($\psi = 90.7\%$), and KG06-800-200 ($\psi = 93.8\%$); standard conditions: $p_{nom} = 1.3\ kPa$, $\dot{q}_{nom} = 30\ kW/m^2$; receding front model conception; contact line approach (III); first (left) and second (right) measurement cycle

In the range of elevated refrigerant masses (approx. above 2 g) the simulated U_{ev} curves show a clear trend of increasing thermal transmittance with decreasing porosity, in contrast to the measurement results. At lower refrigerant masses the relations of the simulated curves change and the structure with medium porosity (KG01) reaches the highest U_{ev} maximum, followed by KG06 with highest porosity and KG05 with lowest porosity. The reason for these particular results – which is not very obvious – is the transition from a clear predominance of the conduction resistance of the refrigerant-filled section of the structure (R_{rfs}) (at large refrigerant masses) to conditions with roughly equal influence of R_{rfs} and of the evaporation resistance (R_{ev}) (at low refrigerant masses), as explained in chapter 5.1. According to its definition in equation (4-36), R_{rfs} is directly dependent on the structure's porosity via the effective thermal conductivity of the structure (cf. equations (4-38) and (4-39)). Consequently, the greatest matrix mass (lowest porosity) of KG05 involves the lowest R_{rfs} and thus the highest U_{ev} at large refrigerant masses, followed by KG01 and then KG06. At low refrigerant masses, though, KG06 profits from a low R_{ev} of about 0.016 K/W due to its small wire diameter and extended contact line length for approach (III) – as can be understood from equation (4-44) – while having the disadvantage of a high R_{rfs}. KG01 has a slightly higher R_{ev} of about 0.021 K/W but a considerably lower R_{rfs}. KG05 finally has a high R_{ev} value of 0.037 K/W which cannot fully be compensated by its small R_{rfs}. In sum these relations lead to the lowest total resistance for KG01 at low refrigerant masses and accordingly the highest U_{ev} maximum for KG01 in the simulations, followed by KG06 and then KG05.

Impact of Porosity in Simulations vs. Measurements

Comparing the outcomes from measurements and simulations in regard to the impact of porosity, there are obviously considerable inconsistencies and contradictory conclusions might be drawn. Given that the general curve shapes of the simulations resemble those of the measurements, it can be assumed that the model conception of a "receding front" is basically close to reality for the presented parameters. In that case porosity should have a certain impact on U_{ev} at least at elevated refrigerant masses due to the conduction resistance of the refrigerant-filled section (R_{rfs}) – as reflected by the simulations. The measurement results of KG05 and KG01, however, nearly coincide despite different porosities. A possible explanation for these circumstances might be manufacturing inaccuracies related to the wire mesh. Such inaccuracies in terms of wire diameter and clear mesh width would implicate uncertainty to the calculated nominal porosity values. Since the porosity is incorporated in the calculation of R_{rfs} – which dominates evaporation most of the time – an altered porosity leads to a shift of U_{ev} in all refrigerant mass ranges. As an example, for sample KG05-850-400 (nominal clear mesh width $w_{mesh} = 850\ \mu m$, nominal wire diameter $d_{wire} = 400\ \mu m$) an inaccuracy of clear mesh width of +170 µm (= +20%) and an additional inaccuracy of the wire diameter of -80 µm (= -20%) from the specified values would lead to a calculated porosity of 89.5% compared to the nominal 84.5%. Since this exemplary porosity value is quite close to the 90.7% of sample KG01, the simulated curve for KG05 with manufacturing inaccuracies would draw nearer to that for KG01. Manufacturing inaccuracies are thus considered as a possible reason for the virtually identical measured U_{ev} curves of KG05 and KG01 at elevated refrigerant masses despite their different nominal porosities. However, only rather high deviations of 20% both for wire diameter and clear mesh width could explain the measurement results.

Influence of Resistance Definitions on Simulation Results

At low refrigerant masses the simulation results considerably diverge from the measurements as well. A hypothesis for this discrepancy is that the model overestimates the evaporation resistance (R_{ev}) while underestimating the solder resistance (R_{sldr}). As pointed out before, the simulated U_{ev} curves in that interval are strongly influenced by geometry characteristics of the structure via the evaporation resistance R_{ev}, which is obviously not realistic. This overestimation of the geometry impact indicates that R_{ev} dominates the total resistance to an unrealistic extent and that consequently equation (4-44) produces too

high R_{ev} values. The reason might be a general inadequateness of the R_{ev} approach adapted from Kim (Kim et al. 2003) and Chi (Chi 1976) which originally applies to evaporation from menisci in straight channels (cf. equations (4-42) and (4-43), Figure 34). Another possible explanation is an underestimation of the contact line length by approach (III) (cf. equation (4-49), Figure 35). The evaporation front could for instance be less sharp than assumed but might include a certain vertical region with thin refrigerant films and extended contact lines, similar to the conception of film flow by Laurindo and Prat (Laurindo and Prat 1998) which is described in chapter 2.6 and visualized in Figure 11. Estimating the capillary number Ca for the applicable process conditions according to equation (2-7) (with the front velocity as characteristic velocity) yields a value of about $1.7 \cdot 10^{-9}$ – which according to Laurindo and Prat fulfills the requirements for liquid flow in the roughness of the pore walls. An underestimation of the solder resistance (R_{sldr}), on the other hand, might origin from inaccurate geometry presumptions for the solder contacts (cf. chapter 4.2.3) or from the presumption that the line-shaped cutting edges of the wires are in direct contact with the sample carrier.

Assuming that the model actually overestimates R_{ev}, a reduced R_{ev} would lead to a lower total resistance and consequently to an overestimation of the U_{ev} values in comparison to the measurement results. Assuming further that the solder resistance R_{sldr} is underestimated, a higher R_{sldr} could evoke a reduction of U_{ev} independently of the respective structure geometry and thus counterbalance the effect of a decreased R_{ev}. Figure 52 illustrates the simulation results for modified resistance definitions. R_{ev} was exemplarily reduced to 20% of the original definition and R_{sldr} was increased to 600% of the original definition. The resulting graphs show that the strong geometry impact via R_{ev} at low M_{rf} could be reduced and that the U_{ev} maxima now follow the order of the structure porosities. These relations are in better agreement with the measurements than the original definitions which supports the hypothesis.

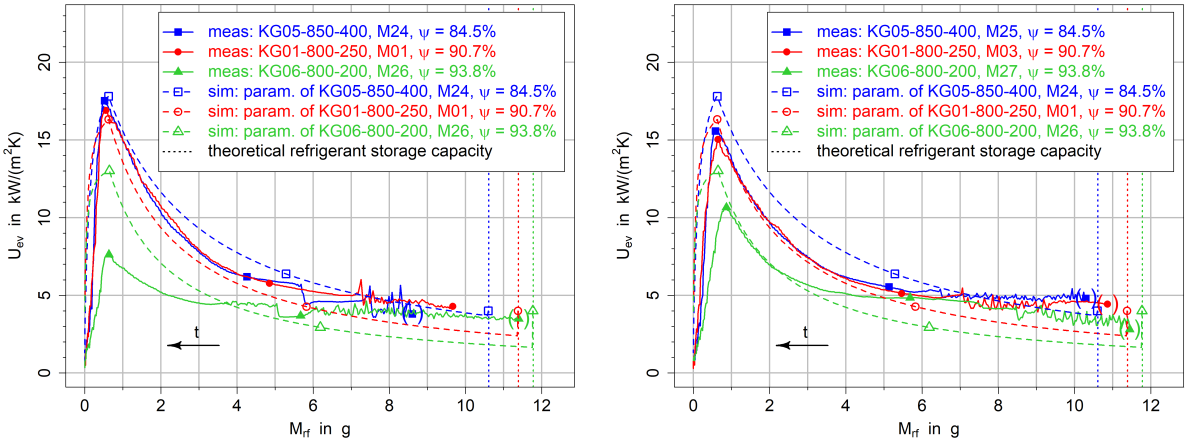

Figure 52: Impact of porosity with modified model resistance definitions – comparison of measured and simulated heat transfer coefficient vs. refrigerant mass for samples KG05-850-400 ($\psi = 84.5\%$), KG01-800-250 ($\psi = 90.7\%$), and KG06-800-200 ($\psi = 93.8\%$); standard conditions: $p_{nom} = 1.3\ kPa$, $\dot{q}_{nom} = 30\ kW/m^2$; receding front model conception; contact line approach (III); reduction of R_{ev} to 20% and increase of R_{sldr} to 600% of original definitions; first (left) and second (right) measurement cycle

Conclusions on Porosity Impact and Comparison with Literature

Summarizing the results on porosity impact, no consistent trend for a dependency of the heat transfer coefficient from porosity can be derived from the measurements. Manufacturing inaccuracies might have promoted the very similar results of sample KG05-850-400 and KG01-800-250, and due to a supposed

contamination of sample KG06-800-200 a distinct interpretation of those results was impeded. Nevertheless, the existence of a general porosity dependence is presumed for a wide refrigerant charge interval. Reason for this presumption is that the model conception of a receding front generally appears to be appropriate for describing evaporation and dewetting dynamics and that this conception implies the relevance of porosity. Simulations accordingly suggest a clear porosity dependence of the heat transfer coefficient for elevated refrigerant filling degrees. As presented in chapter 2.4, published research results on the evaporation from porous structures come to different conclusions in terms of a porosity impact: Li and Peterson found a slight improvement of the heat transfer coefficient for a reduced porosity and ascribe this effect to a small increase of the effective thermal conductivity of the porous structure (Li and Peterson 2006). This argumentation matches the suggested porosity impact of this work, however, it must be taken into account that the investigated geometries and evaporation conditions of Li and Peterson differ distinctly from those of this work. Lanzerath et al. on the contrary report that a reduced porosity has a negative effect on evaporation performance for their investigated porously coated evaporator tubes (Lanzerath et al. 2016), and Pialago et al. suppose similar relations (Pialago et al. 2020). In their case, though, a continuous refrigerant feed to the porous structure by capillary forces is maintained and the porosity effect is accordingly attributed to a stronger limitation of liquid flow at low porosities due to an increased pressure drop. Since in this work evaporation is not carried out under steady-state conditions, the porosity effect caused by a flow limitation does not apply here.

Despite the general agreement of the simulated curve shapes with the measurements, the implemented model definition of the evaporation resistance R_{ev} (cf. equation (4-44)) and its dependence from geometry parameters and from the definitions for the contact line length does obviously not mirror the realistic behavior in a satisfactory way. It is hypothesized that the model overestimates the evaporation resistance (R_{ev}) while underestimating the solder resistance (R_{sldr}) and accordingly modified resistance values lead to a better agreement with the measurements.

Furthermore, the observed outcomes of measurements and simulations support the conclusion that surface properties and wetting / dewetting characteristics crucially determine the evaporation dynamics.

5.4.2 Impact of Pore Size

Measurement Results

Measurements M17, M01, M19 (and in a second cycle M18, M03, M20; cf. Table 3) were carried out with the samples KG03-375-140, KG01-800-250 and KG04-2500-1000, which exhibit distinctly different clear mesh widths w_{mesh} of 0.375 mm, 0.8 mm, 2.5 mm (cf. Table 2). As stated in chapter 4.1.3 the clear mesh width w_{mesh} is used for characterizing the pore size of the structure. The estimated porosity values of the samples are in a comparable range with 88.7% (KG03), 90.7% (KG01), 87.2% (KG04).

Figure 53 shows the heat transfer coefficients of the measurements, plotted against the refrigerant mass in the porous structure. In the measurements with sample KG01 the characteristic oscillations of nucleate boiling can be observed again at higher refrigerant filling degrees, as discussed before. For KG03 (smallest pores) and KG04 (largest pores) such oscillations cannot be seen but the curves also start at U_{ev} values around 5 kW/(m²K) and with a small slope, coming from the initial maximum refrigerant charge. After the nucleate boiling phase U_{ev} rises with decreasing refrigerant mass in all measurements, reaches a maximum and finally drops sharply to zero. The U_{ev} maxima clearly increase with decreasing pore size: While sample KG04-2500-1000 ($w_{mesh} = 2.5\ mm$) reaches maximum values of 10.7 kW/(m²K) (M19) and 7.1 kW/(m²K) (M20), the maxima of KG01-800-250 ($w_{mesh} = 0.8\ mm$) amount to 16.9 kW/(m²K) (M01) and 15.0 kW/(m²K) (M03), and the ones of KG03-375-140 ($w_{mesh} = 0.375\ mm$) to 23.2 kW/(m²K) (M17) and 27.8 kW/(m²K) (M18). While the curves of KG01 from the first and second measurement cycle are

mostly identical within measurement uncertainty, the curve pairs of KG04 and KG03 show pronounced deviations which indicates a relatively poor reproducibility of measurements for these samples. In case of KG04 the poor reproducibility might result from an incomplete drainage of the refrigerant column in the preparation of measurement M20. Possibly the wetting conditions of the structure changed during the involuntarily partially-flooded phase and thus affected the subsequent evaporation dynamics.

The characteristic shapes of the curves are very consistent between first and second measurement cycle for each sample. However, comparing the different samples, their curves have quite heterogeneous characteristic shapes: For KG04 and KG01 on the one hand, the strong increase of U_{ev} (in the direction of decreasing M_{rf}) starts at rather low refrigerant masses around 4 g, their maxima are very sharp and occur at low refrigerant masses of approx. 0.5-1 g and the final drop is consequently relatively steep. For KG03, on the other hand, the strong increase of U_{ev} takes place at higher refrigerant masses around 6-8 g, the maxima are rather broad and occur at relatively high refrigerant masses of approx. 2-4 g and the final drop of U_{ev} is less steep but proceeds with a moderate slope between 2 and 0 g.

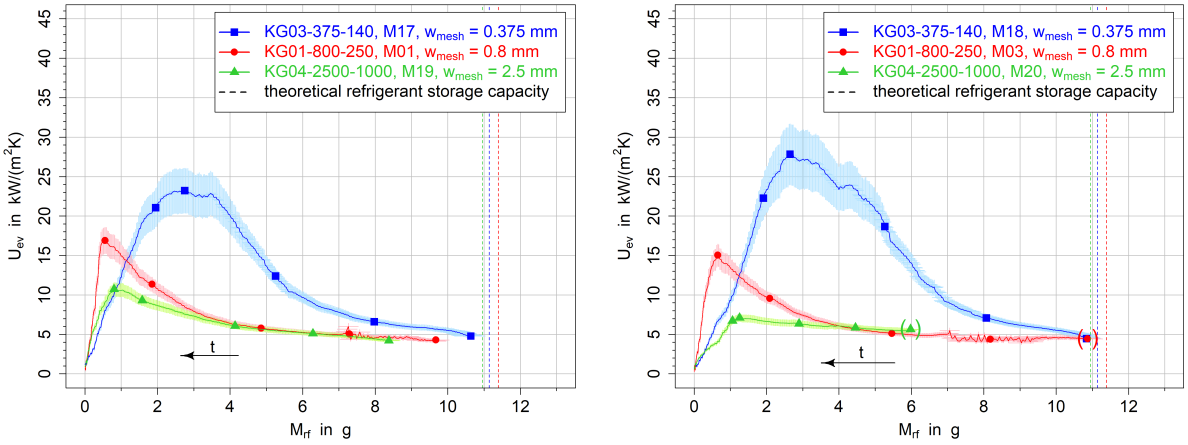

Figure 53: Impact of pore size – heat transfer coefficient vs. refrigerant mass for samples KG03-375-140 ($w_{mesh} = 0.375\ mm$), KG01-800-250 ($w_{mesh} = 0.8\ mm$), and KG04-2500-1000 ($w_{mesh} = 2.5\ mm$); standard conditions: $p_{nom} = 1.3\ kPa$, $\dot{q}_{nom} = 30\ kW/m^2$; first (left) and second (right) measurement cycle

The refrigerant storage capacity of the sample structures seems to increase with decreasing pore size by trend. For the largest pore size (KG04-2500-1000, $w_{mesh} = 2.5\ mm$) the determined relative storage capacity in relation to the theoretical capacity at full saturation amounts to 76% / 55%, for medium pore size (KG01-800-250, $w_{mesh} = 0.8\ mm$) it is 85% / 95% and for smallest pore size (KG03-375-140, $w_{mesh} = 0.375\ mm$) 95% / 97%. Though, as discussed before, the capacity values are of tentative nature due to potential squirting of refrigerant and occasional ambiguity of the starting point of non-flooded thin film evaporation (marked with brackets) due to incomplete drainage. Despite their uncertainty the refrigerant capacity results are in agreement with the fundamentals of capillarity which state that capillary pressure and capillary rise increase with decreasing pore size (cf. chapter 2.6). Calculating the capillary height h_c with equations (2-4) and (2-5) for the assumed range of possible contact angles between 10° and 50° (the actual value is not known) and a liquid temperature of 13°C, the resulting values are 18…27 mm for the finely structured KG03 (which means full saturation of the pore volume, considering the sample height of 10 mm); 8…12 mm for KG01 (80…100% saturation), and 3…4 mm for the coarse KG04 (28…44% saturation). Based on the measurement and calculation results, a virtually full saturation of the pore volume seems to be achievable with pore sizes smaller or equal to a characteristic pore size between 0.375 mm (KG03) and 0.8 mm (KG01) for the employed structure morphologies, materials and process parameters.

Simulation Results

In order to analyze the interrelation between characteristic curve shape and evaporation and dewetting dynamics, such as the impact of the pore sizes on these issues, the measured curves are compared with simulation results from the resistance model: Figure 54 illustrates the heat transfer coefficient curves of the measurements together with the simulated ones based on the "receding front" model approach and approach (III) for the contact line length (two contact lines along each wire, cf. Figure 28). Evidently, the simulated heat transfer coefficient curves increase with decreasing pore size, including their maxima at about 6 kW/(m²K) (parameters of KG04-2500-1000, $w_{mesh} = 2.5\ mm$), 19 kW/(m²K) (parameters of KG01-800-250, $w_{mesh} = 0.8\ mm$) and 38 kW/(m²K) (parameters of KG03-375-140, $w_{mesh} = 0.375\ mm$). This general order of the curves is in agreement with the measurement results, even if in terms of the specific curve shapes not all simulations match their measurements very well (which will be discussed later).

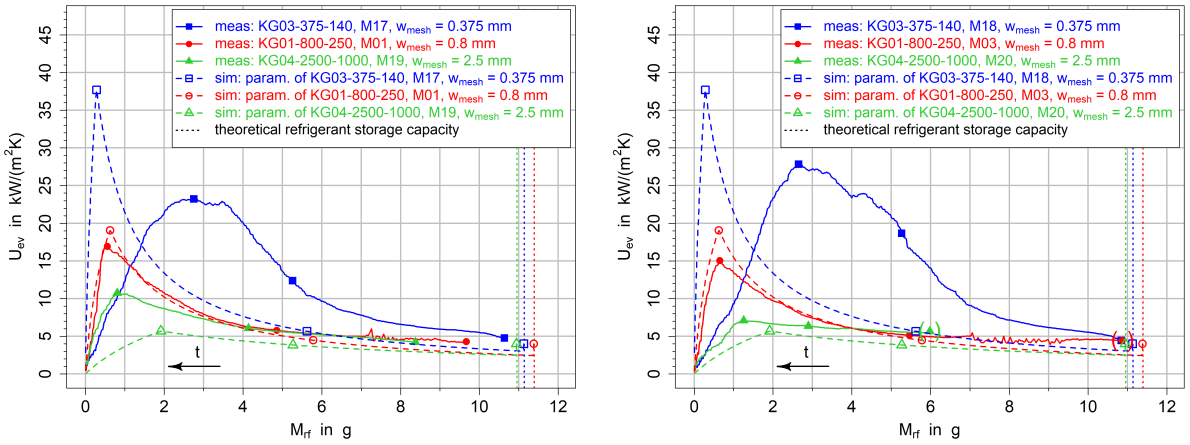

Figure 54: Impact of pore size – comparison of measured and simulated heat transfer coefficient vs. refrigerant mass for samples KG03-375-140 ($w_{mesh} = 0.375\ mm$), KG01-800-250 ($w_{mesh} = 0.8\ mm$) and KG04-2500-1000 ($w_{mesh} = 2.5\ mm$); standard conditions: $p_{nom} = 1.3\ kPa$, $\dot{q}_{nom} = 30\ kW/m^2$; receding front model conception; contact line approach (III); first (left) and second (right) measurement cycle

The origin of the impact of pore size on the simulation results of the "receding front" approach can be analyzed by means of the composition of the individual thermal resistance contributions, depicted in Figure 55 for the parameters of M17/M18 (KG03) and M19/M20 (KG04). (The resistance composition for KG01 was shown earlier in chapter 5.1, Figure 41.) Due to the constant heating power, the height of the refrigerant front h_{front} decreases virtually linearly with time. Respectively, R_{rfs} decreases linearly with the refrigerant mass as R_{rfs} is defined as the conduction resistance of the refrigerant-filled structure section (cf. equation (4-36)). Given that R_{rfs} is directly proportional to the structure's porosity via the effective thermal conductivity (cf. equations (4-38) and (4-39)), R_{rfs} for sample KG03 ($\psi = 88.7\%$) is slightly higher than for KG04 ($\psi = 87.2\%$) for any given front height or refrigerant mass. For the state of full refrigerant saturation ($h_{front} = h_{str}$, $max(M_{rf})$) the difference is about 0.03 K/W. This relation is overcompensated by the evaporation resistance R_{ev}: KG03 has a small ratio of wire diameter and clear mesh width d_{wire}/w_{mesh} and due to its large number of thin wires a considerably larger calculated contact line length of about 9.6 m compared to 4.9 m for KG01 and 1.4 m for KG04 (for all $h_{front}(t_i) > h_{thrsh}$, contact line approach (III)) which both reduces R_{ev} according to equation (4-44) (p. 81). The evaporation resistance R_{ev} of KG03 (small pore size) is consequently about factor 7 lower as against KG04 in its plateau phase ($h_{front}(t_i) > h_{thrsh}$). While for KG03 R_{ev} represents only a comparably small resistance contribution in most of its plateau phase (5% of the total resistance $R_{tot,str}$ at $max(M_{rf})$, it contributes a

considerable share for KG04 (27% of the total resistance $R_{tot,str}$ at $max(M_{rf})$). Due to its geometry dependence (cf. chapter 4.2.3), the simulated solder resistance R_{sldr} of sample KG03 is also considerably lower than that of KG04. Consequently, the total resistance of KG04 is clearly higher (0.14…0.32 K/W for $h_{front}(t_i) > h_{thrsh}$, linear phase of $R_{tot,str}$) compared to KG03 (0.02…0.26 K/W for $h_{front}(t_i) > h_{thrsh}$, linear phase of $R_{tot,str}$) and its heat transfer coefficient U_{ev} is accordingly lower.

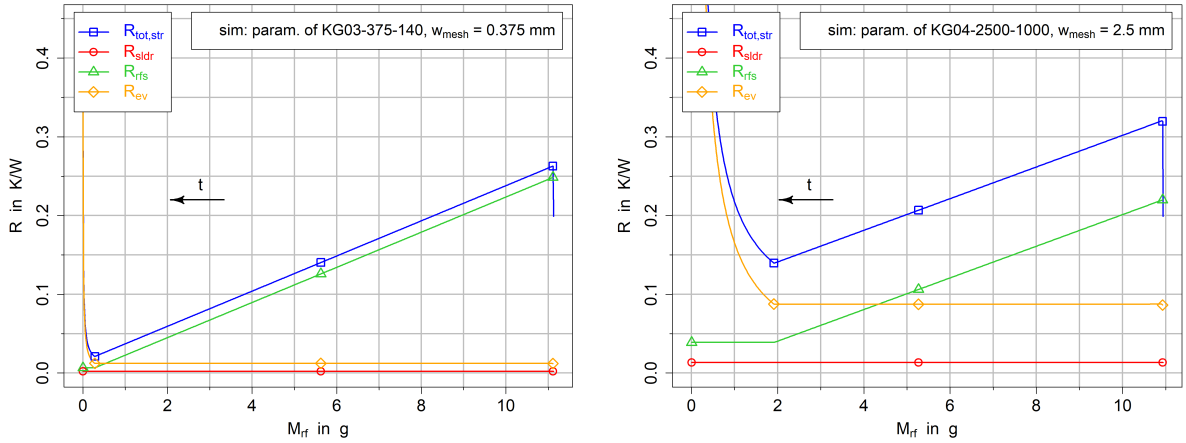

Figure 55: Thermal resistance contributions of simulations for sample KG03-375-140 ($w_{mesh} = 0.375\ mm$, left), and KG04-2500-1000 ($w_{mesh} = 2.5\ mm$, right); standard conditions: $p_{nom} = 1.3\ kPa$, $\dot{q}_{nom} = 30\ kW/m^2$; contact line approach (III)

As mentioned before, the prediction quality of the simulations regarding the evaporation dynamics (or characteristic curve shape) is extremely diverging for the different parameter sets: The simulation for KG01 matches the measurements pretty well (as discussed before in chapter 5.1) which indicates that the assumption of a receding front dewetting process might be suitable. The one for KG04 shows a rough agreement with the measurements in term of curve shape and dimension of U_{ev} values, however, the large deviation between the two measurements impedes a definite assessment. In contrast to KG01 and KG04, the simulated U_{ev} curve shape for KG03 distinctly disagrees with the measured evaporation dynamics. In the following paragraph, explanations for these observations are discussed.

Evaporation Dynamics for Large Pore Size (KG04-2500-1000)

Despite the poor conformity of the two measurements with sample KG04-2500-1000 (M19 and M20) their general curve shape is similar: The heat transfer coefficient U_{ev} rises with decreasing refrigerant mass M_{rf}, reaches a relatively sharp maximum at a refrigerant mass of about 1 g and then drops to zero. The simulated course of U_{ev} shows qualitatively similar characteristics which suggests that also for the large pore size of KG04 ($w_{mesh} = 2.5\ mm$) the conception of a receding refrigerant front might be an appropriate description of the dewetting dynamics. The simulation, though, clearly overestimates the refrigerant mass value of the U_{ev} maximum, which is synonymous with an overestimation of the modeled threshold height h_{thrsh}. As stated in chapter 4.2.3, h_{thrsh} represents the height of the evaporation front at which a transition from a downward-traveling evaporation front with constant contact line length to a static evaporation front with reducing contact line length is supposed. According to its original definition in equations (4-33) and (4-34) (p. 75), h_{thrsh} is directly proportional to the clear mesh width w_{mesh} which causes the position of the U_{ev} maximum to be shifted to higher refrigerant masses with increasing pore size. Figure 54 though reveals that the measured refrigerant masses of the U_{ev} maxima of KG01 and KG04 differ only slightly (0.6 g / 0.7 g for KG01, 0.8 g / 1.3 g for KG04) despite their different pore sizes. These findings suggest that the assumption of a proportionality of h_{thrsh} to the pore size is apparently not valid but that h_{thrsh} is presumably independent or only slightly dependent on pore size. Figure 56 illustrates

the simulated U_{ev} curve for the assumption that the threshold height of KG04 is identical with the one calculated for KG03 (which amounts to 0.57 mm) compared to the standard definition of h_{thrsh} for KG04 (which yields 1.8 mm). The modified definition now slightly underestimates the position of the U_{ev} maximum but shows a better agreement with the measurements than the original definition. These results support the hypothesis that for relatively coarse mesh structures (as KG01 and KG04) the transition to a reduction of the contact line length occurs at a similar threshold height of about 0.5…1 mm, independent of the particular pore size.

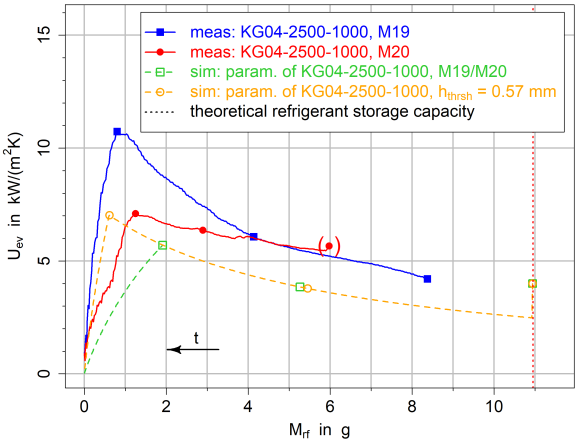

Figure 56: Impact of the modeled threshold height h_{thrsh} on simulated heat transfer coefficients for sample KG04-2500-1000 with large pore size; simulation with original definition of h_{thrsh} and with reduced $h_{thrsh} = 0.57\ mm$; standard conditions: $p_{nom} = 1.3\ kPa$, $\dot{q}_{nom} = 30\ kW/m^2$; contact line approach (III); additionally measurements M19 and M20 for comparison

Besides the doubtfulness of the original threshold height definition, the model seems to generally underestimate the heat transfer coefficient U_{ev} for sample KG04. This supposition in not fully certain since at low refrigerant masses the conformity of the measurements is poor and statements on the appropriateness of the simulation can hardly be made. At higher refrigerant masses, though, the measurements show a better agreement. Moreover, measurement M20 with lower U_{ev} appears less trustworthy due to incomplete drainage in the preparation. Both latter arguments suggest a systematic underestimation of U_{ev} by the model.

A possible explanation is again – as already mentioned in chapter 5.4.1 on the impact of porosity – that the implemented description for the evaporation resistance R_{ev} is generally too high and the resistance of the solder contacts R_{sldr} too low. Since R_{ev} is particularly high for KG04, a reduction would have a stronger impact on KG04 than on KG01. It can further be questioned if the solder resistance is indeed dependent on structure geometry, as implemented in the model, or if it is rather constant for all sample structures. Figure 57 shows a simulation with exemplary modified resistance definitions: R_{ev} was set to 50% of the original definition and R_{sldr} was set to 300% of the original definition of sample KG01 and identically applied to all structures. Additionally, the threshold height h_{thrsh} of sample KG01 was used for all structures, as described before. The resulting U_{ev} graphs for sample KG01 and KG04 are in fairly good agreement with the measurements of the first cycle (which is more trustworthy in case of KG04), both in terms of curve shape and quantitative U_{ev} values, which generally confirms the above-named presumptions. Since the modified resistance values were chosen rather arbitrarily, they certainly cannot be regarded as quantitatively reliable and also the actual relations of the different resistance contributions might be somewhat different. Still, this example indicates that an overestimation of the evaporation resistance (R_{ev}) and underestimation of the solder resistance (R_{sldr}) by the standard definitions of the model is very probable.

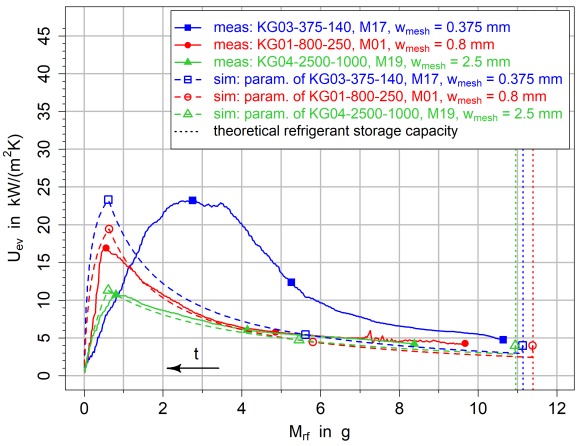

Figure 57: Impact of pore size with modified model resistance definitions – comparison of measured and simulated heat transfer coefficient vs. refrigerant mass for samples KG03-375-140 ($w_{mesh} = 0.375\ mm$), KG01-800-250 ($w_{mesh} = 0.8\ mm$) and KG04-2500-1000 ($w_{mesh} = 2.5\ mm$); standard conditions: $p_{nom} = 1.3\ kPa$, $\dot{q}_{nom} = 30\ kW/m^2$; receding front model conception; contact line approach (III); reduction of R_{ev} to 50% of the original definition and increase of R_{sldr} to 300% of the original definition of sample KG01; h_{thrsh} definition of sample KG01 used for all structures; first measurement cycle

Further possible causes for the presumptive underestimation of the heat transfer coefficient for KG04 and for inaccuracies of the model prediction in general are the following aspects: Firstly, the real dewetting dynamics might to a certain extent deviate from the "receding front" conception and instead follow a less beneficial mechanism with respect to the heat transfer coefficient. A further issue is that nucleate boiling – which can generally promote the heat transfer at high refrigerant masses – is not considered in the model. However, in the measurements with KG04, nucleate boiling could not be clearly observed and the U_{ev} curves do not feature the typical plateau phase, therefore it is not assumed to be the main reason in this case. Another influencing factor might be the solder which was applied to the wire crossings of sample KG04 in order to provide for mechanical stability of the coarse mesh (cf. chapter 4.1.3). The additional solder material causes a deviation from the nominal porosity and might on the other hand have altered the surface properties of the mesh structure. Also manufacturing tolerances of the mesh specifications could lead to discrepancies between measurements and simulations, as discussed in chapter 5.4.1 in the context of structure porosity. Another uncertainty factor might be deviations from the nominal thermal conductivity of the wire material which could affect the resistance of the refrigerant filled section of the structure (R_{rfs}). Test simulations proved, though, that a considerable offset from the nominal conductivity only has a marginal effect on U_{ev}.

Evaporation Dynamics for Small Pore Size (KG03-375-140)

As Figure 54 and Figure 57 show, the simulated curve shape for the finely structured sample KG03-375-140 considerably diverges from the U_{ev} courses of the associated measurements M17 and M18. While the simulated curve is characterized by an increasing slope with decreasing refrigerant mass over nearly the complete mass spectrum and by a sharp maximum at a low refrigerant mass, the measured U_{ev} show an increasing slope pattern only at high refrigerant masses and the maximum is very broad and occurs at elevated M_{rf}. These fundamental differences indicate that the "receding front" model conception in its standard form does not hold for very fine structures with small pore size (KG03-375-140: $w_{mesh} = 0.375\ mm$). Obviously, physical mechanisms linked to structure geometry, such as an increased capillary pressure in the fine structure, lead to a clearly different dewetting behavior and consequently to different evaporation dynamics. In the following paragraph, different mechanisms, which might be responsible for these dynamics, are discussed with aid of several alternative model conceptions for the dewetting

dynamics which are described in chapter 4.2.3. Since model parameters and assumptions for these approaches were partially chosen arbitrarily, the approaches are not expected to produce quantitatively reliable predictions but they are rather intended to illustrate the principal effects of idealized dewetting mechanisms on heat transfer dynamics.

At high refrigerant masses (about 8-11 g) the measured heat transfer coefficient U_{ev} curves virtually remain on a plateau, however, its level of about 5…8 kW/(m² K) is considerable higher than the plateau of the U_{ev} simulated with the "receding front" approach. One reason for this difference could theoretically be an intensified heat transfer due to nucleate boiling which is not covered by the model, but since the U_{ev} plateau also exceeds the measured ones of samples KG01-800-250 and KG04-2500-1000 (where nucleate boiling also took place), nucleate boiling is not considered as the only reason. Since the heat conduction resistance of the structure R_{rfs} is very dominant as long as most of the structure is saturated with refrigerant an increased contact line length in the upper region of the structure would not lead to a considerable decrease of the total resistance. In contrast, e.g. vertical vapor channels reaching the lower region of the structure – possibly generated by rising vapor bubbles – might have generated additional three-phase-contact lines adjacent to a low conduction resistance, yielding a parallel evaporation route of a low resistance and consequently a higher total U_{ev}. Similarly, low resistance evaporation at the structure base adjacent to the gap below the polypropylene ring around the structure (cf. Figure 17, right, p. 45) could contribute to an elevated U_{ev}. However, this effect can take place for the other sample structures as well and is therefore not considered as a satisfactory explanation. The occurrence of vapor channels, though, might be confirmed by a model conception of evaporation from three-phase contact lines in partially-filled pores which are homogeneously distributed over the structure volume, referred to as approach no. 2 "0D static contact lines" (cf. chapter 4.2.3). As displayed in Figure 58, the resulting U_{ev} at high refrigerant filling degrees is higher than with the standard "receding front" model approach because in approach no. 2 evaporation is assumed to take place in the center of the structure on average which leads to a reduced conduction resistance R_{rfs}. For large refrigerant masses, the simulated U_{ev} matches the measurements fairly well. Though, due to the static point of evaporation the total resistance stays on a virtually constant level throughout the evaporation process which does not agree with the measured curves at moderate and low refrigerant masses.

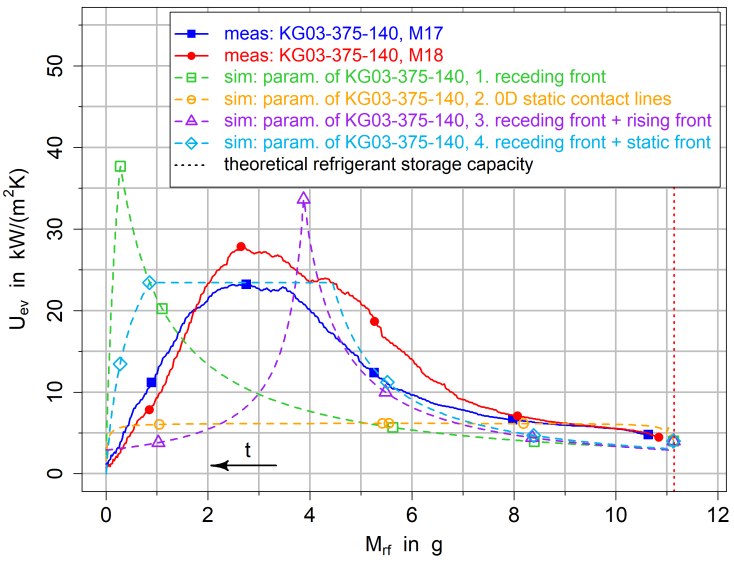

Figure 58: Evaporation dynamics for small pore sizes – Simulations with different model conceptions for the dewetting dynamics and comparison with measurement results (M17, M18) for sample KG03-375-140 ($w_{mesh} = 0.375\ mm$); heat transfer coefficient vs. refrigerant mass; standard conditions: $p_{nom} = 1.3\ kPa$, $\dot{q}_{nom} = 30\ kW/m^2$; receding front model with contact line approach (III); initial filling degree of the partially wetted section: 35% (approach 3. and 4.)

As Figure 58 shows, the measured U_{ev} curves for sample parameters of KG03-375-140 also exhibit the typical "1/x shape" which is associated with a continuous reduction of the conduction resistance R_{rfs} and with a downward movement of the place of evaporation (as discussed in chapter 5.1). However, its characteristic U_{ev} increase with decreasing refrigerant mass appears accelerated, the curve already shows a strong increase at considerably higher M_{rf} compared to the simulations with the "receding front" approach and to the measurements with KG01-800-250 and KG04-2500-1000. Furthermore, it does not continue to near the end ($M_{rf} \approx 0$) but terminates at about one third of the maximum refrigerant charge. These observations adumbrate that also for KG03 a certain downward moving evaporation front occurs but that it is superimposed by other dewetting and evaporation mechanisms: Since the U_{ev} rise with decreasing refrigerant mass is faster than it would be if all refrigerant above the front was evaporated, it is hypothesized that only a certain fraction of refrigerant in the filled pores evaporates as the front passes. The other fraction remains inside the pores at favorable places in terms of surface energy minimization, due to the strong capillary effect in the small pores. In that way the front with access to the vapor phase would reach positions close to the sample carrier – and accordingly high U_{ev} values – already at relatively high total refrigerant masses. This conception of a downward traveling evaporation front between a fully saturated section and partially wetted section of the structure was implemented in model approach no. 3 "receding front + rising front". As described in chapter 4.2.3 it further includes the assumptions that as soon as the evaporation front reaches the structure base it reverses its direction and subsequently travels upwards, now separating the partially wetted part above from the dry part below. As becomes apparent from Figure 58, the resulting simulated U_{ev} curve roughly reflects the faster U_{ev} rise with decreasing M_{rf} of the KG03 measurements, as opposed to the "receding front" approach. The slope of the curve is directly influenced by the assumed initial filling degree of the partially filled pores which was set to 35% for the simulation in Figure 58 and which might increase with decreasing pore size and increasing tortuosity due to a stronger capillary effect. The assumption of a subsequent upward-moving front, on the other hand, does obviously not match the measured course of the heat transfer coefficient at all. While the measured curves pass through a broad maximum with decreasing M_{rf} and finally decrease virtually linearly, the simulated U_{ev} has a sharp peak and then follows a declining "1/x" behavior due to the linearly increasing R_{rfs} with decreasing refrigerant mass.

Based on the conclusions from the abovementioned model conceptions, approach no. 4 "receding front + static front" was set up (cf. chapter 4.2.3). Since this approach also includes the assumption of a receding front between a fully saturated and a partially wetted structure section, its simulated U_{ev} course at high refrigerant charges is similar to approach no. 3 and satisfactorily reproduces the measurements. (The initial pore filling degree of the partially wetted section was taken to be 35% in the simulation.) When the predefined threshold height h_{thrsh} is reached at about 4.5 g, further evaporation is presumed to take place at a constant height of h_{thrsh}. The refrigerant in the partially wetted structure is supposed to be continuously transported to the evaporation position by means of capillary action and gravity. Due to the static position of evaporation and a constant contact line length the simulated U_{ev} values within this phase stay on a constant level and roughly depict the broad U_{ev} maximum of the measurements. The last phase of the model conception begins at about 1 g when the structure section above the evaporation position has run dry. Now, evaporation of the remaining refrigerant below h_{thrsh} is assumed to continue at the same position with a continuously reducing contact line length which leads to a decrease of U_{ev} with decreasing M_{rf} until the complete dry-out of the structure. Considering the simulated U_{ev} curve from this model conception, its course roughly resembles the measured curves of sample KG03-375-140. Certainly, it needs to be respected that this model approach includes some rather arbitrary assumptions and that model parameters were on purpose chosen to match the measurement results. Accordingly, the approximate agreement does not prove the validity of the model presumptions. Still, the results of this dewetting approach (no. 4 "receding front + static front") indicate that the included idealized dewetting and evaporation mechanisms might be incorporated in an actually more complex interaction of different

mechanisms and impacts occurring in structures with small pore diameters. The presented mechanisms certainly do not take place sequentially as the model approach suggests but probably overlap, interact and are superimposed by further unknown mechanisms and by random dewetting effects.

Conclusions on Pore Size Impact and Comparison with Literature

From all measurement and simulation results on the impact of pore size it can be concluded that a small pore size is generally beneficial for reaching high heat transfer coefficients and refrigerant storage capacities. The evaporation dynamics for large and medium investigated pore sizes (KG04-2500-1000: $w_{mesh} = 2.5\,mm$, KG01-800-250: $w_{mesh} = 0.8\,mm$) can obviously be described by the conception of a receding evaporation front with good accuracy. For very small pore sizes (KG03-375-140: $w_{mesh} = 0.375\,mm$) this conception does not hold but dewetting dynamics are possibly characterized by additional partially wetted regions and capillary transport due to a strong capillary effect.

The trend of increasing heat transfer coefficients with decreasing pore size can – apart from different wetting dynamics for small pore sizes – be attributed to an increased total length of three-phase contact lines which is usually positively correlated with the specific surface area of a structure. This finding is in agreement with statements in various publications (e.g. (Ma and Peterson 1997; Hanlon and Ma 2003; Crößmann 2016; Bodla et al. 2013; Wong and Chen 2013)), which are presented in chapters 2.3 and 2.4. Since evaporation from menisci mostly takes place in the narrow evaporating thin film regions close to the three-phase contact line (cf. chapter 2.3, Figure 4, p. 18), an extension of the contact line length in a defined reference area often allows considerable enhancement of the heat transfer coefficient. Crößmann found that the heat transfer coefficient was virtually proportional to the contact line length in his measurements on evaporation from different microchannel evaporator geometries (Crößmann 2016). In the field of porous structures Hanlon and Ma (Hanlon and Ma 2003) and Bodla et al. (Bodla et al. 2013) report increasing heat transfer coefficients with decreasing particle radius (and accordingly smaller pore size) of sintered powder structures which can be attributed to an extended contact line length. Li and Peterson (Li and Peterson 2006), Lanzerath et al. (Lanzerath et al. 2016), and Seiler et al. (Seiler et al. 2019) come to analogous conclusions in experiments with sintered mesh structures, finned heat exchanger tubes and tubes with porous coatings.

The finding of a good agreement of the “receding front” model conception with the measurements of the samples with large (KG04-2500-1000) and medium (KG01-800-250) pore size and its obviously poor agreement with the sample with small pore size (KG03-375-140) is in accordance with the statements of Laurindo and Prat (Laurindo and Prat 1996), presented in chapter 2.6: The authors report that characteristic drying patterns of porous structures can be associated with the value of the Bond number which expresses the relation of gravitational to capillary forces. For conditions with $Bo > 0$ (strong impact of gravity) they found that the refrigerant distribution during the drying process is characterized by a relatively sharp receding front. For $Bo = 0$ the impact of gravity can be neglected compared to capillarity and a pattern of dry and wet clusters results. Table 5 in chapter 4.2.3 (p. 73) lists up the Bond numbers which were calculated for the relevant wire mesh structures of this work (for a pressure of 1.3 kPa and the mesh spacing used as the characteristic length L). The Bond number of sample KG03-375-140 with smallest pore size ($Bo = 0.035$) is very close to zero which suggests that capillary forces prevail over gravitational forces and actually the measurement results match the conception of a relatively irregular pattern of dry and wet clusters. The clearly higher Bond numbers of the samples with larger pore sizes, KG01-800-250 ($Bo = 0.15$) and KG04-2500-1000 ($Bo = 1.6$), are associated with an increasing impact of gravity and a receding front type dewetting behavior according to Laurindo and Prat, which could indeed be found in the measurement and simulation results.

The group around Prat, Bouleux, Plourde further suggest a classification of the drying patterns by means of a phenomenological map (Plourde and Prat 2003), which includes the effect of viscous forces in addition

to gravitational and capillary forces. As described in chapter 2.6, they use the relation of three characteristic length quantities for the classification of a porous structure: The characteristic lengths of the gravity front (L_g), of the viscous front (L_{cap}), and of the porous structure sample (L_{str}) (Prat and Bouleux 1999). An estimation of these quantities for the three sample structures KG03-375-140, KG01-800-250, and KG04-2500-1000 based on equations (2-8)-(2-12) (p. 34) yields the ratios L_{str}/L_g and L_{str}/L_{cap} listed in Table 7. For the calculation of these values, the mesh spacing l_{mesh} was used as characteristic length of the pores, the structure height h_{str} was used for the characteristic height L_{str} of the structure, and the saturation pressure of 1.3 kPa and heat flux of 30 kW/m² of the respective measurements were assumed. Further, the permeability k_p of the structure was roughly estimated with aid of a formulation stated in (Nan et al. 2019) for ideal straight pores with square cross section, which reads $k_p = 0.0351 \cdot d_{edg}^2$ (with the edge length d_{edg} of the square, for which the clear mesh width w_{mesh} was used). A contact angle θ of 30° was arbitrarily assumed which represents an uncertainty factor, however, the general outcome of the characteristic lengths is not very sensitive on the chosen contact angle value.

Table 7: Characteristic length ratios according to the drying patterns characterization of Prat and Bouleux (Prat and Bouleux 1999), calculated for the structure samples KG03-375-140, KG01-800-250, and KG04-2500-1000 (assumptions stated in the text)

		KG03-375-140	KG01-800-250	KG04-2500-1000
w_{mesh}	mm	0.375	0.8	2.5
Bo	–	0.035	0.15	1.6
L_{str}/L_g	–	0.68	1.4	4.6
L_{str}/L_{cap}	–	$1.2 \cdot 10^{-4}$	$5.5 \cdot 10^{-5}$	$1.9 \cdot 10^{-5}$

The calculated characteristic length proportions in Table 7 reveal that for all three samples the ratio L_{str}/L_{cap} is very small. This implies that viscous forces do not play a significant role, which confirms the respective assumption made in the model concept (chapter 4.2.1). The ratio L_{str}/L_g, on the other hand, varies between 0.68 and 4.6 and increases with increasing pore size. These relations indicate again the increasing impact of gravitation compared to capillarity with increasing pore size.

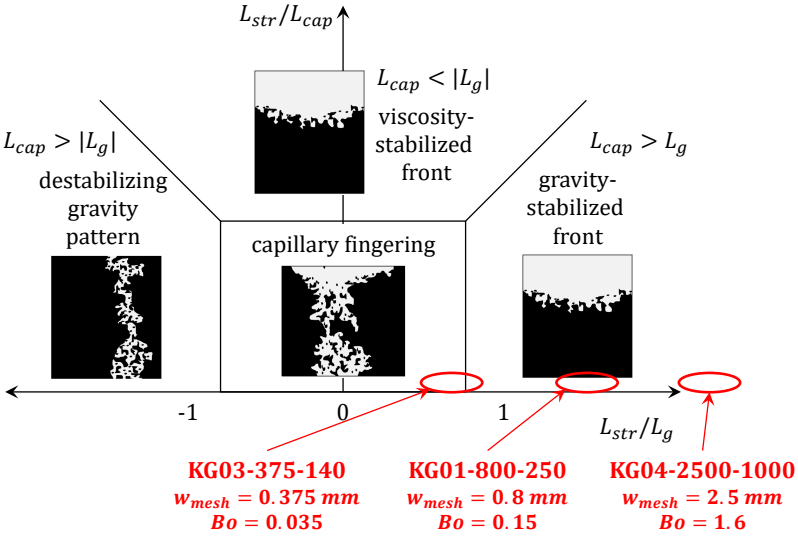

Figure 59: Allocation of the sample structures KG03-375-140, KG01-800-250, and KG04-2500-1000 in the phenomenological map after Plourde and Prat (Phenomenological map of characteristic liquid distribution patterns for porous structures in a slow drying process, developed by Plourde and Prat; simplified reproduction from (Plourde and Prat 2003))

In Figure 59, the length ratios are drawn into the phenomenological map after Plourde and Prat (which was earlier presented in Figure 12, chapter 2.6). While KG01-800-250 and KG04-2500-1000 are clearly in the field of a gravity-stabilized front, KG03-375-140 is located at the transition between gravity-stabilized front and capillary fingering (invasion percolation). This outcome is in good agreement with the interpretations of dewetting patterns from measurement and simulation results, and it adumbrates, that probably parallels can be drawn between (isothermal) drying and evaporation in a single-component system.

5.4.3 Impact of Structure Height

Measurement Results

As listed in Table 3, measurements with samples of three different structure heights of 5 mm (KG07-900-280-05), 10 mm (KG08-900-280-10) and 15 mm (KG09-900-280-15) but with identical wire mesh configuration – which is similar to that of KG01-800-250 (cf. Table 2) – were carried out. The determined dynamic heat transfer coefficients are depicted in Figure 60 for the first (left; M28, M30, M32) and second (right; M29, M31, M33) measurement cycle.

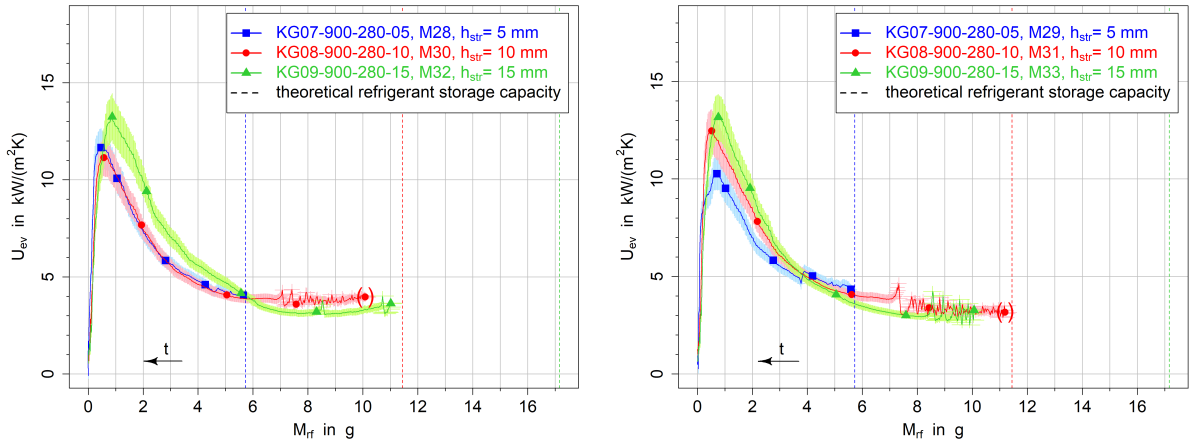

Figure 60: Impact of structure height – heat transfer coefficient vs. refrigerant mass for samples KG07-900-280-05 ($h_{str} = 5\ mm$), KG08-900-280-10 ($h_{str} = 10\ mm$), KG09-900-280-15 ($h_{str} = 15\ mm$); standard conditions: $p_{nom} = 1.3\ kPa$, $\dot{q}_{nom} = 30\ kW/m^2$; first (left) and second (right) measurement cycle

Similar to the measurements with the standard parameter set (cf. chapter 5.1) the U_{ev} curves of KG08 and KG09 show a plateau of about 3-4 kW/(m²K) at high refrigerant masses. The graphs of all samples increase with decreasing M_{rf}, followed by a maximum at 10…13.5 kW/(m²K) and a very steep drop to zero.

The determined maximum refrigerant masses for samples KG08 and KG09 are in a comparable range (KG08, $h_{str} = 10\ mm$: 10.1 g (M30) / 11.2 g (M31); KG09, $h_{str} = 15\ mm$: 11.0 g (M32) / 10.1 g (M33) while sample KG07 only reaches considerably lower values (KG07 / $h_{str} = 5\ mm$: 5.7 g (M28) / 5.6 g (M29)). (As explained in chapter 4.1.7 these values cannot be equated with the actual storage capacity due to squirting and occasional uncertainties of the starting point of thin film evaporation – especially the values of M30 and M31 are uncertain –but they can anyway serve as an indicator.) In relation to their theoretical storage capacities ($M_{rf,th}$) KG07 reaches values of 99% / 98%, KG08 reaches 88% / 98% (uncertain) and KG09 reaches only 64% / 59%. Accordingly, the sample structures with a height of 5 mm and 10 mm were presumably virtually fully saturated with refrigerant at the beginning of the evaporation

process while the pore volume of the sample with 15 mm structure height was only partly filled. These observations are in agreement with fundamentals of capillarity: Using Jurin's law (equation (2-4)) and equation (2-5) for the capillary pressure in porous media, a capillary height h_c of 7…10 mm can be calculated for KG07, KG08 and KG09, assuming a contact angle of 50…10° and a liquid temperature of 13°C. (This capillary height result applies to all three samples since they feature the same nominal geometry parameters.) The relations of the determined capillary height h_c to the respective structure heights h_{str} of the samples are summed up in Table 8 and reveal a calculative full refrigerant saturation for the low-height KG07, a partial to full saturation for the medium KG08 and a partial saturation for the high KG09. Evidently, these outcomes are in good agreement with the conclusions on maximum structure saturation from the measurements, which is represented in the table by the ratio of experimentally determined refrigerant storage capacity $M_{rf,cap}$ to theoretical storage capacity $M_{rf,th}$.

Table 8: Estimated capillary height h_c of samples KG07-900-280-05, KG08-900-280-10, KG09-900-280-15 and its effect on calculative refrigerant saturation (storage capacity); additionally the relative refrigerant storage capacity ($M_{rf,cap}/M_{rf,th}$) derived from measurements is listed for comparison

		KG07-900-280-05	KG08-900-280-10	KG09-900-280-15
h_{str}	mm	5	10	15
h_c	mm	7…10	7…10	7…10
h_c/h_{str}	%	135…207	68…103	45…69
Partial / Full Saturation?	–	full saturation	full / partial saturation	partial saturation
$M_{rf,cap}/M_{rf,th}$	%	98…99	(88… 98)	59…64

At refrigerant masses below 4…6 g it appears that by trend U_{ev} increases with growing structure height. The uncertainty intervals often overlap, though, and in the first measurement cycle the curves of KG07 and KG08 virtually coincide, therefore this supposed trend is not very reliable. Still, this circumstance might be explained by the following hypothesis: Given that sample KG09 ($h_{str} = 15\,mm$) is initially not fully saturated with refrigerant it is assumed that its lower part is saturated while its upper part is partially wetted at favorable places in terms of surface energy which is probably the regions of wire crossings. Thus, additional to the evaporation at the front between fully and partially wetted structure, evaporation can also take place at the contact lines in the partially wetted part and hence increase the total heat transfer. Given that the conduction resistance of the structure matrix to the upper partially wetted region is quite large and the liquid temperature in that region might be close to saturation temperature, it is assumed that most of this refrigerant only starts to evaporate when the refrigerant front reaches the critical height and the contact line length at the front reduces (R_{ev} increases). These circumstances consequently lead to a shift of the U_{ev} curve – including its maximum – to higher refrigerant masses and an extended mass interval of U_{ev} decline. Such a shift of the U_{ev} maximum of KG09 to a slightly higher M_{rf} compared to KG07 and KG08 can be clearly observed in both measurement cycles (but it could also arise from a higher threshold height h_{thrsh}). The apparently increased U_{ev} of KG09 in a wide M_{rf} range might thus mostly be caused by a shifted allocation of U_{ev} to the refrigerant charge state instead of a significant parallel evaporation pathway. In addition or instead this hypothesized evaporation from a partially wetted region, the higher U_{ev} of sample KG09 might also originate from slightly different surface conditions of the structure which influence the wetting behavior and thereby R_{ev}.

Simulation Results

The simulated U_{ev} curves with the "receding front" approach for the sample geometry of KG07-900-280-05, KG08-900-280-10 and KG09-900-280-15 and the respective boundary conditions are displayed in Figure 61.

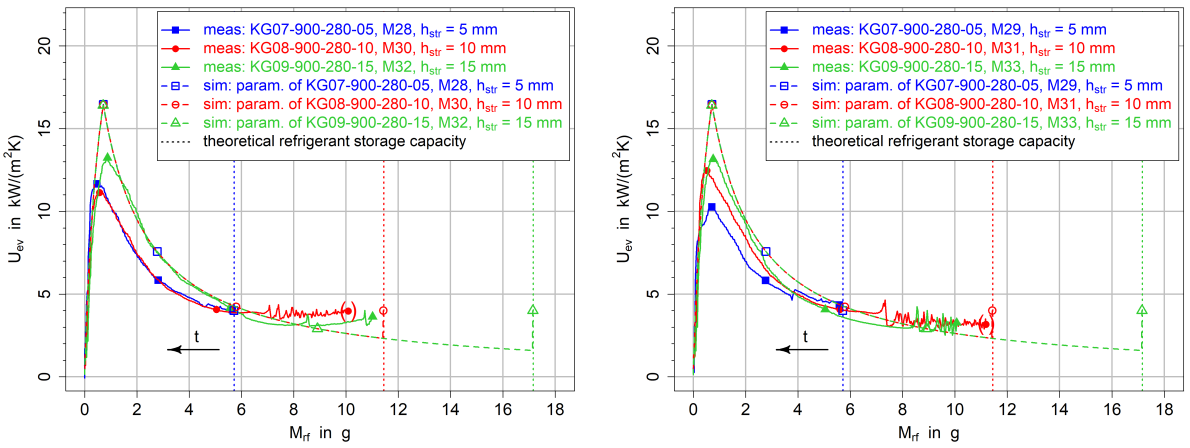

Figure 61: Impact of structure height – comparison of measured and simulated heat transfer coefficient vs. refrigerant mass for samples KG07-900-280-05 ($h_{str} = 5\ mm$), KG08-900-280-10 ($h_{str} = 10\ mm$) and KG09-900-280-15 ($h_{str} = 15\ mm$); standard conditions: $p_{nom} = 1.3\ kPa$, $\dot{q}_{nom} = 30\ kW/m^2$; receding front model conception; contact line approach (III); first (left) and second (right) measurement cycle

As the model presumes an identical dewetting behavior for all cases, the simulated curves for the different structure heights are congruent for lower refrigerant filling degrees. The curves, though, continue up to different maximum refrigerant masses due to the different theoretical storage capacities and the model's condition of an initial full saturation. As in several simulation results discussed before, the simulated heat transfer coefficients at high refrigerant filling degrees partly stay below the measured ones because the enhancing effect of nucleate boiling is not implemented in the model. At lower refrigerant masses the shape of the simulated curves shows a good agreement with all measurements of both cycles which suggests that the "receding front" approach is realistic for the given parameters. This finding is consistent with the respective outcome for sample KG01-800-250 (cf. chapter 5.1) which features very similar geometry parameters as KG07, KG08 and KG09 (cf. Table 2).

Quantitatively, the simulated U_{ev} curves are also in fairly good accordance with the measurements of all samples (and especially with KG09) in a wide refrigerant range, considering the measurement uncertainty intervals and random variations in the dewetting dynamics. Only the simulated U_{ev} maximum of 16.5 kW/(m²K) is distinctly higher than the measured ones which are between 10.3 kW/(m²K) and 13.2 kW/(m²K). Due to the steep slope of the curve the calculated maximum is extremely sensitive on the definition of the threshold height h_{thrsh} and on the dewetting process. However, considering the global refrigerant mass range, the overestimation of U_{ev} around the maximum does not have a large impact on the overall accordance of the simulation with the measurements. A modification of the definitions for the evaporation resistance R_{ev} and the solder resistance R_{sldr} – as done in chapters 5.4.2 and 5.4.3 – though, might provide more accurate simulation results. Figure 62 illustrates, that an exemplarily decrease of R_{ev} to 20% and increase of R_{sldr} to 600% of the original definitions yields a better agreement with the measurements, especially around the U_{ev} maximum.

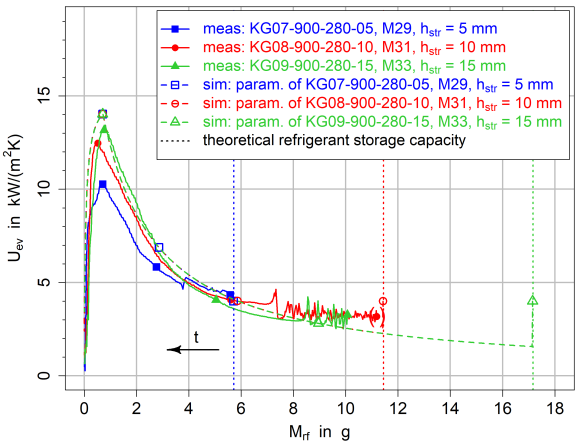

Figure 62: Impact of structure height with modified model resistance definitions – comparison of measured and simulated heat transfer coefficient vs. refrigerant mass for samples KG07-900-280-05 ($h_{str} = 5\ mm$), KG08-900-280-10 ($h_{str} = 10\ mm$) and KG09-900-280-15 ($h_{str} = 15\ mm$); standard conditions: $p_{nom} = 1.3\ kPa$, $\dot{q}_{nom} = 30\ kW/m^2$; receding front model conception; contact line approach (III); reduction of R_{ev} to 20% and increase of R_{sldr} to 600% of original definitions; second measurement cycle

Conclusions on Structure Height Impact and Comparison with Literature

Measurements with three different structure heights and identical mesh characteristics indicate a full capillary saturation of the lowest sample of 5 mm height (KG07-900-280-05), a nearly full saturation for the sample of 10 mm structure height (KG08-900-280-10) and only a partial saturation for a height of 15 mm (KG09-900-280-15). These results are in agreement with the calculated capillary height of 7…10 mm, depending on the contact angle.

At refrigerant masses below the nucleate boiling interval the U_{ev} curves of the different samples are similar but show slightly higher values for KG09 with the largest structure height. It is hypothesized that this advantage is provoked by additional evaporation in the partially filled structure section and / or that the refrigerant mass in the partially filled section only evaporates in the end and thus causes a shift of the curve to higher refrigerant masses.

Simulations with the "receding front" model conception are in good accordance with the measurements except a certain overestimation of the U_{ev} maximum. This overestimation adumbrates – just as results of the previous chapters – that the standard model settings might overestimate the evaporation resistance R_{ev} and underestimate the solder resistance R_{sldr}.

A comparison of the results of structure height impact of this work with according literature proves difficult since the statements presented in chapter 2.4 all refer to completely saturated porous structures. The reported height effects would thus rather allow a comparison with different refrigerant charge states or evaporation front positions within one unsteady measurement of this work. Hanlon and Ma, for instance, report increasing heat transfer coefficients with decreasing structure heights for steady-state capillary-assisted thin-film evaporation measurements (Hanlon and Ma 2003) and similarly Witte states that low structure heights are favorable for an increased heat transfer in capillary-fed evaporation (Witte 2016). Since evaporation is assumed to take place at the structure's surface in these experiments, the observed trend is ascribed to a decreasing conduction resistance with reduced structure height which conforms to the increasing heat transfer coefficients with receding evaporation front positions of this work. The cited publications, though, do not address impacts of structure-height-related differences in wetting conditions and their effect on heat transfer coefficients, which were discussed in this work.

5.4.4 Impact of Wire Mesh Orientation

Measurement Results

Two samples with different wire mesh orientation were compared: While the wires of KG01-800-250 were soldered in a 45° angle to the sample carrier surface, the wires of KG10-800-250-090deg have a 0° and 90° orientation in relation to the carrier surface, as illustrated in Figure 21 (p. 50). In all other aspects both samples have identical mesh parameters (cf. Table 2).

Figure 63 illustrates the measurement results of M01, M03 (KG01-800-250) and M34, M35 (KG10-800-250-090deg) (cf. Table 3), separated into measurement cycle 1 (left) and 2 (right). As the diagrams reveal, the heat transfer coefficient curves of KG10 with a wire orientation of 0°/90° have a distinctly different shape compared to the curves of KG01 with 45° wire orientation: At refrigerant masses ≥ 1.5 g the courses for KG01 and KG10 are not distinguishable considering the uncertainty of measurement and the variation range due to repeatability. Though, at about 1.5 g the U_{ev} curves of KG10 already reach their maxima, which is at a considerably higher mass compared to approx. 0.5 g for KG01. The subsequent decline of the U_{ev} curves of KG10 consequently occurs with a lower slope compared to KG01. The U_{ev} maxima of KG10 appear broader than those of KG01 and they reach clearly lower values of 12.4 kW/(m²K) (M34) and 10.1 kW/(m²K) (M35) compared to those of KG01 of 16.9 kW/(m²K) (M01) and 15.0 kW/(m²K) (M03). This difference is not covered by the uncertainty of measurement.

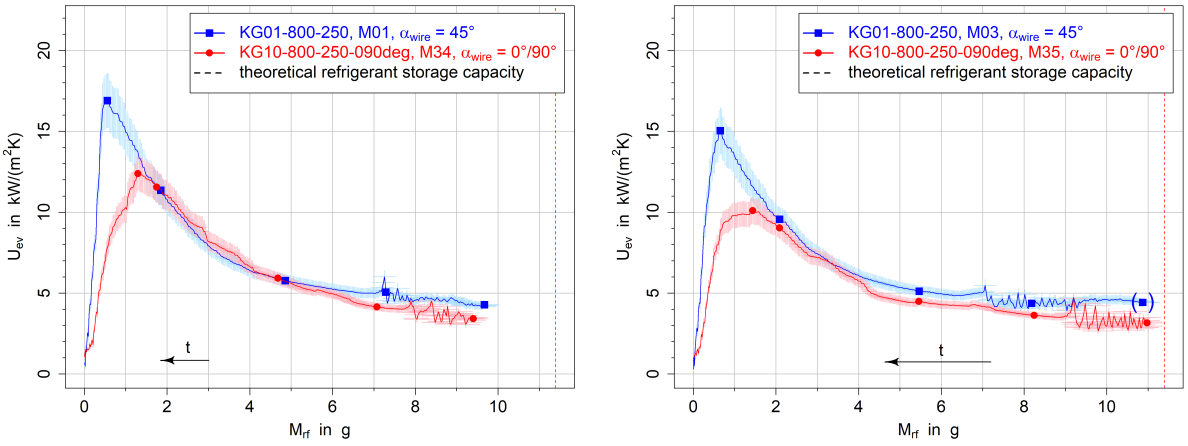

Figure 63: Impact of wire mesh orientation – heat transfer coefficient vs. refrigerant mass for samples KG01-800-250 ($\alpha_{wire} = 45°$) and KG10-800-250-090deg ($\alpha_{wire} = 0°/90°$); standard conditions: $p_{nom} = 1.3\ kPa$, $\dot{q}_{nom} = 30\ kW/m^2$; first (left) and second (right) measurement cycle

Simulation Results

Figure 64 compares the above-mentioned measurement results with two simulated heat transfer curves for the parameters of KG01 and KG10 based on the "receding front" approach and approach (III) for the contact line length. As depicted in chapter 4.2.3, the standard resistance definitions or their underlying quantities partly depend on the wire mesh orientation. For the 45° case of KG01 the effective thermal conductivity of the refrigerant-filled section ($\lambda_{rfs,eff}$) – which is an input quantity of the conduction resistance of the refrigerant-filled section R_{rfs} – is calculated with aid of equation (4-38), assuming that all wires contribute to heat conduction in the vertical heat flux direction, only via an elongated pathway. For the 0°/90° case of KG10 on the other hand $\lambda_{rfs,eff}$ is determined with equation (4-39) which includes the supposition that only the vertically oriented wires contribute to heat conduction. The horizontal ones,

on the other hand, are assumed not to contribute at all since they are oriented perpendicularly to the heat flow direction. Also the evaporation resistance R_{ev} is indirectly defined differently for KG01 and KG10 due to the conceptions for the spatial arrangement of the contact lines which vary for the different mesh orientation cases, as illustrated in Figure 35 (p. 82). The corresponding equations for the maximum contact line length of an elementary cell $l_{cl,ec}$ ((4-45)-(4-50)) are summarized in Table 6. The standard model conception of the threshold height h_{thrsh} is related to the wire mesh orientation as well, which leads to different definitions for 45° and 0°/90° orientation (cf. equations (4-33) and (4-34)).

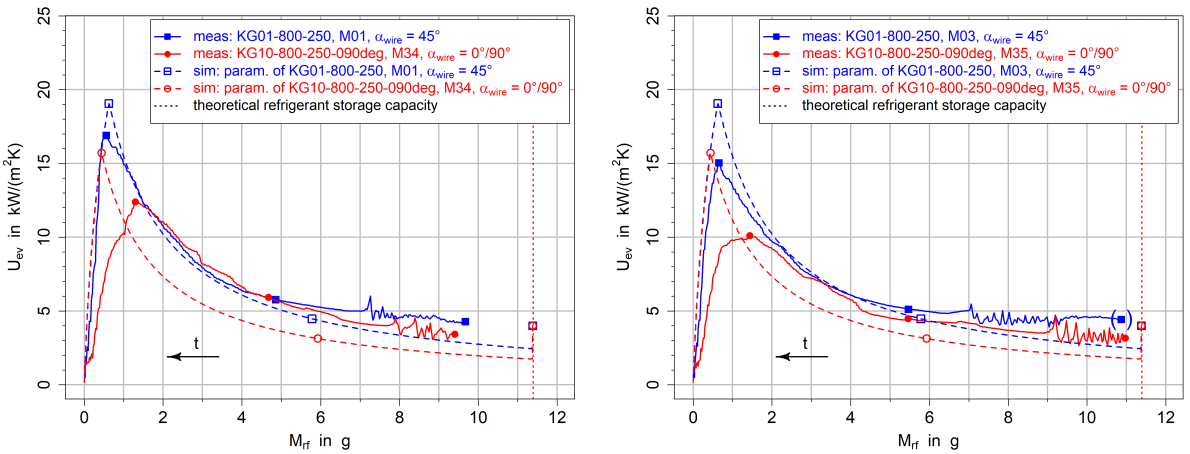

Figure 64: Impact of wire mesh orientation – comparison of measured and simulated heat transfer coefficient vs. refrigerant mass for samples KG01-800-250 ($\alpha_{wire} = 45°$) and KG10-800-250-090deg ($\alpha_{wire} = 0°/90°$); standard conditions: $p_{nom} = 1.3\ kPa$, $\dot{q}_{nom} = 30\ kW/m^2$; receding front model conception; contact line approach (III); first (left) and second (right) measurement cycle

The simulated U_{ev} curve for KG01-800-250 (45° wire mesh orientation) in Figure 64 shows good agreement with the measurement results, as discussed in chapter 5.1. For KG10-800-250-090deg (0°/90°) the simulated U_{ev} values are considerably lower than the measured curves in the refrigerant mass range above 1.5 g. The U_{ev} maximum on the other hand is overestimated by the model. Moreover, the corresponding refrigerant mass value of the U_{ev} maximum is predicted considerably lower: 0.4 g in contrast to 1.3 g (M34) and 1.4 g (M35) in the measurements. In combination, these characteristics lead to the impression of a shift of the simulated U_{ev} curve to lower refrigerant masses. Overall, the measurement results of KG10 with 0°/90° wire orientation are not satisfactorily represented by the described model parameters. As possible explanations for this discrepancy three potentially inadequate model presumptions are analyzed:

Firstly, the assumption that only the vertical wires contribute to heat conduction might be inappropriate. If also the horizontal wires contributed, a higher effective thermal conductivity and a reduced conduction resistance of the refrigerant-filled structure section (R_{rfs}) would be simulated which would lead to a raised simulated U_{ev} curve. This effect can be observed in the left diagram of Figure 65 (label "incr. $\lambda_{rfs,eff}$") where the effective thermal conductivity $\lambda_{rfs,eff}$ was exemplarily raised to the value of a structure with 45° wire orientation (from 18.9 W/(m K) to 26.4 W/(m K)) while keeping all other definitions. Given that R_{rfs} dominates the total resistance in a wide range of refrigerant masses, U_{ev} is quite sensitive on the definition of the effective thermal conductivity which confirms the importance of an accurate description of the latter. Even though an enhanced thermal conductivity specification draws the simulated curve closer to the measurements, it cannot produce the shift and broadening of the U_{ev} maximum and further entails an overestimation of the maximum. Consequently, an inappropriate definition of the effective thermal conductivity of the structure might be a partial explanation for the discrepancy between

the simulation with the standard model version (cf. left diagram of Figure 65, label "standard")) and measurements of KG10, but it cannot be the only reason.

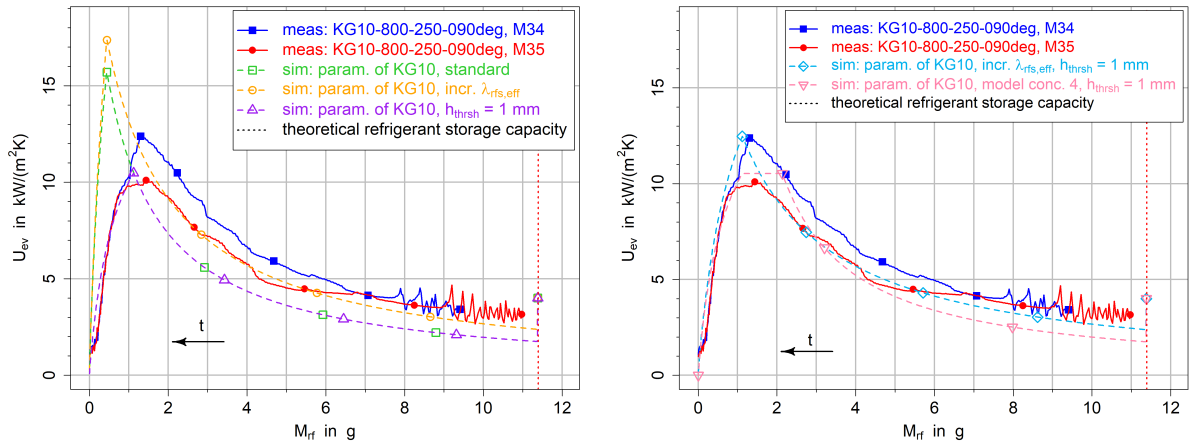

Figure 65: Evaporation dynamics for 0°/90° wire mesh orientation – Simulations with different modifications of the receding front conception; comparison with the standard receding front conception and with measurement results of sample KG10-800-250-090deg (M34, M35); heat transfer coefficient vs. refrigerant mass; standard conditions: $p_{nom} = 1.3\ kPa$, $\dot{q}_{nom} = 30\ kW/m^2$; contact line approach (III)

A second possibly inadequate definition is the chosen value for h_{thrsh} which characterizes the threshold height of the front below which evaporation leads to a reduction of the contact line length (cf. chapter 4.2.3). Exemplarily, a fixed value of $h_{thrsh} = 1.0\ mm$ was used instead of the standard definition for a 0°/90° orientation of half the clear mesh width (cf. equation (4-34)) which gives a value of $h_{thrsh} = 0.4\ mm$ for KG10. The resulting U_{ev} curve is plotted in the left diagram of Figure 65 and labeled with "$h_{thrsh} = 1\ mm$". As shown before, a higher h_{thrsh} shifts the U_{ev} maximum to higher refrigerant masses while at the same time reducing its amplitude, which – in this case – draws the simulated curves closer to the measurements at low refrigerant masses. If the increased h_{thrsh} is combined with a higher effective thermal conductivity of the refrigerant-filled structure $\lambda_{rfs,eff}$ (right diagram of Figure 65, label "incr. $\lambda_{rfs,eff}$, $h_{thrsh} = 1\ mm$"), the resulting curve approximates the measurements which might indicate that these corrections reflect the actual physical phenomena. However, the graph does not mirror the broader maximum region which is especially pronounced in M35, and besides, the measured U_{ev} curve shapes for KG10 could also be provoked by other effects, which are matter of a third hypothesis:

The third possible explanation is that the actual dewetting dynamics of sample KG10 deviate from the "receding front" conception. The shift of the U_{ev} maximum of the KG10 measurements to elevated refrigerant masses and the broadened maximum region adumbrate that some refrigerant remains on the structure surface as the evaporation front passes. This conception is implemented in the dewetting model conception no. 4: "receding front + static front" which is explained in chapter 4.2.3 and which was introduced before with the finely-structured sample KG03-375-140 in chapter 5.4.2. Applied to the structure geometry of sample KG10 with the assumptions of a threshold height h_{thrsh} of 1 mm and an initial filling degree of the partially filled pores of 10%, the U_{ev} curve in the right diagram of Figure 65, labeled with "model conc. 4, $h_{thrsh} = 1\ mm$", results. The graph shows a slightly shortened period of increasing U_{ev} with time, a broader maximum and an extended period of declining U_{ev} for $M_{rf} \rightarrow 0$ which in sum leads to a good agreement with the measurements and which makes the suggested dewetting phenomena of the model conception "receding front + static front" plausible.

A tentative explanation for the differing dewetting and evaporation dynamics of sample KG10 from those of KG01 might be that refrigerant on the surface of horizontal wires of KG10 does not instantaneously

evaporate when the evaporation front passes, due to the poorer thermal contact of horizontal wires to the heat source compared to vertical wires or wires in 45° orientation. This could explain why refrigerant residuals occur at 0°/90° wire orientation (KG10) but not at 45° orientation (KG01). Of course, a different wetting behavior can also be caused by a certain random variance of surface properties which cannot be excluded for the two samples. However, both samples were made from the same sheet of wire mesh which reduces the probability that their surface properties were subject to different influences during the manufacturing process. Furthermore, other samples with a similar mesh geometry but 45° wire orientation (e.g. KG05-850-400, KG08-900-280-10) do not show such a deviation from the "receding front" dynamics as KG10 does, which suggests that the deviating behavior of KG10 might actually relate to the 0°/90° wire orientation.

Conclusions on Impact of Wire Mesh Orientation

The measurements with 45° (KG01-800-250) and with 0°/90° (KG10-800-250-090deg) wire mesh orientation produced noticeably different characteristic U_{ev} curve shapes. For elevated refrigerant filling degrees the graphs of both samples coincide within measurement uncertainty, while at low refrigerant masses the U_{ev} maxima of the 0°/90° orientation (KG10) are lower and broader than those of 45° orientation (KG01). Accordingly, the standard "receding front" model conception does not satisfactorily reflect the measurements with 0°/90° mesh orientation. This discrepancy might originate from inappropriate model assumptions: The conception that horizontal wires of the 0°/90° mesh structure do not contribute to the effective thermal conductivity could be inadequate, the definition of the threshold height h_{thrsh} appears to be unsuitable, and the actual dewetting dynamics might deviate from the model conception of a sharp "receding front" but possibly rather match the "receding front + static front" model conception (no. 4). Potential reasons for the different dewetting behavior of the sample with 0°/90° oriented structure from that with 45° are the inferior thermal coupling of the horizontal wires to the heat source and a randomly poorer surface wettability of the tested sample with 0°/90° wire mesh orientation.

5.4.5 Application-Related Assessment of Geometry Impacts

In the following paragraphs, the impacts of structure geometry factors are assessed with regard to the envisaged application in evaporator heat exchangers for adsorption heat transformation devices. In the first paragraphs the measurement-derived assessment quantities of the first assessment method – described in chapter 4.1.9 – are used as characteristic values, which are the mean (start / maximum) heat transfer coefficient of evaporation per structure height $\overline{U_{ev}}/h_{str}$ ($U_{ev,start}/h_{str}$, $U_{ev,max}/h_{str}$) and the experimentally determined refrigerant storage capacity per structure volume $M_{rf,cap}/V_{str}$. As explained in chapter 4.1.9, these characteristic quantities delineate the general field of possible performance values, since they refer to the complete measurement duration. In matters of the two main optimization targets for an adsorption module (cf. chapters 1, 2.1, 4.1.9), the specific heat transfer coefficient U_{ev}/h_{str} represents the relevant quantity for a high-power design focus, while the specific refrigerant storage capacity $M_{rf,cap}/V_{str}$ is of special importance in case of a high-COP focus.

In the last paragraph ("Performance Map for the Investigated Sample Structures") a performance map for the different sample structures is presented, in which the second assessment method (cf. chapter 4.1.9) is applied. This method allows for a more comprehensive view on the suitability of a porous structure by considering the possibility of running the evaporation process only in a selected advantageous refrigerant charge interval. Thus, it discloses different possible combinations of mean heat transfer coefficient $\overline{U_{ev}}$ and refrigerant mass turnover $M_{rf,to}$. It thereby especially considers the tradeoff between the adsorption module's competing optimization criteria of high power output – which requires a high mean heat transfer coefficient – versus high efficiency (COP) – which requires a sufficient refrigerant turnover. From the

performance map it can thus be judged if a particular wire mesh structure is especially suitable for one of these optimization goals.

Impact of Porosity

The diagram on the left in Figure 66 depicts the characteristic height-specific evaporation heat transfer coefficients for samples with different porosities. The range between the specific U_{ev} in the starting phase and at its maximum for lowest (KG05-850-400, $\psi = 84.5\%$) and medium (KG01-800-250, $\psi = 90.7\%$) porosity is quite broad with about 400…1800 kW/(m³K) and there is no considerable difference between both structures. For KG06-800-200 with the highest porosity ($\psi = 93.8\%$) the maximum value is distinctly lower (800 or 1100 kW/(m³K)) while the value of the starting phase is similar with about 300 kW/(m³K). A low porosity therefore appears beneficial in terms of heat transfer, provided that the effective operational states are utilized.

The specific refrigerant storage capacity in the right diagram shows a vague trend of increasing specific capacity with increasing porosity within the investigated porosity range. However, most of the data points are uncertain due to difficulties in identifying the starting point, and additionally the values for KG05 and KG01 scatter considerably. Anyway, all determined specific storage capacities are rather close to their theoretical storage capacities which proves a pronounced capillary effect. Furthermore, all samples reach relatively high values of about 700…900 kg/m³ which means that the advantage of the structure with highest porosity is relatively small.

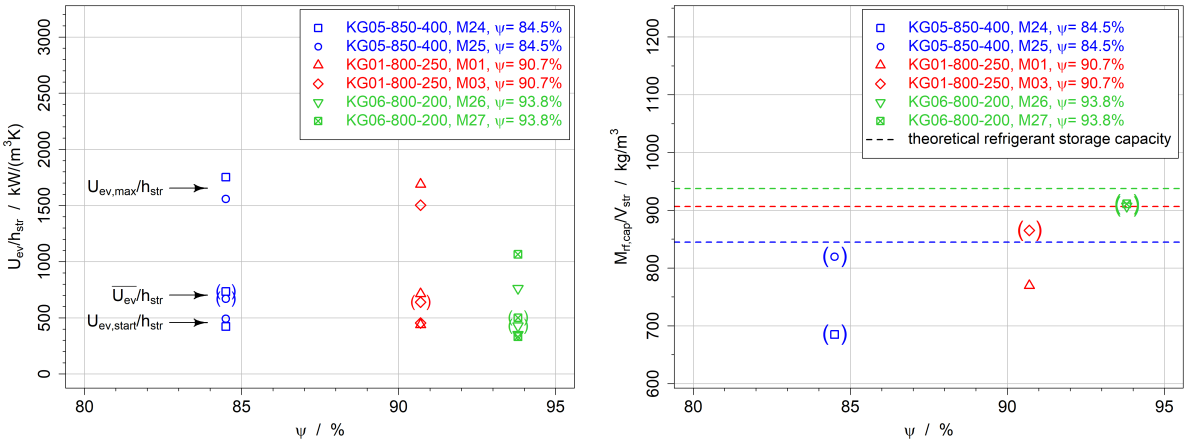

Figure 66: Impact of porosity on assessment quantities – Mean, start and maximum structure-height-specific heat transfer coefficient U_{ev}/h_{str} (left) and structure-volume-specific refrigerant storage capacity $M_{rf,cap}/V_{str}$ (right) for sample structures with different porosities (KG05-850-400, KG01-800-250, KG06-800-200); standard conditions: $p_{nom} = 1.3\ kPa$, $\dot{q}_{nom} = 30\ kW/m^2$

Impact of Pore Size

Mean / starting phase / maximum height-specific heat transfer coefficient and specific refrigerant storage capacity for the structures with different pore sizes (KG03-375-140: $w_{mesh} = 0.375\ mm$, KG01-800-250: $w_{mesh} = 0.8\ mm$, KG04-2500-1000: $w_{mesh} = 2.5\ mm$) are shown in Figure 67. The maximum specific heat transfer coefficient (Figure 67, left) clearly increases with decreasing pore size to up to 2300…2800 kW/(m³K) (KG03). The mean heat transfer coefficient only shows a distinctly higher value for the small pore diameter (KG03) while the advantage of KG01 compared to KG04 is relatively small. These relations show that KG03 profits from its broad maximum which clearly raises the mean heat transfer

coefficient. The heat transfer coefficient of the plateau-shaped starting phase of the evaporation process is virtually identical for all samples. This fact can be explained with the occurrence of nucleate boiling which is obviously not much influenced by the pore structure.

The right diagram of Figure 67 reveals that by trend the specific refrigerant storage capacity increases with decreasing pore size within the considered pore size range. While for the smallest pore size (KG03) the structure virtually reaches the theoretical storage capacity of about 900 kg/m³, the volume-specific capacity of KG01 (medium pore size) appears to be slightly smaller. The specific capacity of KG04 (largest pore size) is with about 480 kg/m³ / 660 kg/m³ distinctly lower, corresponding to the findings in chapter 5.4.2.

The assessment results prove that a small pore size (or clear mesh width) is favorable both in terms of achievable heat transfer coefficients and refrigerant storage capacities within the investigated pore size range and process conditions.

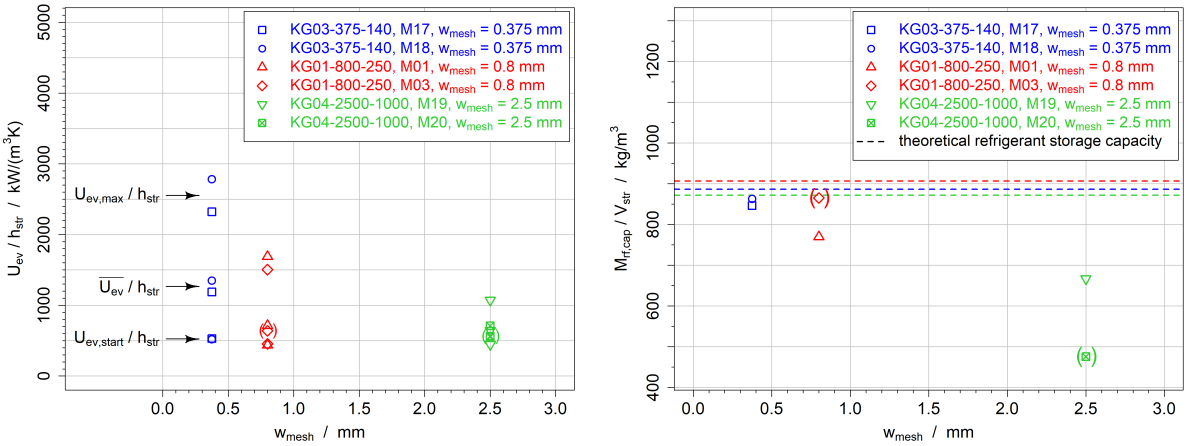

Figure 67: Impact of pore size on assessment quantities – Mean, start and maximum structure-height-specific heat transfer coefficient U_{ev}/h_{str} (left) and volume-specific refrigerant storage capacity $M_{rf,cap}/V_{str}$ (right) for sample structures with different pore sizes (KG03-375-140, KG01-800-250, KG04-2500-1000); standard conditions: $p_{nom} = 1.3\ kPa$, $\dot{q}_{nom} = 30\ kW/m^2$

Impact of Structure Height

The left diagram in Figure 68 shows a clearly increasing height-specific characteristic heat transfer coefficients with decreasing structure height in the considered range. As the results of chapter 5.4.3 already indicated, an additional structure volume on top of the existing cannot reach the same performance, amongst others due to the increasing distance from the heat source and the corresponding increased thermal resistance.

The specific refrigerant storage capacities of the samples with smallest (KG07-900-280-05, $h_{str} = 5\ mm$) and medium (KG08-900-280-10, $h_{str} = 10\ mm$) structure height are very similar and close to their theoretical specific storage capacities of about 900 kg/m³ which corresponds to a virtually full capillary saturation of the structure, as discussed in chapter 5.4.3. The specific capacity values of the structure with a height of 15 mm (KG09-900-280-15) in contrast are considerably lower. Respecting the calculated capillary height value of 7…10 mm (cf. chapter 5.4.3) it can be assumed that the specific storage capacity does not uniformly decrease with increasing structure height but that for structure heights lower than this value the specific capacity is constant and equals full saturation and above this characteristic height the specific capacity decreases reciprocally with increasing structure height.

Concluding from these results, low structure heights appear to be the best choice for evaporators with both a high-power design concept and a high-efficiency (high COP) design concept. However, on a heat exchanger level, not only the structure volume but also the volume of the fluid ducts contribute to the overall construction volume of the heat exchanger, therefore the advantage of a low structure height might be reduced if referred to the overall heat exchanger volume.

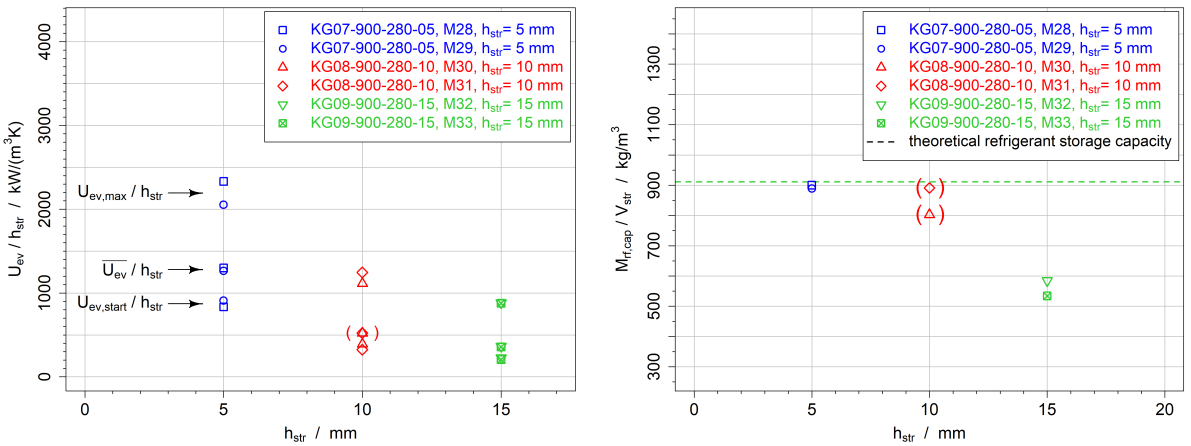

Figure 68: Impact of structure height on assessment quantities – Mean, start and maximum structure-height-specific heat transfer coefficient U_{ev}/h_{str} (left) and volume-specific refrigerant storage capacity $M_{rf,cap}/V_{str}$ (right) for sample structures with different structure heights (KG07-900-280-05, KG08-900-280-10, KG09-900-280-15); standard conditions: $p_{nom} = 1.3\ kPa$, $\dot{q}_{nom} = 30\ kW/m^2$

Impact of Wire Mesh Orientation

The characteristic height-specific heat transfer coefficients in the left diagram of Figure 69 show only slightly higher values of the 45° orientation for the starting phase and mean value while the maximum value of the 45° orientation is noticeably higher than that of the 0°/90° wire mesh orientation. As discussed in chapter 5.4.4, though, it is not completely clear if this apparent advantage only originates from random differences in the wetting behavior or if it is actually related to the geometrical peculiarities. As the right diagram in Figure 69 depicts, no distinct effect of the wire orientation on the specific refrigerant storage capacity can be concluded from the measurements.

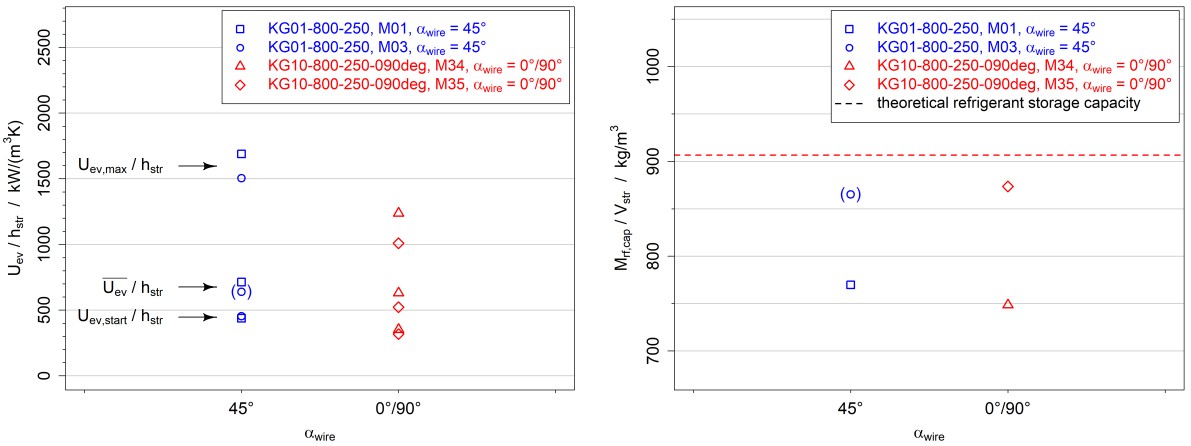

Figure 69: Impact of wire mesh orientation on assessment quantities – Mean, start and maximum structure-height-specific heat transfer coefficient U_{ev}/h_{str} (left) and volume-specific refrigerant storage capacity $M_{rf,cap}/V_{str}$ (right) for sample structures with different wire mesh orientation (KG01-800-250, KG10-800-250-090deg); standard conditions: $p_{nom} = 1.3\ kPa$, $\dot{q}_{nom} = 30\ kW/m^2$

Overall, a 45° wire mesh orientation might have a certain advantage as opposed to the 0°/90° variant but no strongly pronounced trend can be observed.

Performance Map for the Investigated Sample Structures

As described in chapter 4.1.9, for the second assessment method a sequence of structure-volume-specific refrigerant turnover demand values ($M_{rf,to}/V_{str}$) from 100 kg/m³ to 900 kg/m³ is defined. From the dynamic measurement curves the mean heat transfer coefficient of the optimum operation interval ($\overline{U_{ev,opt}}$) for these turnover demands are calculated and related to the structure height h_{str}. The resulting characteristic values for all employed sample structures are aggregated in a performance map, which is depicted in Figure 70. The results of the two measurement cycles of each sample were averaged. Sample KG02-800-250 was left out since it has the same wire mesh configuration as KG01-800-250. (Remark on denomination of the sample structures: KGXY – "clear mesh width in µm" – "wire diameter in µm" – "structure height in mm / wire orientation angle (optional)".)

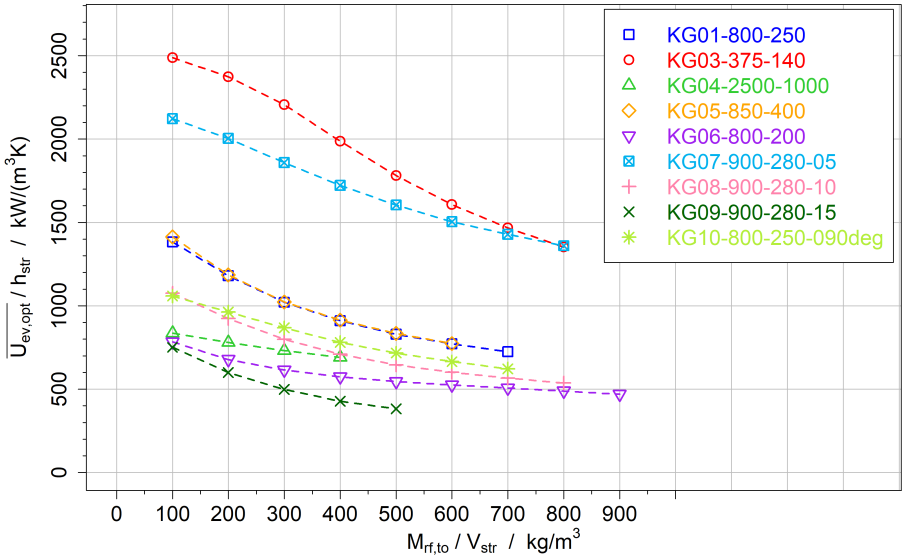

Figure 70: Application-related performance map of all investigated sample structures – structure-height-specific mean heat transfer coefficient of the optimum refrigerant mass interval, $\overline{U_{ev,opt}}/h_{str}$ vs. structure-volume-specific refrigerant turnover demand, $M_{rf,to}/V_{str}$; standard conditions: $p_{nom} = 1.3\ kPa$, $\dot{q}_{nom} = 30\ kW/m^2$

A prominent feature of all curves in Figure 70 is that $\overline{U_{ev,opt}}/h_{str}$ falls with increasing turnover demand $M_{rf,to}/V_{str}$ in all cases. This is a necessary effect of the calculation method since for a low turnover demand a narrow interval around the U_{ev} maximum can be chosen as operation range while for a large turnover demand also the less favorable parts of the dynamic U_{ev} curve need to be included. Correspondingly, the starting points of the curves approximately equal the maximum specific heat transfer coefficients ($U_{ev,max}/h_{str}$) and the end points approximately equal the mean specific heat transfer coefficients ($\overline{U_{ev}}/h_{str}$) used in the previous paragraphs.

The curve of sample KG09-900-280-15 shows the lowest specific heat transfer coefficients of all samples and can only fulfill refrigerant turnover demands of up to 500 kg/m³. Both features are caused by the incomplete refrigerant saturation of the large structure height of 15 mm which entails a poor utilization of the volume. The specific heat transfer coefficients of KG06-800-200 are only slightly higher, especially at low turnover values, which can partially be attributed to the low porosity and the associated high conduction resistance of the refrigerant-filled section but also to a deterioration of the wetting behavior

due to a presumed contamination (cf. chapter 5.4.1). On the other hand, KG06 is the only sample which can fulfill the specific refrigerant turnover demand of 900 kg/m³, thanks to its high porosity and strong capillarity. For an adsorption module with a pronounced design focus on efficiency (COP) maximization this structure might consequently be of interest despite its low heat transfer coefficients. KG04-2500-1000 exhibits a relatively even course of low specific heat transfer coefficients and can only fulfill refrigerant turnover demands up to 400 kg/m³ due to its large pores (clear mesh width $w_{mesh} = 2.5mm$) and the corresponding poor capillary effect and small specific surface area. The samples KG08-900-280-10, KG10-800-250-090deg, KG01-800-250, and KG05-850-400 show specific heat transfer coefficients on a moderate level in similar dimensions and reach specific turnover demands of up to 600…800 kg/m³. The curve of sample KG07-900-280-05 is located at considerably higher specific heat transfer coefficients than those of the aforementioned samples. This can be attributed to its low structure height of 5 mm and the associated small reference volume and low conduction resistance. Sample KG03-375-140 shows the highest characteristic heat transfer coefficients of all investigated sample structures – except for the highest turnover value of 800 kg/m³ where sample KG07 reaches virtually the same heat transfer coefficient. The excellent characteristics of KG03 can be ascribed to its very small pore size ($w_{mesh} = 0.375\ mm$) which ensures a complete initial saturation with refrigerant and extended three-phase contact lines. As discussed in chapter 5.4.2, the mesh conformation of KG03 further provokes particular and beneficial dewetting and evaporation dynamics with an early increase of U_{ev} and a broad maximum (referred to the refrigerant mass charge). These special dynamics are also responsible for the unique curve shape of KG03 in Figure 70: While all other graphs have their largest slope at the lowest turnover values, the curve of KG03 reaches its steepest point at medium turnover values.

As Figure 70 reveals, none of the curves cross each other but only KG03 and KG07 converge at the specific turnover demand of 800 kg/m³. This is not a necessity but other porous structure variants could potentially lead to crossing curves which would imply that a certain structure is to be favored only in a certain range of refrigerant turnover demands while another structure should be chosen for a different turnover demand interval.

Summarizing the application-related assessment of the investigated copper mesh structures, the structure configuration of sample KG03-375-140 with small pore size is the most promising. For large specific refrigerant turnover demands the configuration of sample KG07-900-280-05 with lowest structure height reaches similarly high specific heat transfer coefficients. By further optimization of the mesh topology – e.g. in form of a combination of small pore size and low structure height – it is very likely that even distinctly higher characteristic heat transfer coefficients could be reached at the given specific refrigerant turnover demands.

5.5 Potential Assessment for Wire Mesh Evaporators

Considered Heat Exchanger Designs

In order to assess the potential of evaporator-condenser heat exchangers with wire mesh structures, a performance estimation for an exemplary heat exchanger design was carried out. As a reference, evaporation characteristics of a partially-flooded copper finned tube heat exchanger with internal structure from Seiler and Volmer (Seiler et al. 2020) were used. Utilizing the capillary effect of the fins, this heat exchanger type and operational mode is certainly among the most efficient approaches for evaporation of water and therefore represents a challenging benchmark. To allow for a comparison, a similar tube geometry was assumed for the hypothetical wire mesh heat exchanger, even if the thicker mesh structure leads to a considerably larger total heat exchanger construction volume V_{cnstr} (cf. Figure 71): A round

copper tube was presumed as a fluid duct, with an inner diameter of 9 mm, a wall thickness of 0.5 mm and 2 m total length. Wire mesh sheets were assumed to be perpendicularly soldered onto the tube's cylindrical surface. For the mesh structure the two best-performing structures from the evaporation measurements were chosen, KG03-375-140 (fine mesh structure, 10 mm height) and KG07-900-280-05 (medium mesh size, 5 mm height).

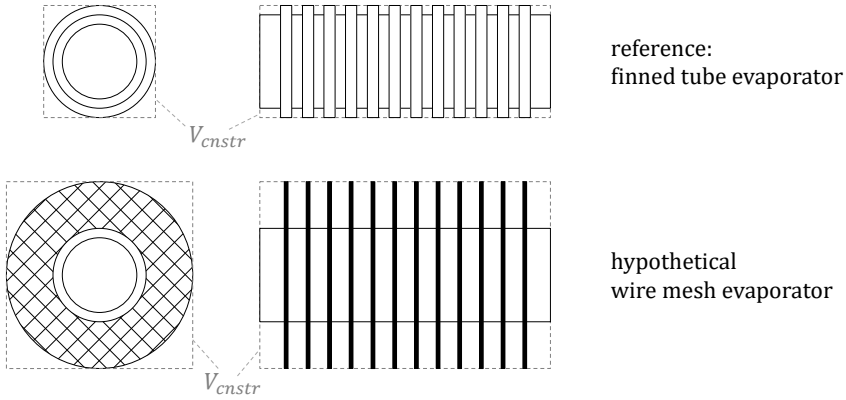

Figure 71: Schematic drawings of the finned tube reference evaporator (top) and the hypothetical wire mesh evaporator (bottom); drawings not to scale

As quantity for evaluation the absolute thermal transmittance (UA value) of the heat exchanger per construction volume V_{cnstr} was employed in order to account for requirement of a compact sorption module. The construction volume was defined as the enveloping cuboid with quadratic cross section around the heat exchanger tube (cf. Figure 71), since void volume between parallel tubes cannot be used. The potential refrigerant mass turnover per evaporation half-cycle was referred to the construction volume as well.

The heat exchanger is treated as a serial connection of a thermal resistance of the fluid-side heat transfer (with corresponding heat transfer coefficient h_{fl}) and the refrigerant-side heat transfer of evaporation (with corresponding heat transfer coefficient U_{ev}). The conduction resistance of the tube wall was neglected, just as the impact of the curved shape of the mesh structure instead of a straight arrangement.

Given that the fluid-side heat transfer depends on several parameters as the duct's internal geometry and surface properties, fluid velocity and thermophysical properties of the fluid, three exemplary heat transfer coefficients of 5 kW/(m²K), 10 kW/(m²K) and 30 kW/(m²K) were used. (For a plain tube without internal structuring or turbulator, with water at 15°C and 1.5 bar as heat transfer fluid, a heat transfer coefficient of 10 kW/(m²K) corresponds to a fluid velocity of about 2.3 m/s, $Re \approx 1.8 \cdot 10^4$ and $Nu \approx 153$, according to the calculation method for fully established turbulent flow from Gnielinski, described in (VDI e.V., VDI-Gesellschaft Verfahrenstechnik und Chemieingenieurwesen 2013, G1). In case of internally structured ducts, these heat transfer coefficients can be reached at distinctly lower fluid velocities.)

The refrigerant-side (evaporation) heat transfer coefficients for structure KG03-375-140 and KG07-900-280-05 were gained from the evaporation measurements at standard conditions ($p_{nom} = 1.3\ kPa, \dot{q}_{nom} = 30\ kW/m^2$), using the mean values of the optimal refrigerant charge intervals for a certain refrigerant turnover demand, $\overline{U_{ev,opt}}$ (cf. values in Figure 70, p. 128, and definition of the quantity in 4.1.9). For the translation into a UA value, the cylindrical reference area through the middle of the structure height was employed.

For the reference case, characteristic total heat transfer coefficients from the tube-fin evaporator measurements at two different driving temperature differences from (Seiler et al. 2020) were used. The corresponding fluid-side heat transfer coefficients were not specified but the fluid-side heat transfer is stated

as not limiting. As exemplary operation points the minimum refrigerant filling level and a relative filling level of 0.5 were chosen. The system pressure was specified as 1.45…1.5 kPa in the supplementary information and the fluid inlet temperature is 15°C, which is considered as comparable conditions. The heat flux was roughly estimated to be in the range of 3…10 kW/m² which is lower than the standard heat flux of this work of 30 kW/m². Though, given that the heat transfer coefficient of the mesh structures would presumably not fall but rather rise with decreasing heat flux (or driving temperature difference), as shown in chapter 5.3.1, the assessment of the hypothetical mesh evaporator can be regarded as conservative in comparison to the reference.

Impact of Fluid-Side Heat Transfer on the Performance of the Hypothetical Mesh Evaporator

Figure 72 compares the fluid-side heat transfer coefficient h_{fl}, the heat transfer coefficient of evaporation U_{ev} and the total heat transfer coefficient U_{tot} of the hypothetical mesh evaporator tube for the cases $h_{fl} = 5\ kW/(m^2K)$ in the left diagram and for $h_{fl} = 30\ kW/(m^2K)$ in the right diagram. For $h_{fl} = 5\ kW/(m^2K)$ the fluid side heat transfer is rather poor compared to the evaporation heat transfer. Consequently, the high performance of the mesh structure cannot be exploited and the total heat transfer coefficient U_{tot} stays at rather low values of 2.8…4.2 kW/(m²K), close to the fluid-side heat transfer coefficient. Despite the large difference between the U_{ev} values of KG03 and KG07, the resulting advantage of the KG03 system compared to KG07 is marginal due to the fluid-side limitation. In case of $h_{fl} = 30\ kW/(m^2K)$ (Figure 72, right) the fluid-side heat transfer is even higher than the evaporation heat transfer coefficients. The resulting total heat transfer coefficients are accordingly higher than for the first case. The KG03 system can now benefit from its better evaporation characteristics and reaches U_{tot} values of 9…14 kW/(m²K) compared to 5.4…8 kW/(m²K) of KG07.

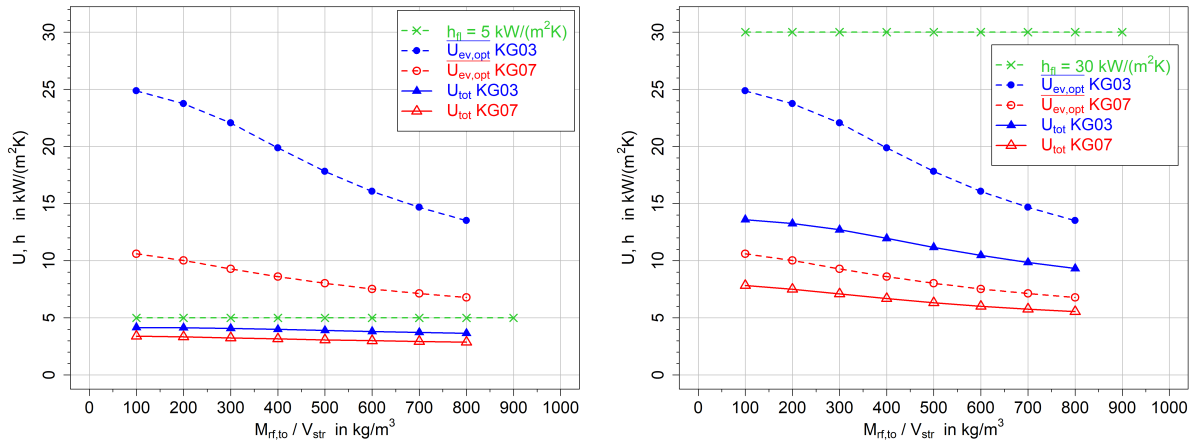

Figure 72: Fluid-side heat transfer coefficient, evaporation heat transfer coefficients and total heat transfer coefficients for the case of low (left) and high (right) fluid-side heat transfer, for a hypothetical wire mesh heat exchangers with mesh structure KG03 and KG07

In Figure 73 the UA values per construction volume V_{cnstr} of the hypothetical mesh evaporator are plotted for different construction-volume-specific refrigerant turnover demands and for the three different assumptions of the fluid-side heat transfer coefficient (5 / 10 / 30 kW/(m²K)). At $h_{fl} = 5\ kW/(m^2K)$ and $h_{fl} = 10\ kW/(m^2K)$ the values for the KG07 heat exchanger slightly exceed those of KG03 due to the lower structure height of KG07 and thus smaller heat exchanger volume. The fluid-side clearly limits the heat transfer and thus hinders the higher evaporation heat transfer coefficient of KG03 to come into effect. At $h_{fl} = 30\ kW/(m^2K)$ there is no fluid-side limitation anymore and the performance advantage of the KG03 structure prevails which leads to higher performance results of the KG03 evaporator compared to the KG07 variant. Despite its negative impact on the heat exchanger volume, the larger structure volume of

KG03 also has a positive effect: For a given refrigerant turnover demand per construction volume the structure can be cycled at lower relative refrigerant filling degrees of the pore volume compared to KG07, which is associated with a more beneficial interval of the dynamic U_{ev} curve.

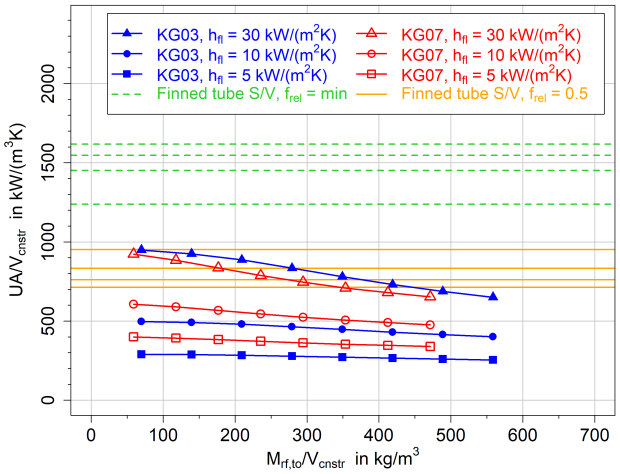

Figure 73: UA values related to construction volume vs. refrigerant turnover demand per construction volume for a hypothetical mesh evaporator with KG03-375-140 or KG07-900-280-05 mesh structure at different fluid-side heat transfer coefficients for the specified conditions; compared to reference results of a partially-flooded tube-fin evaporator from (Seiler et al. 2020)

Comparison of Mesh Evaporator and Reference Evaporator

Figure 73 further shows the derived performance values of the reference finned-tube evaporator, for a minimum relative refrigerant filling level ("Finned tube S/V, f_{rel} = min", dashed lines) and for a filling level of half the tube height ("Finned tube S/V, f_{rel} = 0.5", solid lines). For each filling level, performance data from four different measurement conditions were evaluated which produces four curves. Since a steady-state operation was assumed for the reference evaporator, the specific UA values are constant for all specific mass turnover demands $M_{rf,to}/V_{cnstr}$.

Comparing the results, it appears that the calculated construction-volume-specific UA values of the hypothetical mesh evaporator are roughly in the same dimension as the estimated values of the partially flooded tube-fin evaporator: While the finned tube evaporator reaches about 700…1000 kW/(m³K) for a relative filling level of 0.5, and 1200…1600 kW/(m³K) for minimum filling level, the UA/V_{cnstr} values of the mesh evaporator are in the range of 250…1000 kW/(m³K). Since the reference case is regarded as one of the most efficient concepts among the state of the art, the calculated UA/V_{cnstr} values of a mesh evaporator can be considered as a very promising outcome. Even if an exact prediction of the evaporation performance is not possible with the applied method and the results might be restricted to the presumed process conditions, the approach still provides a rough assessment of the potential of a mesh evaporator in cyclic operation under ideal conditions. For a thorough appraisal of the predicted potential and the comparison, the following issues should be taken into account:

Firstly, the required volume for the refrigerant pool of a partially flooded finned-tube evaporator was not included in the reference volume but only the construction volume V_{cnstr} of the heat exchanger. Incorporating for instance a pool volume equal to the heat exchanger construction volume would reduce the specific performance values of the finned tube concept to 50%. Furthermore, the operation of a partially flooded evaporator at minimum filling level is not a safe working point due to the risk of detachment of the tube from the pool, and thus, it is not realistic for practical use. Respective performance values in Figure 73 ("Finned tube S/V, f_{rel} = min", dashed lines) are therefore rather of theoretical interest than realistic expectations for an evaporator in a sorption module. As regards the hypothetical mesh

evaporator, only two exemplary mesh structures of KG03-375-140 and KG07-900-280-05 were considered. A systematic optimization of the mesh structure (e.g. reduction of the structure height and/or porosity of KG03) is expected to enable further performance enhancement.

Further relevant points for the interpretation of the results are:

- The calculated performance values are based on the process parameters stated above. Due to the dependence of the heat transfer coefficients on temperature, pressure and driving force conditions, deviating conditions could lead to different absolute values and different proportions between the respective heat exchanger types.
- Due to the presumed cylindrical shape of the mesh structure, the choice of the reference area has a crucial impact on the translation from the $\overline{U_{ev,opt}}$ values into UA values. It is not clear if the chosen cylindrical reference area through the middle of the structure height leads to realistic results and therefore it represents a considerable source of uncertainty.
- In the calculation of UA values for the mesh evaporator from $\overline{U_{ev,opt}}$ values, homogeneous and one-dimensional heat transfer over the heat exchanger is assumed. Potential effects from the temperature gradient along the tube axis on the evaporation behavior are not considered but could influence the actual performance results of such an evaporator.
- In an adsorption module, the refrigerant supply to the mesh evaporator-condenser would be realized by condensation of vapor on the structure surface, while in the evaporation experiments of this work the refrigerant was applied by the hydrostatic pressure of a refrigerant column. These different supply methods might be associated with diverging wettability and consequently to deviating evaporation characteristics of a mesh evaporator compared to the measurements on structure level.
- Measurement results of the mesh samples indicate that the evaporation characteristics are distinctly influenced by the surface properties of the porous structure. A slightly different raw material, different pretreatment, aging effects etc. might consequently lead to a diverging behavior of a mesh heat exchanger from the predicted characteristics.
- Since the construction volume of the heat exchanger is only one possible reference figure among others, very different proportions could result if the performance data was referred to another criterion. Other important criteria for the evaporator design are e.g. heat exchanger weight, material and manufacturing cost, mechanical and chemical stability and corrosion resistance, need for additional parts, compatibility with module and operation concept etc.

Apart from direct performance quantities, construction- and operation-related properties are relevant for the assessment of an evaporator concept as well: Since partially flooded finned tubes require a direct contact to a refrigerant pool, the evaporator construction is basically restricted to a flat single-layer arrangement of tubes in a broad pool. The mesh evaporator concept allows for a higher design flexibility in this aspect and might permit virtually any three-dimensional arrangement. Concerning operational reliability, the performance of a partially flooded finned tube is very sensitive on the refrigerant filling level. A very precise filling level adjustment is therefore required and any disturbance can have a dramatic effect. In case of the mesh evaporator, the optimal adjustment of the refrigerant charge interval can similarly be an essential but delicate prerequisite for reliable operation. For certain mesh structures a shift of the interval would lead to a considerable decrease in performance while others with less dynamic characteristics (such as sample structure KG03) are expected to be less sensitive. Another relevant issue for operational reliability is that a mesh evaporator in an adsorption module might occasionally lose refrigerant by means of dropping out of the structure under the impact of gravity. To avoid an irreversible loss of refrigerant it might be necessary in practice to keep the mesh evaporator in contact with a small refrigerant pool.

A decisive difference between the partially-flooded finned tube concept and the mesh evaporator concept is the required refrigerant mass which becomes important if a cyclic operation is envisaged: In order to maintain stable and safe flooding conditions, a relatively large refrigerant mass is needed for the finned tube evaporator. For the mesh evaporator, on the other hand, the refrigerant mass can be reduced to a minimum. Ideally, only the mass is required which is actually evaporated during the adsorption half-cycle, or the mass which allows for cycling in the optimal interval, respectively. Assuming a pool level which equals the tube height (neglecting the refrigerant displacement by the tubes) and a tube distance of one tube diameter, a refrigerant mass of about 2 kg would be required for an evaporator construction volume of 1 liter. The hypothetical mesh evaporator, in contrast, only requires about 0.2…0.58 kg (for structure type KG03-375-140) or 0.09…0.48 kg (KG07-900-280-05) per liter of construction volume, depending on the demanded specific refrigerant turnover $M_{rf,to}/V_{cnstr}$. This comparison illustrates that a wire mesh evaporator has a considerable advantage for a cyclic operational mode (alternating condenser and evaporator function), since the thermal mass plays a crucial role under these conditions. Naturally, also the thermal mass of the heat exchanger needs to be taken into account for a complete evaluation.

Conclusions on the Potential Assessment

Considering the assessment results, it can be concluded that wire mesh evaporators generally have the potential to reach high UA values and therewith high evaporation power but that some issues need to be respected in order to utilize that potential. In order to exploit the mostly high mean heat transfer coefficients of evaporation of the mesh structures, a sufficiently high fluid-side heat transfer must be ensured. This could for example be realized by using ducts with small cross-section and high fluid velocities or by means of ducts with internal structuring or turbulators. A high fluid-side heat transfer is on the other hand associated with an increase in pressure drop which makes a trade-off between performance gain and pumping effort necessary.

As respects the choice of the wire mesh structure, a low structure height should be chosen if the fluid-side heat transfer is the limiting factor, in order to minimize the construction volume. The evaporation heat transfer coefficient is less important in that case, therefore the refrigerant turnover demand can be satisfied by cycling the structure from completely saturated to dry. In case an elevated fluid-side heat transfer coefficient can be provided, it is reasonable to use a mesh structure with high mean U_{ev} values, as e.g. the fine mesh structure of KG03-375-140, since it can enhance the total heat transfer coefficient. A reduction of the structure height (e.g. to 3…5 mm) might also be sensible in this case to reduce the heat exchanger volume and to raise the mean evaporation heat transfer coefficient, except a very high refrigerant mass turnover is required. The choice of the best mesh structure could generally also be dependent on the refrigerant turnover demand. In that case the prioritization of power output or efficiency (COP) in the sorption module concept should be considered. For the operation of a mesh evaporator a precise adjustment of the starting point of the relative refrigerant filling degree is important to ensure passing through the most effective charge states.

Besides performance values, the particularities of a heat exchanger concept in terms of construction and operation in the adsorption module context needs to be taken into account. The partially-flooded finned tube evaporator, which was used as a reference here, is certainly a very good choice if a flat pool design and a precise adjustment of the filling level can be implemented, especially in steady state operation. A mesh (or generally porous structure) evaporator, on the other hand, might be of advantage in an unsteady cyclic condensation-evaporation operation, due to its small refrigerant mass and accordingly low thermal mass. It could thus be suitable for a compact and simple one-chamber adsorption module which only contains one adsorber-desorber heat exchanger and one evaporator-condenser heat exchanger without the need of valves or a refrigerant pump within the vacuum system. Generally, a mesh or porous structure heat exchanger might also be appropriate for steady-state evaporation in a module with separate

evaporator condenser. However, in that case the refrigerant supply would have to take place via capillary transport from a pool. Tests would have to reveal if the porous structures are suited for this kind of refrigerant supply under the given boundary conditions. A further potential advantage of a cyclic wire mesh evaporator is that it is not necessarily bound to a refrigerant pool. This fact could allow for a high degree of flexibility in terms of heat exchanger design and arrangement within the adsorption module which might be of great practical value.

Concerning cost, a wire mesh heat exchanger might benefit from the fact that the required raw materials – wire mesh and heat exchanger tubes or components – are commercially available in a broad variety. However, the assembly process might be more laborious than for other heat exchanger types and the field of application is presumably rather narrow.

6 SUMMARY, CONCLUSION & OUTLOOK

This chapter summarizes the main outcomes of the work and relates them to the defined scientific questions. In consideration of application context and objectives of the work, findings from experiments and simulations are depicted, the capabilities and limitations of the mathematical model are discussed and the potential of the envisaged technology is assessed.

Motivation and Objectives of the Work

Evaporation of the refrigerant water at sub-atmospheric pressures – which is employed in most adsorption heat pumps or chillers – is associated with certain material- and working-point-related challenges which implicate special requirements to a respective evaporator heat exchanger. Evaporation from thin refrigerant films has widely been proven to be an effective solution for this field of application, especially if structures with expanded surface areas are used which can utilize the capillary effect and provide extensive three-phase contact lines.

In this work, porous copper wire mesh structures were investigated as potential components for combined evaporator-condenser heat exchangers which can be operated cyclically in a compact one-chamber adsorption module. The porous structure is able to store refrigerant – which is intermittently supplied by condensation – by means of capillary forces. Additionally, it promotes the formation of thin refrigerant films in the vicinity of three-phase contact lines which allow for efficient evaporation. This cyclic operation inevitably involves unsteady process conditions which are characterized by the interdependence of dewetting dynamics and evaporation dynamics.

One objective of this work – which is addressed in the first scientific question (cf. chapter 3) – was to analyze the heat transfer mechanisms occurring in this unsteady dewetting and evaporation process. Furthermore, the impact of geometry parameters of the porous structure (porosity, pore size, structure height, wire mesh orientation) on these mechanisms was subject of research. In order to investigate these issues, evaporation measurements with ten different wire mesh structure samples were conducted under different thermodynamic conditions. Parallel to the experimental work, a simple resistance-capacitance model was developed which was intended to predict the unsteady evaporation behavior of wire mesh structures in dependence of geometry and boundary conditions, as claimed by the second scientific question. Finally, according to the third scientific question, two assessment methods were established to evaluate the suitability of the different mesh structure geometries for the envisaged application and to estimate the general prospects of wire mesh evaporators compared to state-of-the-art evaporators.

Evaporation and Dewetting Dynamics of the Standard Sample

As the main evaluation quantity for the evaporation performance of a porous structure sample, the effective evaporation heat transfer coefficient U_{ev} was used which refers to the temperature difference between structure base and saturation temperature of the ambient vapor. The connection between the

refrigerant charge state of the structure and its corresponding evaporation performance could be established by relating the heat transfer coefficient to the determined refrigerant mass values. The resulting characteristic curve shape of the standard sample KG01-800-250 (clear mesh width: 0.8 mm, wire diameter: 0.25 mm) for standard conditions ($p_{nom} = 1.3\ kPa$, $\dot{q}_{nom} = 30\ kW/m^2$) indicates that the dewetting process for this structure type basically follows the dynamics of a receding evaporation front: In this conception evaporation only takes place at the three-phase contact lines in a horizontal plane, which separates a completely liquid-saturated structure section below from a completely dry section above the front, and which continuously moves downward.

Impact of Structure Geometry

In regard to the impact of structure porosity, the experimental results do not show a consistent trend. Presumably, manufacturing tolerances of the mesh and contaminations of the surface obscured the appearance of a clear porosity effect. However, there is in all likelihood a general influence of porosity for the structures under consideration, since the U_{ev} dynamics indicate the occurrence of a receding evaporation front which necessarily implies a porosity dependence. Accordingly, a relatively low porosity is recommended for achieving high heat transfer coefficients. On the other hand, a low porosity reduces the volume-specific refrigerant storage capacity of the porous structure and increases material requirements and specific weight. The optimal porosity consequently depends on the individual requirements of the envisaged application.

The pore size of the wire mesh structure turned out to crucially affect evaporation performance, refrigerant storage capacity and dynamic refrigerant distribution during the dewetting process. In case of the large (KG04-2500-1000, $w_{mesh} = 2.5\ mm$) and medium (KG01-800-250, $w_{mesh} = 0.8\ mm$) pore size the heat transfer coefficient curves follow the typical course of a receding front process. The sample with small pore size (KG03-375-140, $w_{mesh} = 0.375\ mm$), in contrast, shows distinctly different dewetting dynamics. These findings are in accordance with a concept of Laurindo and Prat (Laurindo and Prat 1996) for the classification of characteristic drying patterns by means of the Bond number which quantifies the relation of gravitational to capillary forces. Due to a strong impact of capillary forces, a structure with small pore size tends to form a dynamic pattern of wet and dry clusters rather than a regular receding front. Based on comparisons with simulations from the evaporation model it was deduced that for sample KG03 (small pores) a certain receding front mechanism probably occurs as well. Though, instead of leaving a dry section a partially wetted or cluster-like section is assumed to form above the front. As soon as the evaporation front reaches the bottom of the structure, refrigerant from the partially wetted section is hypothesized to be drawn to the evaporation front position by capillary forces until the diminishing amount of refrigerant leads to a reduction of evaporating contact lines and finally to the complete dryout of the structure.

The particular refrigerant distribution and dewetting dynamics of the structure with small pore size has obviously a positive effect on evaporation performance, as the measured mean heat transfer coefficients are about twice as high as those of the samples with larger pore size. This advantage is attributed to the faster reduction of the conduction resistance of the refrigerant-filled section and the extensive three-phase contact lines in the partially wetted area and at the refrigerant front. Also in terms of the second performance-related requirement of cyclic evaporators – the volume-specific refrigerant storage capacity $M_{rf,cap}/V_{str}$ – a small pore size proved beneficial: Due to the pore-size-dependence of the capillary pressure a full (KG03) and nearly full (KG01) initial refrigerant saturation of the pore volume could be achieved for the structures with small and medium pore size, while for the largest pore size (KG04) the structure could only be filled partially. Overall, a small pore size turned out to be of advantage both in terms of heat transfer and refrigerant storage capacity for the investigated parameter range and is thus recommendable for power-focused as well as for efficiency-(COP-)focused adsorption module designs.

Measurements with mesh structures of different heights (5 mm, 10 mm, 15 mm) revealed that – in case of receding front dewetting dynamics – a low structure height is beneficial for reaching a high structure-volume-specific evaporation performance and storage capacity. Due to the fixed capillary height for a certain structure configuration (pore size) any excess structure height will hardly be filled and will only marginally contribute to evaporation. Additionally, a low structure height limits the conduction resistance of the refrigerant-filled section (which proved to widely dominate the total resistance) and thus excludes unfavorable evaporation intervals. On the heat exchanger level, though, a too low structure height might become unreasonable since the performance quantities should then be related to the total construction volume which includes the volume of the fluid ducts.

Investigations on the impact of the orientation angle of the wire mesh related to the carrier surface yielded ambiguous results. The absence of an orientation impact at high refrigerant filling degrees suggests that the horizontal wires without direct solder contact do contribute to vertical heat conduction, unlike assumed in the model conception. The lower U_{ev} level of the structure with 0°/90° wire orientation adumbrates a deviating dewetting behavior compared to that of a structure with 45° orientation. However, the significance of this observation remained unclear. An impact of mesh arrangement on refrigerant storage capacity could not be deduced from the experimental results. Consequently, a 45° orientation of the wire mesh might possibly bring a slight advantage in terms of heat transfer but further investigations would be required to confirm this supposition. On a general level, a high percentage of the thermally conductive material of a porous structure should ideally be oriented in heat flux direction in order to minimize the conduction resistance to the point of evaporation.

Impact of Wettability

Another crucial factor for the evaporation from porous structures which is not directly associated with structure geometry is the wettability of the surface. According to literature, surface topology and chemistry directly influence contact angle and meniscus shape which essentially determine the evaporation conditions in the evaporating thin film region at the three-phase contact lines. Furthermore, the macroscopic refrigerant distribution is certainly also influenced by the surface conditions. Despite the obvious predominance of the conduction resistance of the refrigerant-filled structure section in most refrigerant charge states, the experiments clearly demonstrated the relevance of surface properties for the evaporation dynamics. A deterioration of surface wettability due to contamination or sample aging for instance seem to cause a substantial reduction of the heat transfer coefficient in wide refrigerant charge ranges. Choice of material, structure pretreatment, storage and working conditions etc. should consequently be planned carefully and with consideration of possible effects on wettability.

Resistance-Capacitance Model

The standard version of the resistance-capacitance model is based on the model conception of a receding refrigerant front. The movement of the front position was implemented by means of moving temperature nodes and a time-dependent resistance and capacitance of the diminishing refrigerant filled section of the structure. Besides, thermal resistances for the solder contact between mesh and carrier and for heat conduction plus phase transition at the menisci were defined.

Comparisons of simulated heat transfer coefficients with respective measurement results showed that the predicted evaporation dynamics with decreasing refrigerant charge – i.e. the qualitative curve shape of U_{ev} vs. M_{rf} – matched the measurements for many structure configurations but not for all. As discussed before, the impact of gravitational forces compared to capillarity is strong in case of medium and large pore sizes (large Bond number) which promotes the formation of a receding front pattern. For small pores the relevance of capillary forces increases (small Bond numbers) and the refrigerant rather aggregates in wet and dry clusters. Accordingly, the receding front model could usually reproduce the evaporation

dynamics of structures with a clear mesh width of at least 0.8 mm fairly well but for a fine structure with a clear mesh width of 0.375 mm the agreement was poor. For very coarse mesh structures the prediction quality might be impaired if in the beginning a partially filled structure section forms due to insufficient capillary action.

The definition of the "threshold height" h_{thrsh} proved to crucially influence the simulated curve shape in the region of the U_{ev} maximum, as it defines the front height at which the dryout process starts. The assumption of a proportionality of h_{thrsh} with the clear mesh width turned out to be unrealistic but instead relatively constant threshold heights of about 0.5…1.0 mm appear appropriate, provided that the receding front concept applies. h_{thrsh} might further be dependent on the particular wettability conditions of the structure.

In the course of identifying possible dewetting mechanisms and refrigerant distribution patterns for structures with small pore size, three alternative model conceptions for the dewetting dynamics were developed. With model conception no. 4 "receding front + static front" the experimentally determined evaporation dynamics of sample KG03-375-140 could roughly be reproduced. With aid of this model conception the above-mentioned suppositions on the dewetting process in structures with small pore size were made: A fast receding front is assumed to form between a completely saturated section and a partially filled or cluster-like section. The refrigerant in the partially filled section is further assumed to be continuously transported to the evaporation front by capillary action. As the refrigerant mass diminishes, isolated refrigerant clusters are supposed to evaporate until the structure falls dry. The strictly sequential and idealized succession of these mechanisms in the model conception is certainly not realistic. However, the general principles are considered likely to occur in reality as components of a more complex dewetting process.

The quantitative results of the model predictions with the receding front approach are in good agreement with the measurements for some sample structures, such as the standard sample KG01-800-250. For several other samples, though, the simulated heat transfer coefficients exhibited large deviations from the experiment. Also the impacts of certain geometry factors on the heat transfer coefficient are not correctly mirrored by the standard model version in some cases. These inconsistencies can be attributed to inadequate thermal resistance definitions:

The resistance of the refrigerant-filled section of the structure (R_{rfs}) is calculated with aid of an effective thermal conductivity. For a wire orientation angle of 45° its definition is considered relatively reliable while for a 0°/90° angle the assumption of non-contribution of horizontal wires to the vertical conductivity seems questionable.

The thermal resistance of the solder contacts (R_{sldr}) between mesh structure and sample carrier was defined with the assumption of wedge-shaped wire ends. Its numerical value is very sensitive on the geometry assumptions, and comparisons of simulations with measurements indicate that the model underestimates the solder resistance. Despite its comparably low resistance contribution in most refrigerant charge intervals, it becomes relevant around the U_{ev} maximum where other resistances are small. The identification of the actual quantitative resistance of the solder contacts, for instance by means of separate thermal conduction measurements, might be helpful to find a more accurate resistance definition. In regard to sample manufacturing, the outcomes confirm that accurate soldering – or on a more generalized level: ensuring low-resistance joints – is essential to avoid considerable losses in the heat transfer coefficient.

For the description of the evaporation resistance R_{ev} – which is considered as heat conduction through the refrigerant film plus resistance of phase transition at the liquid-vapor interface in the vicinity of the three-phase contact lines – a modification of a simplified resistance definition for channel structures from

Kim et al. (Kim et al. 2003) and Chi (Chi 1976) was applied. Complementary, three different model conceptions for the arrangement and the corresponding length of the contact lines in the mesh structure were established. Evaluations of simulations indicated that the evaporation resistance is most probably overestimated by the model. This overestimation could either originate from a general inappropriateness of the resistance definition for channel structures or from an inadequacy of all three contact line conceptions. A weakness of the resistance definition itself is that it only covers the evaporation from the evaporating thin film region and disregards evaporation from the macroscopic meniscus. Besides, the parameter choice in the translation from a channel geometry to a mesh geometry might be unsuitable. The contact line length, on the other hand, might be underestimated due to the assumption of an arrangement in a virtually ideal horizontal plane at the evaporation front. Possibly, the evaporation front is actually less sharp but extends over a certain vertical length which might result in a considerably higher total contact line length.

Since the definitions for the solder resistance (R_{sldr}) and evaporation resistance (R_{ev}) are both constant in most refrigerant charge regimes, inaccurate resistance definitions can counterbalance each other and it can hardly be determined from a single measurement if a deviation of the simulation is caused by one or the other. Comparisons with different structure geometries allow for a better judgement and led to the conclusion that R_{sldr} is underestimated and R_{ev} is overestimated by the model. Still, a precise quantitative differentiation would require measurement data on the solder resistance or a fitting procedure with a large data set.

Apart from deficiencies of the model's resistance definitions, it should be noted that discrepancies between simulations and measurements can also arise from other sources. Possible sources are inapplicable simplifications and assumptions in the model (e.g. perfectly one-dimensional heat transfer, homogeneity of the refrigerant front, deviations from the dewetting conception), occurring heat transfer effects which are not covered by the model (e.g. nucleate boiling, boundary effects, evaporation at the gap between structure base and PP ring), deviations of the structure geometry and material properties from the nominal specifications, random variations in the dewetting dynamics, measurement uncertainties, etc.

Considering the outcomes of the model analysis, the resistance-capacitance model developed in this work is assessed as a valuable tool for a rough qualitative and quantitative prediction of the unsteady evaporation performance of wire mesh structures. Its integration into a model on heat exchanger level could allow for a predictive estimation of the dynamic behavior of a cyclically operated evaporator-condenser in a one-chamber adsorption module. In this way it might provide a basis for the development of dimensioning methods for wire mesh evaporators. In order to enhance the model's utility, the above-mentioned resistance definitions should be reviewed to improve the accuracy of the predictions. The inclusion of a model conception for nucleate boiling could positively affect their precision as well. Moreover, the model conception for the dewetting dynamics of structures with small pore sizes (no. 4 "receding front + static front") should be refined since these structures are among the most promising ones. Another decisive factor for the scope of the model is its transferability to other porous topologies and materials than copper wire mesh structures, as for instance metal foams, sintered fiber structures etc. So far, no reliable statement can be made but generally the transfer to different topologies is regarded as compatible with the model concept. Verifying the applicability of the model to different structure types might be an illuminative task for future work.

Potential of Wire Mesh Evaporators

In order to evaluate the prospects of the wire mesh structures for the envisaged application in evaporator heat exchangers, their performance indicators were referred to the structure volume since construction volume is a major limiting factor. Further, the mean specific heat transfer coefficients of the optimal refrigerant charge intervals for certain mass turnover demands were determined in order to enable an

assessment for both a power-focused and an efficiency-(COP-)focused adsorption module design. The structure with the smallest pore size (KG03-375-140) showed the best results for all conditions, with structure-height-specific mean heat transfer coefficients ($\overline{U_{ev,opt}}/h_{str}$) of up to 2500 kW/(m³K). For large mass turnover demands the structure with medium pore size but low structure height (KG07-900-280-05) reached nearly equally good results as KG03. A combination of small pore size and low structure height could allow for even higher performance values and might be interesting for future investigations and evaporator development. Apart from a small mesh spacing, small pore sizes could also be realized by means of dense packing of medium-sized mesh. Considering the goal of fine pores and a relatively low porosity, the utilization of different types of porous structures might be a reasonable option for evaporators with porous structures as well. Metal foams for instance could benefit from a high effective thermal conductivity; sintered fiber structures might be interesting due to the possibility of a fiber arrangement in heat flux direction.

The potential of a hypothetical wire mesh evaporator was assessed by combining the structure-level performance data of the best samples (KG03-375-140 and KG07-900-280-05) with presumptions on heat transfer conditions of a fluid duct concept. Resulting absolute thermal transmittance (UA) values were related to the construction volume of the heat exchanger and compared to data from a partially-flooded finned tube evaporator (Seiler et al. 2020) as a high-performance state-of-the-art reference. The outcomes reveal that in case of a limited fluid-side heat transfer coefficient the potential of a high-performance porous structure cannot be exploited. As a consequence, an application of advanced porous structures in an evaporator is only reasonable if an efficient fluid-side heat transfer can be provided, for instance with aid of high fluid velocities or internal turbulators.

Depending on the assumed operational conditions, the estimated performance of the hypothetical wire mesh evaporators (UA per construction volume of about 250…1000 kW/(m³K)) can reach the same dimensions as the reference data of the very efficient partially flooded finned tubes. Taking into account that the mesh structures have not been optimized in any way and that the refrigerant pool volume of the reference system is not included in the calculation, this outcome is considered as very promising. Certainly, the transfer of the performance data from structure level to heat exchanger level includes several sources of uncertainty. Nevertheless, the approach is regarded as adequate for a rough potential assessment.

In addition to good performance prospects, the potentially low required refrigerant mass (in the range of 0.09…0.58 kg per liter of construction volume) especially qualifies the mesh evaporator for a cyclic condensation / evaporation mode in compact one-chamber adsorption modules. The mesh (or porous structure) evaporator concept further incorporates the advantage of a high constructional flexibility in terms of shape and arrangement within the module. Overall, the outcomes of the potential assessment certainly justify further investigations on the utilization of porous structures for cyclic evaporator-condenser heat exchangers in adsorption heat transformation applications.

Besides the perspective of heat and mass transfer considered in this work, manufacturability, cost and market opportunity aspects naturally need to be taken into account. Generally, the mesh material is widely commercially available and its cost is estimated as moderate. However, the assembly procedure might be relatively laborious and the market opportunities are probably limited. A more profound analysis of these issues is required, though, in order to obtain a comprehensive potential assessment for wire mesh evaporators.

REFERENCES

3M Company (Ed.) (2010): 3M™ Thermally Conductive Acrylic Interface Pads 5589H and 5590H. Product Description. St. Paul, MN (Technical Data).

Alm, Birgit (2004): Keramische Massen für den Niederdruckspritzguss zur Herstellung von Komponenten für die Mikroverfahrenstechnik. Dissertation. Albert-Ludwigs-Universität Freiburg im Breisgau, Freiburg. Institut für Mikrosystemtechnik.

AMETEK GmbH (Ed.) (n.d.): Reference Temperature Calibrator Modell RTC-156 & RTC-157. Jofra. Datenblatt. AMETEK GmbH (Pub code SS-RTC156/157, Issue 0910). Available online at https://www.ametekcalibration.de/-/media/ametekcalibration/download_links/temperature/rtc/reference-temperature-calibrator-rtc-156-157-datenblatt-de.pdf, checked on 8/1/2020.

Baehr, Hans Dieter; Stephan, Karl (2008): Wärme- und Stoffübertragung. 6th ed. Berlin, Heidelberg: Springer.

Batzdorf, Stefan (2015): Heat transfer and evaporation during single drop impingement onto a superheated wall. Dissertation. TU Darmstadt. Available online at http://tuprints.ulb.tu-darmstadt.de/4542/, checked on 8/1/2020.

Bernhard, Frank (2014): Handbuch der Technischen Temperaturmessung. 2. Aufl. Berlin: Springer Vieweg (VDI-Buch).

Bodla, Karthik K.; Murthy, Jayathi Y.; Garimella, Suresh V. (2012): Direct Simulation of Thermal Transport Through Sintered Wick Microstructures. In *Journal of Heat Transfer* 134 (1), p. 187. DOI: 10.1115/1.4004804.

Bodla, Karthik K.; Murthy, Jayathi Y.; Garimella, Suresh V. (2013): Evaporation analysis in sintered wick microstructures. In *International Journal of Heat and Mass Transfer* 61, pp. 729–741. DOI: 10.1016/j.ijheatmasstransfer.2013.02.038.

Boertz, Hendrik (2017): Entwicklung und Bewertung eines Messkonzepts für die Untersuchung instationärer kapillargestützer Verdampfungsprozesse im Niederdruck. Master Thesis. Fraunhofer-Institut für Solare Energiesysteme ISE, Hochschule Kempten. Freiburg.

Boubaker, Riadh; Platel, Vincent; Berges, Alexis; Bancelin, Mathieu; Hannezo, Edouard (2015): Dynamic model of heat and mass transfer in an unsaturated porous wick of capillary pumped loop. In *Applied Thermal Engineering* 76, pp. 1–8. DOI: 10.1016/j.applthermaleng.2014.10.009.

Captec Entreprise (2017): Response time of heat flux sensor. E-Mail to Hendrik Boertz, 4/24/2017.

Captec SARL (Ed.) (2015): Heat flux sensor. delivery note. Lille.

Carey, V. P. (2008): Liquid-vapor phase-change phenomena. An introduction to the thermophysics of vaporization and condensation processes in heat transfer equipment. 2nd ed. New York: Taylor and Francis.

Chang, W.-S.; Wang, C.-C.; Shieh, C.-C. (2007): Experimental study of a solid adsorption cooling system using flat-tube heat exchangers as adsorption bed. In *Applied Thermal Engineering* 27 (13), pp. 2195–2199. DOI: 10.1016/j.applthermaleng.2005.07.022.

Chi, S. W. (1976): Heat pipe theory and practice. A sourcebook. Washington: Hemisphere Pub. Corp (Series in thermal and fluids engineering).

Childs, P. R. N.; Greenwood, J. R.; Long, C. A. (1999): Heat flux measurement techniques. In *Proceedings of the Institution of Mechanical Engineers, Part C: Journal of Mechanical Engineering Science* 213 (7), pp. 655–677. DOI: 10.1177/095440629921300702.

Clausse, Marc; Leprieur, Julien; Meunier, Francis (2011): Experimental test of plate evaporator for sorption refrigeration systems. In : International Sorption Heat Pump Conference (ISHPC11) (Refrigeration Science and Technology Proceedings). International Sorption Heat Pump Conference (ISHPC11). Padua, Italy, April 6–8, 2011, pp. 487–493.

Critoph, R. E. (2013): State of the Art in Gas Driven Heat Pumps. University of Warwick, Department of Energy and Climate Change. London, UK. Available online at http://wrap.warwick.ac.uk/97394/, checked on 8/1/2020.

Critoph, R. E.; Zhong, Y. (2005): Review of trends in solid sorption refrigeration and heat pumping technology. In *Proceedings of the Institution of Mechanical Engineers, Part E: Journal of Process Mechanical Engineering* 219 (3), pp. 285–300. DOI: 10.1243/095440805X6982.

Crößmann, Felix (2016): Untersuchung der Verdampfung aus strukturierten Oberflächen in Reinstoffatmosphäre. Dissertation. Technische Universität Darmstadt, Darmstadt. Available online at https://tuprints.ulb.tu-darmstadt.de/5578/, checked on 8/1/2020.

Czichos, Horst; Hennecke, Manfred (2008): Hütte. Das Ingenieurwissen. 33., aktualisierte Aufl. Berlin, New York: Springer-Verlag.

Dang, Bao Nam; van Helden, Wim; Luke, Andrea (2017): Investigation of water evaporation for closed sorption storage systems. In *Energy Procedia* 135, pp. 504–512. DOI: 10.1016/j.egypro.2017.09.493.

Dawoud, Belal (2013): Gas-Driven Sorption Heat Pumps; A Potential Trend-Setting Heating Technology. In Annett Kühn (Ed.): Thermally driven heat pumps for heating and cooling. Berlin: Universitätsverlag der TU Berlin, pp. 19–26.

Demir, Hasan; Mobedi, Moghtada; Ülkü, Semra (2008): A review on adsorption heat pump. Problems and solutions. In *Renewable and Sustainable Energy Reviews* 12 (9), pp. 2381–2403. DOI: 10.1016/j.rser.2007.06.005.

Deutsches Kupferinstitut (2005): Cu-ETP (Werkstoff-Datenblätter). Available online at https://www.kupferinstitut.de/fileadmin/user_upload/kupferinstitut.de/de/Documents/Shop/Verlag/Downloads/Werkstoffe/Datenblaetter/Kupfer/Cu-ETP.pdf, checked on 8/1/2020.

Deutsches Kupferinstitut Berufsverband e.V. (Ed.) (2019): Beständigkeitstabellen von Kupferwerkstoffen in verschiedenen Medien. Düsseldorf. Available online at https://www.kupferinstitut.de/wp-content/uploads/2020/02/DKI_Bestaendigkeitstabellen_DE.pdf, checked on 5/17/2020.

Dr. Dietrich Müller GmbH (Ed.) (2014): Thermally conductive products. Thermigrease® TG 20032. Ahlhorn. Available online at https://www.mueller-ahlhorn.com/fileadmin/Downloads/PDF/PDFDateien/TG_20032_fr.pdf, checked on 8/1/2020.

European Commission, Directorate-General for Energy (Ed.) (2016): Mapping and analyses of the current and future (2020 - 2030) heating/cooling fuel deployment (fossil/renewables). Executive summary. With assistance of Tobias Fleiter, Jörg Dengler, Felix Reitze, Frédéric Tuillé, Michael Hartner, Ulrich Reiter. European Commission. Available online at https://ec.europa.eu/energy/sites/ener/files/documents/Summary%20WP1%20and%20WP2.pdf, checked on 4/22/2020.

Fischer, D. A.; Cohen, G. G.; Shevchik, N. J. (1980): EXAFS investigation of oxidation processes in metallic Cu. In *Journal of Physics F: Metal Physics* 10 (5), L139-L142. DOI: 10.1088/0305-4608/10/5/004.

Fischer, Sebastian (2015): Experimental Investigation of Heat Transfer during Evaporation in the Vicinity of Moving Three-Phase Contact Lines. Dissertation. Technische Universität Darmstadt, Darmstadt. Fachbereich Maschinenbau.

Franz Meyer (2015): Heating with gas adsorption heat pumps. Edited by FIZ Karlsruhe - Leibniz Institute for Information Infrastructure GmbH. BINE Information Service (BINE-Projektinfo, 3/2015). Available online at http://www.bine.info/fileadmin/content/Publikationen/Projekt-Infos/2015/Projekt_03-2015/ProjektInfo_0315_engl_internetx.pdf, checked on 2/7/2020.

Gennes, P. G. de (1985): Wetting: statics and dynamics. In *Reviews of Modern Physics* 57 (3), pp. 827–863. DOI: 10.1103/RevModPhys.57.827.

Gennes, Pierre-Gilles de; Brochard-Wyart, Françoise; Quéré, David (2004): Capillarity and wetting phenomena. Drops, bubbles, pearls, waves. New York: Springer.

Giraud, Florine (2015a): Vaporization of water at subatmospheric pressure. Fundamentals of boiling phenomena and path towards the design of compact evaporators for sorption chillers. Dissertation. L'Institut National des Sciences Appliquées de Lyon, Lyon.

Giraud, Florine; Rullière, Romuald; Toublanc, Cyril; Clausse, Marc; Bonjour, Jocelyn (2015b): Experimental evidence of a new regime for boiling of water at subatmospheric pressure. In *Experimental Thermal and Fluid Science* 60, pp. 45–53. DOI: 10.1016/j.expthermflusci.2014.07.011.

Giraud, Florine; Rullière, Romuald; Toublanc, Cyril; Clausse, Marc; Bonjour, Jocelyn (2016): Subatmospheric pressure boiling on a single nucleation site in narrow vertical spaces. In *International Journal of Heat and Fluid Flow* 58, pp. 1–10. DOI: 10.1016/j.ijheatfluidflow.2015.12.002.

Hanlon, M. A.; Ma, H. B. (2003): Evaporation Heat Transfer in Sintered Porous Media. In *Journal of Heat Transfer* 125 (4), pp. 644–652. DOI: 10.1115/1.1560145.

Heubner, Ulrich (2014): Edelstahl Rostfrei – Eigenschaften. 5th ed. Edited by Informationsstelle Edelstahl Rostfrei (ISER). Düsseldorf (Merkblatt, 821). Available online at https://www.edelstahl-rostfrei.de/publikationen/iser-publikationen/merkblatt-821-edelstahl-rostfrei-eigenschaften, checked on 8/1/2020.

Höhmann, C.; Stephan, P. (2002): Microscale temperature measurement at an evaporating liquid meniscus. In *Experimental Thermal and Fluid Science* 26 (2–4), pp. 157–162. DOI: 10.1016/S0894-1777(02)00122-X.

Holmgren, Magnus (n.d.): XSteam. Thermodynamic properties of water and steam. Version XSteam.R. Translated from Matlab to R by Patrick Wagner.

Hong, Kwang Taek; Imadojemu, Harris; Webb, R. L. (1994): Effects of oxidation and surface roughness on contact angle. In *Experimental Thermal and Fluid Science* 8 (4), pp. 279–285. DOI: 10.1016/0894-1777(94)90058-2.

Hukseflux Thermal Sensors B.V. (Ed.) (2016): User Manual HFP01SC. Self-calibrating heat flux sensor. Hukseflux Thermal Sensors B.V. Available online at https://www.hukseflux.com/uploads/product-documents/HFP01SC_manual_v1624.pdf, checked on 8/1/2020.

Irawan, Anton (2006): Isothermal Drying of Pore Networks: Influence of Pore Structure on Drying Kinetics. Dissertation. Otto-von-Guericke-Universität Magdeburg, Magdeburg. Available online at https://opendata.uni-halle.de/bitstream/1981185920/10756/1/antirawan.pdf, checked on 8/1/2020.

Iverson, Brian D.; Davis, Tyler W.; Garimella, Suresh V.; North, Mark T.; Kang, Sukhvinder S. (2007): Heat and Mass Transport in Heat Pipe Wick Structures. In *Journal of Thermophysics and Heat Transfer* 21 (2), pp. 392–404. DOI: 10.2514/1.25809.

Joint Committee for Guides in Metrology (Ed.) (2008): Evaluation of measurement data - Guide to the expression of uncertainty in measurement. GUM 1995 with minor corrections. 1st ed. Joint Committee for Guides in Metrology (JCGM/WG 1). Available online at https://www.bipm.org/utils/common/documents/jcgm/JCGM_100_2008_E.pdf, checked on 8/1/2020.

Jousten, K.; Jitschin, W.; Sharipov, F.; Lachenmann, R. (2010): Wutz Handbuch Vakuumtechnik. 10th ed. Wiesbaden: Vieweg+Teubner Verlag (Vieweg + Teubner Praxis).

Keil, P.; Lützenkirchen-Hecht, D.; Frahm, R. (2006): Investigation of Room Temperature Oxidation of Cu in Air by Yoneda-XAFS. In : AIP Conference Proceedings. X-Ray Absorption Fine Structure - XAFS13: 13th International Conference. Stanford, California (USA), 9-14 July 2006: AIP, pp. 490–492.

Keysight Technologies (Ed.) (2014): Keysight 34970A/34972A Data Acquisition/Switch Unit. User's Guide. 4th ed. Loveland, CO, USA.

Khrustalev, D.; Faghri, A. (1995): Heat transfer in the inverted meniscus type evaporator at high heat fluxes. In *International Journal of Heat and Mass Transfer* 38 (16), pp. 3091–3101. DOI: 10.1016/0017-9310(95)00003-R.

Kim, Sung Jin; Ki Seo, Joung; Hyung Do, Kyu (2003): Analytical and experimental investigation on the operational characteristics and the thermal optimization of a miniature heat pipe with a grooved wick structure. In *International Journal of Heat and Mass Transfer* 46 (11), pp. 2051–2063. DOI: 10.1016/S0017-9310(02)00504-5.

Kühn, Annett; Ziegler, Felix (2013): Cycle Basics of Thermally Driven Heat Pumps. In Annett Kühn (Ed.): Thermally driven heat pumps for heating and cooling. Berlin: Universitätsverlag der TU Berlin, pp. 5–18.

Kummer, Harry; Füldner, Gerrit; Henninger, Stefan K. (2015): Versatile siloxane based adsorbent coatings for fast water adsorption processes in thermally driven chillers and heat pumps. In *Applied Thermal Engineering* 85, pp. 1–8. DOI: 10.1016/j.applthermaleng.2015.03.042.

Kunkelmann, Christian; Ibrahem, Khalid; Schweizer, Nils; Herbert, Stefan; Stephan, Peter; Gambaryan-Roisman, Tatiana (2012): The effect of three-phase contact line speed on local evaporative heat transfer: Experimental and numerical investigations. In *International Journal of Heat and Mass Transfer* 55 (7-8), pp. 1896–1904. DOI: 10.1016/j.ijheatmasstransfer.2011.11.044.

Lang, R.; Roth, M.; Stricker, M.; Westerfeld, T. (1999): Development of a modular zeolite-water heat pump. In *Heat and Mass Transfer* 35 (3), pp. 229–234. DOI: 10.1007/s002310050318.

Lang, Rainer; Dawoud, Belal; Miltkau, Thorsten; Stricker, Marc (2001): Sorptionswärmepumpe. Applied for by Vaillant GmbH on 8/6/2001. Patent no. EP1178269A1.

Lanzerath, Franz; Seiler, Jan; Erdogan, Meltem; Schreiber, Heike; Steinhilber, Matthias; Bardow, André (2016): The impact of filling level resolved. Capillary-assisted evaporation of water for adsorption heat pumps. In *Applied Thermal Engineering* 102, pp. 513–519. DOI: 10.1016/j.applthermaleng.2016.03.052.

Laurindo, Joao Borges; Prat, Marc (1996): Numerical and experimental network study of evaporation in capillary porous media. Phase distributions. In *Chemical Engineering Science* 51 (23), pp. 5171–5185. DOI: 10.1016/S0009-2509(96)00341-7.

Laurindo, Joao Borges; Prat, Marc (1998): Numerical and experimental network study of evaporation in capillary porous media. Drying rates. In *Chemical Engineering Science* 53 (12), pp. 2257–2269. DOI: 10.1016/S0009-2509(97)00348-5.

Lee, Shao-Kuan; Hsu, Hsiu-Ching; Tuan, Wei-Hsing (2016): Oxidation Behavior of Copper at a Temperature below 300 °C and the Methodology for Passivation. In *Materials Research* 19 (1), pp. 51–56. DOI: 10.1590/1980-5373-MR-2015-0139.

Li, Chen; Peterson, G. P. (2006): Evaporation/Boiling in Thin Capillary Wicks (II) - Effects of Volumetric Porosity and Mesh Size. In *Journal of Heat Transfer* 128 (12), p. 1320. DOI: 10.1115/1.2349508.

Li, Chen; Peterson, G. P.; Wang, Yaxiong (2006): Evaporation/Boiling in Thin Capillary Wicks (l) - Wick Thickness Effects. In *Journal of Heat Transfer* 128 (12), p. 1312. DOI: 10.1115/1.2349507.

Ludwig Schneider Messtechnik GmbH (Ed.) (2017): Kalibrierschein. Messkette mit Fühler. Physics 1000; WT-MI-303-D-30E-So, Pt100. With assistance of Andreas Bleifuß, Lilia Wittenbeck. Wertheim.

Ma, H. B.; Peterson, G. P. (1997): Temperature Variation and Heat Transfer in Triangular Grooves with an Evaporating Film. In *Journal of Thermophysics and Heat Transfer* 11 (1), pp. 90–97. DOI: 10.2514/2.6205.

MakeItFrom.com (Ed.) (2009): ISO Solder Alloy 402 (IEC C30, Sn97Cu3). Iron Boar Labs Ltd. Available online at https://www.makeitfrom.com/material-properties/ISO-Solder-Alloy-402-IEC-C30-Sn97Cu3, checked on 8/1/2020.

Marek, R.; Straub, J. (2001): Analysis of the evaporation coefficient and the condensation coefficient of water. In *International Journal of Heat and Mass Transfer* 44 (1), pp. 39–53. DOI: 10.1016/S0017-9310(00)00086-7.

Mayekawa Mycom (Ed.) (n.d.): AdRef-Noa. Adsorption Chiller with Zeolite. Available online at https://www.mayekawausa.com/pdf/brochures/AdRef-Noa_brochure.pdf, checked on 1/30/2020.

McGillis, Wade R.; Fitch, John S.; Hamburgen, William R.; Carey, Van P. (1990): Pool Boiling Enhancement Techniques for Water at Low Pressure. Western Research Laboratory. Palo Alto, USA (WRL Research Report, 90/9). Available online at https://www.hpl.hp.com/techreports/Compaq-DEC/WRL-90-9.pdf, checked on 8/1/2020.

Meunier, F. (2001): Adsorptive cooling: a clean technology. In *Clean Products and Processes* 3 (1), pp. 8–20. DOI: 10.1007/s100980000096.

Meunier, Francis (2013): Adsorption heat powered heat pumps. In *Applied Thermal Engineering* 61 (2), pp. 830–836. DOI: 10.1016/j.applthermaleng.2013.04.050.

Mittelbach, Walter; Daßler, Ingo (2011): Verfahren und Vorrichtung zum Ausführen eines alternierenden Verdampfungs- und Kondensationsprozesses eines Arbeitsmediums. Applied for by SorTech AG on 3/25/2011. App. no. DE102011015153A1.

MKS Instruments, Inc. (Ed.) (2014-2018): a-Baratron® Absolute Analog Heated Capacitance Manometer. Datasheet. MKS Instruments, Inc. Andover, MA, USA. Available online at www.mksinst.com, checked on 4/27/2018.

Müller, Michael; Dr. Dietrich Müller GmbH (2019): Spezifische Wärmekapazität von Thermigrease TG 20032 (specific heat capacity of Thermigrease TG 20032). E-Mail to Rahel Volmer, 7/20/2019.

Nan, Tongchao; Wu, Jichun; Li, Kaixuan; Jiang, Jianguo (2019): Permeability Estimation Based on the Geometry of Pore Space via Random Walk on Grids. In *Geofluids* 2019, pp. 1–10. DOI: 10.1155/2019/9240203.

National Institute of Standards and Technology (NIST) (1998): Molar gas constant R. Available online at https://physics.nist.gov/cgi-bin/cuu/Value?r|search_for=gas+constant, updated on 12/12/2017, checked on 8/1/2020.

Nau, Matthias (2002): Elektrische Temperaturmessung. Mit Thermoelementen und Widerstandsthermometern. Fulda: JUMO - M. K. Juchheim GmbH & Co.

Nicholas, J. V.; White, D. R. (2001): Traceable temperatures. An introduction to temperature measurement and calibration. 2nd ed. Chichester, New York: Wiley.

Núñez, Tomas; Mittelbach, Walter; Henning, Hans-Martin (2007): Development of an adsorption chiller and heat pump for domestic heating and air-conditioning applications. In *Applied Thermal Engineering* 27 (13), pp. 2205–2212. DOI: 10.1016/j.applthermaleng.2005.07.024.

Pezzutto, Simon; Croce, Silvia; Zambotti, Stefano; Kranzl, Lukas; Novelli, Antonio; Zambelli, Pietro (2019): Assessment of the Space Heating and Domestic Hot Water Market in Europe - Open Data and Results. In *Energies* 12 (9), p. 1760. DOI: 10.3390/en12091760.

Pfeiffer Vacuum GmbH: HiCube 80 Eco, DN 40 ISO-KF, MVP 015-2. Datasheet. Edited by Pfeiffer Vacuum GmbH. Available online at https://static.pfeiffer-vacuum.com/productPdfs/PMS7310000.de.pdf, checked on 4/11/2019.

Pialago, Edward Joshua T.; Yoo, Jinho; Zheng, Xiru; Kim, Byung Ryeon; Hong, Sung Joo; Kwon, Oh Kyung; Park, Chan Woo (2020): Experimental investigation of the heat transfer performance of capillary-assisted horizontal evaporator tubes with sintered porous hydrophilic copper-carbon nanotube-titanium dioxide (Cu-CNT-TiO2) composite coatings for adsorption chiller. In *International Journal of Heat and Mass Transfer* 147, p. 118958. DOI: 10.1016/j.ijheatmasstransfer.2019.118958.

Plourde, F.; Prat, M. (2003): Pore network simulations of drying of capillary porous media. Influence of thermal gradients. In *International Journal of Heat and Mass Transfer* 46 (7), pp. 1293–1307. DOI: 10.1016/S0017-9310(02)00391-5.

Potash, M.; Wayner, P.C (1972): Evaporation from a two-dimensional extended meniscus. In *International Journal of Heat and Mass Transfer* 15 (10), pp. 1851–1863. DOI: 10.1016/0017-9310(72)90058-0.

Prat, M.; Bouleux, F. (1999): Drying of capillary porous media with a stabilized front in two dimensions. In *Physical review. E, Statistical physics, plasmas, fluids, and related interdisciplinary topics* 60 (5 Pt B), pp. 5647–5656. DOI: 10.1103/physreve.60.5647.

R Core Team (n.d.): R. A language and environment for statistical computing. Vienna, Austria: R Foundation for Statistical Computing. Available online at http://www.R-project.org/, checked on 8/1/2020.

Raben, I. A.; Beaubouef, R. T.; Commerford, G. E. (1965): A Study of Heat Transfer in Nucleate Pool Boiling of Water at Low Pressure. In *Chemical engineering progress symposium series* 61 (57), pp. 249–257.

Ranjan, Ram; Murthy, Jayathi Y.; Garimella, Suresh V. (2009): Analysis of the Wicking and Thin-Film Evaporation Characteristics of Microstructures. In *Journal of Heat Transfer* 131 (10), p. 101001. DOI: 10.1115/1.3160538.

Ranjan, Ram; Murthy, Jayathi Y.; Garimella, Suresh V. (2011): A microscale model for thin-film evaporation in capillary wick structures. In *International Journal of Heat and Mass Transfer* 54 (1–3), pp. 169–179. DOI: 10.1016/j.ijheatmasstransfer.2010.09.037.

Ranjan, Ram; Patel, Abhijeet; Garimella, Suresh V.; Murthy, Jayathi Y. (2012): Wicking and thermal characteristics of micropillared structures for use in passive heat spreaders. In *International Journal of Heat and Mass Transfer* 55 (4), pp. 586–596. DOI: 10.1016/j.ijheatmasstransfer.2011.10.053.

Röckelein GmbH (Ed.) (2010): Scotch 5590 H. Rechnung (Invoice). Nürnberg.

Sabir, H. M.; Bwalya, A. C. (2002): Experimental study of capillary-assisted water evaporators for vapour-absorption systems. In *Applied Energy* 71 (1), pp. 45–57. DOI: 10.1016/S0306-2619(01)00042-3.

Scheller, Gerd; Krummeck, Stefan (2018): Messunsicherheit einer Temperaturmesskette. mit Beispielrechnungen. Fulda: JUMO - M. K. Juchheim GmbH & Co (FAS625).

Schnabel, Lena; Füldner, Gerrit; Velte, Andreas; Laurenz, Eric; Bendix, Philip; Kummer, Harry; Wittstadt, Ursula (2018a): Innovative Adsorbent Heat Exchangers: Design and Evaluation. In Hans-Jörg Bart, Stephan Scholl (Eds.): Innovative Heat Exchangers, vol. 61. Cham: Springer International Publishing, pp. 363–394.

Schnabel, Lena; Scherr, Christopher; Weber, Christine (2008a): Water as Refrigerant - Experimental Evaluation of Boiling Characteristics at Low Temperatures and Pressures. In : Proceedings of International Sorption Heat Pump Conference 2008 (ISHPC2008). Seoul, KOREA.

Schnabel, Lena; Scherr, Christopher; Weber, Christine (2008b): Water as Refrigerant - Experimental Evaluation of Boiling Characteristics at Low Temperatures and Pressures. In : Proceedings of the VII Minsk International Seminar. VII Minsk International Seminar “Heat Pipes, Heat Pumps, Refrigerators, Power Sources”. Minsk, Belarus, September 8–11, 2008.

Schnabel, Lena; Volmer, Rahel; Warlo, Alexander; Schossig, Peter (2018b): Evaluation of Different Evaporator Designs and Concepts for Sorption Processes Using Water as Refrigerant. In International Institute of Refrigeration (IIR) (Ed.): 13th IIR Gustav Lorentzen Conference on Natural Refrigerants. Proceedings. 13th IIR Gustav Lorentzen Conference on Natural Refrigerants. Valencia, Spain, June 2018, 18 to 20. Institute for Energy Engineering, Universitat Politècnica de València - UPV. Paris, France.

Schnabel, Lena; Witte, Kai Thomas; Kowol, Jacek; Schossig, Peter (2010): Vergleich von Verdampferstrukturen für das Kältemittel Wasser. In Deutscher Kälte- und Klimatechnischer Verein e.V. (Ed.): Tagungsband Deutsche Kälte- und Klimatagung 2010. Deutsche Kälte- und Klimatagung 2010. Magdeburg, November 17-19, 2010. Magdeburg.

Schnabel, Lena; Witte, Kai Thomas; Kowol, Jacek; Schossig, Peter (2011): Evaluation of Different Evaporator Concepts for Thermally Driven Sorption Heat Pumps and Chillers. In : International Sorption Heat Pump Conference (ISHPC11) (Refrigeration Science and Technology Proceedings). International Sorption Heat Pump Conference (ISHPC11). Padua, Italy, April 6–8, 2011.

Seiler, Jan; Lanzerath, Franz; Jansen, Christoph; Bardow, André (2019): Only a wet tube is a good tube. Understanding capillary-assisted thin-film evaporation of water for adsorption chillers. In *Applied Thermal Engineering* 147, pp. 571–578. DOI: 10.1016/j.applthermaleng.2018.08.024.

Seiler, Jan; Volmer, Rahel; Krakau, Dennis; Pöhls, Julien; Ossenkopp, Franziska; Schnabel, Lena; Bardow, André (2020): Capillary-assisted evaporation of water from finned tubes – Impacts of experimental setups and dynamics. In *Applied Thermal Engineering* 165, p. 114620. DOI: 10.1016/j.applthermaleng.2019.114620.

Spahn, H. J.; Szuder, T. F. (2014): Verdampfer-Wärmetauscher. Applied for by Vaillant GmbH on 11/14/2014. App. no. DE102014223250A1.

Spahn, H. J.; Szuder, T. F. (2015): Wärmetauscher für einen Verdampfer. Applied for by Vaillant GmbH on 7/16/2015. App. no. DE102015213320A1.

Stahmer, Klaus-Werner; Teske, Hans-Jörg; Gerhold, Malte (2012): Widerstand von Staubschüttungen. Messverfahren und Einflussgrößen. In *Gefahrstoffe - Reinhaltung der Luft* 72 (10), pp. 437–445. Available online at http://www.dguv.de/medien/ifa/de/pub/grl/pdf/2012_131.pdf, checked on 8/2/2020.

Stephan, Karl (1988): Wärmeübergang beim Kondensieren und beim Sieden. Berlin, Heidelberg: Springer (Wärme- und Stoffübertragung).

Stephan, P. C.; Busse, C. A. (1992): Analysis of the heat transfer coefficient of grooved heat pipe evaporator walls. In *International Journal of Heat and Mass Transfer* 35 (2), pp. 383–391. DOI: 10.1016/0017-9310(92)90276-X.

Stephan, Peter (1992): Wärmedurchgang bei Verdampfung aus Kapillarrillen in Wärmerohren. Düsseldorf: VDI-Verlag (Fortschritt-Berichte VDI Reihe 19: Wärmetechnik, Kältetechnik, 59).

Stephan, Peter (2013): Wärmerohre. N5. In VDI e.V., VDI-Gesellschaft Verfahrenstechnik und Chemieingenieurwesen (Ed.): VDI-Wärmeatlas. Mit 320 Tabellen. 11th ed. Berlin: Springer Vieweg, pp. 1675–1686.

The European Parliament and the Council of the European Union (4/16/2014): Regulation (EU) No 517/2014 of the European Parliament and of the Council of 16 April 2014 on fluorinated greenhouse gases and repealing Regulation (EC) No 842/2006. In *Official Journal of the European Union* L 150/195. Available online at https://eur-lex.europa.eu/legal-content/EN/TXT/PDF/?uri=CELEX:32014R0517&from=EN, checked on 1/30/2020.

The International Association for the Properties of Water and Steam (Ed.) (2003): Advisory Note No. 1. Uncertainties in Enthalpy for the IAPWS Formulation 1995 for the Thermodynamic Properties of Ordinary Water Substance for General and Scientific Use (IAPWS-95) and the IAPWS Industrial Formulation 1997 for the Thermodynamic Properties of Water and Steam (IAPWS-IF97). Vejle, Denmark. Available online at http://iapws.org/relguide/Advise1.pdf, checked on 8/2/2020.

The International Association for the Properties of Water and Steam (Ed.) (2007): Revised Release on the IAPWS Industrial Formulation 1997 for the Thermodynamic Properties of Water and Steam. Lucerne, Switzerland. Available online at http://www.iapws.org/relguide/IF97-Rev.pdf, checked on 8/2/2020.

Thimmaiah, Poovanna Cheppudira; Sharafian, Amir; Huttema, Wendell; Bahrami, Majid (2015): Effects of Fin Spacing and Fin Height of Capillary-Assisted Tubes on the Performance of a Low Operating Pressure Evaporator for an Adsorption Cooling System. In *Heat Pipe Science and Technology, An International Journal* 6 (3-4), pp. 195–204. DOI: 10.1615/HeatPipeScieTech.2016017181.

Thimmaiah, Poovanna Cheppudira; Sharafian, Amir; Huttema, Wendell; McCague, Claire; Bahrami, Majid (2016a): Effects of capillary-assisted tubes with different fin geometries on the performance of a low-operating pressure evaporator for adsorption cooling system applications. In *Applied Energy* 171, pp. 256–265. DOI: 10.1016/j.apenergy.2016.03.070.

Thimmaiah, Poovanna Cheppudira; Sharafian, Amir; Huttema, Wendell; Osterman, Chantal; Ismail, Ameer; Dhillon, Aashkaran; Bahrami, Majid (2016b): Performance of finned tubes used in low-pressure capillary-assisted evaporator of adsorption cooling system. In *Applied Thermal Engineering* 106, pp. 371–380. DOI: 10.1016/j.applthermaleng.2016.06.038.

Thimmaiah, Poovanna Cheppudira; Sharafian, Amir; Rouhani, Mina; Huttema, Wendell; Bahrami, Majid (2017): Evaluation of low-pressure flooded evaporator performance for adsorption chillers. In *Energy* 122, pp. 144–158. DOI: 10.1016/j.energy.2017.01.085.

Touzé, Ewen; Cougnon, Charles (2018): Study of the air-formed oxide layer at the copper surface and its impact on the copper corrosion in an aggressive chloride medium. In *Electrochimica Acta* 262, pp. 206–213. DOI: 10.1016/j.electacta.2017.12.187.

Tuller, Markus; Or, Dani (2001): Hydraulic conductivity of variably saturated porous media: Film and corner flow in angular pore space. In *Water Resources Research* 37 (5), pp. 1257–1276. DOI: 10.1029/2000WR900328.

Vaillant GmbH (Ed.) (n.d.): zeoTHERM. Zeolith-Gas-Wärmepumpe. Betriebsanleitung. Remscheidt (0020107399_04). Available online at https://www.vaillant.de/documents/download/280037, checked on 2/7/2020.

van Stralen, S.J.D.; Cole, R.; Sluyter, W. M.; Sohal, M. S. (1975): Bubble growth rates in nucleate boiling of water at subatmospheric pressures. In *International Journal of Heat and Mass Transfer* 18 (5), pp. 655–669. DOI: 10.1016/0017-9310(75)90277-X.

VDI e.V., VDI-Gesellschaft Verfahrenstechnik und Chemieingenieurwesen (Ed.) (2013): VDI-Wärmeatlas. Mit 320 Tabellen. 11th ed. Berlin: Springer Vieweg.

Viessmann Deutschland GmbH (Ed.) (2013): Gas-Wärmepumpe VITOSORP 200-F. Allendorf (Eder). Available online at https://www.esb.de/fileadmin/user_upload/download/energieeffizienz/Infobroschuere_Viessman_Gaswaermepumpe_Vitosorp.pdf, checked on 8/2/2020.

Volmer, Rahel; Eckert, Julia; Füldner, Gerrit; Schnabel, Lena (2017): Evaporator development for adsorption heat transformation devices – Influencing factors on non-stationary evaporation with tube-fin heat exchangers at sub-atmospheric pressure. In *Renewable Energy* 110, pp. 141–153. DOI: 10.1016/j.renene.2016.08.030.

W. Baelz & Sohn GmbH & Co. (Ed.) (n.d.): Technische Beschreibung. Absorptionskälteanlage Typ «Biene». Heilbronn. Available online at https://www.baelz.de/systeme/kaelte/biene/, checked on 4/24/2020.

Wang, Chad-Yang; Tu, Chuan-Jing (1988): Effects of non-condensable gas on laminar film condensation in a vertical tube. In *International Journal of Heat and Mass Transfer* 31 (11), pp. 2339–2345. DOI: 10.1016/0017-9310(88)90165-2.

Wang, Hao; Garimella, Suresh V.; Murthy, Jayathi Y. (2007): Characteristics of an evaporating thin film in a microchannel. In *International Journal of Heat and Mass Transfer* 50 (19–20), pp. 3933–3942. DOI: 10.1016/j.ijheatmasstransfer.2007.01.052.

Wayner, P. C. (1982): Adsorption and capillary condensation at the contact line in change of phase heat transfer. In *International Journal of Heat and Mass Transfer* 25 (5), pp. 707–713. DOI: 10.1016/0017-9310(82)90176-4.

Wayner, P. C.; Coccio, C. L. (1971): Heat and mass transfer in the vicinity of the triple interline of a meniscus. In *AIChE Journal* 17 (3), pp. 569–574. DOI: 10.1002/aic.690170317.

Wayner, P. C.; Kao, Y. K.; LaCroix, L. V. (1976): The interline heat-transfer coefficient of an evaporating wetting film. In *International Journal of Heat and Mass Transfer* 19 (5), pp. 487–492. DOI: 10.1016/0017-9310(76)90161-7.

Wayner, Peter C. (1999): Intermolecular forces in phase-change heat transfer. 1998 Kern award review. In *AIChE Journal* 45 (10), pp. 2055–2068. DOI: 10.1002/aic.690451004.

Wee, Sang-Kwon (2004): Microscale observables for heat and mass transport in sub-micron scale evaporating thin film. Dissertation. Texas A&M University. Available online at http://oaktrust.library.tamu.edu/handle/1969.1/312, checked on 8/2/2020.

Wen, Rongfu; Xu, Shanshan; Lee, Yung-Cheng; Yang, Ronggui (2018): Capillary-driven liquid film boiling heat transfer on hybrid mesh wicking structures. In *Nano Energy* 51, pp. 373–382. DOI: 10.1016/j.nanoen.2018.06.063.

White, Lee R. (1982): Capillary rise in powders. In *Journal of Colloid and Interface Science* 90 (2), pp. 536–538. DOI: 10.1016/0021-9797(82)90319-8.

Wieser, M. E. (2006): Atomic weights of the elements 2005 (IUPAC Technical Report). In *Pure and Applied Chemistry* 78 (11), pp. 2051–2066. DOI: 10.1351/pac200678112051.

Witte, Kai Thomas (2016): Experimentelle Untersuchungen zum Sieden in Metallfaserstrukturen im Bereich niederer Drücke. Dissertation. Technische Universität Darmstadt, Darmstadt. Available online at http://tuprints.ulb.tu-darmstadt.de/5126, checked on 8/2/2020.

Witte, Kai Thomas; Schnabel, Lena; Andersen, Olaf (2009): Verdampferentwicklung für den Einsatz in thermisch betriebenen Kältemaschinen. In Deutscher Kälte- und Klimatechnischer Verein e.V. (Ed.): Tagungsband Deutsche Kälte- und Klimatagung 2009. Deutsche Kälte- und Klima-Tagung 2009. Berlin, November 18-20, 2009.

Wittstadt, Ursula; Füldner, Gerrit; Andersen, Olaf; Herrmann, Ralph; Schmidt, Ferdinand (2015): A New Adsorbent Composite Material Based on Metal Fiber Technology and Its Application in Adsorption Heat Exchangers. In *Energies* 8 (8), pp. 8431–8446. DOI: 10.3390/en8088431.

Wittstadt, Ursula; Füldner, Gerrit; Laurenz, Eric; Warlo, Alexander; Große, André; Herrmann, Ralph et al. (2017): A novel adsorption module with fiber heat exchangers. Performance analysis based on driving temperature differences. In *Renewable Energy* 110, pp. 154–161. DOI: 10.1016/j.renene.2016.08.061.

Wong, Shwin-Chung; Chen, Chung-Wei (2013): Visualization experiments for groove-wicked flat-plate heat pipes with various working fluids and powder-groove evaporator. In *International Journal of Heat and Mass Transfer* 66, pp. 396–403. DOI: 10.1016/j.ijheatmasstransfer.2013.07.012.

Xia, Z. Z.; Yang, G. Z.; Wang, R. Z. (2008): Experimental investigation of capillary-assisted evaporation on the outside surface of horizontal tubes. In *International Journal of Heat and Mass Transfer* 51 (15–16), pp. 4047–4054. DOI: 10.1016/j.ijheatmasstransfer.2007.11.042.

Yiotis, A. G.; Boudouvis, A. G.; Stubos, A. K.; Tsimpanogiannis, I. N.; Yortsos, Y. C. (2004): Effect of liquid films on the drying of porous media. In *AIChE Journal* 50 (11), pp. 2721–2737. DOI: 10.1002/aic.10265.

Yiotis, A. G.; Stubos, A. K.; Boudouvis, A. G.; Tsimpanogiannis, I. N.; Yortsos, Y. C. (2005): Pore-Network Modeling of Isothermal Drying in Porous Media. In *Transport in Porous Media* 58 (1-2), pp. 63–86. DOI: 10.1007/s11242-004-5470-8.

Yuan, Yuehua; Lee, T. Randall (2013): Contact Angle and Wetting Properties. In Gianangelo Bracco, Bodil Holst (Eds.): Surface Science Techniques, vol. 51. Berlin, Heidelberg: Springer, pp. 3–34.

Zhao, T.S; Liao, Q. (2000): On capillary-driven flow and phase-change heat transfer in a porous structure heated by a finned surface. Measurements and modeling. In *International Journal of Heat and Mass Transfer* 43 (7), pp. 1141–1155. DOI: 10.1016/S0017-9310(99)00206-9.

NOMENCLATURE

In the following tables the symbols and abbreviations employed in the work are listed, subdivided into latin symbols, greek symbols and abbreviations. All symbols are listed strictly in alphabetical order (relating to variables and indices), irrespective of upper or lower case or additional accent signs (dot, bar). If numeric elements and / or latin plus greek symbols are included in the symbol, the order is determined firstly by numeric elements, secondly by latin symbols and thirdly by greek symbols.

Latin Symbols

Symbol	Unit	Denotation
A	$°C^{-1}$	coefficient of Pt100 standard characteristic polynomial (cf. B.2)
a		half width of "error limit" interval
A_{hfs}	m^2	cross-sectional area of the heat flux sensor
a_s	m^2/kg	mass-specific surface area of the porous solid
A_{str}	m^2	cross-sectional area of the sample structure
B	$°C^{-2}$	coefficient of Pt100 standard characteristic polynomial (cf. B.2)
Bo	$-$	Bond number (equation (2-6))
Ca	$-$	capillary number (equations (2-7), (2-11))
C_{crr}	J/K	absolute heat capacity of the sample carrier (model)
c_{crr}	$J/(kg\,K)$	specific heat capacity of sample carrier material
c_{CuETP}	$J/(kg\,K)$	specific heat capacity of copper, type CuETP (cf. Table 20)
C_{htr}	J/K	absolute heat capacity of the heater block (model)
c_{rf}	$J/(kg\,K)$	specific heat capacity of liquid refrigerant
$C_{rfs,rf}$	J/K	absolute heat capacity of the refrigerant in the refrigerant-filled section of the porous structure (receding front model conception)
$C_{rfs,str}$	J/K	absolute heat capacity of the mesh material in the refrigerant-filled section of the porous structure (receding front model conception)
D_{crr}	m	diameter of the sample carrier (cf. Table 20)
d_{edg}	m	edge length of the square cross section of ideal straight cuboid pores
$D_{htr,tb}$	m	diameter of the large-diameter section of the upper part of the heater block (cf. Table 20)
$D_{htr,tt}$	m	diameter of the small-diameter section of the upper part of the heater block (cf. Table 20)
D_{str}	m	diameter of porous sample structure (cf. Table 20)
d_{wire}	m	wire diameter of mesh structure

e	$kg/(m^2 s)$	evaporation flux density (equation (2-12))
g	m/s^2	gravitational acceleration
h_{adf}	m	height (thickness) of adhesive foil (cf. Table 20)
h_c	m	capillary height (equation (2-4))
h_{crr}	m	height of the sample carrier (cf. Table 20)
h_{ec}	m	height of an elementary cell of a mesh structure
$h_{eff,tf}$	$W/(m^2 K)$	effective heat transfer coefficient of the evaporating thin film region of a meniscus in a groove, after Chi (Chi 1976), cf. equation (4-43)
h_{fin}	m	fin height of a groove structure, cf. equation (4-42)
h_{fl}	$W/(m^2 K)$	fluid-side heat transfer coefficient
h_{front}	m	height position of the evaporation front in the porous structure, referring to the structure base (receding front model conception)
$h_{front,init}$	m	initial height position of the evaporation front in the porous structure, referring to the structure base (receding front model conception)
$h_{hfs,Cu}$	m	height (thickness) of each copper layer of the heat flux sensor (cf. Table 20)
$h_{hfs,epx}$	m	height (thickness) of epoxy layer inside the heat flux sensor (cf. Table 20)
$h_{htr,tb}$	m	height of the large-diameter section of the upper part of the heater block (cf. Table 20)
$h_{htr,tt}$	m	height of the small-diameter section of the upper part of the heater block (cf. Table 20)
h_{rf}	$W/(m^2 K)$	refrigerant-side heat transfer coefficient (cf. Table 1)
h_{str}	m	height of the wire mesh structure
h_{tcf}	m	height (thickness) of thermally conductive foil (between heat flux sensor and sample carrier) (cf. Table 20)
h_{thrsh}	m	threshold height for the evaporation front below which the dewetting mechanism changes (receding front model conception; cf. chapter 4.2.3, equations (4-33) and (4-34), Figure 28)
k	$-$	coverage factor (for expanded uncertainty U)
k_p	m^2	permeability
L	m	characteristic length (= distance between two pore nodes in equation (2-6))
L_{cap}	m	characteristic length of the viscous front (equation (2-10))
l_{cl}	m	total length of three-phase contact lines in a wetted porous structure
$l_{cl,ec}$	m	length of three-phase contact lines per elementary cell of a wetted porous structure
L_g	m	characteristic length of the gravity front (equation (2-8))
l_{ly}	m	layer spacing (distance between centers of two neighboring mesh layers)
l_{mesh}	m	mesh spacing of mesh structure (distance between the axes two neighboring wires within one piece of mesh)
L_{str}	m	characteristic length (height) of the porous structure sample
l_{strp}	m	strip spacing of mesh structure (distance between centers of two neighboring mesh strips / layers)
M_{crr}	kg	mass of sample carrier
M_{cum}	kg	cumulated evaporated refrigerant mass
M_{H2O}	kg/mol	molar mass of water vapor (cf. Table 20)
$\dot{M}_l$	kg/s	liquid mass flow rate
M_{rf}	kg	total refrigerant mass inside the porous structure

$M_{rf,cap}$	kg	experimental refrigerant storage capacity of a porous structure sample
$M_{rf,init}$	kg	initial refrigerant mass inside the porous structure (model)
$M_{rf,th}$	kg	theoretical refrigerant storage capacity of a porous structure (full saturation of pore volume assumed)
$M_{rf,to}$	kg	refrigerant mass turnover demand (predefined requirement of a refrigerant mass which needs to be evaporated within one evaporation half-cycle of an evaporator-condenser heat exchanger; assessment method 2)
M_{str}	kg	mass of the wire mesh structure (without carrier)
$\dot{M}_{vap}$	kg/s	vapor mass flow rate
$\dot{M}_{vap,init}$	kg/s	initial vapor mass flow rate (model)
n_{ec}	$-$	total number of elementary cells in a mesh structure
Nu	$-$	Nusselt number
p	kPa	pressure
P_{htr}	W	heating power
p_{ncg}	kPa	partial pressure of non-condensable gases
p_{nom}	kPa	nominal system pressure (for a particular parameter set)
p_{sat}	kPa	water vapor saturation pressure (above sample surface)
p_{vc}	kPa	measured absolute pressure inside the vacuum chamber, corrected for time delay
$p_{vc,raw}$	kPa	measured absolute pressure inside the vacuum chamber, uncorrected
$\dot{Q}$	W	heat flow
$\dot{q}$	W/m^2	heat flux
$\dot{Q}_{cap}$	W	capacitive heat flow of the sample carrier
$\dot{Q}_{ev}$	W	heat flow of evaporation
$\dot{q}_{ev}$	W/m^2	effective heat flux of evaporation (in model / measurements: related to A_{str})
$\dot{Q}_{hfs}$	W	heat flow through the heat flux sensor
$\dot{q}_{hfs}$	W/m^2	heat flux through the heat flux sensor (in measurements: corrected for time delay and inaccuracy of characteristic curve)
$\dot{Q}_{hfs,meas}$	W	heat flow measured by the heat flux sensor, uncorrected (used in B.5)
$\dot{q}_{hfs,meas}$	W/m^2	heat flux measured by the heat flux sensor, uncorrected (used in B.5)
$\dot{q}_{hfs,raw}$	W/m^2	measured heat flux through the heat flux sensor, uncorrected
$\dot{q}_{hfs,tcorr}$	W/m^2	measured heat flux through the heat flux sensor, corrected for scanning time delay
$\dot{q}_{htr}$	W/m^2	heat flux applied by the heating element, referring to the cross-sectional area of the sample structure (A_{str}) (model)
$\dot{Q}_{htr,loss}$	W	heat loss from the heater block to the ambient (cf. B.5)
$\dot{Q}_k$	W	heat flow through element k (model)
$\dot{Q}_{k,init}$	W	initial heat flow through element k (model)
Q_{leak}	$mbar\ l/s$	leak rate of the vacuum system
$\dot{q}_{nom}$	W/m^2	nominal heat flux (for a particular parameter set)
$\dot{q}_{real}$	W/m^2	actual heat flux through the heat flux sensor (cf. B.7.2)
R	K/W	absolute thermal resistance

$\bar{r}$	m	average pore size (equation (2-8))
R_0	Ω	nominal ohmic resistance of a Pt100 resistance thermometer at 0°C (cf. B.2)
R_{crr}	K/W	absolute thermal resistance of the sample carrier (model)
Re	$-$	Reynolds number
R_{ev}	K/W	absolute thermal resistance of evaporation at the refrigerant front (definition according to equation (4-44); receding front model conception)
$r_{ev,tf}$	$m\,K/W$	length-specific thermal resistance for the heat transfer through the evaporating thin film region of a meniscus in a groove, after Chi (Chi 1976), cf. equation (4-42)
R_{H2O}	$J/(kg\,K)$	specific gas constant of water vapor (cf. Table 20)
R_{hfs}	K/W	absolute thermal resistance of the heat flux sensor unit, consisting of heat flux sensor, thermally conductive foil, adhesive foil and contact resistances (model)
R_{htr}	K/W	absolute thermal resistance of the heater block (model)
R_{ohm}	Ω	ohmic resistance
R_{Pt}	Ω	actual electric resistance of the sensor element of the Pt100 resistance thermometer during evaporation measurements (cf. B.7.1)
$R_{Pt,cal}$	Ω	actual electric resistance of the sensor element of the Pt100 resistance thermometer during calibration process (cf. B.7.1)
$R_{Pt,cal,meas}$	Ω	measured electric resistance signal of the Pt100 resistance thermometer during calibration process (cf. B.7.1)
$R_{Pt,meas}$	Ω	measured electric resistance signal of the Pt100 resistance thermometer during evaporation measurements (cf. B.7.1)
R_{rfs}	K/W	absolute thermal conduction resistance of the refrigerant-filled section of the porous structure (receding front model conception)
R_{sldr}	K/W	absolute thermal resistance of the solder contacts between wire ends of the mesh structure and sample carrier (model)
r_{tb}	m	tube radius
$R_{tot,str}$	K/W	total thermal resistance of the mesh structure (between temperature at the structure base ϑ_{strb} and saturation temperature ϑ_{sat}) (model)
R_{univ}	$J/(mol\,K)$	universal gas constant (cf. Table 20)
S_{hfs}	Vm^2/W	sensitivity of the heat flux sensor
S_p	V/Pa	sensitivity of the pressure sensor
t	s	time
t_i	s	point in time of evaporation measurement or simulation (elapsed time since beginning of evaporation from capillary-stored refrigerant; counter i)
t_{init}	s	initial point in time
U		expanded uncertainty (equation (4-21))
u		standard uncertainty
UA	W/K	absolute thermal transmittance ("UA value"; product of overall heat transfer coefficient $U_{fl,rf}$ and reference area A)
u_c		combined standard uncertainty
U_{ev}	$W/(m^2K)$	overall heat transfer coefficient of evaporation (from sample structure) (related to A_{str} and to the temperature difference $\vartheta_{strb} - \vartheta_{sat}$)
$\overline{U_{ev}}$	$W/(m^2K)$	mean evaporation heat transfer coefficient (referring to the complete evaporation measurement)
$U_{ev,init}$	$W/(m^2K)$	initial condition for the overall heat transfer coefficient of evaporation from sample structure (related to A_{str}; model)

$U_{ev,max}$	$W/(m^2K)$	maximum evaporation heat transfer coefficient of a measurement
$\overline{U_{ev,opt}}$	$W/(m^2K)$	mean evaporation heat transfer coefficient of the optimum refrigerant charge interval for a certain refrigerant mass turnover demand (assessment method 2)
$U_{ev,start}$	$W/(m^2K)$	evaporation heat transfer coefficient of the starting phase (first minute) of a measurement
$U_{fl,rf}$	$W/(m^2K)$	overall heat transfer coefficient (from heat transfer fluid to vapor atmosphere)
U_{hf}	V	heat flux sensor voltage (cf. B.7.2)
U_p	V	pressure sensor voltage (cf. B.7.3)
u_{rel}	%	relative standard uncertainty
U_{rf}	$W/(m^2K)$	refrigerant-side heat transfer coefficient (cf. Table 1)
U_{tot}	$W/(m^2K)$	overall heat transfer coefficient of a hypothetical mesh evaporator (fluid side heat transfer coefficient h_{fl} plus heat transfer coefficient of evaporation U_{ev}; cf. chapter 5.5)
V_{cnstr}	m^3	construction volume of a hypothetical mesh evaporator (defined as the enveloping cuboid with quadratic cross section around the heat exchanger tube; cf. chapter 5.5)
V_{crr}	l	volume of the sample carrier (cf. Table 20)
V_{htr}	l	total volume of heater block (top plus bottom part) (cf. Table 20)
V_{str}	m^3	total volume of a wire mesh structure
V_{vs}	m^3	empty volume of the vacuum system
v	m/s	characteristic velocity
w_{fin}	m	fin width of a groove structure, cf. equation (4-43)
w_{mesh}	m	clear mesh width (void distance between two adjacent parallel wires within a mesh layer; cf. Figure 19)
z	m	height coordinate (cf. chapter 2.2)

Greek Symbols

Symbol	Unit	Denotation
α_{wire}	°	wire orientation angle of mesh structure (angle between carrier surface and wire axis)
γ_{lg}	N/m	interfacial tension between liquid and gas phase (surface tension)
γ_{sg}	N/m	interfacial tension between solid and gas phase
γ_{sl}	N/m	interfacial tension between solid and liquid phase
Δh_v	J/kg	specific enthalpy of vaporization
$\Delta h_{v,init}$	J/kg	initial specific enthalpy of vaporization (model)
Δp_c	Pa	capillary pressure
$\Delta p_{p,cal}$	Pa	pressure deviation due to calibration inaccuracy of the pressure sensor (cf. B.7.3)
$\Delta p_{p,drift}$	Pa	pressure deviation due to drift of the pressure sensor's characteristic (cf. B.7.3)
$\Delta p_{p,\vartheta}$	Pa	pressure deviation due to temperature coefficients (cf. B.7.3)
Δp_{sat}	Pa	inaccuracy of saturation pressure (cf. B.7.6)
$\Delta p_{sat,appr}$	Pa	approximation inaccuracy of the vapor pressure curve according to IAPWS IF-97 (cf. B.7.6)
$(\Delta p/\Delta t)_{leak}$	kPa/s	pressure rise rate of the total vacuum system due to leakage, determined from a pressure rise test

$\Delta\dot{Q}_{cc}$	W	heat flow difference due to deviation of the characteristic curve of the heat flux sensor (used in B.5)
$\Delta\dot{q}_{hf,cal}$	W/m^2	heat flux deviation due to calibration inaccuracy of the heat flux sensor (cf. B.7.2)
$\Delta\dot{q}_{hf,resp}$	W/m^2	heat flux deviation due to the heat flux sensor's response time behavior (cf. B.7.2)
$\Delta R_{\vartheta,DAQ}$	Ω	difference between actual and measured resistance of the Pt100 resistance thermometer during evaporation measurement, due to inaccuracy of data acquisition unit (cf. B.7.1)
$\Delta R_{\vartheta,DAQ,cal}$	Ω	difference between actual and measured resistance of the Pt100 resistance thermometer during calibration procedure, due to inaccuracy of data acquisition unit (cf. B.7.1)
$\Delta R_{\vartheta,drift}$	Ω	deviation due to drift of the electric resistance of the sensor element in the Pt100 resistance thermometer (cf. B.7.1)
$\Delta S_{hfs,drift}$	Vm^2/W	deviation of the heat flux sensor's sensitivity due to drift (cf. B.7.2)
$\Delta t_{delay,x}$	s	time delay between time stamp and actual scanning time of the measurand x, caused by data acquisition
Δt_{leak}	s	elapsed time since end of the last system evacuation
$\Delta U_{hf,DAQ}$	V	difference between actual and measured heat flux sensor voltage, due to inaccuracy of data acquisition unit (cf. B.7.2)
$\Delta U_{p,DAQ}$	V	difference between actual and measured pressure sensor voltage, due to inaccuracy of data acquisition unit (cf. B.7.3)
$\Delta z_{strb,mp}$	m	distance between structure base and measuring position of sample carrier temperature ϑ_{crr}
$\Delta\rho_{lg}$	kg/m^3	density difference between liquid and gas (or between two fluids)
$\Delta\vartheta$	K	driving temperature difference (wall superheat) of the evaporation process (= $\vartheta_{strb} - \vartheta_{sat}$ (this work) or= $\vartheta_{wall} - \vartheta_{sat}$ (general))
$\Delta\vartheta_{block}$	K	temperature difference between actual temperatures of the sensor elements of Pt100 and reference thermometer due to thermal non-homogeneity inside the block calibrator (cf. B.7.1)
$\Delta\vartheta_{fit}$	K	temperature fit inaccuracy of the characteristic curve of the Pt100 resistance thermometer after calibration (cf. B.7.1)
$\Delta\vartheta_{lm}$	K	logarithmic mean temperature difference (cf. Table 1)
$\Delta\vartheta_{ref,sens}$	K	temperature difference between actual and measured temperature of the reference thermometer during calibration procedure (cf. B.7.1)
$\Delta\vartheta_{resp}$	K	temperature difference between sample carrier and sensor element of Pt100 resistance thermometer due to response time behavior of the thermometer (cf. B.7.1)
θ	°	apparent contact angle
ϑ	$°C$	temperature
$\overline{\vartheta_{cc}}$	$°C$	mean ambient temperature inside the climatic chamber
ϑ_{crr}	$°C$	temperature of the sample carrier (measurements: on height of temperature sensor; model: central temperature node of the carrier)
$\vartheta_{crr,raw}$	$°C$	measured temperature of the sample carrier, uncorrected
$\vartheta_{crr,sldr}$	$°C$	temperature at the interface between sample carrier and solder contacts which connect the wire mesh strips to the carrier (model)
ϑ_{front}	$°C$	temperature of the mesh material at the current position of the evaporation front (h_{front}) (receding front model conception)
ϑ_{he}	$°C$	temperature of the heating element inside the heater block (model)
$\vartheta_{hfs,crr}$	$°C$	temperature at the interface between heat flux sensor unit and sample carrier (model)

ϑ_{htr}	$°C$	temperature in the center of the heater block (model)
$\vartheta_{htr,hfs}$	$°C$	temperature at the interface between heater block and the heat flux sensor unit (model)
ϑ_k	$°C$	temperature of temperature node k (model)
$\vartheta_{k,init}$	$°C$	initial temperature of temperature node k (model)
ϑ_l	$°C$	temperature of the liquid
ϑ_{Pt}	$°C$	actual temperature of the sensor element inside the tip of the Pt100 resistance thermometer (cf. B.7.1)
$\vartheta_{Pt,cal}$	$°C$	actual temperature of the sensor element inside the tip of the Pt100 resistance thermometer during calibration procedure (cf. B.7.1)
$\vartheta_{ref,cal}$	$°C$	actual temperature of the sensor element inside the tip of the reference thermometer during calibration procedure (cf. B.7.1)
$\vartheta_{ref,cal,meas}$	$°C$	measured temperature of the reference thermometer in calibration procedure (cf. B.7.1)
ϑ_{rfs}	$°C$	temperature in the center of the refrigerant-filled section of the porous structure (receding front model conception)
ϑ_{sat}	$°C$	saturation temperature of water vapor (above the sample structure)
$\vartheta_{sldr,str}$	$°C$	temperature at the interface between solder contacts and mesh structure (receding front model conception)
ϑ_{strb}	$°C$	temperature at the base of the porous structure
ϑ_{wall}	$°C$	wall temperature (pool boiling)
ϑ_∞	$°C$	equilibrium temperature (cf. B.7.5)
λ_{adf}	$W/(m\,K)$	thermal conductivity of adhesive foil (cf. Table 20)
λ_{crr}	$W/(m\,K)$	thermal conductivity of the sample carrier material
λ_{eff}	$W/(m\,K)$	effective thermal conductivity of a composite structure (e.g. fluid-filled porous solid)
λ_{epx}	$W/(m\,K)$	thermal conductivity of epoxy resin (cf. Table 20)
λ_{CuETP}	$W/(m\,K)$	thermal conductivity of copper, type CuETP (cf. Table 20)
λ_{fl}	$W/(m\,K)$	thermal conductivity of the fluid
λ_l	$W/(m\,K)$	thermal conductivity of the liquid
$\lambda_{rf,k}$	$W/(m\,K)$	thermal conductivity of the liquid refrigerant at temperature node k (model)
$\lambda_{rf,k,init}$	$W/(m\,K)$	initial thermal conductivity of the liquid refrigerant at temperature node k (model)
$\lambda_{rf,l}$	$W/(m\,K)$	thermal conductivity of the liquid refrigerant (water)
$\lambda_{rfs,eff}$	$W/(m\,K)$	effective thermal conductivity of the refrigerant-filled section of the porous structure (receding front model conception; cf. equations (4-41) and (4-42))
λ_s	$W/(m\,K)$	thermal conductivity of the solid
λ_{sldr}	$W/(m\,K)$	thermal conductivity of the solder material (cf. Table 20)
λ_{tcf}	$W/(m\,K)$	thermal conductivity of thermally conductive foil (between heat flux sensor and sample carrier) (cf. Table 20)
μ		expected value of a measurand (uncertainty analysis)
μ_l	$Pa\,s$	dynamic viscosity of the liquid
ρ_{crr}	kg/m^3	density of the sample carrier material
ρ_{CuETP}	kg/m^3	density of copper, type CuETP (cf. Table 20)
ρ_l	kg/m^3	density of the liquid

$\rho_{rf,k}$	kg/m^3	density of the refrigerant at temperature node k (model)
$\rho_{rf,k,init}$	kg/m^3	initial density of the refrigerant at temperature node k (model)
ρ_s	kg/m^3	density of the solid
τ	s	time constant characterizing the step response of a dynamic first-order system
τ_{crr}	s	time constant of the sample carrier
ϕ	$-$	volume fraction of the solid in porous media
ψ	%	porosity of wire mesh structure / porous structure

Abbreviations

Abbreviation	Denotation
ABS	acrylonitrile butadiene styrene
COP	coefficient of performance
DAQ	data acquisition (device)
DC	direct current
DMM	digital multimeter
ETP (Cu-ETP)	Electrolytic-Tough-Pitch (copper material type)
GUM	Guide to the expression of uncertainty in measurement (Joint Committee for Guides in Metrology 2008)
IAPWS	The International Association for the Properties of Water and Steam
IAPWS IF-97	Industrial Formulation 1997 for the Thermodynamic Properties of Water and Steam, released by The International Association for the Properties of Water and Steam (IAPWS)
LED	light-emitting diode
LES	linear equation system
PC	personal computer
PMMA	polymethyl methacrylate
PP	polypropylene
Pt100	platinum resistance thermometer with a nominal ohmic resistance of 100 Ω at 0°C
PVDF	polyvinylidene fluoride
RTD	resistance temperature detector

LIST OF FIGURES

LIST OF TABLES

APPENDIX

In the appendix, additional information on theoretical background (A), evaporation measurements (B), and the mathematical model (C) is provided.

A Theoretical Background

A.1 Vapor Pressure Curve of Water

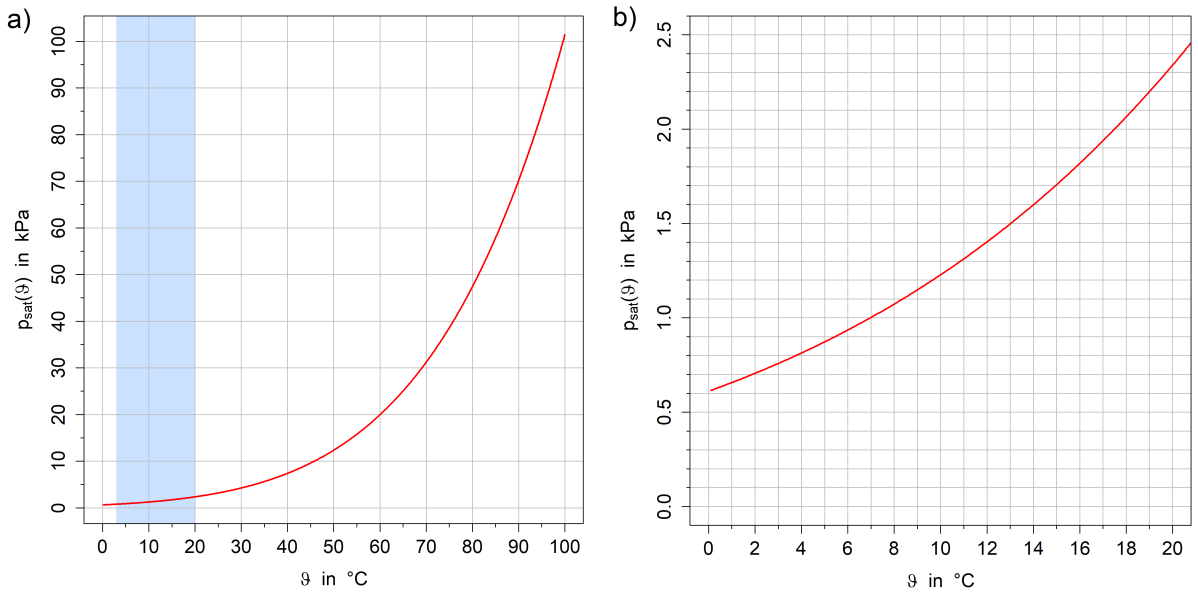

Figure 74: Vapor pressure curve of water for a) the temperature range 0.1…100°C (left), and b) the temperature range 0.1…20°C which includes typical evaporation temperatures of adsorption heat transformation devices (right); values based on the formulation of IAPWS IF-97 (The International Association for the Properties of Water and Steam 2007)

B Measurements

B.1 Specifications of Devices and Sensors

Table 9: Specifications of test rig devices and parts

Component	Model / Type	Supplier	Specifications
vacuum chamber	- (custom product)	VACOM GmbH	stainless steel DIN 1.4404, basic dimensions: 350 mm x 313.9 mm (DxH)
scroll vacuum pump	nXDS 6iC	Edwards Ltd	nom. rotational speed: 1800 rpm, displacement: 6.8 m^3/h, motor power: 260 W, ultimate vacuum (total pressure): 0.02 mbar
condenser heat exchanger (tube-fin HX)	- (custom product)	WätaS GmbH	nominal thermal output: 5.57 kW, dimensions: 380 mm x 90 mm x 296 mm (LxWxH), material: stainless steel V4A
electropneumatic bellows angle valve	XLA-50G-M9	SMC Corporation	flange size: ISO-KF 50, internal leakage: 10^{-10} Pa m^3/s, external leakage: 10^{-11} Pa m^3/s, operating time: 0.24 s
thermostat (condenser)	RK 8KP	Lauda Dr. R. Wobser GmbH & Co. KG	working temperature range: -45…200°C, temperature constancy: +/- 0.02 K (at -10°C in bath), cooling power at +20°C: 800 W, cooling power at 0°C: 700 W, cooling power at -30°C: 400 W, heating power: 2 kW, pumping capacity: 24 l/min (0.5 bar), bath volume: 8 l
thermostat (anti-cavitation heat exchanger)	Thermostat K22S C20	medingLab GmbH & Co. KG	working temperature range: -20…120°C, temperature constancy: +/- 0.02 K (at 70°C in bath), cooling power at +20°C: 780 W, cooling power at 0°C: 450 W, cooling power at -10°C: 250 W, heating power: 1.8 kW, pumping capacity: 25 l/min (0.5 bar), bath volume: 10 l

(Table 9 continued:)

Component	Model / Type	Supplier	Specifications
thermostat (refrigerant thermal conditioning)	ministat 230w-cc-NR	Peter Huber Kältemaschinenbau GmbH	working temperature range: -40…200°C, temperature constancy: +/- 0.02 K (at -10°C in bath), cooling power at +20°C: 420 W, cooling power at 0°C: 380 W, cooling power at -10°C: 330 W, heating power: 1.5 kW, pumping capacity: 27 l/min (0.7 bar), bath volume: 3.2 l
anti-cavitation heat exchanger (tube-fin HX)	- (custom product)	-	material: copper
refrigerant pump (peristaltic pump)	LabDos P 100	HiTec Zang GmbH	dosing range: 0…100 ml/min, rotational speed: 0…200 rpm, conveyance stability: < 1%
heat exchanger for refrigerant thermal conditioning (counterflow heat exchanger)	- (custom product)	-	material: stainless steel
heating element (el. heating wire)	- (custom product)	Watlow GmbH	max. power: 140 W, el. resistance: approx. 86 Ω, total diameter: 1.47 mm, total length: 830 mm, shape: double spiral
refrigeration unit of climatic chamber	LAIKA EL 04123 N	CIBIN s.r.l.	temperature range: -2 … 15°C; cooling power: 754 W at 0°C and ambient temperature
climatic chamber	Z 1812	Tam Europe limited	dimensions: 1.20 m x 1.20 m x 2.00 m (LxWxH)
data acquisition/switch unit	34972A	Keysight Technologies, Inc.	3-slot mainframe with built-in 6½ digit DMM, USB interface
20-channel multiplexer modules (2x)	34901A	Keysight Technologies, Inc.	20+2 channels (2/4 wire), scanning speed: 60 ch/s
multifunction module	34907A	Keysight Technologies, Inc.	two 8-bit digital I/O ports, 26-bit event counter, two 16-bit analog outputs
DC power supply unit	Genesys™ GENH750W GENH150-5	TDK Lambda	power output: 0…750 W, output voltage: 0…150 V, output current: 0…5 A
PC	Optiplex 780	Dell Technologies Inc.	Windows 7 (64 bit); CPU: Intel® Core™ 2 Quad CPU Q9650 @ 3.00 GHz 3.00 GHz, RAM: 4.0 GB

Table 10: Sensor specifications

Sensor	Measured quantity	Measurement principle	Model / Type	Supplier	Specifications
temperature sensor (sample carrier)	temperature in $°C$	Pt100 resistance thermometer	WK 93.0 1xPt100	Temperaturmeß-technik Geraberg GmbH (tmg)	diameter: 1.6 mm, sheath length: 360 mm, 4-wire connection, tolerance class: B, screened
heat flux sensor	heat flux in W/m^2	thermopile	heat flux sensor for high pressure	Captec Entreprise	sensitivity: 7.06 µV/(W/m²), diameter: 40 mm, total thickness: 0.75 mm, thickness of outside copper layers: 0.3 mm, gap filled with resin
pressure sensor (vacuum chamber)	absolute pressure in $mbar$	capacitance manometer	a-Baratron® AA02A12MGAS2 1B000000	MKS Instruments, Inc.	range: 0…100 mbar; output signal: 0…10 VDC; internally heated to 100°C; time constant: < 0.02 s for ≥ 1 Torr (0.133 kPa), < 0.04 s for < 1 Torr

B.2 Calibration of Pt100 Resistance Thermometer

The relation of temperature ϑ and electric resistance R_{ohm} of a Pt100 temperature sensor for the temperature range 0…850°C is – according to IEC 751 / DIN EN 60751 – described by the following polynomial equation:

$$R_{ohm}(\vartheta) = R_0 \cdot (1 + A \cdot \vartheta + B \cdot \vartheta^2) \tag{B-1}$$

Solving for ϑ the equation becomes

$$\vartheta(R_{ohm}) = \frac{-A + \sqrt{A^2 + 4B \cdot \left(\frac{R_{ohm}}{R_0} - 1\right)}}{2B} \tag{B-2}$$

The quantity R_0 represents the nominal ohmic resistance at 0°C – which is 100 Ω for a Pt100 sensor – and the standard values for the coefficients A and B are $A = 3.90802 \cdot 10^{-3}\ °C^{-1}$ and $B = -5.775 \cdot 10^{-7}\ °C^{-2}$ (Nau 2002). Using these coefficients the measurement uncertainty of the sensor is relatively high due to small differences in the characteristic curves of different sensor specimens. For tolerance class A error limits of $\Delta\vartheta = \pm(0.15 + 0.002 \cdot \vartheta)$ and for class B $\Delta\vartheta = \pm(0.30 + 0.005 \cdot \vartheta)$ are given (Nau 2002). To enhance accuracy specific coefficients of a certain sensor in certain setup conditions can be obtained by means of a calibration process. Regular calibration is furthermore recommended since characteristic curves of sensors alter over time due to aging effects etc. (Nau 2002).

Prior to the measurement series described in this work the Pt100 sample temperature sensor was calibrated in a calibration block (Ametek / Jofra RTC-157-A) using a reference temperature measurement chain from Ludwig Schneider GmbH & Co. KG (sensor: WT-MI-303-D-30E-So, Pt100; measurement device: PHYSICS 1000) as measurement standard. Pt100 sensor and reference sensor were first tied together to ensure a close positioning and then placed to maximum depth into a socket of the calibration block. The socket was then filled with aluminium oxide powder to secure a homogeneous temperature distribution inside the block. The sections of the sensors outside the calibrator were finally insulated to avoid heat loss to the ambient during calibration. Adapted to the envisaged measurement range of the sensor the calibration block was programmed to run two cycles of six temperature steps from 5°C to 30°C (5, 10, 15, 20, 25, 30°C), holding each step for 120 minutes after reaching a steady temperature. The resistance of the Pt100 was recorded by the data acquisition system while the temperature of the reference sensor was processed by the PHYSICS 1000 measurement device before both signals were sent to the measurement PC.

To obtain coefficients for the characteristic curve of the sensor the steady points of the first set of six temperature steps were used to generate a fit of the resistance values to the reference temperature values. The resulting coefficients are $R_0 = 100.0511\ \Omega$, $A = 3.925652 \cdot 10^{-3} °C^{-1}$, $B = -6.889563 \cdot 10^{-7} °C^{-2}$. Based on the second cycle the inaccuracy of the sensor's new characteristic curve was determined. More details on uncertainty calculations can be found in chapter B.7.1.

B.3 Heat Treatment of Samples – Literature Review on the Effects of Heat Treatment on Copper Surface Chemistry and Wetting Behavior

As depicted in chapter 4.1.3, all wire mesh structure samples of this work were subjected to a heat treatment procedure prior to measurement. The choice of suitable treatment parameters was deduced from the following literature review:

According to Keil et al. and Fischer et al., a thin oxide layer will form on a copper surface under exposure to air even at ambient temperatures (Keil et al. 2006; Fischer et al. 1980). The oxygen concentration within such a layer is usually not constant but its profile indicates that the outmost part of the layer mainly consists of CuO while the region underneath essentially consists of Cu_2O (Keil et al. 2006; Lee et al. 2016). As several authors found, temperature and duration of the heat treatment play a decisive role for the resulting oxide layer thickness and its oxide species composition. Fischer et al. subjected sanded copper surfaces to a heat treatment at 200°C or 300°C for 1 h and observed Cu_2O formation in the intermediate phase while CuO formed rather in the later period (Fischer et al. 1980). Also Touzé and Cougnon found with a treatment at 90°C that a short heating duration mostly provoked Cu_2O generation while longer durations result in oxide films with a high CuO content (Touzé and Cougnon 2018). Oxygen profiles from Lee at al. of copper samples which were exposed to passivation step and subsequent heat treatment at 200°C or 300°C showed a considerably higher penetration depth of oxide species for the specimens treated at higher temperature level (Lee et al. 2016). With respect to the characteristics of the Cu_2O and CuO species Touzé and Cougnon associate a smaller contact angle with water with CuO-rich films compared to Cu_2O-rich films (Touzé and Cougnon 2018). Moreover, they assessed CuO to be more robust against corrosion processes due to its dense conformation in contrast to the more porous Cu_2O. Both properties attributed to CuO – a low contact angle and a protective effect – are considered beneficial for the mesh samples employed in this work. Consequently, a high temperature and long duration was envisaged for the heat treatment since these factors are associated with a high CuO content. Since Lee et al. found copper oxide particles of 50…200 nm diameter on his surfaces an oxide layer thickness of at least 300 nm was

sought in order to obtain a continuous film. Based on Lee's oxygen profiles a required dwell time of about 120 min (at 200°C) or 60 min (at 300°C) was derived for that thickness. Due to risk of re-melting or destabilization of the solder contact at higher temperatures, the maximum feasible treatment temperature for the mesh structure / carrier assemblies was estimated to 180°C. For this reason – and for the lack of knowledge on the quantitative effects of the passivation pretreatment carried out by Lee et al. prior to the actual heat treatment – a longer duration of 4 days was chosen.

B.4 Sample Installation Workflow

Prior to installation in the test rig, the assembly of sample and PMMA container is prepared: After carefully cleaning all involved parts the polypropylene ring is mounted on the circumferential surface of the mesh structure. The drainage hose is screwed to the ABS support ring with PTFE sealing tape and a thin stainless steel wire is placed in the groove in the ABS support and in the drainage hose to facilitate refrigerant drainage. The ABS support ring of the sample is then screwed to the flange of the PMMA container, sealed by an O-ring.

Subsequently, the open vacuum chamber of the test rig is cleaned with isopropanol to remove possible contaminants. The copper surface of the heat flux sensor is cleaned with special carefulness and lint-free wipes in order to ensure a good thermal contact between sample and sensor. In each installation a fresh circular cutout of thermally conductive foil is applied on the heat flux sensor surface and the sample / container assembly is positioned on top, so that the bottom side of the sample carrier is in flush and even contact with the thermally conductive foil. By screwing the bolts of the pressing appliance into the heater support, the compression springs on the bolts exert force to the flange and thereby press the sample carrier on the heater / heat flux sensor setup. Thermally conductive paste is then applied into the blind hole for the sample temperature sensor and the sensor is inserted into the hole and fixed under slight pressure. The refrigerant drainage hose on the sample is then coupled to the drainage system and the refrigerant feed hose inside the vacuum chamber is mounted in the hole at the upper edge of the PMMA container. The "squirt prevention appliance" is fit onto the PMMA container as well and the auxiliary temperature sensors for vapor atmosphere and refrigerant feed are positioned. Finally, sealing faces and sealing ring of the vacuum chamber are cleaned and the lid is placed on the vacuum chamber and fixed with claw clamps.

B.5 Correction of the Measured Heat Flux

Measurements at steady-state conditions revealed that the characteristic curve of the heat flux sensor is subjected to a certain inaccuracy. In order to determine a correctional function for the heat flux measurement, its heat flow output signal $\dot{Q}_{hfs,meas}$ was compared to the applied heating power P_{htr} in steady-state conditions. Considering the experimental setup, the steady-state energy balance for the heater block is depicted in Figure 75 and – employing the actual heat flow through the sensor, $\dot{Q}_{hfs}$, and the deviation of the characteristic curve, $\Delta\dot{Q}_{cc}$, – it can be described as:

$$P_{htr} = \dot{Q}_{htr,loss} + \dot{Q}_{hfs} = \dot{Q}_{htr,loss} + \dot{Q}_{hfs,meas} + \Delta\dot{Q}_{cc} \qquad \text{(B-3)}$$

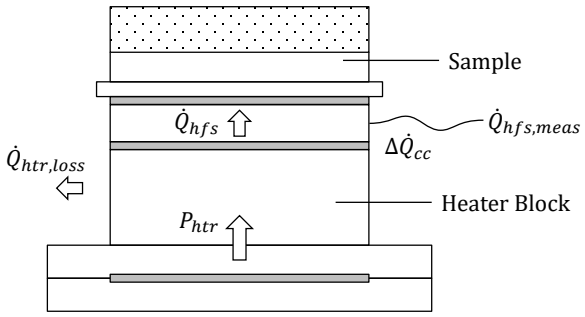

Figure 75: Correction of heat flux measurement – visualization of the energy balance of the heater block in steady-state conditions (drawing not true to scale)

The heat loss from the heater block to the ambient, $\dot{Q}_{htr,loss}$, in dependence of the applied heating power P_{htr} was derived from simulation results from Boertz (Boertz 2017). For his simulations Boertz used an approach from VDI heat atlas which describes heat transfer for natural convection conditions by means of an equivalent total thermal conductivity that comprises heat transfer contributions from conduction, convection and radiation. He calculated heat loss values for different imposed heating power values between 2.5 W and 126 W, assuming similar boundary conditions (e.g. setup geometry, saturation pressure, and heating-power-dependent evaporation heat transfer coefficients of the sample structure) as apply to the measurements of this work. The resulting heat loss values in dependence of the imposed heating power can be approximated by a linear relation with sufficient accuracy. This relation is depicted in Figure 76 and reads:

$$\dot{Q}_{htr,loss} = 0.035 \cdot P_{htr} \tag{B-4}$$

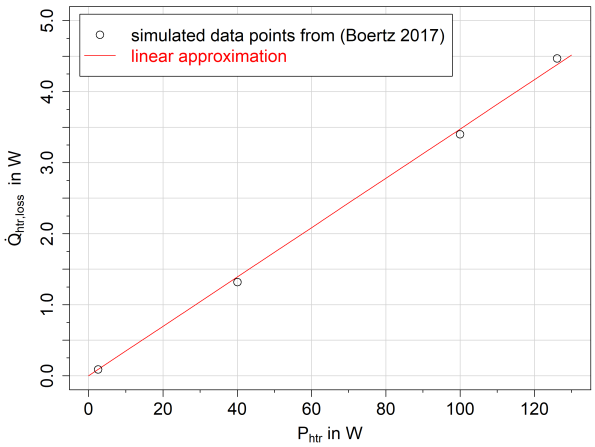

Figure 76: Estimated heat losses from heater block to ambient in dependence of applied heating power

Due to the dependence of the heat losses $\dot{Q}_{htr,loss}$ from evaporation heat transfer coefficient and applied system pressure (vapor saturation temperature), the calculated losses can only be considered as an estimation. However, since heat losses are rather small in relation to the imposed heating power P_{htr}, the incorporated inaccuracy is considered tolerable. Furthermore, the inaccuracy of the calculated heat loss values is expected to be well covered by the heat flux sensor's specified calibration uncertainty, which was included in the uncertainty analysis despite re-calibration, as described in chapter B.7.2 (appendix).

The deviation of the characteristic curve of the heat flux sensor was determined by means of steady-state pool boiling measurements. Sample KG07-900-280-05 was installed in the setup and flooded with a

constant refrigerant column of 5 mm above structure surface. Steady-state output signals were measured consecutively at five different heating power levels of about 53 / 27 / 10 / 1 / 0 W (which corresponds to heat fluxes through sensor or sample of about 42 / 22 / 8 / 0.9 / 0 kW/m²). An interval of 5 minutes was selected for each heating power level in which a linear regression lead to measured heat flow change of less than 10^{-7} W/s. These intervals were considered as steady-state and the arithmetic mean of the included heating power values and measured heat flow values were taken as characteristic steady-state points. The derived data points turned out to follow a quasi linear relationship and can be well approximated by the following equation:

$$P_{htr} = 0.95 \cdot \dot{Q}_{hfs,meas} \tag{B-5}$$

The actual heat flow through the heat flux sensor, $\dot{Q}_{hfs}$, can thus be described by:

$$\begin{aligned} \dot{Q}_{hfs} = P_{htr} - \dot{Q}_{htr,loss} &= 0.95 \cdot \dot{Q}_{hfs,meas} - 0.035 \cdot P_{htr} \\ &= 0.91 \cdot \dot{Q}_{hfs,meas} \end{aligned} \tag{B-6}$$

Analogously, the corrected heat flux can be calculated from the measured heat flux:

$$\dot{q}_{hfs} = 0.91 \cdot \dot{q}_{hfs,meas} \tag{B-7}$$

Figure 77 illustrates the relations of the different quantities involved in the correction against the measured heat flow $\dot{Q}_{hfs,meas}$.

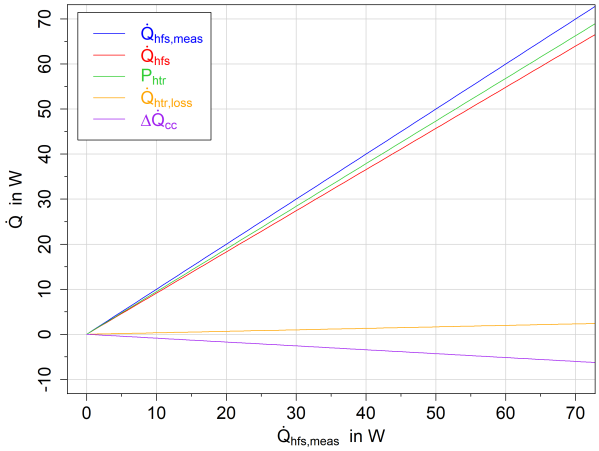

Figure 77: Heat flow quantities involved in the determination of the correction function for the heat flow

Uncertainties associated with the derivation of the correction function are considered in the measurement uncertainty analysis in appendix B.7.2.

B.6 Determination of the Leak Rate

In order to estimate the amount of non-condensable gases which leak into the vacuum system during evaporation measurements (see pressure correction in chapter 4.1.7), the leak rate Q_{leak} and the corresponding pressure rise rate $(\Delta p/\Delta t)_{leak}$ was determined from a pressure rise test. According to

(Jousten et al. 2010, p. 816-818) the leak rate of a closed vacuum system can be determined from the pressure rise $\Delta p/\Delta t$ and the volume V_{vs} of the vacuum system:

$$Q_{leak} = V_{vs} \cdot \frac{\Delta p}{\Delta t} \tag{B-8}$$

At very low pressures adsorbed vapor on the container surfaces tend to desorb and superimpose the pressure rise caused by leakage. Therefore, the pressure rise test must be pursued until the pressure gradient turns into a linear behavior which corresponds to external leakage. The measured pressure gradient $\Delta p/\Delta t$ from this linear period can be inserted into equation (B-8) to calculate the leak rate. (Jousten et al. 2010, p. 816-818)

In order to estimate the leakage behavior of the employed vacuum system during evaporation measurements as realistic as possible, the conditions for the pressure rise test were chosen as similar as possible to the conditions of evaporation measurements: The climatic chamber was set to 13°C to keep the vacuum system at a constant temperature. The fluid inlet temperature of the condenser was set to 10.54°C which approximately corresponds to a saturation pressure of 1.3 kPa. Prior to the pressure rise test the sealing faces of the vacuum chamber lid were carefully cleaned and the chamber was closed. Subsequently, the vacuum chamber (containing the evaporation container with a smooth copper surface sample) was evacuated for three days and after a break of 45 minutes for another 16 hours with closed valves to the condenser. Afterwards the closed condenser was evacuated three times for 5 minutes with respective waiting times of 4 minutes in between. The valve between vacuum chamber and condenser was then opened which caused vapor to flow into the vacuum chamber. The valves of the liquid refrigerant lines were opened as well. The whole vacuum system was again evacuated three times for 5 minutes with the vacuum pump connected to the condenser. Finally, the valve to the vacuum pump was closed which started the pressure rise test. The system pressure was recorded with the pressure sensors of the vacuum chamber and condenser, the former being used for evaluation because of its higher accuracy.

The mean pressure rise due to leakage was calculated by linear regression of the vacuum chamber pressure values from a defined evaluation period. The beginning of the evaluation period was chosen at minimum 24 h after start of the pressure rise test to assure that the linear period of "pure leakage" without impacts of gas desorption on pressure rise is reached. Due to small temperature fluctuations of the condenser thermostat the system pressure showed corresponding fluctuations (with an amplitude of about 7.5 Pa) according to the saturation conditions. In order to level out these fluctuations a rather long evaluation period of 24 h was used to determine the mean pressure gradient. Since the mean fluid temperature and the mean ambient temperature inside the climatic chamber are constant, the impact of temperature on the system pressure is considered as compensated.

For the volume V_{vs} in equation (B-8) the total void volume of the vacuum system was estimated. The void volume of the vacuum chamber is approximately 13.5 l, the void volume of the condenser chamber – considering the displacement of the condenser heat exchanger and of the refrigerant pool – was estimated as 7.4 l and the volume of the vapor connecting line as 2.7 l. The total void volume thus sums up to approximately 23.6 l.

The resulting leak rate determined from the pressure rise test amounts to $Q_{leak} = 5.3 \cdot 10^{-6} mbar\ l/s$ which is judged as an acceptable value. The corresponding pressure rise rate which is considered in the calculation of the vapor pressure (equation (4-13) in chapter 4.1.7) is $(\Delta p/\Delta t)_{leak} = 2.25 \cdot 10^{-5} Pa/s$. To account for potential minor differences in the leakage characteristics of different installation dates an uncertainty of the pressure rise rate equal to the pressure rise rate itself is presumed (cf. measurement uncertainty analysis in chapter B.7.6).

Comparing the pressure gradients of the whole vacuum system with previous tests of the closed vacuum chamber only, it becomes noticeable that pressure gradients of the whole system are considerably smaller than those of the vacuum chamber. One possible reason for this observation could be that with its large sealed lid the vacuum chamber exhibits a bigger leakage potential compared to the other parts of the setup which only include small flanges. Another explanation might be that non-condensable gases intruding the whole vacuum system dissolve in the refrigerant to a certain extent and thus do not entirely result in pressure rise. On the contrary, in the closed vacuum chamber there is no refrigerant which causes the gases to fully contribute to pressure rise. Provided that the hypothesis of partial dissolution of non-condensable gases is true, the calculated leak rate for the whole vacuum system does not describe the total amount of gases intruding the system but only the share which is not dissolved but stays in the gas phase. However, since the leak rate is exactly used for the correction of the measured pressure from non-condensable gases in the gas phase (see chapter 4.1.7), the described method for determination of the leak rate is considered as valid for the purpose of this work.

B.7 Measurement Uncertainty Analysis

The fundamental equations and methods which were employed for the uncertainty analysis of this work were derived from GUM (Joint Committee for Guides in Metrology 2008), and they are summarized in chapter 4.1.8. In this section, the application of the said methods to the measured and evaluated quantities is described.

Due to the unsteady character of the evaporation process, the corresponding uncertainties are usually time-dependent as well. Consequently, all uncertainty values are calculated for each time datum t_i of the evaluation period and compiled to a time series, which is depicted as a shaded area adjacent to the measurement curves in the diagrams of chapter 5. Besides time-dependence, the combined uncertainties depend on input quantities which vary among the measurements. Accordingly, the combined uncertainties u_c presented in the following paragraphs cannot be expressed as fixed numeric values but instead they are specified in the form of equations. In order to provide an overview of size ranges of the different uncertainty components, numeric uncertainty values for exemplary measurement conditions are listed in Table 4 at the end of chapter 4.1.8 (p. 67).

For a better readability, time-dependent quantities are named without indicating the time datum t_i in the following text, e.g. $u_c(\dot{q}_{hfs})$ instead of $u_c(\dot{q}_{hfs}(t_i))$. Exempt from this practice are equations which exhibit values at different time data – here the indicators t_i, t_{i-1}, t_{i+1} etc. are specified.

In the first paragraphs, the uncertainties of the directly measured quantities are addressed: those of temperature (B.7.1), heat flux (B.7.2) and pressure (B.7.3) measurement. Afterwards, the uncertainty components of derived quantities (temperature of the structure base in B.7.4, effective evaporation heat flux in B.7.5, saturation temperature in B.7.6) are presented. Finally, the derivation of uncertainties of the main evaluation quantities – the overall heat transfer coefficient of evaporation U_{ev} and the refrigerant mass M_{rf} – are addressed in B.7.7 and B.7.8.

B.7.1 Uncertainty of Temperature Measurement

As described in appendix B.2, the measurement accuracy of a Pt100 temperature sensor can considerably be improved by deduction of a sensor-specific characteristic curve from a calibration process. The sample temperature sensor was therefore calibrated according to the procedure specified in B.2. However, some

uncertainty contributions still arise from the calibration process and further uncertainties origin from the measurement chain in the experimental setup.

For clarity, uncertainty contributions from calibration are pointed out first in the following paragraph. Afterwards contributions from the experimental setup are discussed. Finally, the quantification of the uncertainty contributions is explained. All uncertainty values and sensitivity coefficients are listed up in Table 12.

Uncertainty Contributions from Calibration

Figure 78 schematically depicts the calibration setup with the corresponding quantities (cf. description of the calibration process in B.2).

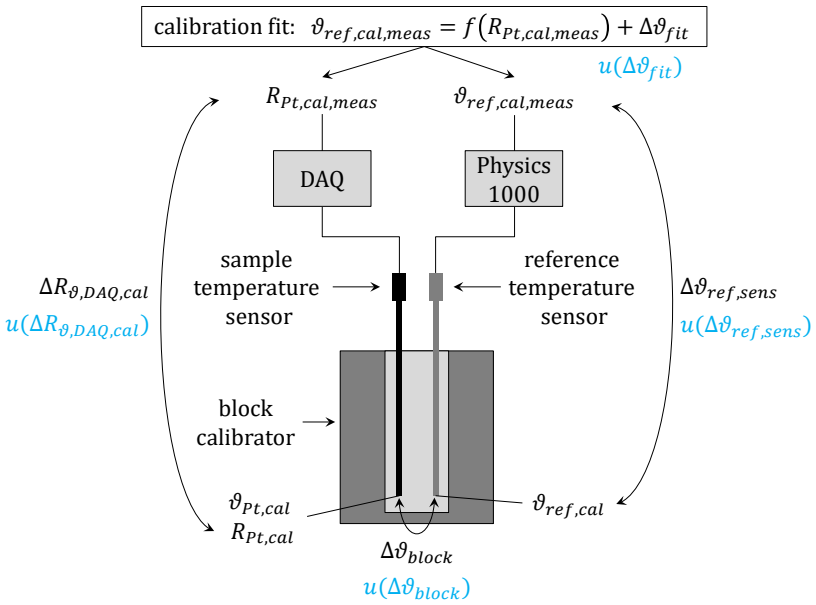

Figure 78: Sketch of the calibration setup, including relevant quantities, deviations, and uncertainties

The characteristic curve for the Pt100 is obtained by fitting the averages of the measured resistance values $R_{Pt,cal,meas}$ to the averages of the measured temperature values of the reference sensor $\vartheta_{ref,cal,meas}$ at several distinct temperature levels. Since the fitting algorithm represents an approximation technique it includes a certain inaccuracy $\Delta\vartheta_{fit}$. Despite the systematic character of the fit inaccuracy it is considered as an uncertainty here since the precise relation between resistance and temperature is unknown and thus systematic deviations cannot systematically be corrected. Incorporating equation (B-2), the functional relation of $\vartheta_{ref,cal,meas}$ and $R_{Pt,cal,meas}$ including the deviation $\Delta\vartheta_{fit}$ from fit uncertainty can be written as:

$$\vartheta_{ref,cal,meas} = f(R_{Pt,cal,meas}) + \Delta\vartheta_{fit} = \frac{-A + \sqrt{A^2 + 4B \cdot \left(\frac{R_{Pt,cal,meas}}{R_0} - 1\right)}}{2B} + \Delta\vartheta_{fit} \qquad \text{(B-9)}$$

Due to the impact of electromagnetic fields on cables and similar random effects the individual observations of $\vartheta_{ref,cal,meas}$ and $R_{Pt,cal,meas}$ within the evaluation period for a certain temperature step scatter around their mean. Since only a finite number of values is used for averaging, the average does not exactly match the expectation μ of the quantity. This deviation is referred to by GUM as the "experimental standard deviation of the mean" or "type A standard uncertainty" which can be evaluated according to equation (4-20) (Joint Committee for Guides in Metrology 2008, p. 10). Due to the very high constancy of the

recorded values and the large number of observations ($n = 300$), the standard deviation of the mean is extremely small compared to other uncertainty contributions (in the range of 10^{-5} Ohm and 10^{-5} K) and is therefore neglected.

$\vartheta_{ref,cal,meas}$ and $R_{Pt,cal,meas}$ are not identical with the resistance and temperature at the measuring tip of the Pt100 ($R_{Pt,cal}$ and $\vartheta_{Pt,cal}$) – which are the quantities of interest – due to additional uncertainties:

The measured reference temperature value $\vartheta_{ref,cal,meas}$ differs from the actual temperature of the platinum winding inside the tip of the reference temperature sensor $\vartheta_{ref,cal}$ by a difference $\Delta\vartheta_{ref,sens}$ caused by the inaccuracy of the reference measurement chain:

$$\vartheta_{ref,cal} = \vartheta_{ref,cal,meas} + \Delta\vartheta_{ref,sens} \tag{B-10}$$

Generally, drift of the reference measurement chain could cause additional deviation of $\vartheta_{ref,cal,meas}$ from $\vartheta_{ref,cal}$. Surely, the reference measurement chain is subject to drift to a certain degree since its calibration. But given that drift is less pronounced for Pt100 sensors compared to thermoelements (Scheller and Krummeck 2018) and calibration of the reference sensor chain was done less than 2 years before calibration of the sample temperature sensor this uncertainty contribution is neglected.

The temperatures of the platinum windings in the tips of the Pt100 thermometer in calibration ($\vartheta_{Pt,cal}$) and of the reference sensor ($\vartheta_{ref,cal}$) should ideally be identical since they are both located inside the isothermal block calibrator. However, a small temperature non-homogeneity inside the block can still occur which then causes a temperature deviation $\Delta\vartheta_{block}$. Further potential sources of divergence are heat dissipation / gain and self-heating of the sensors. Heat dissipation / gain through the sensors' sheathings to / from the ambient would cause temperature differences between the aluminum oxide powder inside the block calibrator, the sensors' sheathings and their actual platinum windings. However, both sensors were positioned at maximum depth inside the calibrator socket, the section of the sensors outside the block calibrator was well insulated and the differences between calibration temperature and ambient temperature were comparably low. Applying a respective error estimation method from Nicholas and White (Nicholas and White 2001) with an estimated immersion depth of more than 60 thermometer diameters, the deviation due to heat dissipation / gain ("immersion error") can be neglected. Self-heating of the sensors necessarily takes place to some extent due to current flow through the platinum resistance. The measurement current is only 1 mA, though, and the dissipated heat flow 10^{-4} W. According to (Nau 2002, p. 61) the effect of self-heating is mostly relevant for static surrounding media with low density, thermal conductivity and heat capacity as for example static air. In the calibration setup the thermal coupling to the surrounding aluminum oxide powder can be assumed to be fairly good and the thermal capacity is quite large; therefore the effect of self-heating is neglected. Considering only the temperature non-homogeneity of the block calibrator $\Delta\vartheta_{block}$ the functional relation of $\vartheta_{Pt,cal}$ and $\vartheta_{ref,cal}$ becomes

$$\vartheta_{Pt,cal} = \vartheta_{ref,cal} + \Delta\vartheta_{block} \tag{B-11}$$

Measurement of the Pt100 resistance during calibration is done with the data acquisition unit. Therefore the uncertainty of resistance measurement of the device leads to a deviation $\Delta R_{\vartheta,DAQ,cal}$ from the actual resistance of the sensor $R_{Pt,cal}$:

$$R_{Pt,cal,meas} = R_{Pt,cal} + \Delta R_{\vartheta,DAQ,cal} \tag{B-12}$$

Further deviations between $R_{Pt,cal}$ and $R_{Pt,cal,meas}$ could potentially be caused by cable resistance, voltage drop at electric junctions, thermoelectric effects at junctions of different metals (Seebeck effect) and a deficient electric resistance of the insulation material between platinum winding and sheathing. These

factors could cause additional voltage drops and thus create a deviation between the platinum resistance inside the measuring tip and the total resistance effective for data acquisition. However, they are systematic effects and therefore eliminated by the calibration process because the resistance shift is included in the evaluated characteristic curve. Moreover, the impact of cable resistance is expected to be negligible since the Pt100 sensor is configured in four-wire connection. The impact of a deficient insulation resistance of the sensor – according to (Nau 2002, p. 60) – does not play a significant role for platinum resistance temperature sensors, especially if they are only exposed to rather low temperatures as it is the case.

Combining equations (B-9) to (B-12), a functional relation between temperature and resistance of the Pt100 sensor can be formed, which is the characteristic curve of the calibrated Pt100 sensor:

$$\vartheta_{Pt} = f\left(R_{Pt,cal} + \Delta R_{\vartheta,DAQ,cal}\right) + \Delta\vartheta_{fit} + \Delta\vartheta_{ref,sens} + \Delta\vartheta_{block} = \frac{-A + \sqrt{A^2 + 4B \cdot \left(\frac{R_{Pt,cal} + \Delta R_{\vartheta,DAQ,cal}}{R_0} - 1\right)}}{2B} + \Delta\vartheta_{fit} + \Delta\vartheta_{ref,sens} + \Delta\vartheta_{block} \tag{B-13}$$

Uncertainty Contributions from the Experimental Setup

When the temperature sensor is installed in the experimental setup after calibration, additional uncertainty components affect temperature measurement, as illustrated in Figure 79.

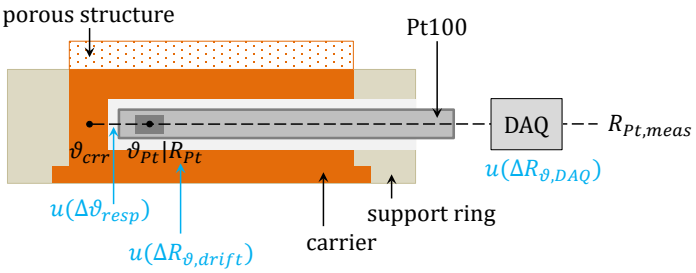

Figure 79: Sketch of sample temperature measurement in the experimental setup, including relevant quantities and uncertainties (illustration simplified and not true to scale)

Between calibration of the temperature sensor and measurement in the experimental setup the resistance-temperature relation of the sensor (= characteristic curve) must be expected to drift to some extent. Since direction and magnitude of this systematic effect is unknown, the drift in resistance for a certain temperature ϑ_{Pt}, is regarded as an uncertainty which can cause a deviation $\Delta R_{\vartheta,drift}$:

$$R_{Pt,cal}(\vartheta_{Pt}) = R_{Pt}(\vartheta_{Pt}) + \Delta R_{\vartheta,drift} \tag{B-14}$$

The uncertainty of the resistance measurement by the data acquisition unit can cause a resistance deviation $\Delta R_{\vartheta,DAQ}$ between actual and recorded resistance:

$$R_{Pt} = R_{Pt,meas} + \Delta R_{\vartheta,DAQ} \tag{B-15}$$

Analogous to the calibration setup, cable resistance, voltage drop at electric junctions, thermoelectric effects at junctions of different metals and a deficient insulation resistance can theoretically distort the relation of R_{Pt} and $R_{Pt,meas}$. As mentioned before, these systematic factors – if relevant at all – are

compensated for by the characteristic curve from calibration. Since none of the electrical connections were changed between calibration procedure and evaporation measurements the characteristic curve still applies for the evaporation measurement setup.

Impact of electromagnetic fields on cables and similar parasitic effects cause a statistic noise overlying the measurement signal. The deviation by these random effects can generally be reduced by averaging over several measurement observations and its uncertainty can be quantified by means of a "type A" uncertainty evaluation. A certain averaging process is carried out by the integration time of the data acquisition unit. However, due to the dynamic character of the evaporation measurements, the estimate of a measured quantity for a certain time step cannot be taken from a mean value but only from a single recorded value. In order to quantify the impact of statistic scattering of measured values anyway, a type A evaluation of the temperature's resistance signal in nearly steady-state conditions was performed. The resulting experimental standard deviation of the observations (according to equation (4-19)) amounts to approximately $1 \cdot 10^{-3}\Omega$ which is considerably smaller than other uncertainty contributions. Consequently, the uncertainty due to noise is neglected in the uncertainty analysis for temperature measurement.

The temperature of the platinum winding ϑ_{Pt} can differ from the temperature of the sample carrier ϑ_{crr} – which is the quantity of interest – due to the dynamic response time behavior of the sensor:

$$\vartheta_{crr} = \vartheta_{Pt} + \Delta\vartheta_{resp} \tag{B-16}$$

Heat dissipation or gain from the sensor's sheathing ("immersion error") could induce a deviation between ϑ_{Pt} and ϑ_{crr} as well. However, analog to the case of the calibration setup, the estimation method by Nicholas and White (Nicholas and White 2001) proved this uncertainty contribution negligible.

Inserting equations (B-14) and (B-15) into the characteristic equation of the Pt100 sensor from calibration (B-13) and combining with equation (B-16), the following relation between the measured resistance $R_{Pt,meas}$ and the actual temperature of the sample carrier ϑ_{crr} results:

$$\begin{aligned}\vartheta_{crr} = {} & f\left(R_{Pt,meas} + \Delta R_{\vartheta,DAQ,cal} + \Delta R_{\vartheta,DAQ} + \Delta R_{\vartheta,drift}\right) + \Delta\vartheta_{fit} + \Delta\vartheta_{ref,sens} + \Delta\vartheta_{block} \\ & + \Delta\vartheta_{resp} \\ = {} & \frac{-A + \sqrt{A^2 + 4B \cdot \left(\frac{R_{Pt,meas} + \Delta R_{\vartheta,DAQ,cal} + \Delta R_{\vartheta,DAQ} + \Delta R_{\vartheta,drift}}{R_0} - 1\right)}}{2B} \\ & + \Delta\vartheta_{fit} + \Delta\vartheta_{ref,sens} + \Delta\vartheta_{block} + \Delta\vartheta_{resp}\end{aligned} \tag{B-17}$$

Based on the principle of uncertainty propagation for uncorrelated input quantities (equation (4-23)) the combined standard uncertainty for the sample carrier temperature is:

$$\begin{aligned}u_c(\vartheta_{crr}) = \sqrt{} & \left(\frac{\partial\vartheta_{crr}}{\partial\Delta R_{\vartheta,DAQ,cal}} \cdot u\left(\Delta R_{\vartheta,DAQ,cal}\right)\right)^2 + \left(\frac{\partial\vartheta_{crr}}{\partial\Delta R_{\vartheta,DAQ}} \cdot u\left(\Delta R_{\vartheta,DAQ}\right)\right)^2 \\ & + \left(\frac{\partial\vartheta_{crr}}{\partial\Delta R_{\vartheta,drift}} \cdot u\left(\Delta R_{\vartheta,drift}\right)\right)^2 + \left(\frac{\partial\vartheta_{crr}}{\partial\Delta\vartheta_{fit}} \cdot u\left(\Delta\vartheta_{fit}\right)\right)^2 \\ & + \left(\frac{\partial\vartheta_{crr}}{\partial\Delta\vartheta_{ref,sens}} \cdot u\left(\Delta\vartheta_{ref,sens}\right)\right)^2 + \left(\frac{\partial\vartheta_{crr}}{\partial\Delta\vartheta_{block}} \cdot u\left(\Delta\vartheta_{block}\right)\right)^2 \\ & + \left(\frac{\partial\vartheta_{crr}}{\partial\Delta\vartheta_{resp}} \cdot u\left(\Delta\vartheta_{resp}\right)\right)^2\end{aligned} \tag{B-18}$$

Technically speaking, the two input quantities $u(\Delta R_{\vartheta,DAQ,cal})$ and $u(\Delta R_{\vartheta,DAQ})$ are not uncorrelated. However, since their uncertainty contributions are very small the utilization of the equation for uncorrelated input quantities is considered applicable.

All individual derivatives (sensitivity coefficients) and numerical values of uncertainty contributions are listed in Table 12. The deduction of the latter is pointed out as follows.

Quantification of Uncertainty Contributions

The resistance uncertainty $u(\Delta R_{\vartheta,DAQ,cal})$ from data acquisition during calibration is determined from a "type B" evaluation with aid of accuracy information from the DAQ unit's datasheet (Keysight Technologies 2014). It is assumed that the specified uncertainty arises from systematic effects or from random deviations of the mean value which cannot be extinguished by repeated measurements. Regularly fluctuating random uncertainty components (e.g. noise from electromagnetic fields) on the other hand are taken to be extinguished by averaging during each steady-state temperature step of the calibration process. With a measurement range of 1 kΩ, a maximum resistance of 115 Ω and the accuracy specifications for "1 year" after DMM calibration (0.01% of resistance reading plus 0.001% of range) an expanded uncertainty (with $k = 3$) of 0.0215 Ω results from the DAQ specifications, which leads to a standard uncertainty value of $u(\Delta R_{\vartheta,DAQ,cal}) = U(\Delta R_{\vartheta,DAQ,cal})/k = 7.2 \cdot 10^{-3}\Omega$, using equation (4-21).

For the uncertainty of resistance measurement of the data acquisition unit during evaporation measurements also the datasheet information is used. The coefficients for the same resistance range of 1 kΩ are employed and multiplied with the resistance reading of the particular time step and with the maximum range of 1 kΩ, respectively. Since ambient temperatures in the laboratory might occasionally have exceeded the specified threshold of 28°C, an additional uncertainty component is included, using the specified temperature coefficients (0.0006% of resistance reading per K plus 0.0001% of range per K, for the 1 kΩ range), the same input parameters as before and a maximum ambient temperature difference of 4 K above the upper threshold. The standard uncertainty $u(\Delta R_{\vartheta,DAQ})$ is then calculated from the expanded uncertainty of both components, using equation (4-21).

An estimation for the uncertainty caused by drift behavior of the Pt100 resistance $u(\Delta R_{\vartheta,drift})$ was deduced from two different calibration procedures: Resistance values for temperatures in the calibration range from 5 to 30°C were calculated with the coefficients from the last calibration and with coefficients from a calibration which was done several months before. The differences between the resistance values for each temperature step were calculated and the largest difference was chosen, which is $7.2 \cdot 10^{-3}$ Ω. Under the assumption that resistance changed linearly with time, a mean rate of $3.2 \cdot 10^{-5}$ Ω/d was calculated, using the time difference between both calibrations (227 d). Employing a conservatively assumed time difference between last calibration and last evaporation measurement of 264 d, an expected maximum resistance difference of $8.3 \cdot 10^{-3}$ Ω for all evaporation measurements results. This resistance difference cannot directly be associated with resistance drift since it also includes possible deviations caused by the fitting algorithm which yielded the coefficients. Furthermore, the observed resistance change between the two calibration procedures can only be regarded as an exemplary occurrence, so that net resistance change after the last calibration could likely be larger or smaller. In order to cover these aspects and to make a conservative estimation the uncertainty of resistance drift was taken as the calculated resistance change multiplied by factor 3 which yields a value of $u(\Delta R_{\vartheta,drift}) = 2.5 \cdot 10^{-2}\Omega$.

The inaccuracy of the polynomial fit is generally a systematic effect but cannot be quantified and corrected. Therefore it is treated as a random effect and expressed as an uncertainty $u(\Delta\vartheta_{fit})$. As a basis for evaluation of the fit uncertainty, measured resistance and reference temperature data from the second

calibration run through the different temperature steps is used: For each set temperature step the differences between reference temperature and temperature from the polynomial fit are calculated and the mean difference of the temperature step is evaluated. These mean differences are considered as the inaccuracy of the fit for the particular temperature step. The maximum difference of 0.005 K occurred for the 20°C step and was taken as the uncertainty of the polynomial fit: $u(\Delta\vartheta_{fit}) = 0.005K$.

The expanded uncertainty (coverage factor $k = 2$) for the reference measurement chain used in the calibration setup – consisting of sensor plus measurement device PHYSICS 1000 – is specified in a calibration certificate (calibration standard DAkkS-DKD-3) as 0.02 K for the applicable temperature ranges between 0 and 90°C (Ludwig Schneider Messtechnik GmbH 2017). The standard uncertainty for the reference measurement chain is consequently $u(\Delta\vartheta_{ref,sens}) = 0.02K/2 = 0.01K$.

The temperature non-homogeneity inside the block calibrator is quantified as 0.01 K by the manufacturer (AMETEK GmbH n.d.). If the non-homogeneity was assumed to be constant during calibration it had to be regarded as a systematic effect. Since no information on constancy, direction and magnitude is available, it is still considered as a random effect. The specified value is taken as an error limit with rectangular distribution which yields a standard uncertainty of $u(\Delta\vartheta_{block}) = 0.01K/\sqrt{3} \approx 5.8 \cdot 10^{-3}K$, using equation (4-22).

The different thermal conductivities of measurement object and sensor in combination with thermal resistances and capacities leads to a temperature difference $\Delta\vartheta_{resp}$ between sensor and measurement object in case of dynamic temperature changes. This effect is commonly referred to as response time or response behavior. The response behavior is actually a systematic effect but since it cannot be described in a sufficient exactness for the presented setup, it is not systematically corrected but handled as a random effect. In (Bernhard 2014, pp. 97–100) an approach of Gordov et al. is suggested for an estimation of the temperature deviation caused by response time behavior: If the temperature of a solid measurement object changes linearly with time, the dynamic thermal measurement deviation $\Delta\vartheta_{th}(t)$ of a cylindrical embedded sensor ($\vartheta_S(t)$) from the surrounding measurement object ($\vartheta_M(t)$) can be approximated by the following equation:

$$\Delta\vartheta_{th}(t) = \vartheta_S(t) - \vartheta_M(t) = (\tau_M - \tau_S) \cdot \frac{d\vartheta_S(t)}{dt} \tag{B-19}$$

Equation (B-19) includes two time constants τ_M and τ_S and the temperature change of the sensor $\frac{d\vartheta_S(t)}{dt}$. Usually the temperature changes of the sensor and of the surrounding object are very similar so that equation (B-19) can be modified to:

$$\Delta\vartheta_{th}(t) = \vartheta_S(t) - \vartheta_M(t) = (\tau_M - \tau_S) \cdot \frac{d\vartheta_M(t)}{dt} \tag{B-20}$$

If the sensor is not flush mount inside the hole or surroundings but the setup includes gaps and/or additional sensor insulation layers, the time constants τ_S and τ_M can be approximated by the following equations

$$\tau_S = \frac{1}{16} \cdot \frac{D_{dh}^2}{\lambda_{eff}} \cdot \frac{\lambda_M + 2\lambda_{eff}}{\lambda_M} \cdot c_{eff} \cdot \rho_{eff} \tag{B-21}$$

$$\tau_M = \frac{3}{16} \cdot \frac{D_{dh}^2}{\lambda_M} \cdot c_M \cdot \rho_M \tag{B-22}$$

where D_{dh} is the drill hole diameter, λ_M, c_M, ρ_M the thermal conductivity, specific heat capacity and density of the measurement object. The effective thermal conductivity λ_{eff} refers to the layers between sensor and measurement object. In our case there is only the drill hole gap filled with thermally conductive paste which makes $\lambda_{eff} = \lambda_{tcp}$ with the thermal conductivity λ_{tcp} of the thermally conductive paste. The product of effective specific heat capacity and effective density $c_{eff} \cdot \rho_{eff}$ can be calculated by means of the material properties (c_i, ρ_i) and volumes (V_i) of the components i within the drill hole and the total volume V_{tot}:

$$c_{eff} \cdot \rho_{eff} = \frac{1}{V_{tot}} \cdot \sum_i c_i \cdot \rho_i \cdot V_i \tag{B-23}$$

Considering the sensor construction of a stainless steel (1.4571) sheathing containing an Al_2O_3 powder filling and the gap filled with thermally conductive paste, the equation becomes

$$c_{eff} \cdot \rho_{eff} = \frac{1}{D_{dh}^2} \cdot \Big(c_{Al2O3} \cdot \rho_{eff,Al2O3} \cdot D_{Al2O3}^2 + c_{SS} \cdot \rho_{SS} \cdot (D_s^2 - D_{Al2O3}^2) + c_{tcp} \cdot \rho_{tcp} (D_{dh}^2 - D_s^2) \Big) \tag{B-24}$$

with the drill hole diameter D_{dh}, the diameter of the Al_2O_3 filling D_{Al2O3}, the sensor diameter D_s, the specific heat capacities of Al_2O_3 (c_{Al2O3}), stainless steel (c_{SS}) and thermally conductive paste (c_{tcp}), an estimated effective density of the Al_2O_3 powder filling $\rho_{eff,Al2O3}$ and the densities of stainless steel (ρ_{SS}) and of the thermally conductive paste (ρ_{tcp}).

Using the numerical values listed in Table 11, the following values can be calculated for the employed measurement setup:

$$c_{eff} \cdot \rho_{eff} = 2.7 \cdot 10^6 \, J/(m^3 K)$$

$$\tau_S = 0.2211 \, s$$

$$\tau_M = 0.005315 \, s$$

Table 11: Numerical values for calculations of temperature sensor response behavior

Symbol	Unit	Value	Remark / Reference
D_{Al2O3}	m	0.001	(estimation)
D_s	m	0.0016	(manufacturing information)
D_{dh}	m	0.0018	(manufacturing information)
c_{Al2O3}	$J/(kg\ K)$	(750+1050)/2 = 900	(Alm 2004)
c_{SS}	$J/(kg\ K)$	500	(Heubner 2014); type 1.4571 @20°C
c_{tcp}	$J/(kg\ K)$	818	(Müller, Dr. Dietrich Müller GmbH 7/20/2019)
$c_M\ (= c_{CuETP})$	$J/(kg\ K)$	386	(Deutsches Kupferinstitut 2005); Cu-ETP @20°C
$\rho_{eff,Al2O3}$	kg/m^3	1410	(Stahmer et al. 2012)
ρ_{SS}	kg/m^3	8000	(Heubner 2014); type 1.4571 @20°C
ρ_{tcp}	kg/m^3	(2100+2300)/2 = 2200	(Dr. Dietrich Müller GmbH 2014); @25°C
$\rho_M\ (= \rho_{CuETP})$	kg/m^3	8930	(Deutsches Kupferinstitut 2005); Cu-ETP @20°C
$\lambda_{tcp}\ (= \lambda_{eff})$	$W/(m\ K)$	2.5	(Dr. Dietrich Müller GmbH 2014)
$\lambda_M\ (= \lambda_{CuETP})$	$W/(m\ K)$	394	(Deutsches Kupferinstitut 2005); Cu-ETP @20°C

For the uncertainty analysis the absolute value of the temperature deviation is taken as an uncertainty component. Applied to the discrete measurement values of the sample carrier temperature $\vartheta_{crr}(t_i)$ and time t_i a modification of equation (B-20) with a central difference quotient allows an estimation of the standard uncertainty caused by response behavior of the temperature sensor setup:

$$u(\Delta\vartheta_{resp})(t_i) = |\Delta\vartheta_{th}(t_i)| = |\vartheta_{Pt}(t_i) - \vartheta_{crr}(t_i)| = \left|(\tau_M - \tau_S) \cdot \frac{\vartheta_{crr}(t_{i+1}) - \vartheta_{crr}(t_{i-1})}{t_{i+1} - t_{i-1}}\right| \qquad \text{(B-25)}$$

For the initial value $u(\Delta\vartheta_{resp})(t_1 = 0) = 0$ is appointed and for the last value n of the time series $u(\Delta\vartheta_{resp})(t_n) = u(\Delta\vartheta_{resp})(t_{n-1})$.

Table 12: Uncertainty contributions and sensitivity coefficients of temperature measurement

$\frac{\partial\vartheta_{crr}}{\partial\Delta R_{\vartheta,DAQ,cal}} = \frac{1}{R_0 \cdot \sqrt{A^2 + \frac{4B \cdot (-R_0 + R_{Pt,meas})}{R_0}}}$
$u(\Delta R_{\vartheta,DAQ,cal}) = 7.2 \cdot 10^{-3}\Omega$
$\frac{\partial\vartheta_{crr}}{\partial\Delta R_{\vartheta,DAQ}} = \frac{1}{R_0 \cdot \sqrt{A^2 + \frac{4B \cdot (-R_0 + R_{Pt,meas})}{R_0}}}$
$u(\Delta R_{\vartheta,DAQ}) = \frac{(1 \cdot 10^{-4} + 6 \cdot 10^{-6}\frac{1}{K} \cdot 4K) \cdot R_{Pt,meas} + (1 \cdot 10^{-5} + 1 \cdot 10^{-6}\frac{1}{K} \cdot 4K) \cdot 1000\Omega}{3}$
$\frac{\partial\vartheta_{crr}}{\partial\Delta R_{\vartheta,drift}} = \frac{1}{R_0 \cdot \sqrt{A^2 + \frac{4B \cdot (-R_0 + R_{Pt,meas})}{R_0}}}$
$u(\Delta R_{\vartheta,drift}) = 2.5 \cdot 10^{-2}\Omega$
$\frac{\partial\vartheta_{crr}}{\partial\Delta\vartheta_{fit}} = 1$
$u(\Delta\vartheta_{fit}) = 5 \cdot 10^{-3}K$
$\frac{\partial\vartheta_{crr}}{\partial\Delta\vartheta_{ref,sens}} = 1$
$u(\Delta\vartheta_{ref,sens}) = \frac{1}{k} \cdot U(\Delta\vartheta_{ref,sens}) = \frac{1}{2} \cdot 0.02K = 1 \cdot 10^{-2}K$
$\frac{\partial\vartheta_{crr}}{\partial\Delta\vartheta_{block}} = 1$
$u(\Delta\vartheta_{block}) = 0.01K/\sqrt{3} \approx 5.8 \cdot 10^{-3}K$
$\frac{\partial\vartheta_{crr}}{\partial\Delta\vartheta_{resp}} = 1$
$u(\Delta\vartheta_{resp})(t_i) = \left\|(\tau_M - \tau_S) \cdot \frac{\vartheta_{crr}(t_{i+1}) - \vartheta_{crr}(t_{i-1})}{t_{i+1} - t_{i-1}}\right\|$

B.7.2 Uncertainty of Heat Flux Measurement

As pointed out in chapter 4.1.7, a calibration of the heat flux sensor was carried out (which is described in detail in appendix B.5) in order to deduce a correction of its characteristic curve. Due to this re-calibration, the calibration uncertainty specified by the manufacturer can be expected to be compensated to a large extent. However, since it is unclear if all uncertainty-causing mechanisms which are meant to be covered by the calibration uncertainty specification are erased by means of the re-calibration (e.g. a temperature-dependence of the sensitivity might remain), the specified uncertainty contribution of calibration

$u(\Delta\dot{q}_{hf,cal})$ is still included in the uncertainty analysis. Furthermore, the re-calibration process itself is subject to an uncertainty of the assumed heat loss value and an uncertainty of the heater voltage and current measurement by the data acquisition unit. Since their quantities are small, these components are not explicitly considered in the uncertainty analysis but they are regarded as covered by the calibration uncertainty. According to the manufacturer's specifications the corresponding error limits of calibration are 5% of reading. Assuming a rectangular distribution the standard uncertainty can be calculated according to equation (4-22). (The explicit formulation for this and all other uncertainty contributions and sensitivity coefficients for heat flux measurement are listed in Table 13.)

Another source of uncertainty is the non-stability (drift) of the sensor's sensitivity $u(\Delta S_{hfs,drift})$ which can occur during service life since last calibration. Due to a lack of information for the applied Captec sensor a specification for the thermopile heat flux sensor Hukseflux HFP01SC of „< 1%/yr" (Hukseflux Thermal Sensors B.V. 2016) is employed instead and interpreted as an error limit with rectangular probability distribution and $a = 1\%/\text{a}$. Taking the maximum time span between measurements and re-calibration of about 1 year, the error limit due to drift of sensitivity amounts to 1%. Despite drift phenomena are usually systematic effects, direction, magnitude and dynamics of drift are unknown. Therefore it is considered as an uncertainty in this context, using equation (4-22) for the conversion into a standard uncertainty $u(\Delta S_{hfs,drift})$.

The uncertainty of voltage measurement $u(\Delta U_{hf,DAQ})$ which the digital multimeter of the data acquisition device is subjected to, represents a further uncertainty contribution. As a conservative estimation, uncertainty coefficients for the 100 mV DC range are used in combination with 1 V as range factor since the autoranging function is used and these specifications yield the largest uncertainty values within the applicable ranges of 100 mV and 1 V. The expanded uncertainty with a coverage factor of $k = 3$ (normal probability distribution) for the 100 mV range is specified as 0.005% of voltage reading plus 0.004% of range (within 1 year after multimeter calibration) (Keysight Technologies 2014). Due to the elevated ambient temperatures during some measurements, an additional uncertainty component is calculated with the specified temperature coefficients (0.0005% of reading per K plus 0.0005% of range per K, for the 100 mV range) and a maximum temperature difference of 4 K, analogously to the approach for temperature measurement. Adding up the two components to a total expanded uncertainty $U(\Delta U_{hf,DAQ})$ and using equation (4-21), the standard uncertainty of voltage measurement $u(\Delta U_{hf,DAQ})$ can be calculated.

As already mentioned in chapter 4.1.7, the correction of the DAQ scanning time delay incorporates an uncertainty due to the assumption of a linear trend between the data points. However, this uncertainty is considered negligible compared to other uncertainty contributions of heat flux measurement.

The response time of a sensor generally distorts a measurement systematically. However, since a realistic correction is not possible, it is treated as an uncertainty component here, as done for the temperature sensor. Due to their thermal capacitances and resistances, sensors often react to an input step function $0 \rightarrow x_{in}$ with an exponential behavior of the form:

$$x_{out} = x_{in} \cdot \left(1 - e^{-\frac{t}{\tau}}\right) \tag{B-26}$$

A characteristic "response time" of a sensor represents the time the sensor needs to reach a certain specified percentage of the steady-state value x_{in}. This information allows to calculate the time constant τ, which represents the required time for the system to reach an output value x_{out} of about 63% of the input x_{in}.

In the case of the employed heat flux sensor a response time of 2 s is specified by the manufacturer (Captec Entreprise (Florian Raucoules) 4/24/2017). Due to a lack of information on the corresponding percentage, 90% is assumed. The time constant τ can be calculated to

$$\tau = \frac{-t}{ln\left(1 - \frac{x_{out}}{x_{in}}\right)} = \frac{-2s}{ln(1 - 0.9)} \approx 0.87s \tag{B-27}$$

In fact, the input heat flux of the measurements in this work behaves dynamically and not like one step function with a constant value the measured value is converging to. To respect these circumstances, each heat flux change between two time steps is considered as a step function and the effective driving force on the sensor is described as the difference of the "real" heat flux of the current time step $\dot{q}_{real}(t_i)$ and the measured heat flux of the previous time step $\dot{q}_{hfs}(t_{i-1})$. This approach – adopted from (Boertz 2017) – leads to a modification of equation (B-26):

$$\dot{q}_{hfs}(t_i) = \dot{q}_{hfs}(t_{i-1}) + (\dot{q}_{real}(t_i) - \dot{q}_{hfs}(t_{i-1})) \cdot \left(1 - e^{-\frac{t_i - t_{i-1}}{\tau}}\right) \tag{B-28}$$

The remaining absolute difference between input value (= "real" heat flux $\dot{q}_{real}(t_i)$) and measured value $\dot{q}_{hfs}(t_i)$ is taken as a measure for the uncertainty contribution of the sensor's response time. Using equation (B-28) it can be described as:

$$u\left(\Delta\dot{q}_{hf,resp}\right)(t_i) = \left|\dot{q}_{real}(t_i) - \dot{q}_{hfs}(t_i)\right| = \left|\left(\dot{q}_{hfs}(t_i) - \dot{q}_{hfs}(t_{i-1})\right) \cdot \frac{1}{e^{\frac{t_i - t_{i-1}}{\tau}} - 1}\right| \tag{B-29}$$

Equation (B-29) is valid for $i \geq 2$. As initial condition $u\left(\Delta\dot{q}_{hf,resp}\right)(t_1 = 0) = 0$ is set.

Potentially, a „deflection error" can occur in heat flux measurements if the field of heat flux exceeds the sensor dimensions and if thermal conductivity of the surrounding material differs from the conductivity of the sensor material (Hukseflux Thermal Sensors B.V. 2016). However, in the present measurement setup a heat flux is only applied to the cross section of the sensor therefore such a non-representativeness of heat flux measurement does not apply. Nevertheless, a certain deflection of heat flow lines through the sensor could occur due to heat losses from the heater block and from the sample carrier to the ambient and thus lead to an inhomogeneous heat flux distribution within the sensor area. Earlier simulations in (Boertz 2017) though revealed that maximum total heat losses (from heater block and carrier) are in the range of 3.5% of the applied heating power which makes a significant inhomogeneity of heat flux lines unlikely, considering the high thermal conductivity of the heater block and sample carrier.

Since the heat flux sensor is connected to the heater block and to the sample carrier by manually mounted adhesive layers, a certain spatial inhomogeneity of the quality of thermal coupling might occur. The potentially resulting inhomogeneity in heat flux distribution within the sensor area could lead to a measurement inaccuracy. However, the manufacturer states that a heat flux inhomogeneity does not cause a significant measurement deviation and additionally, tests with deteriorated thermal coupling did not show a remarkable effect in the measurement results. Therefore, the effect of inhomogeneous heat flux distribution is neglected.

Voltage drop due to cable resistance can potentially lead to measurement deviations. However, in voltage measurements there is hardly any current flow in the cables due to the high internal resistance of the multimeter which makes the impact of voltage drop in cables negligible. Similarly, thermally induced

voltages due to the thermoelectric effect at junctions of different metals (Seebeck effect) are assumed to be negligibly small.

In addition to the aforementioned uncertainty components which refer to the estimate of the measured quantity, noise effects lead to a deviation of the individual observation from the estimate. Analogous to the procedure for temperature measurement (appendix B.7.1), the experimental standard deviation of recorded voltage values of the heat flux sensor under nearly steady-state conditions was calculated according to the "type A" evaluation procedure. With an order of magnitude of 10^{-7} V (which corresponds to a heat flux uncertainty in the order of magnitude of 10^{-2} W/m²) this uncertainty component is extremely small compared to other impacts and therefore not considered in the uncertainty analysis.

Including all relevant sources of uncertainty the functional relation for the measured heat flux $\dot{q}_{hfs}$ can thus be written as

$$\dot{q}_{hfs} = \frac{U_{hf} + \Delta U_{hf,DAQ}}{S_{hfs} + \Delta S_{hfs,drift}} + \Delta\dot{q}_{hf,cal} + \Delta\dot{q}_{hf,resp} \tag{B-30}$$

with the measured voltage signal U_{hf}, the sensitivity of the heat flux sensor S_{hfs} and their corresponding deviation estimates.

Using the uncertainty propagation approach (equation (4-23)) and the functional relation (equation (B-30)) the combined standard uncertainty for the heat flux measurement can be derived:

$$u_c(\dot{q}_{hfs}) = \sqrt{\begin{aligned}&\left(\frac{\partial\dot{q}_{hfs}}{\partial\Delta U_{hf,DAQ}}\cdot u\left(\Delta U_{hf,DAQ}\right)\right)^2 + \left(\frac{\partial\dot{q}_{hfs}}{\partial\Delta S_{hfs,drift}}\cdot u\left(\Delta S_{hfs,drift}\right)\right)^2\\ &+\left(\frac{\partial\dot{q}_{hfs}}{\partial\Delta\dot{q}_{hf,cal}}\cdot u\left(\Delta\dot{q}_{hf,cal}\right)\right)^2 + \left(\frac{\partial\dot{q}_{hfs}}{\partial\Delta\dot{q}_{hf,resp}}\cdot u\left(\Delta\dot{q}_{hf,resp}\right)\right)^2\end{aligned}} \tag{B-31}$$

The individual numerical values or formulations of the uncertainty contributions and corresponding sensitivity coefficients are summarized in Table 13.

Table 13: Uncertainty contributions and sensitivity coefficients of heat flux measurement

$\frac{\partial\dot{q}_{hfs}}{\partial\Delta U_{hf,DAQ}} = \frac{1}{S_{hfs}}$
$u\left(\Delta U_{hf,DAQ}\right) = \frac{(5\cdot10^{-5}+5\cdot10^{-6}\frac{1}{K}\cdot4K)\cdot U_{hf}+(4\cdot10^{-5}+5\cdot10^{-6}\frac{1}{K}\cdot4K)\cdot1V}{3}$
$\frac{\partial\dot{q}_{hfs}}{\partial\Delta S_{hfs,drift}} = -\frac{U_{hf}}{S_{hfs}^2}$
$u\left(\Delta S_{hfs,drift}\right) = \frac{0.01}{\sqrt{3}}\cdot S_{hfs}$
$\frac{\partial\dot{q}_{hfs}}{\partial\Delta\dot{q}_{hf,cal}} = 1$
$u\left(\Delta\dot{q}_{hf,cal}\right) = \frac{0.05\cdot\dot{q}_{hfs}}{\sqrt{3}}$
$\frac{\partial\dot{q}_{hfs}}{\partial\Delta\dot{q}_{hf,resp}} = 1$
$u\left(\Delta\dot{q}_{hf,resp}\right)(t_i) = \left\lvert\left(\dot{q}_{hfs}(t_i) - \dot{q}_{hfs}(t_{i-1})\right)\cdot\frac{1}{e^{\frac{t_i-t_{i-1}}{\tau}}-1}\right\rvert$

B.7.3 Uncertainty of Pressure Measurement

The uncertainty of pressure measurement in the vacuum chamber is mainly affected by uncertainty contributions of the sensor's calibration ($u(\Delta p_{p,cal})$), temperature coefficients ($u(\Delta p_{p,\vartheta})$), zero drift / non-stability ($u(\Delta p_{p,drift})$), and of the voltage signal measurement ($u(\Delta U_{p,DAQ})$).

Calibration accuracy of the pressure sensor (MKS Baratron), including non-linearity, hysteresis and non-repeatability, is specified as 0.2% of reading for the pressure range 1-1000 Torr (approx. 0.133-133 kPa) and 0.4% of reading for pressures < 1 Torr (MKS Instruments 2014-2018). Assuming a rectangular probability distribution with a total probability of 1 the uncertainty $u(\Delta p_{p,cal})$ can be calculated according to equation (4-22) as listed in Table 14.

Zero temperature coefficients amount to 0.002% of Full Scale (FS) per Kelvin for 1-1000 Torr (approx. 0.133-133 kPa) and 0.01% FS/K for < 1 Torr (MKS Instruments 2014-2018, 2014-2018). Full Scale (= measurement range) of the particular sensor equals 100 mbar (10 kPa) and as reference temperature of calibration the normal temperature of 20°C is assumed. The ambient temperature $\overline{\vartheta_{cc}}$ the pressure sensor is exposed to, varies among the measurements due to different settings of the climatic chamber, which are 9°C, 13°C or 15°C. Since some of these ambient temperature settings are slightly below the sensor's lower operating temperature limit of 15°C, the higher uncertainty specifications for < 1 Torr are used for all pressure readings. The span temperature coefficient is specified as 0.02% of reading / K (MKS Instruments 2014-2018). Under the assumption of a rectangular probability distribution the resulting equation for the uncertainty due to temperature coefficients $u(\Delta p_{p,\vartheta})$ is specified in Table 14.

Due to aging of electronic components and other impacts a certain zero drift (non-stability) can gradually occur during service life of the sensor which induces an offset to the measured data. In principle this is a systematic effect, however, direction and intensity of the drift is unknown which makes a systematic data correction impossible. Consequently, a potential zero drift is considered as an uncertainty factor. In order to quantify this effect the zero point was checked repeatedly with a time lag of several months. To do so, the pressure sensor was connected to a turbomolecular pumping station (Pfeiffer HiCube 80 Eco DN 40 ISO-KF (Pfeiffer Vacuum GmbH)) and evacuated to a steady-state minimum pressure. The ultimate pressure of the turbomolecular pump is specified as < $1 \cdot 10^{-7}$ mbar (Pfeiffer Vacuum GmbH) which is far below the sensor's resolution of $2 \cdot 10^{-3}$ mbar, therefore the steady-state pressure was considered as 0 kPa. For the first and second test (11 months time lag) the difference between the average steady state pressures was approximately $1.5 \cdot 10^{-3}$ kPa which yields an average drift rate of $1.35 \cdot 10^{-4}$ kPa per month. Between the second and third test (7.5 months time lag) a pressure difference of $1.9 \cdot 10^{-4}$ kPa was determined which corresponds to a drift rate of $2.5 \cdot 10^{-5}$ kPa per month. Since the dynamics of drift are unknown, the drift is not considered as a gradual process with a constant rate here but for simplicity it is assumed that measurement deviation due to drift can take an arbitrary value within certain boundaries in each measurement. For a conservative estimation the largest determined difference of $1.5 \cdot 10^{-3}$ kPa is employed as a constant drift uncertainty $u(\Delta p_{p,drift})$ here even if the time lag between last zero check and evaporation measurements of less than 5 months is shorter than between the tests, and drift effects are usually expected to decrease during sensor service life.

For the expanded uncertainty of voltage measurement by the data acquisition unit $U(\Delta U_{p,DAQ})$ uncertainty coefficients for the 100 mV range are used (0.005% of reading plus 0.004% of range) because these are the largest values within the used ranges of 100 mV, 1 V and 10 V. For the range the maximum range of 10 V is applied. The elevated ambient temperatures are respected again by using the specified temperature coefficients (0.0005% of reading per K plus 0.0005% of range per K, for the 100 mV range) and a temperature deviation of 4 K.

As mentioned before in the context of heat flux measurement, uncertainties caused by the resistance of cables (voltage drop) and thermally induced voltages by thermoelectric effect are as well assumed to be negligible in pressure measurement.

Since the time constant of the pressure sensor is rather small with < 20 ms for pressures ≥ 1 Torr (0.133 kPa) and < 40 ms for pressures < 1 Torr and the vacuum chamber pressure during capillary evaporation is relatively stable, potential measurement deviations due to the response time of the sensor are neglected.

Analog to the proceeding for temperature and heat flux measurement, the impact of noise on the pressure signal is respected by means of a "type A" evaluation of voltage values in nearly steady-state conditions. The experimental standard deviation of the individual observations (equation (4-19)) of the voltage signal U_p is in the range of 10^{-4} V which corresponds to approx. 10^{-4} kPa. This value is considerably smaller than other uncertainty contributions and is thus neglected in the analysis.

Including all relevant sources of measurement deviation and the sensor's sensitivity of $S_p = \frac{10\,V - 0\,V}{10\,kPa - 0\,kPa} = 1\,\frac{V}{kPa}$ the functional relation for the pressure measurement can be expressed as

$$p_{vc} = \frac{U_p + \Delta U_{p,DAQ}}{S_p} + \Delta p_{p,cal} + \Delta p_{p,\vartheta} + \Delta p_{p,drift} \tag{B-32}$$

According to equation (4-23) the combined standard uncertainty for pressure measurement is

$$u_c(p_{vc}) = \sqrt{\begin{matrix}\left(\frac{\partial p_{vc}}{\partial \Delta U_{p,DAQ}} \cdot u\left(\Delta U_{p,DAQ}\right)\right)^2 + \left(\frac{\partial p_{vc}}{\partial \Delta p_{p,cal}} \cdot u\left(\Delta p_{p,cal}\right)\right)^2 \\ + \left(\frac{\partial p_{vc}}{\partial \Delta p_{p,\vartheta}} \cdot u\left(\Delta p_{p,\vartheta}\right)\right)^2 + \left(\frac{\partial p_{vc}}{\partial \Delta p_{p,drift}} \cdot u\left(\Delta p_{p,drift}\right)\right)^2\end{matrix}} \tag{B-33}$$

with the uncertainty contributions and sensitivity coefficients specified in Table 14.

Table 14: Uncertainty contributions and sensitivity coefficients of pressure measurement

$\frac{\partial p_{vc}}{\partial \Delta U_{p,DAQ}} = \frac{1}{S_p}$
$u\left(\Delta U_{p,DAQ}\right) = \frac{(5\cdot 10^{-5} + 5\cdot 10^{-6}\frac{1}{K}\cdot 4K)\cdot U_p + (4\cdot 10^{-5} + 5\cdot 10^{-6}\frac{1}{K}\cdot 4K)\cdot 10V}{3}$
$\frac{\partial p_{vc}}{\partial \Delta p_{p,cal}} = 1$
$u\left(\Delta p_{p,cal}\right) = \begin{cases} \frac{0.002\cdot p_{vc}}{\sqrt{3}} & for\, 0.133\ kPa \le p_{vc} \le 133\ kPa \\ \frac{0.004\cdot p_{vc}}{\sqrt{3}} & for\, p_{vc} < 0.133\ kPa \end{cases}$
$\frac{\partial p_{vc}}{\partial \Delta p_{p,\vartheta}} = 1$
$u\left(\Delta p_{p,\vartheta}\right) = \frac{(0.0001\ K^{-1}\cdot 10\ kPa + 0.0002\ K^{-1}\cdot p_{vc})\cdot(20°C - \overline{\vartheta_{cc}})}{\sqrt{3}}$
$\frac{\partial p_{vc}}{\partial \Delta p_{p,drift}} = 1$
$u\left(\Delta p_{p,drift}\right) = 1.5\cdot 10^{-3} kPa$

B.7.4 Uncertainty of Temperature at the Structure Base

Applying the uncertainty propagation approach (equation (4-23)) under the assumption of uncorrelated input quantities to equation (4-7), the combined standard uncertainty $u_c(\vartheta_{strb})$ for the structure base temperature can be calculated:

$$u_c(\vartheta_{strb}) = \sqrt{\begin{matrix}\left(\frac{\partial \vartheta_{strb}}{\partial \vartheta_{crr}} \cdot u_c(\vartheta_{crr})\right)^2 + \left(\frac{\partial \vartheta_{strb}}{\partial \dot{q}_{hfs}} \cdot u_c(\dot{q}_{hfs})\right)^2 \\ + \left(\frac{\partial \vartheta_{strb}}{\partial \Delta z_{strb,mp}} \cdot u(\Delta z_{strb,mp})\right)^2 + \left(\frac{\partial \vartheta_{strb}}{\partial \lambda_{crr}} \cdot u(\lambda_{crr})\right)^2\end{matrix}} \tag{B-34}$$

The uncertainty of the distance between structure base and temperature measuring height $u(\Delta z_{strb,mp})$ is derived from the manufacturing tolerance of the drill hole position of +/- 0.05 mm and the possible off-centered positioning of the sensor inside the drill hole due to the gap width of 0.1 mm. Presuming the sum of these values to be an error limit with rectangular probability distribution $u(\Delta z_{strb,mp})$ is estimated according to equation (4-22). The uncertainty of the thermal conductivity of the sample carrier $u(\lambda_{crr})$ is estimated as 10 W/(m K), considering the variance of individual alloy compositions, different literature data and the temperature dependence of the conductivity.

The assumption of a linear temperature gradient in the sample carrier in heat flow direction is generally only valid for steady-state heat conduction, which is not the case for the presented measurements. Therefore the approximation for ϑ_{strb} involves an inaccuracy. In order to estimate this inaccuracy the response behavior of the carrier element between temperature sensor level and top of the carrier (= structure base) to a temperature step input is considered: Modelling the carrier element (index “el”) as a RC unit consisting of a resistor and a capacitance its time constant is

$$\tau_{el} = R_{el} \cdot C_{el} = \frac{\Delta z_{strb,mp}^2 \cdot \rho_{crr} \cdot c_{crr}}{\lambda_{crr}} \approx 0.02s \tag{B-35}$$

(Equation (B-35) employs the distance between structure base plane and temperature sensor axis: $\Delta z_{strb,mp} = 1.5\ mm$, the density of the sample carrier material (Cu-ETP): $\rho_{crr} = 8930\ kg/m^3$, the specific heat capacity of the carrier (Cu-ETP): $c_{crr} = 386\ J/(kgK)$, the thermal conductivity of the carrier (Cu-ETP): $\lambda_{crr} = 394\ W/(mK)$; the latter three values adopted from (Deutsches Kupferinstitut 2005).) According to the exponential asymptotic behavior of an RC element, after a time delay of 3τ the output has reached 95% of the step input amplitude. Applied to the measurement situation, $3\tau = 0.06s$ after a step shaped change in the temperature ϑ_{strb} the temperature on sensor height ϑ_{crr} would have reached 95% of the step amplitude. Since both the scanning interval of the temperature sensor (approx. 2 s) and the response time of the sensor are considerably longer, the impact of the non-linear temperature gradient within the carrier on the determined temperature at the structure base ϑ_{strb} is considered negligible and not included in the combined uncertainty.

The combined standard uncertainties of the carrier temperature $u_c(\vartheta_{crr})$ and of the heat flux through the heat flux sensor $u_c(\dot{q}_{hfs})$ are employed as calculated in appendix B.7.1 and B.7.2. Sensitivity coefficients and uncertainty values of the other contributions are listed up in Table 15.

Table 15: Uncertainty contributions and sensitivity coefficients of the temperature at the structure base ϑ_{strb}

$\frac{\partial \vartheta_{strb}}{\partial \vartheta_{crr}} = 1$
$\frac{\partial \vartheta_{strb}}{\partial \dot{q}_{hfs}} = -\frac{\Delta z_{strb,mp}}{\lambda_{crr}}$
$\frac{\partial \vartheta_{strb}}{\partial \Delta z_{strb,mp}} = -\frac{\dot{q}_{hfs}}{\lambda_{crr}}$
$u(\Delta z_{strb,mp}) = \frac{(5+10)\cdot 10^{-5} m}{\sqrt{3}}$
$\frac{\partial \vartheta_{strb}}{\partial \lambda_{crr}} = \frac{\Delta z_{strb,mp}}{\lambda_{crr}^2} \cdot \dot{q}_{hfs}$
$u(\lambda_{crr}) = 10\ W/(m\ K)$

B.7.5 Uncertainty of Effective Evaporation Heat Flux

For the combined uncertainty of the evaporation heat flow $u_c(\dot{Q}_{ev})$ the uncertainty inputs from the heat flow through the heat flux sensor $u_c(\dot{Q}_{hfs})$ and from the capacitive heat flow in the sample carrier $u_c(\dot{Q}_{cap})$ are required. All sensitivity coefficients and numerical values of uncertainty contributions for these combined uncertainties – which are discussed below – are listed up in Table 16.

Derived from equation (4-8) and the law of propagation of uncertainty for uncorrelated inputs (equation (4-23)), the combined uncertainty $u_c(\dot{Q}_{hfs})$ of the heat flow through the heat flux sensor reads:

$$u_c(\dot{Q}_{hfs}) = \sqrt{\left(\frac{\partial \dot{Q}_{hfs}}{\partial \dot{q}_{hfs}} \cdot u_c(\dot{q}_{hfs})\right)^2 + \left(\frac{\partial \dot{Q}_{hfs}}{\partial A_{hfs}} \cdot u(A_{hfs})\right)^2} \tag{B-36}$$

The uncertainty of the cross-sectional area of the heat flux sensor $u(A_{hfs})$ is assessed from an estimated tolerance of $a = \pm 3 \cdot 10^{-5} m^2$ (which corresponds to a diameter tolerance of 0.5 mm) and equation (4-22).

The approximation of the capacitive heat flow $\dot{Q}_{cap}$ in equation (4-11) includes measured values of the sample carrier temperature at two different times, $\vartheta_{crr}(t_{i+1})$ and $\vartheta_{crr}(t_{i-1})$. Given that these values are recorded with the same sensor, they have to be considered as correlated input quantities. Consequently, the uncertainty propagation approach for uncorrelated quantities in equation (4-23) cannot be applied. For reasons of simplification and for making a conservative assessment, not the universal equation for correlated input quantities (equation (4-25)) is applied but as a "worst-case estimation" the approach for fully correlated input quantities in equation (4-26) is used instead. Accordingly, the combined standard uncertainty of $\dot{Q}_{cap}$ becomes:

$$\begin{aligned} u_c(\dot{Q}_{cap}(t_i)) = &\left|\frac{\partial \dot{Q}_{cap}}{\partial \vartheta_{crr}(t_{i+1})} \cdot u(\vartheta_{crr}(t_{i+1}))\right| + \left|\frac{\partial \dot{Q}_{cap}}{\partial \vartheta_{crr}(t_{i-1})} \cdot u(\vartheta_{crr}(t_{i-1}))\right| \\ &+ \left|\frac{\partial \dot{Q}_{cap}}{\partial M_{crr}} \cdot u(M_{crr})\right| + \left|\frac{\partial \dot{Q}_{cap}}{\partial c_{crr}} \cdot u(c_{crr})\right| \end{aligned} \tag{B-37}$$

To the time values occurring in equation (4-11), t_{i+1} and t_{i-1}, no uncertainty components are assigned since t_{i+1} and t_{i-1} refer to the inaccuracy of absolute time stamps which is assumed to be very small

compared to other uncertainty sources. The uncertainty of the carrier mass $u(M_{crr})$ is estimated as 0.5 g based on weighing of several carrier specimens. For the uncertainty of the carrier's specific hat capacity a value of $u(c_{crr}) = 10\,J/(kg\,K)$ is assesed, based on different literature specifications and respecting potential differences of individual alloys and the temperature dependence. The combined standard uncertainties of the carrier temperature for the different time steps are inserted as calculated in B.7.1.

The fact that $\dot{Q}_{cap}$ is only determined by an approximation inevitably entails a certain inaccuracy, especially in pronounced dynamic periods. In order to assess this inaccuracy, the time constant of the whole sample carrier τ_{crr} is calculated, analogous to the approach for ϑ_{strb} (equation (B-35)) (with same material constants, but the height of the carrier h_{crr}):

$$\tau_{crr} = R_{crr} \cdot C_{crr} \approx \frac{h_{crr} \cdot \rho_{crr} \cdot c_{crr}}{\lambda_{crr}} \approx 0.14s \tag{B-38}$$

Assuming an input temperature step at the structure base (e.g. due to sudden transition from pool boiling to capillary assisted evaporation with different heat transfer coefficients) the temperature at the bottom of the carrier – where the response is the slowest – would approximately reach 95% of its steady-state value after $3\tau_{crr} \approx 0.42s$. Inserting the duration of two scanning time intervals $t_{i+1} - t_{i-1} \approx 4s$ (as used for the balance in equation (4-11)) and τ_{crr} as the maximum time constant into the step response function

$$\frac{\vartheta(t)}{\vartheta_{\infty}} = 1 - e^{-t/\tau} \tag{B-39}$$

a value of $\vartheta_{crr}(t = 4s)/\vartheta_{crr,\infty} = 1$ results (based on a common resolution of decimal places) which means that the temperature at every point of the carrier has reached its stationary value. Consequently, all capacitive heat associated with the input temperature step would be covered by evaluating the temperature difference measured at t_{i-1} and t_{i+1}. Equation (4-11) is thus regarded as very accurate for determining the capacitive heat flow in the sample carrier, even if it provides an average value of the evaluation interval. An uncertainty is accordingly not assigned.

With the functional relation of $\dot{Q}_{ev}$ in equation (4-9) and the uncertainty propagation approach in equation (4-23) – all input quantities are assumed to be uncorrelated – the combined standard uncertainty of the evaporation heat flow $u_c(\dot{Q}_{ev})$ can be determined:

$$u_c(\dot{Q}_{ev}) = \sqrt{\left(\frac{\partial \dot{Q}_{ev}}{\partial \dot{Q}_{hfs}} \cdot u_c(\dot{Q}_{hfs})\right)^2 + \left(\frac{\partial \dot{Q}_{ev}}{\partial \dot{Q}_{cap}} \cdot u_c(\dot{Q}_{cap})\right)^2} \tag{B-40}$$

The combined standard uncertainty for the effective evaporation heat flux $\dot{q}_{ev}$ is calculated with equations (4-12) and (4-23), presuming uncorrelated input quantities:

$$u_c(\dot{q}_{ev}) = \sqrt{\left(\frac{\partial \dot{q}_{ev}}{\partial \dot{Q}_{ev}} \cdot u_c(\dot{Q}_{ev})\right)^2 + \left(\frac{\partial \dot{q}_{ev}}{\partial A_{str}} \cdot u(A_{str})\right)^2} \tag{B-41}$$

For the uncertainty of the cross-sectional area of the sample structure $u(A_{str})$ error limits of $a = \pm 6 \cdot 10^{-5} m^2$ are set, which corresponds to a diameter tolerance of about 1 mm.

Table 16: Uncertainty contributions and sensitivity coefficients of the effective evaporation heat flux $\dot{q}_{ev}$

$\frac{\partial \dot{Q}_{hfs}}{\partial \dot{q}_{hfs}} = A_{hfs}$
$\frac{\partial \dot{Q}_{hfs}}{\partial A_{hfs}} = \dot{q}_{hfs}$
$u(A_{hfs}) = \frac{3 \cdot 10^{-5} m^2}{\sqrt{3}}$
$\frac{\partial \dot{Q}_{cap}}{\partial \vartheta_{crr}(t_{i+1})} = \frac{M_{crr} \cdot c_{crr}}{t_{i+1} - t_{i-1}}$
$\frac{\partial \dot{Q}_{cap}}{\partial \vartheta_{crr}(t_{i-1})} = -\frac{M_{crr} \cdot c_{crr}}{t_{i+1} - t_{i-1}}$
$\frac{\partial \dot{Q}_{cap}}{\partial M_{crr}} = c_{crr} \cdot \frac{\vartheta_{crr}(t_{i+1}) - \vartheta_{crr}(t_{i-1})}{t_{i+1} - t_{i-1}}$
$u(M_{crr}) = 5 \cdot 10^{-4} kg$
$\frac{\partial \dot{Q}_{cap}}{\partial c_{crr}} = M_{crr} \cdot \frac{\vartheta_{crr}(t_{i+1}) - \vartheta_{crr}(t_{i-1})}{t_{i+1} - t_{i-1}}$
$u(c_{crr}) = 10\, J/(kg\, K)$
$\frac{\partial \dot{Q}_{ev}}{\partial \dot{Q}_{hfs}} = 1$
$\frac{\partial \dot{Q}_{ev}}{\partial \dot{Q}_{cap}} = -1$
$\frac{\partial \dot{q}_{ev}}{\partial \dot{Q}_{ev}} = \frac{1}{A_{str}}$
$\frac{\partial \dot{q}_{ev}}{\partial A_{str}} = -\frac{\dot{Q}_{ev}}{A_{str}^2}$
$u(A_{str}) = \frac{6 \cdot 10^{-5} m^2}{\sqrt{3}}$

B.7.6 Uncertainty of Saturation Temperature

According to the functional relation of p_{sat} in equation (4-13) the combined uncertainty of the vapor pressure above the sample structure $u_c(p_{sat})$ depends on the uncertainty components of the vacuum chamber pressure p_{vc} and of the pressure rise rate $(\Delta p/\Delta t)_{leak}$. The time lag since end of evacuation Δt_{leak} is not considered to involve an uncertainty contribution due to the rather high accuracy of time measurement. Since both vapor pressure and pressure rise rate are based on pressure measurement they are regarded as correlated input quantities and as a conservative approach equation (4-26) for fully correlated input quantities is applied:

$$u_c(p_{sat}) = \left|\frac{\partial p_{sat}}{\partial p_{vc}} \cdot u_c(p_{vc})\right| + \left|\frac{\partial p_{sat}}{\partial (\Delta p/\Delta t)_{leak}} \cdot u((\Delta p/\Delta t)_{leak})\right| \qquad \text{(B-42)}$$

As described in appendix B.6 the leak rate (and pressure rise rate) of the vacuum system was determined from a pressure rise measurement. Since the vacuum system is opened and closed with each new sample installation the leak rate might vary slightly for each measurement. Consequently, an uncertainty is presumed for the pressure rise rate which is – as a best guess – defined equal to the measured pressure rise rate itself: $u((\Delta p/\Delta t)_{leak}) \stackrel{\text{def}}{=} (\Delta p/\Delta t)_{leak} = 2.25 \cdot 10^{-5} Pa/s$.

Derivatives and uncertainty components of equation (B-42) are specified in Table 17.

Respecting that the IAPWS formulations of the saturation pressure and – as the inverse equation – the saturation temperature are approximations, they involve a certain inaccuracy. Using a notation with the expected value plus deviation components and employing the deviation caused by the saturation pressure formulation $\Delta p_{sat,appr}$, the saturation temperature ϑ_{sat} can be described as:

$$\vartheta_{sat} = f\left(p_{sat} + \Delta p_{sat} + \Delta p_{sat,appr}\right) \tag{B-43}$$

For the calculation of the combined standard uncertainty $u_c(\vartheta_{sat})$ the law of uncertainty propagation for uncorrelated input quantities (equation (4-23)) is used. In principle, the uncertainty of the saturation curve approximation is correlated to the pressure (The International Association for the Properties of Water and Steam 2007, Fig. 6) but since a maximum estimation for $u(\Delta p_{sat,appr})$ is used, the input quantities are regarded as uncorrelated. $u_c(\vartheta_{sat})$ then is:

$$u_c(\vartheta_{sat}) = \sqrt{\left(\frac{\partial f}{\partial \Delta p_{sat}} \cdot u(\Delta p_{sat})\right)^2 + \left(\frac{\partial f}{\partial \Delta p_{sat,appr}} \cdot u\left(\Delta p_{sat,appr}\right)\right)^2} \tag{B-44}$$

According to (Joint Committee for Guides in Metrology 2008) the derivatives in the uncertainty propagation equation are evaluated in the point of the estimate, therefore we can write:

$$\frac{\partial f}{\partial p_{sat}} = \frac{\partial f}{\partial \Delta p_{sat}} = \frac{\partial f}{\partial \Delta p_{sat,appr}} = \left.\frac{\partial \vartheta_{sat}}{\partial p_{sat}}\right|_{p_{sat}(t_i)} \tag{B-45}$$

Inserting equation (B-45) into (B-44) $u_c(\vartheta_{sat})$ becomes:

$$u_c(\vartheta_{sat}) = \sqrt{\left(\left.\frac{\partial \vartheta_{sat}}{\partial p_{sat}}\right|_{p_{sat}(t_i)} \cdot u(\Delta p_{sat})\right)^2 + \left(\left.\frac{\partial \vartheta_{sat}}{\partial p_{sat}}\right|_{p_{sat}(t_i)} \cdot u\left(\Delta p_{sat,appr}\right)\right)^2} \tag{B-46}$$

(The International Association for the Properties of Water and Steam 2007, Fig. 6) specifies the "Uncertainties in saturation pressure, $\Delta p_S/p_S$" for IAPWS IF-97 formulation in the relevant temperature interval to be maximum 0.03%. Since it is unclear if this value is meant as a relative standard uncertainty or error limit, it is taken as uncertainty as a conservative estimation, which yields $u\left(\Delta p_{sat,appr}\right) = 0.0003 \cdot p_{sat}$.

To avoid forming the derivative $\partial \vartheta_{sat}/\partial p_{sat}$ of the complex saturation temperature curve formulation, the following linear approximation is used to estimate the local slope of the curve at the point $p_{sat}(t_i)$ (with $\varepsilon = 10^{-3} Pa$):

$$\left.\frac{\partial \vartheta_{sat}}{\partial p_{sat}}\right|_{p_{sat}(t_i)} \approx \frac{\vartheta_{sat}(p_{sat}(t_i) + \varepsilon) - \vartheta_{sat}(p_{sat}(t_i) - \varepsilon)}{2 \cdot \varepsilon} \tag{B-47}$$

Again, derivatives and uncertainty components are specified in Table 17.

Table 17: Uncertainty contributions and sensitivity coefficients of the saturation temperature ϑ_{sat}

$\frac{\partial p_{sat}}{\partial p_{vc}} = 1$
$\frac{\partial p_{sat}}{\partial (\Delta p/\Delta t)_{leak}} = -\Delta t_{leak}$
$u((\Delta p/\Delta t)_{leak}) \stackrel{\text{def}}{=} (\Delta p/\Delta t)_{leak} = 2.25 \cdot 10^{-5} Pa/s$
$\frac{\partial \vartheta_{sat}}{\partial p_{sat}} = \frac{\vartheta_{sat}(p_{sat}(t_i)+\varepsilon) - \vartheta_{sat}(p_{sat}(t_i)-\varepsilon)}{2 \cdot \varepsilon}$
$u(\Delta p_{sat}) = u_c(p_{sat})$
$u(\Delta p_{sat,appr}) = 0.0003 \cdot p_{sat}$

B.7.7 Uncertainty of the Overall Heat Transfer Coefficient of Evaporation

Based on the equation for the driving temperature difference (implicit in equation (4-4)) its combined uncertainty can be calculated with equation (B-48). All input quantities are assumed to be uncorrelated. The derivatives are specified in Table 18.

$$u_c(\Delta\vartheta) = \sqrt{\left(\frac{\partial \Delta\vartheta}{\partial \vartheta_{strb}} \cdot u_c(\vartheta_{strb})\right)^2 + \left(\frac{\partial \Delta\vartheta}{\partial \vartheta_{sat}} \cdot u_c(\vartheta_{sat})\right)^2} \tag{B-48}$$

As equation (4-4) reveals, the input quantities of the evaporation heat transfer coefficient U_{ev} are $\dot{q}_{ev}$ and $\Delta\vartheta$, which both indirectly include the sample carrier temperature ϑ_{crr} in their calculation chain. Consequently, they are correlated quantities and equation (4-23) is not valid for the determination of the combined standard uncertainty $u(U_{ev})$. Instead, $u(U_{ev})$ is calculated with the "worst-case approach" for correlated input quantities in equation (4-26):

$$u_c(U_{ev}) = \left|\frac{\partial U_{ev}}{\partial\, \dot{q}_{ev}} \cdot u(\dot{q}_{ev})\right| + \left|\frac{\partial U_{ev}}{\partial \Delta\vartheta} \cdot u(\Delta\vartheta)\right| \tag{B-49}$$

Table 18: Uncertainty contributions and sensitivity coefficients of the overall heat transfer coefficient of evaporation U_{ev}

$\frac{\partial \Delta\vartheta}{\partial \vartheta_{strb}} = 1$
$\frac{\partial \Delta\vartheta}{\partial \vartheta_{sat}} = -1$
$\frac{\partial U_{ev}}{\partial\, \dot{q}_{ev}} = \frac{1}{\Delta\vartheta}$
$\frac{\partial U_{ev}}{\partial \Delta\vartheta} = -\frac{\dot{q}_{ev}}{\Delta\vartheta^2}$

B.7.8 Uncertainty of Refrigerant Mass

Based on equation (4-15) and the uncertainty propagation law in equation (4-23) the combined standard uncertainty for the evaporation mass flux $u_c(\dot{M}_{vap})$ is calculated. Input quantities are assumed to be uncorrelated.

$$u_c(\dot{M}_{vap}) = \sqrt{\left(\frac{\partial \dot{M}_{vap}}{\partial \dot{Q}_{ev}} \cdot u_c(\dot{Q}_{ev})\right)^2 + \left(\frac{\partial \dot{M}_{vap}}{\partial \Delta h_v} \cdot u(\Delta h_v)\right)^2} \tag{B-50}$$

The "absolute uncertainties" for the enthalpy of vaporization after IAPWS-IF97 formulation are specified for the relevant temperature range as 0.5 kJ/kg in (The International Association for the Properties of Water and Steam 2003, Fig. 8). This value is taken as a standard uncertainty $u(\Delta h_v)$. Derivatives and numerical values of equation (B-50) are listed up in Table 19.

The input quantities of the equation for the cumulated refrigerant mass M_{cum} (equation (4-16), p. 62) are correlated because the equation employs vapor mass flow values of different time steps, which depend on data from the same measurement devices. Accordingly, equation (4-26) for correlated input quantities is used as a "worst-case" estimation:

$$u_c(M_{cum}(t_i)) = \sum_{j=2}^{i} \left|\frac{\partial M_{cum}(t_i)}{\partial \dot{M}_{vap}(t_j)} \cdot u\left(\dot{M}_{vap}(t_j)\right)\right| = \sum_{j=2}^{i} \left|(t_j - t_{j-1}) \cdot u\left(\dot{M}_{vap}(t_j)\right)\right| \tag{B-51}$$

Like the functional equation of $M_{cum}(t_i)$, equation (B-51) is only valid for $2 \leq i \leq n$ and the initial condition is set to $u_c(M_{cum}(t_1 = 0)) = 0$. Just like in the calculation of the $u_c(\dot{Q}_{cap})$ no uncertainty is assigned to the time values t_j and t_{j-1} occurring in the function of M_{cum} because time stamps are expected to be very exact.

The combined standard uncertainty of the refrigerant inside the sample structure $u_c(M_{rf})$ is again determined with the "worst-case" approach for uncertainty propagation (equation (4-26), p. 66) since the input quantities of the functional relation (equation (4-17), p. 62) – which are $\dot{M}_{vap}(t_j)$ of different time steps j – are correlated:

$$u_c\left(M_{rf}(t_i)\right) = \sum_{j=i+1}^{n} \left|\frac{\partial M_{rf}(t_i)}{\partial \dot{M}_{vap}(t_j)} \cdot u\left(\dot{M}_{vap}(t_j)\right)\right| = \sum_{j=i+1}^{n} \left|(t_j - t_{j-1}) \cdot u\left(\dot{M}_{vap}(t_j)\right)\right| \tag{B-52}$$

Generally, the uncertainty of the refrigerant mass involves additional uncertainty sources due to the simplifying assumptions that the structure is completely dry at the end of the measurement ($M_{rf}(t_n) = 0$) and that change in refrigerant mass is only caused by evaporation ($dM_{rf}/dt = -dM_{cum}/dt = -\dot{M}_{vap}$). Both assumptions lead to the condition $M_{rf}(t_1 = 0) = M_{cum}(t_n)$ and involve uncertainties. Given that the residual refrigerant mass at the end of the measurement and the refrigerant losses due to squirting cannot be quantified reasonably, these uncertainty components cannot be quantified either and need to be considered in the interpretation of the measurement results.

Table 19: Uncertainty contributions and sensitivity coefficients of the refrigerant mass M_{rf}

$\frac{\partial \dot{M}_{vap}}{\partial \dot{Q}_{ev}} = \frac{1}{\Delta h_v}$
$\frac{\partial \dot{M}_{vap}}{\partial \Delta h_v} = -\frac{\dot{Q}_{ev}}{\Delta h_v^2}$
$u(\Delta h_v) = 500\ J/kg$

C Model

C.1 Geometry and Material Data Employed in the Model

Table 20: Geometry and material data employed in the model

Symbol	Unit	Value	Denotation	Reference
c_{CuETP}	$J/(kg\ K)$	386	specific heat capacity of CuETP (at 20°C)	(Deutsches Kupferinstitut 2005)
D_{crr}	mm	40	diameter of sample carrier	CAD drawing
$D_{htr,tb}$	mm	62	diameter of the large-diameter section of the upper part of the heater block	CAD drawing
$D_{htr,tt}$	mm	39.9	diameter of the small-diameter section of the upper part of the heater block	CAD drawing
D_{str}	mm	40	diameter of porous sample structure	-
h_{adf}	mm	0.13	thickness of adhesive foil	data sheet 3M VHB 9469
h_{crr}	mm	4	height of sample carrier	CAD drawing
$h_{hfs,Cu}$	mm	0.3	thickness of each copper layer of heat flux sensor	(Captec SARL 2015)
$h_{hfs,epx}$	mm	0.15	thickness of epoxy layer inside heat flux sensor	derived from (Captec SARL 2015)
$h_{htr,tb}$	mm	6	height of large-diameter section of upper part of heater block	CAD drawing
$h_{htr,tt}$	mm	9.5	height of small-diameter section of upper part of heater block	CAD drawing
h_{tcf}	mm	0.5	thickness of thermally conductive foil	(Röckelein GmbH 2010)
M_{H2O}	kg/mol	0.01801528	molar mass of water vapor (derived from atomic weights of hydrogen and oxygen)	(Wieser 2006)
R_{H2O}	$J/(kg\ K)$	461.5	specific gas constant of water vapor (calculated from $R_{H2O} = R_{univ}/M_{H2O}$)	-
R_{univ}	$J/(mol\ K)$	8.3144598	universal gas constant	(National Institute of Standards and Technology 1998)
V_{crr}	l	0.005	volume of sample carrier	CAD drawing
V_{htr}	l	0.04	total volume of heater block (top + bottom part)	CAD drawing
λ_{adf}	$W/(m\ K)$	0.16	thermal conductivity of adhesive foil	data sheet 3M VHB 9469
λ_{CuETP}	$W/(m\ K)$	394	thermal conductivity of CuETP (at 20°C)	(Deutsches Kupferinstitut 2005)
λ_{epx}	$W/(m\ K)$	0.34	thermal conductivity of epoxy resin (average of different specifications)	(Czichos and Hennecke 2008, D72, Tab. 9-6)
λ_{sldr}	$W/(m\ K)$	61	thermal conductivity of solder material (estimation with value of solder alloy Sn97Cu3)	(MakeItFrom.com 2009)
λ_{tcf}	$W/(m\ K)$	3	thermal conductivity of thermally conductive foil	(3M Company 2010)
ρ_{CuETP}	kg/m^3	8930	density of CuETP (at 20°C)	(Deutsches Kupferinstitut 2005)